Imperial College of Science, Technology and Medicine

Royal School of Mines

Department of Earth Science and Engineering

# Integrated Modelling of the Thermal, Chemical and Geomechanical Processes in Underground Coal Gasification

**By**

**Epameinondas Andrianopoulos**

A thesis submitted for the degree of

Doctor of Philosophy of Imperial College London

September 2017

# Abstract

The considerate focus on unconventional fossil fuel resources is a natural consequence of emerging global energy requirements and the ever more limited opportunities to deploy new conventional resources. Underground Coal Gasification (UCG) is an unconventional method for recovering energy from coal resources through in-situ conversion to gas. An oxidising gas agent is injected to initiate and sustain the in-situ coal gasification. The quality of the collected product syngas is characterised by its carbon monoxide (CO), hydrogen ($H_2$) and methane ($CH_4$) content. However, as it is an unconventional method of energy production it evolves through research conducted through modelling studies, laboratory and in-situ trials which support this evolution process.

The purpose of this PhD research project is to identify and model the critical parameters which will give increased control on the underground process and ultimately the composition of the final syngas product. In order to achieve this objective, it is necessary to breakdown the UCG process to interrelated stages and design component models that realistically simulate the chemical and physical processes that take place. In the core of the UCG lays the coal gasification process and the simultaneous cavity growth within the coal seam and these will be studied as part of this PhD research. An integrated simulation methodology, which considers the thermal, chemical and geomechanical processes has led to the development of the coupled Thermo-Mechanical-Chemical (TMC) model. Experimental and literature data is used to validate and calibrate the developed models. In addition to increased understanding of the UCG process and its control, this research allows for UCG investors to maximise the financial value sourced from the end-product gas as well as reduce the risk of making unprofitable investments.

A number of geologically representative UCG scenarios are simulated through the developed TMC model. The scenarios aim at evaluating the impact of various operational parameters to the UCG operation.

The coal panel thickness, the panel depth below the surface, the operating pressure, the type of the injected agent as well as the type of coal where UCG takes place are among the tested parameters.

The simulation methodology is based on coupling two industry standard simulators, Advanced System for Process ENgineering (ASPEN) Plus, used for the thermo-chemical simulation, and FLAC$^{3D}$, which enables the thermo-mechanical simulation of the UCG process. The coupling of the two simulation tools is achieved through sequential interchange of data and through the development of an additional transitional Gasification Support module. The Gasification Support module facilitates the exchange of data between the two simulators and focus on the participating heat and mass transport phenomena within the growing UCG cavity.

Principally, the Aspen Plus model simulates the chemical processes taking place in the coal seam and focuses on the thermodynamic, mass and heat transfer modelling components in order to calculate the amount of produced heat, as well as gas under restricted Gibbs minimisation and equilibrium conditions. In addition to the different chemical reactors that constitute the Aspen Plus model constructed, calculator blocks written in Fortran code were introduced to regulate modelling performance in line with experimental data. The Aspen Plus simulation also facilitated the development of different process designs depending on the employed UCG layout (i.e. Linked Vertical Wells, Continuous Retracting Injection Point). The FLAC$^{3D}$ model reflects realistically the 3D spatial features of a gasified coal seam underground. This module produces the resulting thermo-mechanical stress distributions on the coal seam and the surrounding strata, taking account of both mechanical failure and coal spalling effects, heat transfer rates within the cavity and the surrounding strata.

The cavity growth modelling results include the extent and the growth rate of the developing UCG cavity given the specified operational parameters such as the coal characteristics (e.g. composition, formation thickness, depth), the composition of reagents injected (i.e. air, oxygen, steam) and the feed rate, the pressure, the gasification and the combustion temperatures. In addition, the UCG product gas characteristics (e.g. composition, heating value) and the participating heat and mass transfer phenomena are also analysed in comparison with the operational parameters of the UCG process.

*DEDICATED TO MY PARENTS*

## Affirmation

The work submitted in this thesis is my own and has not been submitted previously for any other degree. The following publications and presentations have resulted from this work:

E. Andrianopoulos, A. Korre, S. Durucan, 2015, Chemical Process Modelling of Underground Coal Gasification and Evaluation of Produced Gas Quality for End Use, Energy Procedia, Volume 76, Pages 444-453, ISSN 1876-6102, http://dx.doi.org/10.1016/j.egypro.2015.07.870.

E. Andrianopoulos, A. Korre, S. Durucan, S. Franzsen, 2016, Coupled Thermo-Mechanical-Chemical modelling of underground coal gasification, In: Zdravko Kravanja and Miloš Bogataj, Editor(s), Computer Aided Chemical Engineering, Elsevier, Volume 38, Pages 1069-1074, ISSN 1570-7946, ISBN 9780444634283, http://dx.doi.org/10.1016/B978-0-444-63428-3.50183-1.

S. Durucan, A. Korre, E. Andrianopoulos, G. Si, J-Q. Shi, S. Franzsen, 2016, Coupled Thermo-Chemical-Mechanical Modelling Of Cavity Growth And Far-field Geomechanical Assessment. In: Underground Coal Gasification, International Pittsburgh Coal Conference, 8$^{th}$ – 12$^{th}$ Aug, 2016, Cape Town, South Africa.

E. Andrianopoulos, A. Korre, S. Durucan*, G. Si, J-Q Shi, S. Franzsen, 2016, Coupled Thermo-Chemical-Mechanical-Modelling Of Underground Coal Gasification Cavity Growth. In: International Conference on Geomechanics, Geo-energy and Geo-resources (IC3G), 28$^{th}$ -29$^{th}$ Sept, 2016, Monash University, Melbourne, Australia.

## Copyright declaration

## Acknowledgements

I would like to thank my supervisors Professor Sevket Durucan and Professor Anna Korre for the considerable moral support they have provided me over the past 3 years. I also extend my thanks to the partners of the project: *Technology Options for Coupled Underground Coal Gasification and $CO_2$ Capture And Storage (TOPS-UCG).* Thanks to my colleagues and friends from the Mining and Environmental Engineering Research Group (MERG) who have accompanied and supported me through these years: Ji-Quan Shi, Zhenggang Nie, Rajesh Govindan, Guangyao Si, Mojgan Hadi Mosleh, Nasim Elahi, Maria Lathouri, Masoud Babaei, Amer Syed, Indranil Pan, Jorge de La Torre Guzman, Tareq Al Ansari, Saba Manzoor, Wenzhuo Cao and Betul Yildirim.
Thank you all!

Last, but definitely not the least, I would like to thank my family and my partner Stella for their support and constant encouragement.

# Table of Contents

# List of Figures

# List of Tables

# Chapter 1 Introduction and Objectives

## 1.1 *The Motivation for Underground Coal Gasification (UCG)*

According to the "Statistical Review of World Energy" published by BP in June 2016, there are contradictory energy observations between the countries included in the OECD (Organization for Economic Cooperation and Development) and the emerging economies. Overall, the universal primary energy use increased by 1.0% in 2015. This increase resulted from the increased energy consumption by the developing economies (non-OECD members), especially those of India (+5.2%) and China (+1.5%). Emerging economies accounted for 58.1% of global energy consumption and for 97% of the increase in 2015. Although China chronicled its 15$^{th}$ consecutive increase on its energy consumption reaching new record number, its percentage growth continued its decline. On the other hand, the energy consumption in Europe increased by 1.6% compensating for the decreases in US (-0.9%) and Japan (-1.2%). The global increase in energy consumption was lower than the 10-year average increase (+1.9%) while Russia reported the largest volumetric decrease globally. (BP plc, 2015)

Table 1.1 provides a detailed overview on how the different energy sectors in the different world regions progressed from 2014 to 2015.

**Table 1.1**: Percentage changes for the energy consumption in 2015 compared to 2014 (overall and per energy sector) (BP plc, 2015).

| **Incremental change in 2015 to 2014 (%)** | Total energy | Oil | Natural gas | Coal | Nuclear |
|---|---|---|---|---|---|
| India | + 5.2 | + 8.1 | - 0.1 | + 4.8 | + 9.5 |
| China | + 1.5 | + 6.3 | + 4.7 | - 1.5 | + 28.9 |
| US | - 0.9 | + 1.6 | + 3.0 | - 12.7 | - 0.05 |
| Europe | + 1.6 | + 1.5 | - 4.6 | - 1.8 | - 0.1 |
| Japan | - 1.2 | - 3.9 | - 3.9 | - 0.6 | - |

As Table 1.1 presents the nuclear energy consumption significantly increased (+28.9%) in China during 2015. In addition, India also reported a considerable increase (+9.5%) in its corresponding nuclear energy consumption levels. The facts shown in Table 1.1 provide the opportunity to discuss which factors decide the energy sources of the future. The World Energy Council (WEC) as published in its 2015$^{th}$ World Energy Issues Monitor (WEC, 2015) classifies the dominant factors that affect the world energy issues into four categories:

- Macroeconomic risk and vulnerabilities
- Energy policies and business environment
- Energy geopolitics and regional issues
- Energy vision and technology

The *Macroeconomic risk and vulnerabilities* category includes sub-categories such as the global recession, the volatility of energy prices, the energy affordability, the currency uncertainty and the possibility for large-scale accidents. This last sub-category can justify why Japan radically decreased its nuclear activities in 2014 compared to 2013 after its large scale accident (BP plc, 2015).

In addition the volatility of the energy prices and especially the rapid decrease of the oil prices – from $108 per barrel in January 2014 to below $50 in 2015 – can explain the reason that oil consumption had an increased share among the most regions and especially in India and China (Table 1.1).

The *Energy policies and business environment* category includes the uncertainty over the environmental regulations and the corresponding subsidies. In addition, it includes the development of the energy markets and the role of the interconnected and decentralised systems.

The *Energy geopolitics and regional issues* category addresses how the political reforms affect the energy market and especially analyses the global political fragility in an energy context.

Finally, the *Energy vision and technology* category assesses how the scientific progress on certain technological areas can benefit existing and new energy solutions (WEC, 2015). In this category, the progress of unconventional fossil fuels is included. Shale gas, oil shale and Underground Coal Gasification (UCG) are alternative forms of fossil fuels that can affect the energy market dynamics.

Regarding UCG, the specific focus on coal consumption figures is important. The challenge of achieving higher energy efficiency and more sustainable utilisation of this energy resource attracts higher focus every year. The worldwide utilisation of coal decreased by 1.8% in 2015 compared to 2014, in contrast to the annual average increase of the last 10 years (+2.9%). Coal consumption in the non-OECD and OECD countries decreased by 0.3% and 6.1% respectively in 2015 compared to 2014. However, out of the worldwide coal energy consumption in 2015 the proportions of the OECD and non-OECD members remained as high as 72.9% and 27.1% respectively (BP plc, 2015).

Regarding supply, the global decrease (4%) of coal-produced energy in 2015 compared to 2014 was mainly driven by the reduced production in China (2.0 %), which accounts for 47.7% of the available coal resources produced globally. In addition, a decrease of 10.4% in coal production in the US (controlling 11.9% of the global coal production) completes the supply-side overview (BP plc, 2015). As a result, the increase of the nuclear energy share in the non-OECD countries in combination with the reducing oil prices and the shrinking global energy needs decrease the role of coal as an energy source. Another interesting aspect is associated with the debate whether the available coal deposits are adequate enough to meet the increased global energy needs (WEC, 2010).

For this reason, a methodology has been developed to estimate the available coal resources (WEC, 2010). It identifies five categories with two of them to assess the recoverability of the resource and the remaining three the reliability of the coal quantity estimate (Table 1.2). The purpose is to minimise the risk and inconsistency for the available coal reserves. In addition, the 3x2 identification matrix can be facilitates the comparison of the available coal seams and prioritises the possible solutions for their exploitation (Table 1.2).

**Table 1.2**: Criteria for the classification of the available coal resources (WEC, 2010)

| Coal resource estimate | Recoverable | Non-recoverable |
|---|---|---|
| Proved (or measured) | ✓ | ✓ |
| Probable (or indicated) | ✓ | ✓ |
| Possible (or inferred) | ✓ | ✓ |

The criteria for the classification of the available coal resources are particularly important as they reveal the potential of UCG especially through the non-recoverable coal resources, which might become recoverable through UCG. In addition, different coal types facilitate different end-uses. Electricity generation, steel and aluminium production, cement manufacturing and as a liquid fuel are among them (WEC, 2010) while coal is the primary raw input for 33.3% of surface gasifiers worldwide (UCG-Engineering, 2006). From the lowest to the highest rank, coal types are classified as peat, lignite, sub-bituminous coal, bituminous coal and anthracite. Table 1.3 provides an overview of where the biggest coal reserves exist on a worldwide basis while classifying them according to the rank of coal they include.

**Table 1.3**: Indicative distribution of coal reserves on a worldwide basis (WEC, 2013)

| Proved reserves | Anthracite & Bituminous ($10^9$ T) | Sub-bituminous & Lignite ($10^9$ T) | Share of Total (%) |
|---|---|---|---|
| Main coal reserves (regionally) | | | |
| China | 62.2 | 52.3 | 12.8 |
| USA | 108.5 | 128.8 | 26.6 |
| Columbia | 6.8 | - | 0.8 |
| India | 56.1 | 4.5 | 6.8 |
| Australia | 37.1 | 39.3 | 8.6 |
| South Africa | 30.2 | - | 3.4 |
| Russia | 49.1 | 107.9 | 17.6 |
| EU | 4.8 | 51.2 | 6.3 |
| Total (globally) | 403.2 | 488.3 | - |

## 1.2 *Underground Coal Gasification (UCG) - Overview*

The considerate focus on unconventional fossil fuel resources is a natural consequence of increasing global energy requirements and the ever more limited opportunities to deploy new conventional resources.

In addition, the abundance of coal resources found in many countries has led to Underground Coal Gasification (UCG) concepts to become relevant one again since their initial appeal, recorded during the late 19th century (Self et al., 2012).

UCG is an unconventional method for recovering energy from coal resources through in-situ conversion to gas (Self et al., 2012). The quality of the collected product syngas is characterised by its carbon monoxide (CO), hydrogen ($H_2$) and methane ($CH_4$) content. UCG field applications have taken place in the past, particularly in USA, France, Spain and China (DTI, 2005; Kapusta and Stańczyk, 2011). However, the optimum control over the UCG process remains the main issue.

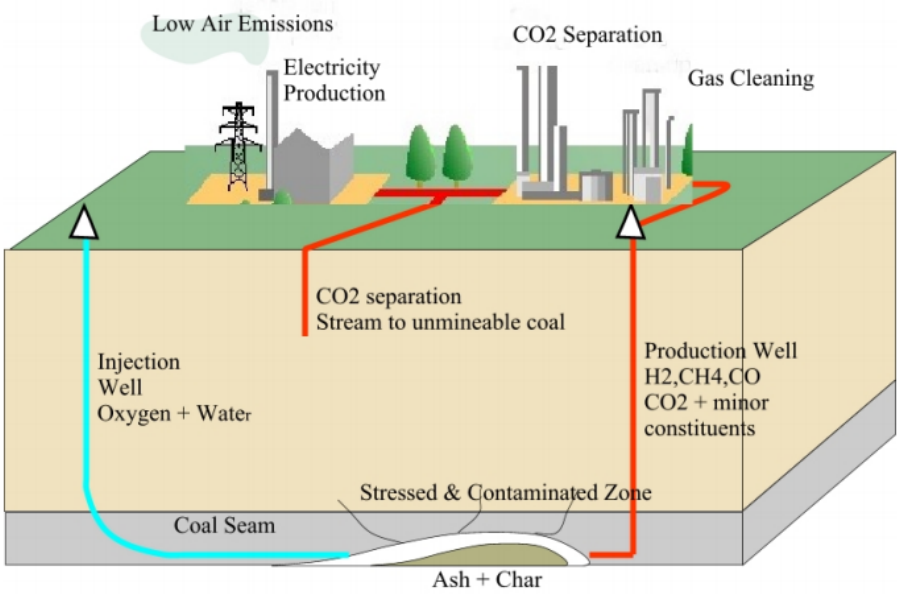


**Figure 1.1:** Simplified representation of the UCG process (DTI, 2005).

UCG operation involves the injection of a gasification reagent in the coal seam in order to ignite and burn the available coal in-situ. Depending on the composition of the produced syngas, it can be used either as a fuel or chemical feedstock (Kariznovi et al., 2013).

The main advantage of the UCG is the sustainable exploitation of coal resources which cannot be recovered under the conventional mining methods. In addition, UCG processes do not include any underground labour work, although land subsidence and groundwater reserve pollution through gas leakage incur serious safety concerns (Khadse et al., 2007). For this reason, modelling studies can reduce the risk offering increased control over the UCG processes.

## 1.3 *Knowledge gaps*

The detailed knowledge over the UCG processes is a prerequisite for its successful field application. This knowledge can occur either through experimental or modelling trials. However, experimental studies (either in-situ or ex-situ) are expensive and time-consuming (Nourozieh et al., 2010; Yang et al., 2014). As a result, modelling results remain the main tool for the decisions over the feasibility analysis, design and prediction of UCG operation. However, when the focus is on reliable models for three-dimensional UCG shapes, then serious concerns arise (Daggupati et al., 2011a; Daggupati et al., 2011b). Lack of such models is attributed to both the limited understanding of the UCG operations and the absence of proper software packages, which could provide a coherent overview of the process.

Many research studies (Daggupati et al., 2011a; Daggupati et al., 2011b; Sarraf Shirazi et al., 2011; Yang et al., 2014) recognise the need for a comprehensive as well as inclusive UCG model because the processes involved are remarkably complex. For instance, UCG involves physical and chemical processes such as homogenous and heterogeneous chemical reactions as well as heat and mass transport phenomena. In addition, consideration of the thermo-mechanical behaviour of the coal seam and its surrounding formation is also necessary.

In addition, Daggupati et al. (2011a), Daggupati et al. (2011b) and Sarraf Shirazi et al. (2011) highlighted that the already developed computational efforts can be classified into two groups. The first group assumes that the coal seam is highly porous during the simulation period. In this group, the UCG process takes place between the layers of the material thus the generated gas moves through the body of the material. In contrast, the second group supports the assumption that the process takes place through a continually escalating channel (cavity).

Perkins (2005) in his work commented on the lack of specific site characterisation work and confirmed that UCG field observations combined with modelling work may serve as template for future UCG projects. Finally, the same author commented on the knowledge gap in gasification simulations tailored for UCG purposes since the specification of the significantly higher number of variables – compared to surface processes – increases the level of uncertainty and, as a result, the risk of low accuracy in estimations.

## 1.4 *Research objectives and aims*

UCG process is so complex that many computational efforts fall short, due to their imbalanced focus on certain aspects while others are forced to ignore parameters in order to downsize the computational requirements. Thus, it is not possible to cover and model the wide scope of the UCG processes using a single software package, unless either a relative large number of assumptions is made or important process details are omitted. In addition, UCG researchers should consider the precious balance between uniformity (regarding how feasible it would be to integrate various stages of a process into one model) and accuracy (regarding the precision and straightforwardness of the results retrieved from the simulations) that should be met in every UCG study.

Considering the limitations of earlier works, the overall PhD objective is to identify and model the critical parameters which will give increased control on the underground processes and ultimately on the composition of the final syngas product. A detailed understanding of the UCG processes will facilitate their prioritisation and will lead to the development of an accurate as well as comprehensive UCG model.

As a result, the main objective is:

*To build a coupled thermo-chemical-mechanical model, which increases the understanding and ultimately improves the controllability of the complex UCG operation.*

The objective can be achieved by focusing on three key areas:

- On the chemical processes of coal gasification: By understanding the sequence of the chemical reactions occurring during coal gasification as well as identifying the similarities and differences between surface gasifiers (i.e. fixed-bed, fluidised etc.) and UCG operations. This comparison aims to analyse the common aspects in order to investigate whether it would be feasible to build on surface gasification models for the development of a chemical process model tailored for UCG operations.
- On the geomechanical phenomena associated with UCG operation. The emphasis is on understanding the cavity growth mechanism during UCG. Mainly, the knowledge sourced by studying the coal gasification process will be used to evaluate the effects of coal gasification on a subsurface environment. More specifically, this stage will define the physical boundaries of the coal-syngas conversion and will determine how the gasification process discussed in the first section will be applied on a continuously growing cavity.
- On the heat and mass transport phenomena taking place within the escalating UCG cavity. The operating temperature and pressure conditions in combination with the composition of the product gas accumulating within the UCG cavity significantly affect the heat and mass transfer mechanisms. The purpose is to link the quality and quantity of the end-product gas with the operating conditions, identifying how preferential end-product gas can be achieved through targeted UCG operation.

Extensive modelling work was required in order to develop the coupled UCG simulation tool. It has been formulated through selected software packages each dedicated to a different UCG process. For this reason, careful selection and understanding of the appropriate software packages had been necessary. The Advanced System for Process ENgineering (Aspen) Plus software, a standard tool for the simulation of complex processes in the chemical industry, is used for the thermo-chemical simulation of coal gasification. On the other hand, the FLAC$^{3D}$ software, which is a numerical modelling tool for conducting advanced geomechanical analysis encountered in geotechnical engineering applications, is used for the thermo-mechanical simulation of the UCG process.

The coupling of the two simulation tools is achieved through the Gasification Support Unit module, which facilitates the sequential interchange of data between the two software packages and focuses on the heat and mass transport phenomena within the UCG cavity.

## 1.5 *Thesis structure*

Chapter 2 reviews the principles of geomechanics, of gasification chemistry and of heat and mass transport phenomena. The aim is to equip the reader with the necessary background literature upon which the following chapters will be based in order to explain how the developed models operate.

Chapter 3 reviews the UCG concepts by highlighting the main concerns and benefits of UCG as well as describing the different UCG layouts and their historical implementations. The aim is to provide an understanding of the UCG operational performance and in addition to review the literature and categorise the experimental and modelling efforts that focused on explaining the UCG processes.

Chapter 4 performs a detailed explanation of the chemical process model synthesised and developed as part of the current PhD work through the Aspen Plus software tool. A literature review on existing computational studies through the Aspen Plus software is also included. In addition, the performance of the developed chemical process model is compared against experimental results for two different coal types.

Chapter 5 details the methodology for the developed coupled Thermo-Mechanical-Chemical (TMC) model. The workflow is analysed and the controlling factors of the coupled process are evaluated. In addition, indicative results are also presented during the explanation of the methodology.

Chapter 6 presents the first set of results generated by the coupled TMC model. The coupled. TMC model is tested across different scenarios. The input parameters of different scenarios are explicitly detailed. Different scenarios include different coal types at multiple depths. In addition, oxygen ($O_2$) and air are studied as injected oxidants and the effect of seam thickness on UCG process is also analysed. Different performance indicators facilitate the cross-comparison between the results of the different test case scenarios.

Chapter 7 performs an assessment of UCG performance for different coal types at the same operational conditions. Specifically, different coal types are cross-compared through a number of performance indicators under identical operating conditions. In contrast to Chapter 6, where the all the simulating scenarios were analysed on a coal type basis, within this chapter all the coal types will be cross-compared at the same depth. In addition, supplementary results on the heat and mass transport phenomena within the growing UCG cavity are included within this Chapter.

Finally, Chapter 8 presents the main conclusions of this thesis. Recommendations for potential accomplishments through future research are also presented.

# Chapter 2 Background theory

## 2.1 *Principles of coal gasification*

The conversion of coal material to gaseous fuel which mainly consists of carbon monoxide (CO), methane ($CH_4$) and hydrogen ($H_2$) is called gasification. Many researchers use gasification as a term for describing the whole conversion process, while gasification is only an intermediate stage of the above conversion process (Beath, 1996; Perkins, 2005; Roberts, 2000). Roberts (2000) classified the whole process into two stages:

1. the pyrolysis or devolatilisation
2. the char combustion and gasification.

This classification relies on the different speed of the phenomena taking place in each of the two stages. The rapid hydrocarbon and tar losses, which occur during the first stage, take place much faster than the heterogeneous reactions of the second stage. Thus, since the slowest reactions control the overall kinetics, it is reasonable to assume that the second stage controls the speed of the overall conversion (Roberts, 2000). Furthermore, according to Littlewood (1977), the gasification term describes whichever process involves the increase of hydrogen ($H_2$) and the decrease of carbon (C) content in a fuel.

Regarding coal resources, the ratio of $H_2$/C varies between 0.4 and 0.9, the lowest attributed to anthracite and the highest to lignite. Moreover, this indicator could be considered as a performance criterion for competing gasification methods, as well as a basis when comparing different fuels (Table 2.1)

**Table 2.1**: Comparison of H/C ratio for different fuels (Perkins, 2005; Littlewood, 1977);

| Fuel | $H_2$/C ratio |
|---|---|
| Natural gas | 4 |
| Oil | 2 |
| Coal | 0.4 – 0.9 |

### 2.1.1 Devolatilisation

During coal devolatilisation, the temperature and the surroundings conditions decide the extent to which coal will be converted to char. The following equation (E2.1) characterises the main devolatilisation process.

$$Coal \rightarrow Char + Volatiles \qquad \text{(E2.1)}$$

As temperature increases, the carbon purity of the char increases, while the amount of the low molecular weight compounds also increases. The least-stable components, which increase as the temperature increases, tend to be converted into gases and are released from the carbon matrix. On the other hand, the components that do not escape from the matrix remain in it as solvents and soften the char (Beath, 1996). Moreover, during the devolatilisation process the constituents that already managed to vaporise, participate in secondary interactions either on their own or with the surface of the solid material (Solomon et al., 1992).

Furthermore, the distinction between devolatilisation and pyrolysis needs to be discussed. The understanding of the devolatilisation process, which occurs inside the gasifier is achieved experimentally through pyrolysis. However, although pyrolysis and devolatilisation are similar they are not identical processes. It is an assumption that pyrolysis is alike devolatilisation and thus the first can be studied instead of the second.

Devolatilisation occurs rapidly within a very combustible environment where also oxygen ($O_2$) is in excess and as a result the replication of such conditions in a laboratory's less reactive environment is quite challenging (Visagie, 2009; Beath, 1996).

Since pyrolysis is a complicated procedure difficult to be modelled and understood because of its sensitivity to various parameters (Anthony and Howard, 1976), many analysts choose to assume a pre-defined composition of the volatile gases rather than developing their own results. More specifically, Yoon et al. (1979a, b) in his work developed volatile gas data (Table 2.2) and his analysis according to Visagie (2009) is widely accepted and commonly met in the literature.

**Table 2.2**: Proportion of coal devolatilised products (Yoon et al., 1979a, b).

| Constituent | Volume (%) |
|---|---|
| $CH_4$ | 50.3 |
| CO | 20.6 |
| $H_2$ | 13.1 |
| $H_2S$, $NH_3$ | 9.9 |
| $CO_2$ | 6.1 |

The most important modelling parameters while considering devolatilisation are (a) the rate of the devolatilisation process; (b) the yield of the produced volatiles; (c) the chemical composition of the volatiles gases (e.g. Table 2.2) and (d) the resultant char formation (Beath, 1996). Another crucial debate regarding devolatilisation is whether volatiles or char are more desirable as devolatilisation products. The answer to this debate would also help to clarify the preferable devolatilisation temperature. High devolatilisation temperature increased the generated volatile matter and the remaining char purity (Beath, 1996). In addition, different coal types (e.g. bituminous, sub-bituminous etc.) demonstrate different sensitivity during devolatilisation and especially on how easily their initial structure can be converted to volatile matter. For instance, coking coals display limited volatility since the less volatile a material is, the more energy it releases during combustion.

On the other hand, increased volatility means that the ignition stage is easier, while the energy released during combustion is partially sacrificed. Thus on average restrained volatility is considered as optimum (Visagie, 2009).

### 2.1.2 Combustion and gasification

The main difference between combustion and gasification relies on the oxygen concentrations participating in each case. Analysts make a distinction between *complete* and *partial* oxidation with the first to happen during combustion and the second during gasification (Beath, 1996; Perkins, 2005; Roberts, 2000; Visagie, 2009). Moreover, according to Visagie (2009), a comparison of the oxygen ($O_2$) quantities present in each case would reveal that 50% more oxygen is required during combustion compared to gasification.

Figure 3.1 illustrates how the oxygen concentration determines both the difference between gasification and combustion as well as the proportions of the various components in the end-product gas (Phillips, 2006). According to this, if the ratio of oxygen ($O_2$) to the moisture-ash-free (MAF) coal is over 2.5, then the carbon dioxide ($CO_2$) concentration in the product gas varies between 50% and 60% (Figure 3.1). As the above ratio decreases the carbon dioxide ($CO_2$) proportion declines and shifts to carbon monoxide (CO). In addition, steam ($H_2O$) and hydrogen ($H_2$) contents follow reverse routes with lower $O_2$/coal ratios to benefit hydrogen ($H_2$) formation.

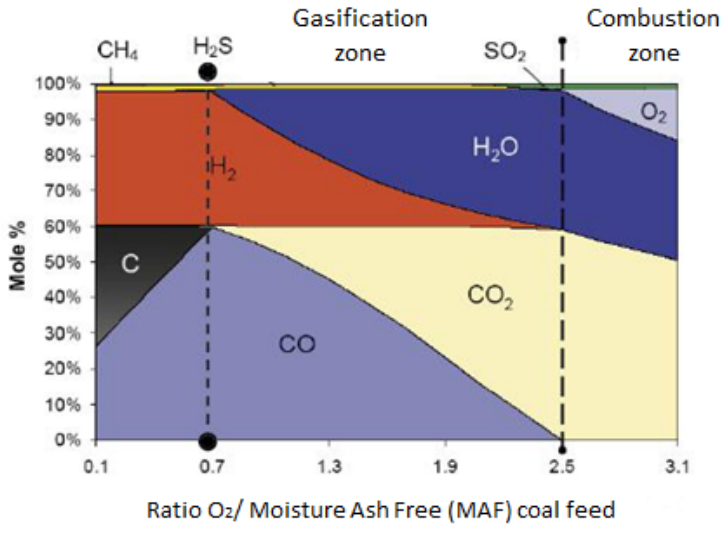


**Figure 2.1:** Product-gas synthesis in relation to the oxygen concentration expressed as ratio of $O_2$/MAF (Phillips, 2006)

Furthermore, the combustion stage plays the role of the "energy source" in order to supply the necessary heat (or activation energy) to the gasification reactions (Beath, 1996; Perkins, 2005; Roberts, 2000; Visagie, 2009). Thus, according to Visagie (2009), although after combustion reactions most of their energy is discharged as heat; after gasification 65% of the input's energy content remains in the final product (syngas), thus increasing energy efficiency.

#### 2.1.2.1 Chemical reactions

The chemical reactions taking place during the conversion of coal to product gas can be grouped to homogenous and heterogeneous. Table 2.3 is also indicative of how the corresponding reactions can also be grouped to endothermic and exothermic with regards to the stage at which they take place.

**Table 2.3**: Main combustion and gasification reactions (Begum et al., 2013; Chen et al., 2010; Perkins, 2005; Preciado et al., 2012).

| | | | |
|---|---|---|---|
| **Combustion** | **Exothermic reactions** | **Heterogeneous** | |
| | | $C + ½\ O_2 \rightarrow CO$ Char combustion | (R1) |
| | | $C + O_2 \rightarrow CO_2$ Char combustion | (R2) |
| | | **Homogeneous** | |
| | | $H_2 + ½\ O_2 \rightarrow H_2O$ Volatiles combustion | (R3) |
| | | $CO + ½\ O_2 \rightarrow CO_2$ Volatiles combustion | (R4) |
| | | $CH_4 + 2\ O_2 \rightarrow CO_2 + H_2O$ Volatiles combustion | (R5) |
| **Gasification** | **Endothermic reactions** | **Heterogeneous** | |
| | Steam gasification | $C + H_2O \rightarrow H_2 + CO$ | (R6) |
| | Boudouard reaction | $C + CO_2 \rightarrow 2CO$ | (R7) |
| | | **Homogeneous** | |
| | Reverse methanation *($H_2$/CO ratio determinants)* | $CH_4 + H_2O \leftrightarrow CO + 3H_2$ | (R8) |
| | **Exothermic reactions** | **Heterogeneous** | |
| | Methanation *(Sensitive to high P)* | $C + 2H_2 \rightarrow CH_4$ | (R9) |
| | | **Homogeneous** | |
| | Water-gas shift reaction *($H_2$/CO ratio determinants)* | $CO + H_2O \leftrightarrow CO_2 + H_2$ | (R10) |

### 2.1.3 Performance of the thermo-chemical conversion processes

Regarding the performance of the above reactions (Table 2.3) these are sensitive to various parameters, the most important being temperature, pressure and reactants concentration e.g. air or oxygen ($O_2$) proportions compared to feedstock amount (Begum et al., 2013; Preciado et al., 2012; Chen et al., 2010; Perkins, 2005) .

However, as the temperature increases, the yield of the exothermic reactions decreases resulting to decreased product output. In this category falls the *water-gas shift reaction* (R10) (Table 2.3) – which plays a crucial role in determining the hydrogen ($H_2$) to carbon monoxide (CO) ratio – by benefitting the hydrogen ($H_2$) and carbon dioxide ($CO_2$) proportions at low temperatures and reversibly carbon monoxide (CO) and steam ($H_2O$) proportions as temperature increases (Basu, 2006; Roddy, 2013; Smith et al., 2010).

On the contrary, the endothermic reactions display increased output production rate (or consumption rate, if considering the reactants) in high temperature environments. The *Boudouard* reaction (R7) as well as the *reverse methanation* (R8) (Table 2.3) support this point with increased carbon monoxide (CO) and hydrogen ($H_2$) proportions as temperature rises (Basu, 2006; Fischer et al., 1979a; Li et al., 2001; Roddy, 2013). In addition, lower pressures increase the forward reaction rate of the *Boudouard* reaction and as a result, the carbon monoxide (CO) output increases (Basu, 2006; Fischer et al., 1979a; Roddy, 2013).

A relevant consideration at this point is which temperature should be considered as suitable for the gasification, since it affects the equilibrium of the process reactions (Cimini et al., 2005). Visagie (2009) commented that gasification temperature should be on average above 700°C, while for lignite gasification the lowest limit has to be increased to 1,000°C. However, Chen et al. (2010) investigated gasification performance for biomass feedstocks and their analysis was conducted at a temperature range between 500°C - 700°C.

Regarding the pressure conditions, methane ($CH_4$) proportion in the final product-gas increases as pressure rises through the *methanation* reaction (R9) (Table 2.3), especially if temperature is kept at low levels (Roddy, 2013; Smith et al., 2010).

Perkins (2005) also commented on how the composition of the end-product gas is linked to its final use. The most common purposes of the end product-gas are for power generation and chemical feedstock. In power generation use, the main criterion is the lower heating value (LHV) of the product gas, which need be as high as possible in order to release high amounts of energy during combustion.

The proportional relation between the constituents of the product-gas and their added value to LHV is addressed by the following formula:

$$CO: 0.85\ H_2: 2.85\ CH_4 \qquad \text{(E2.2)}$$

Thus, the carbon monoxide (CO) content is more valuable than the corresponding hydrogen ($H_2$) content, when the end use of the product gas is power generation. Also according to the performance of the exothermic *water-gas shift* reaction R10 (Table 2.3) – high temperatures are more favourable in order to maintain at low levels the shift of carbon monoxide (CO) to hydrogen ($H_2$) (Littlewood, 1977; Perkins, 2005).

On the other hand, if the product gas is supposed to be used as chemical feedstock then hydrogen ($H_2$) proportions are more appreciated than the corresponding carbon monoxide (CO) proportions. Accordingly, the Fisher Tropsh process requires double the proportion of hydrogen ($H_2$) compared to carbon monoxide (CO) (Moulijn et al., 2013; Perkins, 2005).

### 2.1.4 Coal gasification in the context of UCG

Gregg and Edgar (1978) developed a coherent chemical analysis describing the UCG procedure and summarised the main points of an earlier study by von Von Fredersdorff and Elliott (1963). Specifically, their analysis breaks down UCG process into four distinct zones.

The first zone includes the reactions which are dominated by the presence of oxygen and more specifically reactions R1, R2 and R4 described in Table 2.3. One UCG-orientated comment was that reaction R6 occurs extensively within this zone resulting, unfortunately, to increased carbon dioxide ($CO_2$) quantities (Von Fredersdorff and Elliott, 1963). According to Rossberg (1956) this is attributed to the fact that there is parallel generation of both carbon dioxide ($CO_2$) and carbon monoxide (CO) with the temperature level to control the balance between the two. High temperature levels benefit carbon monoxide (CO) formation, while lower temperature levels assist carbon dioxide ($CO_2$) production.

The second zone includes the reactions R6 and R7 presented in Table 2.3. This zone reduces the initial carbon dioxide ($CO_2$) content by shifting it to carbon monoxide (CO). This alteration necessitates heat supply, a large share of which is consumed by reaction R7 (Table 2.3). However, after a certain amount of supplied and absorbed heat by reaction R7, excess heat is used up in reaction R6. The carbon monoxide (CO) quantity produced by reaction R7 cannot further increase leading, inevitably, to heat losses if reaction R6 was not participating. For this reason, steam injection is required, so that leftover heat is absorbed through reaction R6, while minimising energy losses and at the same time increasing carbon monoxide (CO) quantities. As a result, steam supply is crucial for the whole process and this can also be provided through water influx from the surrounding strata into the coal seam (Gregg and Edgar, 1978). However, as Antonova et al. (1967) commented in their work, disproportionate steam presence can drop the temperature and reduce the rates of the chemical reactions.

The third zone includes the exothermic reactions R9 and R10 (Table 2.3). In this zone, supplementary outputs (e.g. methane $CH_4$) are affected by pressure and temperature variations. Additionally, methane ($CH_4$) content can increase through the reverse R8 reaction which is favoured at low temperatures (as exothermic) and high pressures. In particular, as pressure increases the reverse R8 reaction can facilitate a drop in the number of molecules involved (Schaaf et al., 2014; Takenaka et al., 2004).

The fourth zone includes both reactions R9 and R10 from previous stage as well as reaction R7 in its reverse form. This zone describes the gas performance during the gas subsurface flow towards collection, which is characterised by continuous temperature decrease. Gregg and Edgar (1978) considered a highly relevant and important issue in their work, namely the debate whether the product gas components are produced in equilibrium or not. According to these authors, as the reactions rates are slow in the fourth zone, equilibrium is very rarely achieved. Subsequently to the above argument, they added that although methane ($CH_4$) fraction was expected to increase in the fourth zone due to the lower participating temperatures – and also balance the LHV losses caused by the decreased carbon monoxide (CO) and hydrogen ($H_2$) fractions – its increase is insignificant and the LHV offset cannot be achieved.

According to Lavrov et al. (1971), the negative effect of a lengthy route between the production and the collection point of UCG product gas on its LHV, motivated the development of UCG subsurface layouts with reduced route length. On the other hand Perkins (2005) referred to more optimistic opinions (i.e. Antonova et al., 1967). He mentioned that the growing carbon dioxide ($CO_2$) load – at the expense of carbon monoxide (CO) (through reactions R6 and reverse R7) – and the consequent negative effect of the underground gas flow has on the final LHV can be balanced by simultaneous increase of methane ($CH_4$) (through reaction R8) (Table 2.3).

## 2.2 *Principles of geomechanics*

The purpose of this section aims to discuss the background theory of geomechanics as they significantly impact the UCG process. The understanding of the UCG thermo-mechanical effects requires a solid background in the principle of geomechanics.

### 2.2.1 Stress

Stress is called the ratio of the applied force over the surface that is exercised on.

$$Stress = \frac{Force}{Area} = \frac{F}{A} \qquad \text{(E2.3)}$$

Every sediment that exists below the earth's surface is compressed through stresses applied to it from the above formations. The magnitude of these compressive stresses depends on the depth, the pore pressure and the active processes that take place in the underground structure. However, depending on the angle between the applied force and its corresponding surface, the stresses can be classified into two main categories (Aadnoy and Looyeh, 2011; Fjar et al., 2008).

- *Normal (or Principal) stresses*, when the applied force is perpendicular to the corresponding surface.
- *Shear* stresses, when the applied force is in parallel with the corresponding surface.

As a result, in the case of a 3-dimensional state (i.e. cube) a 3x3 matrix (M1) of vectors (taking into account symmetry as well) would be representative of the applied stresses (Aadnoy and Looyeh, 2011):

$$\begin{bmatrix} \sigma_{xx} & \tau_{xy} & \tau_{xz} \\ \tau_{yx} & \sigma_{yy} & \tau_{yz} \\ \tau_{zx} & \tau_{zy} & \sigma_{zz} \end{bmatrix} \quad \text{(M1)}$$

As it is presented in the matrix (M1), each of the surfaces accounts for its *normal (or principal) stress* (i.e. $\sigma_{xx} - \sigma_{yy} - \sigma_{zz}$) and its two *shear stresses* (i.e. $\tau_{xy}$, $\tau_{xz} - \tau_{yx}$, $\tau_{yz} - \tau_{zx}$, $\tau_{zy}$ ) related to the horizontal forces lying on the plane of this surface.

According to the literature presented above and assuming a 3D grid-block sediment lying below the earth's surface it is exposed to three *normal (or principal) stresses* (3 due to symmetry – 6 in total) with one of them being vertical and the other two horizontal to the earth's surface. Depending on the depth of the coal seam considered, the vertical stress (often annotated as $\sigma_v$) due to the weight of the overlaying layers can be smaller in magnitude compared to the horizontal tectonic stresses (defined as *horizontal maximum* ($\sigma_{Hmax}$) and *horizontal minimum* ($\sigma_{Hmin}$) stresses) (Zhao et al., 2015), however the rest of the current research work was carried out under the assumption that the vertical overburden stresses are higher in magnitude compared to the horizontal stresses (Fjar et al., 2008; Zoback, 2010).

In the ideal case where all the underground layers are isotropic (having identical density values) the following equation (E2.4) would be adequate to provide the vertical stress value at depth *z* (Zoback, 2010).

$$\sigma_v = \rho g z \quad \text{(E2.4)}$$

Where,

$\rho$: represents the density value (kg/m$^3$)

*g*: the gravitational acceleration (9.81 m/s$^2$)

*z*: the depth from the earth's surface (m)

However, the fact that the underground geological strata is composed by layers with different geomechanical properties leads to the following equation (E2.5) to be appropriate for the vertical stress ($\sigma_v$) calculation:

$$\sigma_v = \int_0^z \rho(z) g dz \quad \text{(E2.5)}$$

This equation (E2.5) considers the density differences for all the layers up to the corresponding *z*-depth layer, where the vertical stress is calculated. In addition, equation (E2.6) presents the formula for the calculation of the horizontal principal stresses.

$$\sigma_{H\max} = \sigma_{H\min} = \rho g z \frac{v}{1-v} \quad \text{(E2.6)}$$

Where,
*v*: represents the Poisson ratio

It has to be highlighted that equation (E2.6) is valid under the assumptions of material homogeneity and linear elasticity. In addition, its isotropic assumption implies that the principal horizontal stresses ($\sigma_{Hmax}$, $\sigma_{Hmin}$), which occur when the sediment is compressed vertically due to gravity, are less strong than the corresponding principal vertical stresses ($\sigma_v$) (Amadei et al., 1987). The tendency for horizontal expansion triggers the counteracting horizontal forces applied to the sediment from its neighbouring strata (Zoback, 2010). The Poisson ratio found in the equation (E2.6) expresses this tendency of the sediment to expand horizontally when a vertical force is applied to it, as it will be explicitly analysed in Chapter 2.2.2.

Figure 2.2 presents the different fault types that can occur as result of the in-situ stresses. Across all cases (Figure 2.2a-Figure 2.2c), non-existing uniaxial strain conditions are assumed. When the horizontal principal stresses are different, *Normal* fault can occur (Figure 2.2a). In the cases, when the vertical stress is not the maximum of all the principal stresses, the *Strike-slip* and the *Reverse* faults occur (Figure 2.2b-2.2c). It can be concluded that the fault always occurs on the plane, which has the two lowest-value principal stresses perpendicular to its plane (Anderson, 1951).

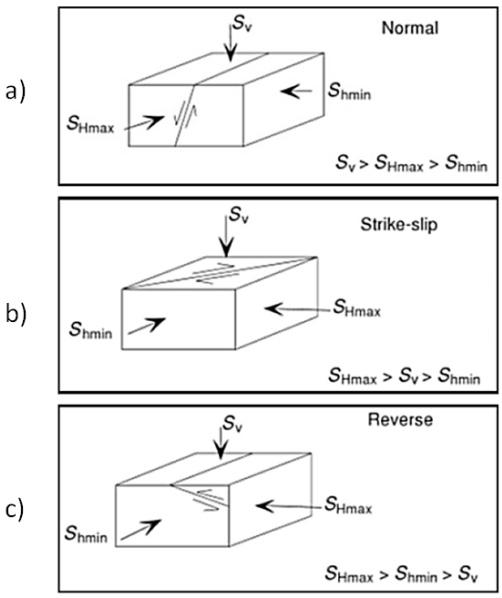


**Figure 2.2:** Categorisation of faults to Normal, Strike-slip and Reverse depending on the applied stress magnitudes (Zoback, 2010)

Apart from the compressive stresses that act to an underground formation due to the overburden weight, additional stresses can be caused by thermal changes or active geological activities. For instance, an on-going tectonic activity can result to changes in the stress profile of an underground formation or thermal effects can cause changes to the thermal expansion coefficient of a rock body and as a result additional forces (Amadei and Stephansson, 1997).

Furthermore, a rock body is subject to additional stresses due to fluid flow through their porous structure. The pore pressure can be seen as tensile stress and as a result the total effective stress applied to an underground rock body can be calculated by the following equation (E2.7) (Terzaghi, 1943):

$$\sigma_1' = \sigma_1 - a_0 P_0 \qquad \sigma_2' = \sigma_2 - a_0 P_0 \qquad \sigma_3' = \sigma_3 - a_0 P_0 \tag{E2.7}$$

Where,

$\sigma_i$: represents the compressive stress (positive direction assumed) (Pa)

$a_0$: represents the effective stress Biot's coefficient

$P_o$: represents the pore pressure (Pa)

The pore pressure ($P_o$) at a certain depth is associated with the hydrostatic pressure at that depth and its is calculated according to the following equation (E2.8):

$$\sigma_v = \int_0^z \rho_w(z) g dz \qquad \text{(E2.8)}$$

Where,

$\rho_w$: represents the density of a water column at different depths (kg/m$^3$)

### 2.2.2 Deformation

The following figure (Figure 2.3) presents how a rock body (in the shape of a cylinder) deforms when uniaxial compressive stresses are applied to it. However, the strain concept needs to be explained before discussing how the rock deformation and the stress values are related. When stresses are applied to a rock body, these can cause deformation (either permanent or not) and as a result strain is the ratio between the change in the length of the rock body in one dimension and the initial length of the body in the same direction:

$$Strain = \frac{Change\ in\ Length}{Initial\ Length} = \frac{\Delta l}{l} \qquad \text{(E2.9)}$$

As it can be seen in (Figure 2.3), the rock body strain deforms differently when increasing uniaxial compressive stresses are applied to it. The rock behaviour can be classified into three different categories (Jaeger et al., 2007; Fjar et al., 2008):

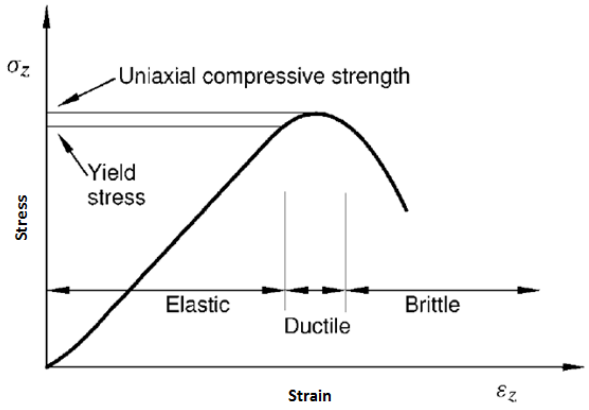


**Figure 2.3:** Deformation behaviour against uniaxial compressive stresses (Fjar et al., 2008)

- *Elastic.* During the elastic stage, the rock deforms but when the applied load is removed the rock body can return to its initial size and shape. The elastic deformation of the rock body can be defined through the *Young's modulus* (*E*) and the *Poisson ratio* (*v*).

  The *Young's modulus* (*E*) describes the ratio of the stress applied to a rock body in one direction (i.e. vertical to the earth's surface) to the strain caused in the same direction. The higher the value of this ratio, the more rigid is the material as more stress is required for the same amount of deformation to be caused.

$$E = \frac{\sigma_z}{\varepsilon_z} \tag{E2.10}$$

  The *Poisson ratio* (*v*) describes the ratio between strain relationship between two different dimensions. It represents the tendency of the rock body to deform vertically to the applied force. The numerator ($\varepsilon_x$) represents the strain vertically to the applied force and because it represents expansion will have a negative while the denominator ($\varepsilon_z$) represents the strain horizontally to the applied force. The higher the value of this ratio, the greater the horizontal expansion for the same vertical displacement.

$$v = -\frac{\varepsilon_x}{\varepsilon_z} \tag{E2.11}$$

  Additional elastic moduli parameters exist such as the *bulk modulus (K)*, the *shear modulus (G)* or the *Lame's first parameter (λ)* although the definition two of them (e.g. *Poisson ratio (v)* and *Young's modulus (E)*) facilitates the definition of the rest of them.

- Plastic. When the uniaxial compressive stress reaches a value called *yield stress*, the transition from the elastic to plastic behaviour occurs. When the applied load becomes greater than the *yield stress* value then permanent deformation takes place and the rock body cannot return to its initial shape and size even when the applied load is removed. This plastic behaviour can be classified into stages:

- *Ductile.* This stage represents the intermediate stage, in-between the elastic deformation and the abrupt loss of the resistance of the rock body. During this stage, the rock body gradually weakens.

- *Brittle.* This is the stage that the ability of the rock body to oppose to any load rapidly drops.

The level of the *yield stress* value for a rock body depends on its confining stress. As the confining stress increases the level of the *yield stress* value also increases. Furthermore, the ductile behaviour is relatively limited for underground rock formations with the brittle behaviour to become the dominant one after the end of its elastic deformation. For this reason, rock bodies that experience an inelastic deformation before their abrupt failure are often referred as ductile materials while rock bodies with an abrupt transition from elastic behaviour to complete loss of their resistance are often referred as brittle rocks (Fjar et al., 2008).

The rock failure occurs firstly at microscopic level with the expansion of its pores and at a macroscopic level by the development of breaks within the rock body. Two types of failure are discussed, namely shear failure and tensile failure (Fjar et al., 2008; Jaeger et al., 2007).

#### 2.2.2.1 Shear Failure

The Mohr-Coulomb criterion is often employed to analyse whether the developed shear stress applied to a rock body is adequate to cause a permanent shear fault (Figure 2.4) or it still lies within the elastic deformation region.

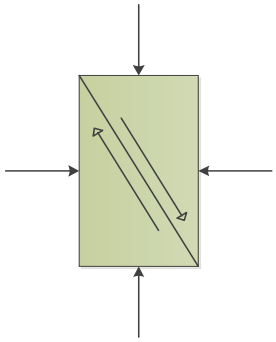

**Figure 2.4:** Representation of shear failure under compressive stresses (Fjar et al., 2008)

The following equation describes the connection between the shear stress (E2.12) and the effective normal (to the failure plane) stress:

$$|\tau| = S_0 + \mu\sigma' \qquad \text{(E2.12)}$$

Where,

$\sigma'$: represents the effective normal stress (Pa)

$S_0$: represents the ultimate shear strength of coal (also known as cohesion)

$\mu$: represents the internal friction coefficient, $\mu = \tan\varphi$ where $\varphi$ is the internal friction angle

#### 2.2.2.2 Tensile Failure

On the other hand, the tensile failure is caused when the minimum principal effective stress becomes higher than the tensile strength value ($T_o$) of the rock.

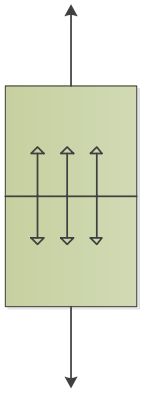

**Figure 2.5:** Representation of tensile failure under tensile stresses (Fjar et al., 2008).

$$a_0 P_0 - \sigma_3 \geq T_o \qquad \text{(E2.13)}$$

By comparing, equation (E2.13) with the effective stress equation (E2.7), it can be concluded that tensile failure occurs when the effective stress transforms from compressive to tensile and overcomes a specific value ($T_o$). However, due to cracks that might already exist, the tensile strength value turns to zero ($T_o$=0) and as a result equation (E2.14) takes the following form:

$$a_0 P_0 \geq \sigma_3 \qquad \text{(E2.14)}$$

### 2.2.3 Thermo-mechanical properties of rocks

UCG as an underground process is significantly affected by the type of rocks surrounding the coal seam. The mechanical and the thermal properties of these rocks depend both on the type of the rock material and the developed temperature. As a result, a comprehensive UCG model has to take into account the variation of these thermo-mechanical properties with temperature. Furthermore, as a UCG cavity grows within the coal seam, the geo-mechanical stability of the process and its associated phenomena (i.e. roof collapse, surface subsidence, gas leakage) is directly affected by these properties. Table 2.4 presents indicative values regarding the metrics of thermal expansion coefficient and specific heat along with the densities for different rock types.

**Table 2.4**: Rock thermal properties at a temperature range of 20ºC - 100ºC (Robertson, 1988)

| Rock type | Densities ($kg/m^3$) | Thermal expansion ($10^{-5}$ $^oC^{-1}$) | Specific heat (J/(kg K)) |
|---|---|---|---|
| Granite | 2,670 | 2.4 | 950 |
| Diorite | 2,840 | 2.1 | 970 |
| Gabbro | 2,980 | 1.6 | 990 |
| Sandstone | 2,200-2700 | 3.0 | 1000 |
| Quartzite | 2,810 | 3.3 | 970 |
| Limestone | 2,600-2,700 | 2.4 | 940 |
| Marble | - | 2.1 | 1000 |
| Slate | 2,800 | 2.7 | 1000 |
| Shale | 2,400-2,600 | - | 940 |

As literature is reasonably diverse when reporting the thermal properties of different rock types, additional values are summarised within Table 2.5. A cross comparison between the two Tables 2.4-2.5 indicates that the specific heat of sandstone (1000-775 J/(kg K)), quartzite (970-731 J/(kg K)), limestone (940-680 J/(kg K)), marble (1000-883 J/(kg K)) and slate (1000-740 J/(kg K)) should probably be constrained within a range of values instead of just one value.

**Table 2.5**: Specific heat for different rock types at 20°C (Waples and Waples, 2004)

| Rock type | Density ($kg/m^3$) | Specific heat (J/(kg K)) |
|---|---|---|
| Clay | 2680 | 860 |
| Dolomite | 2800 | 900 |
| Limestone | 2770 | 680 |
| Quartzite | 2640 | 731 |
| Marble | 2760 | 883 |
| Sandstone | 2640 | 775 |
| Siltstone | 2680 | 910 |
| Slate | 2780 | 740 |

Furthermore, the specific heat values included in Table 2.5 are consistently lower when compared with the corresponding values of the rock types included in Table 2.5. Additionally, Table 2.6 presents ranges of values for all the thermal properties of shale. As it can be seen, the specific heat value for shale (940 (J/(kg K)) as included in Table 2.4 is within the range of the specific heat values included in Table 2.6.

**Table 2.6**: Shale thermal properties at a temperature range of 20°C – 200°C (Gilliam and Morgan, 1987)

| Rock type | Thermal conductivity (W/(m °C)) | Thermal expansion ($10^{-5o}C^{-1}$) | Specific heat (J/(kg K)) |
|---|---|---|---|
| Shale | 0.68-1.01 | 0.9 – 4.8 | 879.2-1088.6 |

Additional comparisons regarding the specific heat values of the different rocks can be drawn as additional values by Eppelbaum et al. (2014) are presented in Table 2.7. Especially for sandstone, quartzite and limestone the specific heat values presented in Table 2.7 are included within the in accordance with the corresponding value presented in Tables 2.4-2.5.

This fact indicates that an average value within the earlier developed ranges would form a close estimate for the specific heat of these rocks. Furthermore, thermal conductivity is an additional property that is included in Table 2.7.

**Table 2.7**: Average thermal properties for different rock materials (Eppelbaum et al., 2014)

| Rock type | Densities ($kg/m^3$) | Thermal conductivity (W/(m $^oC$)) | Specific heat (J/(kg K)) |
|---|---|---|---|
| Chalk | 1,810 | 0.82 | 959 |
| Marl | 1,970 | 1.38 | 1,734 |
| Dolomite | 2,573 | 2.11 | 802 |
| Limestone | 2,714 | 2.20 | 851 |
| Clay | 2,080 | 1.42 | 2,127 |
| Sandy shale | 2,057 | 1.42 | 2,151 |
| Sandstone | 2,198 | 1.70 | 737 |
| Siltstone | 2,566 | 2.22 | 795 |
| Quartzite | 2,710 | 4.19 | 858 |

**Table 2.8**: Average conductivities for different rock materials (Midttømme et al., 1998)

| Rock type | Thermal conductivity (W/(m $^oC$)) |
|---|---|
| Claystone and siltstone | 0.80-1.25 |
| Shale | 1.05-1.45 |
| Sand | 1.70-2.50 |
| Sandstone | 2.5-4.2 |
| Sandy mudstone | 2.38-2.52 |
| Mudstone | 1.42-2 |

Both Table 2.6 and Table 2.8 include thermal conductivity values for the same rock types. As a result, a comparison would reveal the boundaries when an average estimate is required. For instance, thermal conductivity of shale is estimated between 0.68-1.01 (W/(m $^oC$)) according to Table 2.6 while reasonably higher range (1.05-1.45) is provided in Table 2.8. Furthermore, thermal conductivity of sandstone is estimated 1.70 (W/(m $^oC$)) in Table 2.7 while the corresponding range in Table 2.8 is 2.5-4.2 (W/(m $^oC$)). As a result, it can be concluded that the values provided by Midttømme et al. (1998) are consistently higher than the ones cited by Eppelbaum et al. (2014).

Furthermore, qualitative trends can be developed through careful analysis of the thermal conductivity data in Tables 2.6-2.8. High density materials such as quartzite experience higher thermal conductivity compared to lower density materials such shale or mudstone. Table 2.9 provides average values for various thermo-mechanical properties of roof rocks commonly met in UCG projects.

**Table 2.9**: Indicative thermo-mechanical properties for rock materials (Min, 1983)

| Property | Unit | Value |
|---|---|---|
| Density | $kg/m^3$ | 2000-2400 |
| Thermal conductivity | W/(m $^oC$) | 2 |
| Specific heat | J/(kg $^oC$) | 600-900 |
| Elastic Modulus | GPa | 5-10 |
| Poisson's ratio | - | 0.15-0.25 |
| Thermal expansion | ($10^{-5o}C^{-1}$) | 0.8-1.0 |
| Tensile strength | MPa | 1-6 |
| Cohesion | MPa | 0.8-2 |
| Friction angle | Deg | 20-30 |

Tan et al. (2008) (Table 2.10) developed an in-detail comparison between sandstone and mudstone among selected thermo-mechanical properties. A characteristic difference between mudstone and sandstone can be seen in the cohesion values with the sandstone to experience 10 times higher value than mudstone. In addition, the thermal expansion coefficient value significantly differs between the two rock types (mudstone vs. sandstone) with the mudstone's value to be approximately four times higher the corresponding one for sandstone. However, the thermal expansion coefficient value for sandstone value cited by Tan et al. (2008) (Table 2.10) is significantly lower than the one cited by Robertson (1988) (Table 2.4) and still lower than the range presented by Min (1983) (Table 2.9). Furthermore, the variation of thermal expansion coefficient with temperature for sandstone and mudstone is presented in Figure 2.6

**Table 2.10**: Indicative thermo-mechanical properties for mudstone and sandstone under ambient conditions (Tan et al., 2008)

| Property | Unit | Mudstone | Sandstone |
|---|---|---|---|
| Thermal conductivity | W/(m $^oC$) | 0.679 | 0.535 |
| Elastic Modulus | GPa | 37.8 | 52.8 |
| Poisson's ratio | - | 0.23 | 0.27 |
| Thermal expansion | ($10^{-5}$ $^oC^{-1}$) | 0.792 | 0.2 |
| Cohesion | MPa | 3 | 30 |
| Friction angle | Deg | 28 | 42 |

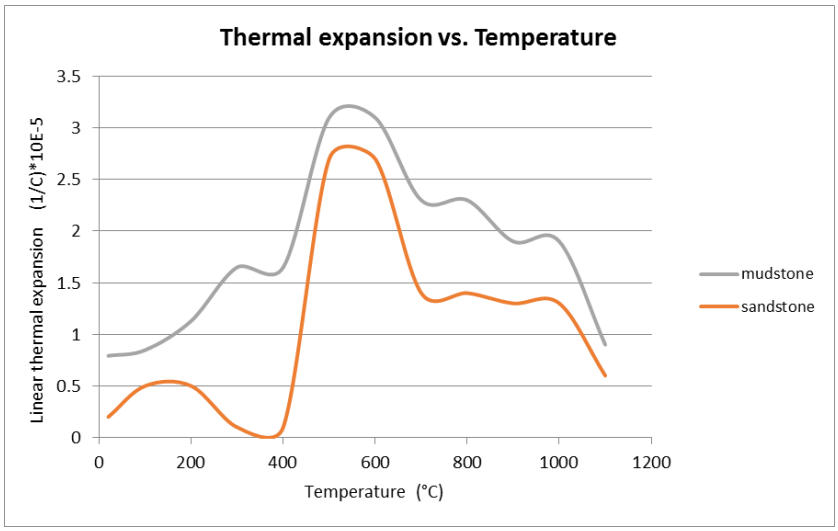


**Figure 2.6:** Variation of thermal expansion coefficient with temperature (Tan et al., 2008)

Figure 2.7 presents how the thermal conductivity of various rock materials varies as temperature increases. However, different rock types behave in a different way. In addition, even the variation with temperature for the same rock type is cited in a different way from different authors in the literature. For this reason, multiple sources are cited in the same chart in order to enable a cross-comparison among the different authors. As it can be seen (Figure 2.7), Birch and Clark (1940) and Robertson (1988) present consisting behaviour for the thermal conductivity of the sandstone as temperature increases. On the other hand, the thermal conductivities of shale and mudstone increase as temperature increases according to Robertson (1988) and Tan et al. (2008) respectively.

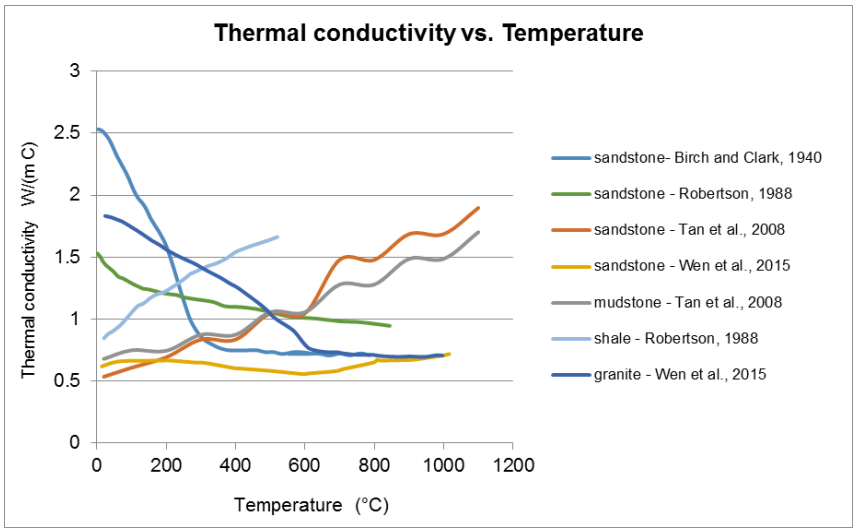


**Figure 2.7:** Comparative analysis of how thermal conductivity varies with temperature for selected rock materials

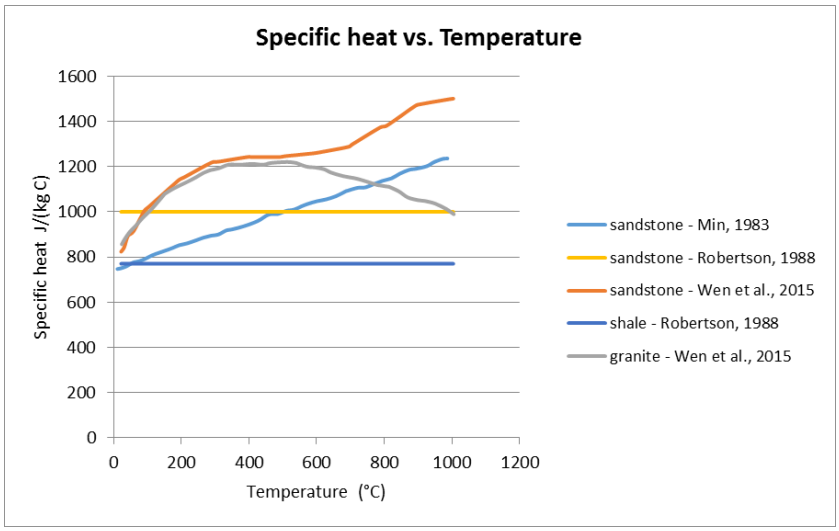


**Figure 2.8:** Comparative analysis of specific heat profile as temperature increases for different rock materials

Furthermore, how the specific heat of selected rock types varies with temperature is presented in Figure 2.8. Both Min (1983) and Wen et al. (2015) indicate an increasing trend as temperature increases while Robertson (1988) highlighted a steady behaviour for the corresponding specific heat values of shale.

Apart from the thermal properties of rocks, their mechanical properties have also the tendency to change when they are exposed to growing temperatures. Figure 2.9 provides the profile of tensile strength as temperature increases. The tensile strength of sandstone experiences a steady performance until 400$^{o}$C with the thermal stresses to rapidly decrease its value further on ("thermal rock failure") (Figure 2.9).

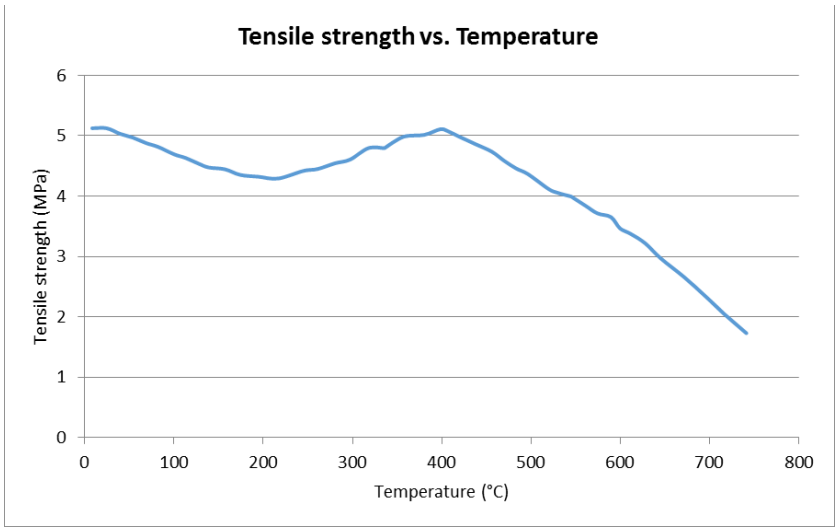


**Figure 2.9:** Sandstones tensile strength as a function of temperature (Yin et al., 2011)

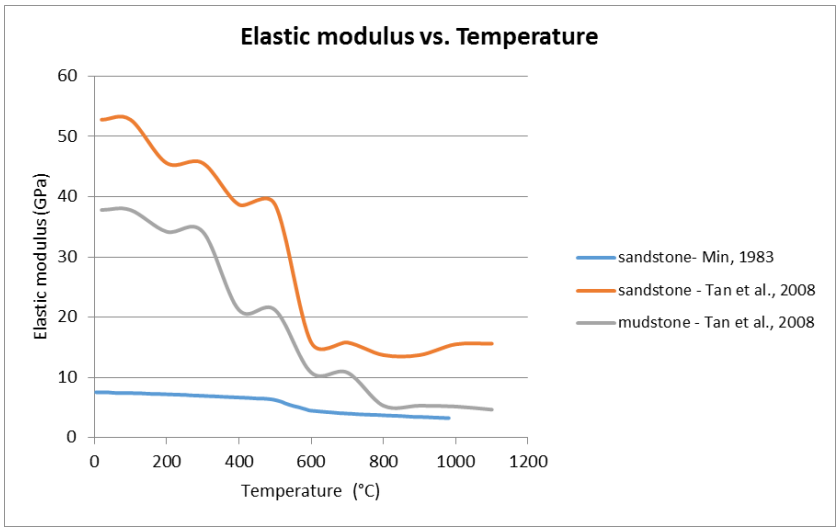


**Figure 2.10:** Profile of elastic modulus variation with temperature for mudstone and sandstone

Furthermore, Figure 2.10 presents the elastic modulus profiles for sandstone and mudstone as temperature rises. Both Min (1983) and Tan et al. (2008) highlighted that the elastic modulus values for sandstone are lower than 10 GPa for temperatures above 700$^{o}$C. In addition, as it can be seen, Tan et al. (2008) reported a similar behaviour for the elastic modulus values of sandstone and mudstone as temperature increases although the corresponding values for mudstone are slightly higher.

### 2.2.4 Thermo-mechanical properties of coal

The thermo-mechanical properties of coal significantly affect the UCG process and as a result Table 2.11 provides an overview of nominal values for selected properties.

**Table 2.11**: Indicative thermo-mechanical properties for bituminous coal under ambient conditions (Tan et al., 2008)

| Property | Unit | Coal |
|---|---|---|
| Thermal conductivity | W/(m $^{o}$C) | 0.3 |
| Elastic modulus | GPa | 3.82 |
| Poisson's ratio | - | 0.25 |
| Thermal expansion | ($10^{-5}$ $^{o}C^{-1}$) | 0.8 |
| Cohesion | MPa | 1 |
| Friction angle | Deg | 22 |

**Table 2.12**: Indicative thermo-mechanical properties for bituminous coal (Min, 1983)

| Property | Unit | Value |
|---|---|---|
| Density | $kg/m^3$ | 1300 |
| Thermal conductivity | W/(m $^oC$) | 0.272 |
| Specific heat | J/(kg K) | 800 |
| Elastic Modulus | GPa | > 2.0 |
| Poisson's ratio | - | 0.44 |
| Thermal expansion | ($10^{-5}$ $^oC^{-1}$) | 0.5 |
| Tensile strength | MPa | 0.5-1 |
| Cohesion | MPa | 0.1-0.8 |
| Friction angle | Deg | 20-30 |

A cross-comparison between the data included in Tables (2.11-2.12) shows high consistency between the corresponding values. Specifically, the elastic modulus value (3.82 GPa) included in Table 2.11 is above the benchmark limit (>2 GPa) listed in Table 2.12. In addition, the friction angle (22 Degrees) reported by Tan et al. (2008) (Table 2.11) is within the corresponding range (20-30 degrees) of Min (1983) (Table 2.12). In contrast, the cohesion value reported in Table 2.11 (1 MPa) is slightly above the range given in Table 2.12 (0.1-0.8 MPa). Furthermore, Figure 2.11 presents how the thermal expansion coefficient changes with increasing temperature. As the coal temperature increases, the thermal expansion coefficient decreases. This decreasing effect comes in contrast to how the thermal expansion coefficients of mudstone and sandstone fluctuate as temperature increases (Figure 2.6).

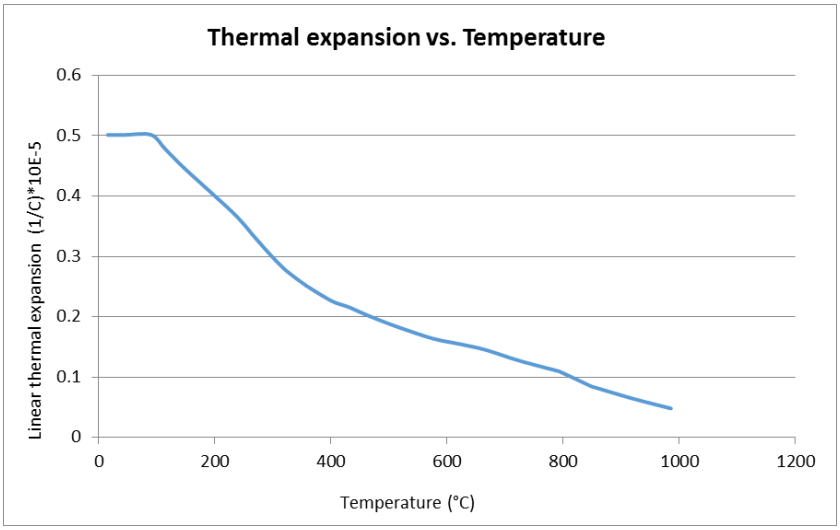


**Figure 2.11:** Coal thermal expansion coefficient profile against temperature (Singer and Tye, 1979)

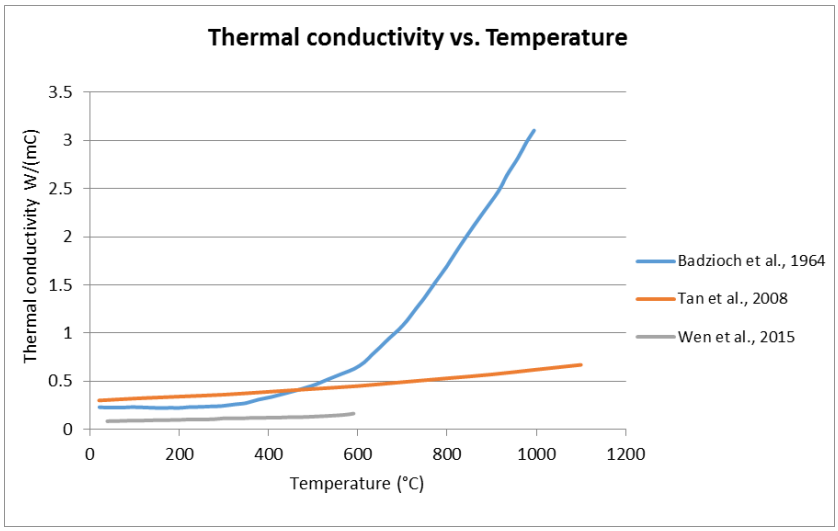


**Figure 2.12:** Coal thermal conductivity profile as a function of temperature

Moreover, Figures 2.12 - 2.13 indicate how the thermal conductivity and the specific heat of coal varies with time. Tan et al. (2008) and Wen et al. (2015) reported consistent trends on how thermal conductivity varies with temperature, in contrast to the trend reported by Badzioch et al. (1964). On the other hand, higher consistency is achieved among the different studies when the specific heat variation with temperature is reported (Figure 2.13). Specifically, Hanrot et al. (1994) and Wen et al. (2015) reported consistently fluctuating curves regarding how coal specific heat coefficient varies with temperature. In contrast to roof rock materials (i.e. mudstone or sandstone), whose corresponding property has an increasing (or at least steady) route as temperature increases (Figure 2.8).

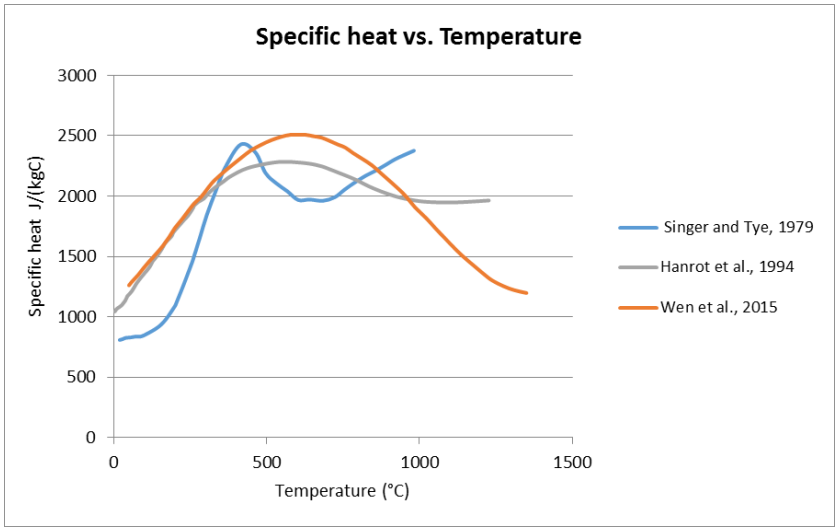


**Figure 2.13:** Coal specific heat variation as a function of temperature

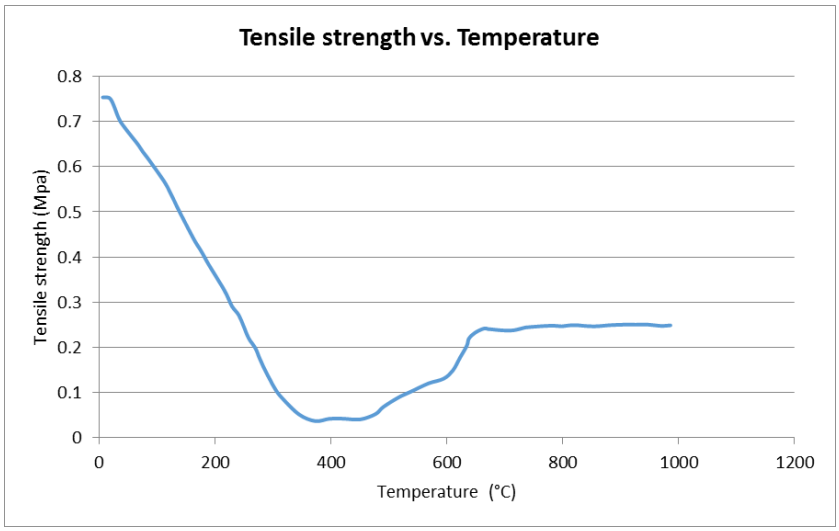


**Figure 2.14:** Coal tensile strength variation as a function of temperature (Singer and Tye, 1979)

Furthermore, Figure 2.14 presents how the tensile strength of coal changes with increasing temperature. As it can be seen, the value of the tensile strength drops rapidly as the temperature approaches 400°C, which is a critical temperature where the pyrolysis of coal occurs. On the other hand, consistency exists among the studies referring to elastic modulus behaviour with temperature (Figure 2.15). Both trends indicate a gradual decrease to the elastic modulus value before reaching the 300°C. This gradual decrease is converted to a rapid drop between the 300°C – 600°C. However, Tan et al. (2008) reports a less stiffer slope compared to the corresponding one by Shoemaker et al. (1977).

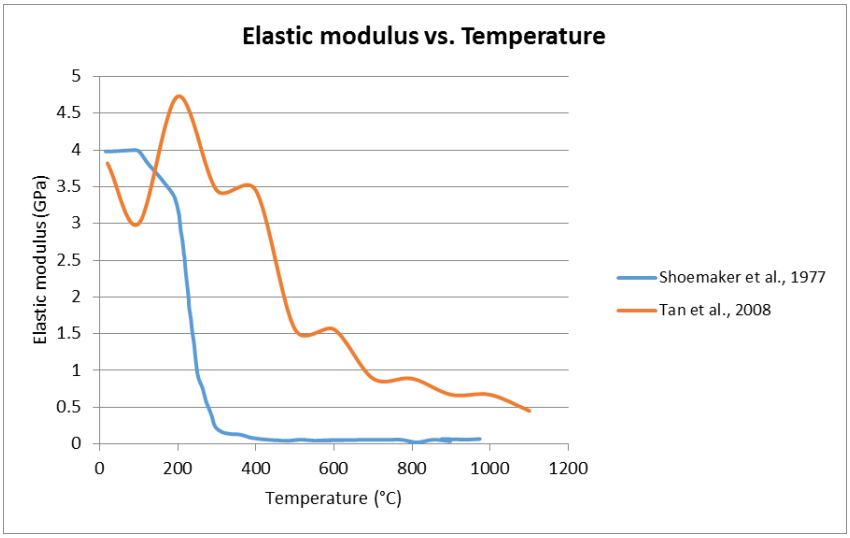


**Figure 2.15:** Coal elastic modulus behaviour as function of temperature

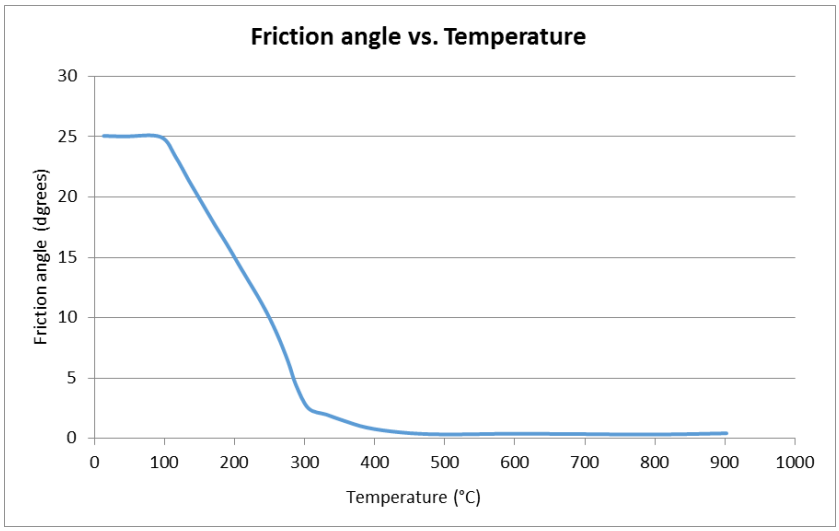


**Figure 2.16:** Coal friction angle behaviour as function of temperature (Min, 1983)

Both the coal friction angle (Figure 2.16) and the coal cohesion (Figure 2.17) as a function of temperature experience a similar behaviour to the elastic modulus values against temperature (Figure 2.15).

Finally, when the behaviour of the thermo-mechanical properties of coal are compared against the corresponding ones for roof rock materials (i.e. sandstone, shale etc.) it can be seen that the more distinct differences are noticed on how the thermal properties vary as a function of temperature, and especially on how thermal conductivity changes with increasing temperatures (Figure 2.7- Figure 2.12).

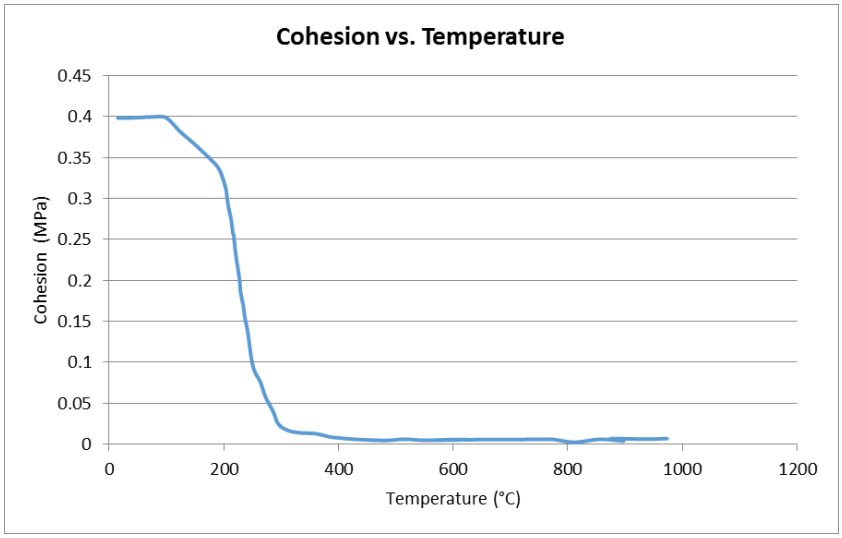


**Figure 2.17:** Coal cohesion behaviour as function of temperature (Min, 1983)

## 2.3 *Heat and mass transport phenomena*

### 2.3.1 Fluid flow

Fluid flow is the term usually employed when the dynamic motion of fluids (liquid or gases) is analysed. Fluid should be seen as a continuum of molecules travelling along with it. However, in gases the distance between the molecules is much higher compared to their size while this is not exactly the case in liquids. The molecules within a liquid matter are relatively closer between each other compared to what happens in gases. The molecular distance is an important component of fluid motion with the fluids to deform as they flow and, in contrast to solids, they do not have the ability oppose even to the slightest shear stress. The above distinction between the fluid flow and the solid matter facilitates the conclusion that the shear forces tend to zero as the velocity of the caused fluid deformation tends to zero. On the other hand, in the case of the static solid matter the corresponding shear forces tend to zero if the caused deformation (and not its velocity) to the accounting solid tends to zero (Aaltosalmi, 2005). In addition, fluid flow should be governed and regulated by principle equations for the conservation of mass (E2.15), momentum (E2.17) and energy equation (E2.18) (Fox and McDonald, 1994; Ghil and Childress, 2012; White, 1999):

$$\partial_t \rho + \nabla \cdot (\rho u) = 0 \qquad \text{(E2.15)}$$

Where,

$\rho$: represents the fluid density value (kg/m$^3$)

$g$: the gravitational acceleration (9.81 m$^2$/s)

$u$: the flow vector (m/s)

As a result, the mass conservation equation reassures that the mass balance change with time and space remains zero. The above equation (E2.15) is valid for both compressible and incompressible fluid flows. However, in the case of incompressible flows where the density remains steady against time and space, equation (E2.15) takes the following form (E2.16):

$$\nabla \cdot u = 0 \qquad \text{(E2.16)}$$

Additionally, the momentum equation focus on the balance of the applied forces per unit of volume (kg/(m$^2$ s$^2$)). By analysing the first part of the following equation the applied forces per unit of volume consists of the sum of rate of change with time in the product of speed and density and the divergence in the product of density and the square of speed. On the other hand, the second part of the equation consists of the gravitational force per unit volume ($\rho g$) and the divergence of the stress tensor ($\sigma$).

$$\partial_t(\rho u) + \nabla \cdot (\rho u u) = \nabla \sigma + \rho g \quad \text{(E2.17)}$$

Where,

$\rho$: represents the fluid density value (kg/m$^3$)

$g$: represents the gravitational acceleration (9.81 m/s$^2$)

$\sigma$: represents the acting stress (kg/(m s$^2$))

Furthermore, in the case of steady and incompressible fluids the equation becomes (Hageraats, 2006):

$$\rho u \cdot (\nabla u) = \nabla \sigma + \rho g \quad \text{(E2.18)}$$

Furthermore, the energy conservation equation (E2.19) represents the rate of energy transfer per unit volume with time (J/(m$^3$ s)). The energy transfer per unit volume comes as the product of specific heat (J/(kg K)) with the temperature (K) and density (kg/m$^3$). Furthermore, the right-hand side of the equation (E2.19) includes the heat flux due to conduction ($k\nabla T$) and the viscous dissipation function ($H$).

$$\frac{\partial \rho c_p T}{\partial t} + \nabla \cdot (\rho c_p T u) = \nabla \cdot (k \nabla T) + H \quad \text{(E2.19)}$$

Where,

$T$: represents the temperature (K)

$k$: the coefficient of thermal conductivity (W/(m K)))

$c_p$: represents the specific heat (J/(kg K))

$H$: represents the energy transfer due to species diffusion and viscous dissipation

Furthermore, a dimensionless number that helps analysing the flow behaviour of a fluid is the *Reynolds* number (E2.20). This number expresses the ratio of the inertia to viscous forces applying to a fluid. The value of this ratio provides an insight on whether laminar or turbulent flow occurs. This implies that density is the metric to indicate the resistance of fluid to any velocity changes while on the other hand viscosity represents the resistance to any deformation that could be caused by the friction of the moving molecules within the fluid. A low *Reynolds* number indicates laminar flow while a high *Reynolds* number indicates turbulent flow (Bergman et al., 2011; Bovo, 2014; Lienhard, 2013).

$$\mathrm{Re} = \frac{\rho u L}{\mu} \tag{E2.20}$$

Where,

*Re*: represents the dimensionless Reynolds number

*L*: the characteristic length (m)

$\mu$: represents the dynamic viscosity (kg/(m s))

As it can be seen in (E2.20), the *Re* number is reversely proportional to the dynamic viscosity of the fluid which is in accordance with the earlier fact as highly viscous fluids follow more laminar flows. In the case of laminar flow through porous media such as a permeable coal bed, Darcy's law (E2.21) becomes highly relevant (Aaltosalmi, 2005; Scheidegger, 1957):

$$q = -\frac{kA}{\mu}\nabla p \tag{E2.21}$$

Where,

*q*: represents the volumetric flow rate ($m^3/s$)

*p*: represents the pressure ($kg/(m^2\ s)$)

*k*: represents the permeability coefficient ($m^2$)

*A*: represents the surface area ($m^2$)

As Darcy's law illustrated (E21), fluid flow can occur due to a pressure gradient ($\nabla p$) from the higher to the lower pressure regions.

For this reason, the negative sign (-) implies that the flow will be reverse to the direction of the positive pressure difference.

### 2.3.2 Convection

Convection is called the collective movement of the molecules within a fluid and it can be expressed through either advection or diffusion. Convection is a phenomenon that can refer to both heat and mass transfer. The advection refers to the collective movement of the molecules of a substance due to the fluid's bulk motion. On the other hand, diffusion represents the random movement of the molecules within a fluid due to the presence of a gradient. In case concentration differences are developed within a fluid mixture, mass transfer diffusion phenomena take place due to the developed concentration gradients (Frentrup, 2014).

Diffusion phenomena are commonly described by *Fick's law* (E2.22) (Bird et al., 2007) or by the *Stefan-Maxwell diffusion* equation (E2.23) (Taylor and Krishna, 1993).

$$J_i^D = -D\frac{\partial \varphi}{\partial x} \tag{E2.22}$$

Where,

$J$: represents the diffusion flux (mol/(m$^2$ s))

$D$: represents the Fickian diffusion coefficient (m$^2$/s)

$\varphi$: represents the concentration (mol/m$^3$)

As it can be seen, equation (E2.22) correlates the mass flux with the concentration gradient showing how the flux develops from the high to the low concentration regions within the fluid mixture. The diffusion flux unit (mol/(m$^2$ s)) shows how the flow develops per unit of surface per unit of time. On the other hand, the *Stefan-Maxwell diffusion* model (E2.23) is often employed in multi-component mixtures and considers the chemical potential gradient:

$$\frac{\nabla \mu_i}{RT} = \sum_{j=1}^{n} \frac{X_i X_j}{D_{ij}} (u_j - u_i) = \sum_{j=1}^{n} \frac{c_i c_j}{c^2 D_{ij}} \left( \frac{J_j}{c_j} - \frac{J_i}{c_i} \right) \tag{E2.23}$$

Where,

$\mu_i$: represents the chemical potential of the *i* component

$X_i$: represents the mole fraction of the *i* component

$D_{ij}$: represents the Stefan-Maxwell diffusion coefficient

$c_i$: represents the molar concentration the *i* component

#### 2.3.2.1 Convective heat transfer parameters

The discipline of fluid mechanics is highly associated with the convective heat transfer mechanism either within the fluid or between the fluid and a surface especially when the phenomenon of fluid flow close to a boundary layer is studied. In addition, this interaction between the moving fluid and the surface boundary is affected by different parameters such as the temperature difference between the boundary and the fluid, the velocity of the fluid close to the boundary layer and the length of the bounding surface. As a result, different metrics are used in order to group similar flow patterns. The *Nusselt* number (E2.24) presents the ratio of convective to conductive heat transfer. It is dimensionless number which correlates the total heat transfer of the fluid when it is in motion (convection) with the heat transfer that would occur with a completely motionless fluid (conduction) (Bergman et al., 2011; Bovo, 2014; Lienhard, 2013):

$$Nu = \frac{hL}{k} \tag{E2.24}$$

Where,

*Nu*: represents the dimensionless Nusselt number

*h*: represents the convective heat transfer coefficient (W/(m$^2$ K))

*L*: represents the characteristic length (m)

*k*: represents the thermal conductivity of the fluid (W/(m s))

A high Nusselt number (100-1000) would often refer to turbulent flow taking place close to the boundary surface while corresponding low values (~1) would refer to stagnant flows. Furthermore, depending on the cause of the convective heat transfer it can be classified to *natural* and *forced convection*. Natural convection occurs when buoyancy forces dominate the flow while forced convection is exhibited when external means (e.g. fan, pump) induce the flow.

The following metrics (E2.25)-(E2.26) are necessary in order to classify the flow accordingly. The *Grashof* number is an additional dimensionless number which expresses the fraction of the buoyancy to viscous forces (Bergman et al., 2011; Lienhard, 2013).

$$Gr_L = \frac{g\beta\Delta T L^3}{v^2} \tag{E2.25}$$

Where,

$Gr_L$: represents the dimensionless Grashof number

$\beta$: represents the thermal expansion coefficient (1/K)

$\Delta T$: represents the temperature difference (K)

$v$: represents the kinematic viscosity ($\mu/\rho$) ($m^2/s$)

Furthermore, the ratio of the Grashof number to the square of Reynolds number is called *Archimedes* ratio and expresses the ratio of the buoyancy to inertial forces (Lienhard, 2013):

$$Ar = \frac{Gr}{\mathrm{Re}^2} \tag{E2.26}$$

Where,

$Ar$: represents the Archimedes ratio dimensionless number

$Gr$: represents the Grashof number

$Re$: represents the Reynolds number

For high Archimedes ratio values (Ar >>1) natural convection dominates the flow while correspondingly low values (Ar <<1) indicate that forced convection takes place. For Archimedes ratio close to unit (Ar ~1) then a balanced performance between forced and natural convection exists. As a result, in the case that natural convection dominates the flow (Ar >>1) then Grashof number ($Gr_L$) is often used to decide whether turbulent flow exists and the buoyancy forces dominate or laminar flows takes place and the viscous forces dominate. Furthermore, the viscous diffusion rate to thermal diffusion rate is expressed through the Prandtl number (E2.27) (Bergman et al., 2011; Lienhard, 2013):

$$\Pr = \frac{v}{a} \qquad \text{(E2.27)}$$

Where,

*Pr*: represents the Prandtl dimensionless number

*a*: represents the thermal diffusivity ($m^2/s$)

The Prandtl number characterises the fluid and at defined conditions (i.e. pressure, temperature) its value can be found in property tables. Finally, when natural convection dominates the flow an additional dimensionless number should be studied. This is the Rayleigh number which can be calculated through the product of the Prandtl and the Grashof number (E2.28). This number studies if the heat transfer within that fluid occurs primarily through convection or conduction.

High Rayleigh numbers would indicate heat convection as the primary transfer mechanism while reversely low Rayleigh numbers would indicate heat conduction as the main mechanism (Bergman et al., 2011; Lienhard, 2013).

$$Ra_L = Gr_L \Pr \qquad \text{(E2.28)}$$

Where,

*Pr*: represents the Prandtl dimensionless number

*a*: represents the thermal diffusivity ($m^2/s$)

### 2.3.3 Radiation

In contrast to other forms of heat transfer (i.e. conduction, convection) where the matter in-between the different temperature bodies is necessary for the development of a temperature gradient which will allows the energy transfer, radiation does not involve the presence of matter. However, a participating or a non-participating medium may intervene between two different temperature surfaces between which the heat transfer takes place. Furthermore, due to the fact that radiation can be considered as the joint movement of particles called photons its two important characteristics are its wavelength (λ) and frequency (v) (Lienhard, 2013).

Furthermore, as radiation occurs between two surfaces at different temperatures its measurement unit is the flux ($W/m^2$) – the power transferred per unit of surface. The different forms of heat radiation fluxes can be classified accordingly (Bergman et al., 2011):

- The *emissive power (E)*, which is the heat flux radiated to all directions across all wavelengths. In the case of a *blackbody* the magnitude of this flux is linked with following equation (E2.29) – which is also known as Stefan-Boltzmann Law:

$$E = \sigma T^4 \tag{E2.29}$$

Where,
$E$: represents the emitted power flux ($W/m^2$)
$\sigma$: represents the Stefan-Boltzmann constant ($5.670 * 10^8$) ($W/(m^2 T^4)$)

In addition, for a surface to be considered as *blackbody*, certain assumptions need to be made:

  - Firstly, a blackbody absorbs all the clashing radiation regardless of its wavelength and direction.
  - Secondly, under specific operating parameters (i.e. temperature and wavelength), the blackbody radiates the highest heat flux than any other surface.
  - Finally, a blackbody diffuses its emitted heat irrespective of direction.

- The *irradiation (G)*, which represents the total amount of flux falling over a surface or semi-transparent medium coming from all directions and wavelengths. However, the question that remains to be answered is how the proportion of the heat flux leaving one surface and reaching another is calculated. For this reason, this view factor coefficient (E2.30) was developed:

$$Fij = \frac{1}{A_i} \iint_{A_i A_j} \frac{\cos\theta_i \cos\theta_j}{\pi R^2} dA_i dA_j \tag{E2.30}$$

This view factor coefficient (E2.30) analyses how the heat flux emitted from one elemental surface $dA_i$ can be intercepted by another elemental surface $dA_j$. Specifically, $dA_i$ represents the high temperature surface while $dA_j$ the corresponding low temperature. By assuming that a straight line (R) connects the middle points of the two surfaces $\theta_i$ represents the angle between the straight line and the normal plane to the $dA_i$ surface while correspondingly $\theta_j$ represents the angle between the connecting line and the normal plane to the $dA_j$ surface. This cosine transformation aims to calculate the equivalent of the emitted and received radiations if both elemental surfaces were parallel to each other and normal to the connecting line (R). Finally, the double integral indicates that the same procedure has to be followed for the whole of the emitting and accepting surface.

The irradiative heat flux (G) has three possible routes:

- Reflected
- Absorbed
- Transmitted

Especially, in the case that the radiative heat flux is transmitted the Beer's Law decay term (E2.31) is highly relevant. This decay term also known as transmissivity coefficient expresses how much of the initial radiative intensity ($I_{\lambda,0}$) passes through a semi-transparent one-dimensional medium of length L and reaches its end ($I_{\lambda,L}$) (Bergman et al., 2011).

$$\frac{I_{\lambda,L}}{I_{\lambda,0}} = e^{-\kappa_\lambda L} \qquad \text{(E2.31)}$$

Where,

$I_{\lambda,0}$: represents the intensity of the initial radiative heat flux at the beginning of the medium per unit of wavelength $\lambda$ ($W/(m^2\ \mu m)$)

$I_{\lambda,L}$: represents the intensity of the radiative heat flux at the end of the medium per unit of wavelength $\lambda$ ($W/(m^2\ \mu m)$)

L: represents the length of the semi-transparent medium (m)

$\kappa_\lambda$: represents the absorption coefficient of a semi-transparent medium ($m^{-1}$)

# Chapter 3 Underground Coal Gasification

## 3.1 *Introduction*

The aim of Chapter 3 is to provide a clear understanding over the characteristics of the UCG processes. For this reason, the first step is to detail the description of a typical UCG plant while presenting a timeline of the developed UCG projects. In addition, the reasons that UCG has attracted a renewed interest in the recent years and its potential limitations and concerns are discussed. Furthermore, different operational designs and subsurface layouts have been developed for UCG over the years and as a result these are discussed and analysed. Finally, the literature that discusses the physical and chemical processes of UCG through experimental or modelling studies is analysed. Specific focus is given on the studies that constitute the backbone for the modelling work of this thesis, as included in Chapters 4-7.

## 3.2 *Underground Coal Gasification Process Description*

Underground coal gasification (UCG) is the term which describes how underground coal quantities can be converted to useful gas products (Burton et al., 2007; Gregg and Edgar, 1978). This conversion takes place below ground and it is dependent upon both chemical and physical parameters.

A generic approach to the whole process involves pumping a blend of gasification agents (mainly air blended with oxygen, steam and commonly with carbon dioxide) to the subsurface coal formation propagating its gasification (Figure 3.1). The composition of the out-flowing gas (syngas, comprising carbon dioxide, tar products and steam together with useful carbon monoxide, hydrogen and methane loads) depends on the operational parameters as well as on the coal formation characteristics. In fact, the extensive UCG syngas dependency on numerous interrelated parameters has been the main constraint to various modelling efforts. In addition to that, the limited controllability of the underground processes indicates that the well constraint surface experiments cannot fully describe the subsurface processes (Gregg and Edgar, 1978).

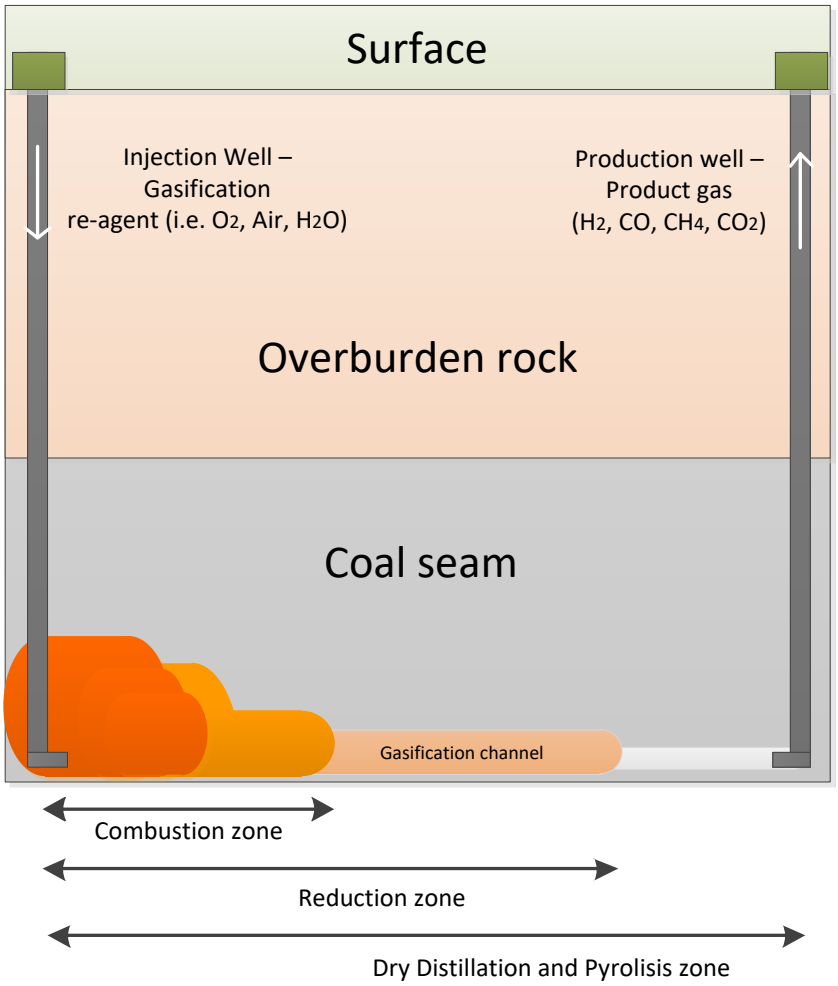


**Figure 3.1:** Schematic overview of one of the available designs for the UCG process (after Lee et al., 2014).

### 3.2.1 Historical Overview

The German scientist, Sir William Siemens, was the first to introduce the idea of burning coal in-situ in 1868. However, around the same period, Dimitri Mendeleyev, from Russia, advanced the UCG idea by suggesting that a coal resource can be gasified in-situ through injection and production wells (Olness and Gregg, 1977).

The first patent for UCG is recorded in 1909 in Great Britain and it is attributed to A.G. Betts. Later on, Sir William Ramsey further developed Bett's idea on UCG and his speeches attracted the interest of Lenin from Russia. After a disruption on UCG development plans during World War I, Stalin became one of the main admirers of UCG and for this reason Former Soviet Union (FSU) took the lead on UCG implementation for the next 50 years following 1928 (Burton et al., 2007).

**Table 3.1**: Timeline of UCG trials.

| Time period | Countries | Notes | Source |
|---|---|---|---|
| Up to 1970s | USSR | UCG application in Uzbekistan is still in-use | (Gregg et al., 1976; Olness, 1982) |
| 1970s to 1980s | USA | 30 tests completed in the USA during that period | (Gregg and Edgar, 1978; Klimenko, 2009) |
| 1980s to present (most important) | Spain (1992 – 1999) | Assessed the feasibility of deep and thin coal seams | (Burton et al., 2007; Shafirovich and Varma, 2009) |
| | China (since 1980) | 16 tried were carried out as part of the governmental strategy to diversify the conventional coal utilisation techniques | (Burton et al., 2007; Yang et al., 2003) |
| | Australia (1999 – 2002) | Reinforced the prospects for increased control on the UCG sites | (Shafirovich and Varma, 2009; Walker et al., 2001) |
| | South Africa (since 2001) | The UCG-IGCC integration is the ultimate task | (Shafirovich and Varma, 2009) |

As can be seen in Table 3.1, the UCG progress can be categorised in three zones. The first zone includes the UCG developments in the FSU. Different projects developed during that period with the majority to terminate their operation in the mid-1970s. However, the UCG plant developed in Taskenth (Uzbekistan) in 1961 is still in operation and it is the only commercially operating UCG plant nowadays (Wiatowski et al., 2012). With respect to the US trials, it should be highlighted that although they started after the ones conducted in the FSU they outnumbered them.

Specifically, 50 UCG trials have taken place worldwide with 30 of them to be conducted in the US (Gregg and Edgar, 1978; Klimenko, 2009).

The US trials provided substantial input on the understanding of the UCG and evidenced its feasibility through lengthy and large-scale trials. In addition, the focused nature of the trials helped to evaluate how certain parameters such as the stratigraphy or how the selected process design can impact both the monitor process as well as the UCG operation itself (Thorsness and Britten, 1989). The main trials took place in in Hanna (1973-1978), Hoe Greek (1976-1979), Pricetown (1979), Rawlins (1979-1981) and in Centralia (1981-1983) (Stephens et al., 1985).

The Hoe Greek trial was conducted in three stages (I, II, III). The main difference between the three stages was the implementation of different coal seam permeability techniques in each of them. During Hoe Greek I the explosive fracturing was tested, while the reverse combustion linking and a combination of directional drilling with reverse combustion were tested during Hoe Greek II and Hoe Greek III respectively. Furthermore, air injection was used during Hoe Greek I, while a varying ratio of oxygen to steam during Hoe Greek II and Hoe Greek III respectively (Stephens, 1981).

The Hoe Greek trials (I, II, III) offered important learnings. They were conducted on a coal seam below the water table in order to increase the controllability of the process. This means that the fire extent in the coal seam could have been more easily regulated and avoid any uncontrolled burns. However, the high pressure in the coal seam was also necessary in order to reduce the extensive water influx. The consequence was the migration of gasification products to the surroundings and the consequent groundwater contamination (Stephens et al., 1985).

Furthermore, during the Hoe Greek experiments surface subsidence and roof collapse were noticed. However, another important learning offered by these trials was the instrumentation required in order to monitor the process, the cavity growth and the geotechnical structure. The UCG process was monitored through measurements in the composition of the injection and production flows (e.g. through chromatography) as well as through pressure monitoring. Thermocouples were employed in different places within the coal seam and the cavity evolution was estimated.

Post-burn coring also helped on conclusions over the cavity size and shape. Tracers were also injected to help on density measurements and resident times (Stephens, 1981).

The UCG trials in Centralia were conducted in sub-bituminous coal and their purpose was to both test different steam to oxygen ratios as injected gasification agents and innovative UCG engineering designs such as the Controlled Retractable Injection point (CRIP). The outcome of the trials was that the oxygen to steam ratios didn't have significant on the composition of the product gas. In addition, the reactor zone was self-stabilising and the post-burning assessment proved that the developed cavity was filled with ash, dried coal and char. The Centralia trials were the first to fully develop the CRIP engineering design which involves horizontal drilling within the coal seam. This design increased the utilisation rate of the coal seam up to 20-30 times compared to vertical drilling although some casing around the horizontal wells was found to block the flow of the injected reactants (i.e. $H_2O$, $O_2$) (Hill and Thorsness, 1983a; Hill et al., 1983b).

The European Working Group on UCG in 1989 decided to assess the feasibility of UCG technologies in Europe and especially for high coal seam depths (>500m). The responsible committee suggested a number of sites in Europe. The first trials took place in Spain (in "El Tremedal") from 1992 to 1999. Spain, UK and Belgium in cooperation with the European Committee participated on the trials. The trials were held on 550m depth (Shafirovich and Varma, 2009). The purpose of the trials was to prove the feasibility of directional in-seam drilling in deep coal seams and evaluate the feasibility of UCG for even deeper (>550m) coal seams. These trials consolidated the usefulness of the CRIP for deep coal seam and revealed some limitations such as the less that 50m directional drilling that could be achieved within the coal seam (Burton et al., 2007; Perkins, 2005).

However, as both Burton et al. (2007) and Self et al. (2012) highlighted the progress of the drilling technology through the accumulated experience from the oil and gas industry have contributed to the fact that early stage questions on the engineering aspects of UCG can be answered nowadays.

Since 1980, China has shown significant focus on UCG by developing 16 pilot projects. The trials conducted in China used mainly air and steam as injected gasification reagents and performed in abandoned coal mine galleries. The motivation for UCG in China comes from the governmental efforts for diversification from the conventional coal methods. This is also the reason that in China UCG projects are coupled with surface facilities exploring the different uses of the final product gas. As a result, the UCG product-gas is used for ammonia and hydrogen production, electricity generation and as feedstock in the production of liquid fuels (Burton et al., 2007). Finally, as Shafirovich and Varma (2009) highlighted in their work, China is considered to currently dominate the research and development on UCG.

In Australia , the interest for UCG was created by Prof. Ian Stewart of the University of Newcastle, whose laboratory research in 1983 proved that the UCG product gas can become an economically viable option and compete with the other fuels. However, it wasn't before 1996 that significant progress on UCG took place. Four companies (i.e. Linc Energy Ltd., Cougar Energy Ltd., Carbon Energy Ltd and Ergo Exergy) contributed considerably on developing the commercial status of UCG in Australia. Linc Energy in partnership with Ergo Exergy conducted the UCG trial in Chinchilla (Australia) between 1999 and 2002. During this trial, 30,000 tons of coals were gasified. This trial contributed on achieving higher control over the process (its shutdown and restart) as well as provided satisfactory environmental results regarding the avoided groundwater contamination and surface subsidence. In 2007, Linc Energy decided to take a controlling position in Yerostigaz, the company that owns the only commercially operating UCG plant in Uzbekistan (Shafirovich and Varma, 2009).

UCG projects has also been developed in South Africa and New Zealand while India and Japan show a growing interest on utilizing their coal resources through UCG (Burton et al., 2007; Khadse et al., 2007; Shafirovich and Varma, 2009).

Table 3.2 presents a comparison of different UCG projects with respect to the seam thickness, the depth, the type of the injected gasification agents and the heating value of the produced gas. It can be highlighted that the injection of oxygen ($O_2$) and steam ($H_2O$) instead of air leads to product gas with considerably higher heating value.

**Table 3.2**: The heating values from the product gases of three different UCG projects (sub-bituminous coal in all cases) with respect to their relevant operating conditions.

| Site | Thickness (m) | Depth (m) | Injected reagent | Heating Value ($MJ/Nm^3$) | Source |
|---|---|---|---|---|---|
| Centralia, USA | 6 | 75 | $O_2/H_2O$ | 9.7 | (Oliver et al., 1989) |
| El Tremedal, Spain | 2 | 550 | $O_2/H_2O$ | 10.9 | (Burton et al., 2007; Shafirovich and Varma, 2009) |
| Chinchilla, Australia | 10 | 140 | Air | 6.6 | (Walker et al., 2001) |

Furthermore, Table 3.3 presents a detailed composition of the dried-product gas by comparing two of the three UCG projects whose parameters are already presented in Table 3.2. As it can be seen, the depth of the coal seam affects the operating pressure and indirectly the methane content of the produced gas (Green, 1999). In addition, the air injection during the Chinchilla UCG operation had an effect on the product gas composition with most of the injected air to be collected in the product-gas through its increased nitrogen ($N_2$) content, as it is shown in Table 3.3.

**Table 3.3**: Comparison with respect to the product-gas composition and the operating pressure for the El Tremedal (Spain) and Chinchilla (Australia) UCG project.

| Site | Pressure (bar) | $N_2$ (%) | CO (%) | $CO_2$ (%) | $H_2$ (%) | $CH_4$ (%) | Source |
|---|---|---|---|---|---|---|---|
| Centralia, USA | 7.5 | 0.01 | 0.22 | 0.28 | 0.43 | 0.05 | (Hill and Thorsness, 1982; Perkins and Sahajwalla, 2008) |
| El Tremedal, Spain | 50 | 0.01 | 0.1 | 0.47-0.35 | 0.27-0.17 | 0.15-0.26 | (Nourozieh et al., 2010; Shafirovich and Varma, 2009) |
| Chinchilla, Australia | 14 | 0.43 | 0.07 | 0.19 | 0.22 | 0.08 | (Walker et al., 2001) |

The $CO_2$ content of the product-gas from the El Tremedal project is also more than twice as high the respective one from the Chinchilla project (Table 3.3). Furthermore, Figure 3.2 presents a high-level overview of the developed UCG projects globally. As it can be seen, the developed UCG pilot projects can be categorised into two categories: a) in shallow coal seams (<500m) for a variety of seam thicknesses (1m-18m) and b) for deep coal seams (>500m) of low thickness (<4m). As a result, Figure 3.2 provides the motivation for debate whether UCG can be tested in thick coal seams (>5 m) which are located in high depths (>500m).

According to Perkins (2005), the drilling costs rise as the depth of the coal seam increases. On the other hand, as the seam thickness increases the available coal surface grows and the cost per unit of coal gasified can become lower.

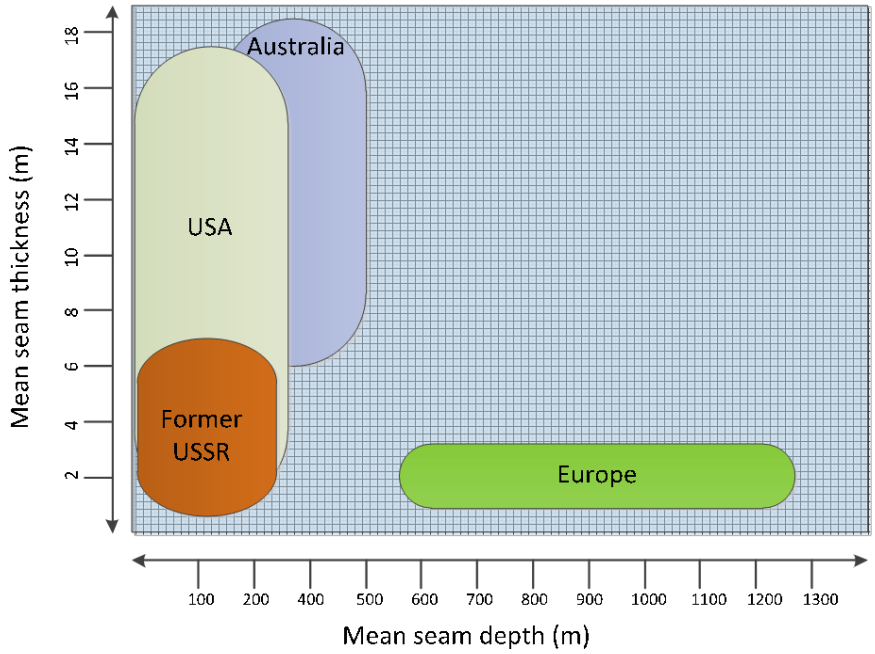


**Figure 3.2:** Classification of UCG operations with reference to coal seam depth and thickness (after Perkins, 2005).

### 3.2.2 Perceived advantages and benefits of UCG

While the supply of oil and gas becomes increasingly dependable on the geopolitics, the abundance of coal resources can facilitate the energy production through coal utilisation as a reliable energy source for many counties (Burton et al., 2007). However, the conventional coal utilisation methods through mining and surface gasification imply both environmental and safety concerns. UCG can become a sustainable alternative to these methods. Firstly, UCG in contrast to conventional mining does not require any underground labour work (reducing labour safety concerns). In addition, conventional mining techniques involve high operating costs and include additional concerns regarding the stability of the mine galleries or potential damages caused on the surface.

It also gives the opportunity for the exploitation of deep coal reserves that cannot – or is not financially reasonable to – be mined through the conventional mining methods. Specifically, the recoverable coal reserves – either through underground work or through open pit – represent 15% to 20% of the total coal reserves globally (WEC, 2007). Secondly, UCG replaces the need for transporting and storing the mined coal for its surface gasification. For this reason, the transporting costs and the supply chain footprint associated with coal gasification are eliminated. UCG also increases the energy efficiency when compared to conventional mining of coal and its subsequent surface gasification by reducing the wasted energy amount required for coal transportation. Thirdly, UCG builds its main environmental and financial advantage when compared to surface gasification. The UCG environmental benefit is attributed to both the reduced emissions due to the subsurface processes and the lack for surface handling of high-volume gasification by-products (e.g. fly-ash, $No_x$-$So_x$ pollutants). As a result, the financial advantage is linked with the reduced capital and operating costs due to the avoided scale of surface equipment (Burton et al., 2007; Shackley et al., 2006). Finally, UCG when compared to other sustainable forms of energy (e.g. renewables, nuclear) offers an additional advantage regarding its option for geologic carbon storage and $CO_2$ sequestration processes which can be combined with the UCG setup. However, the coupled UCG-$CO_2$ storage benefit can only be seen in deep coal seams (800 m – 1,000 m) where the pressures are high and the density of the stored $CO_2$ becomes high enough leading to reduced storage volume (Self et al., 2012).

### 3.2.3 Potential Limitations and Concerns for UCG

Shackley et al. (2006) referred to a group of possible disadvantages while employing conventional coal recovering techniques by mainly referring to cost, environmental and safety issues. However, UCG is a multi-component process which is difficult to precisely regulate. As a proof to the above statement comes the reference of possible threats during UCG practices.

The following considerations are indicative (Khadse et al., 2007; DTI, 2005; Gregg and Edgar, 1978):

- Leakage of the produced gas to surrounding formation before it is pumped up to the surface. This could lead to commercial disadvantage, having to cope with decreased valuable product output, and also raise serious environmental concerns (depending on the amount of leakage) since components of that gas can cause serious safety concerns for both the workers and the local communities, as well as the environment.

- Inflow of excess water into the seam from the surrounding strata. If this occurs then energy is inevitably lost since heat is dissipated from the cool inflowing water and chemical reaction conversion rates are significantly reduced.

- Inefficient coal-to-syngas conversion since significant coal quantities can remain ungasified. Since the advance rate of the conversion process within the coal seam is difficult to control, it is possible that some coal quantities might not to be gasified and, thus, lead to decreased coal utilisation and consequently to reduced energy efficiency levels.

- Roof failure during the process. The roof collapse may also cause excessive water flooding inside the cavity or subsidence of the overlying strata.

## 3.3 *Process design issues and concepts*

The development of a UCG project depends on certain selection criteria for both the UCG site and the chosen UCG design. A list of relevant criteria is the following (Khadse et al., 2007; Shafirovich and Varma, 2009; Sury et al., 2004):

- *Coal seam thickness.* Although the optimal seam thickness is supposed to be above 10 m, trials in thinner coal seam (up to 0.5m) do exist. A benchmark value to the seam thickness is set at 2 m with trials in thinner coal seams to produce gas with considerable lower heating value.

- *Coal seam depth.* As it can be seen in Figure 3.2, UCG trials have been conducted globally at different depths. However, the decision on the depth of the coal seam can be attributed to both environmental and financial parameters. Financially, the depth of a coal seam is crucial for UCG in order to build its competitive advantage over the conventional mining techniques.

For this reason, shallow coal seams (<60m) are not preferable for UCG since conventional mining methods are preferential on that case. On the other hand, UCG at deeper coal seams (>300m) incur increased drilling costs while having certain benefits. The increased operating pressures contribute on product gas with higher heating value and further compression of the produced syngas might not be required on the surface if it is to be used in gas turbines. In addition, surface subsidence is less likely to happen when deep coal seams are chosen while deep UCG sites (>800m) have the potential to be combined with carbon capture and storage options.

- *Coal rank.* The most critical characteristics for UCG are the porosity, permeability and the heating value of the coal resource. High porosity and permeability eases the movement of the injected gases within the coal seam increasing the speed of gasification. Higher porosity and permeability are found in the lower rank coals. In addition, the impurities of these coal varieties can contribute to the rate of the chemical reactions by acting as catalysts. However, the heating values of lower rank coals lead to product gases with lower heating values. In addition, the increased porosity and permeability can also lead to extensive product gas losses and increased water inflow to the seam decreasing the efficiency of the process.

- *Dip of the coal seam.* Inclination or dip of coal seam is not a critical parameter for the UCG site selection. However, slight seam inclination (between 0° and 20° degrees) could contribute to its drainage and the development of a hydrostatic balance within the seam. The reason is that the inclination protects the production well from rubbles that fall to the bottom of the seam while the produced gas flows smoothly to the higher levels of the seam where the production well exists.

- *Groundwater.* The interaction between the coal seam and the groundwater saline aquifers are of significant importance for UCG. Groundwater is considered the main supplier of $H_2O$ to the gasification reactions while on the other hand extensive water influx reduces the energy efficiency. Furthermore, the groundwater contamination through the product gas losses has to be avoided. Stratigraphic analysis can reveal how sealed is the coal seam from the surrounding strata.

The depth of the coal seam and its distance from the subsurface aquifers are critical. Average safe distance between the roof of the coal seam and the saline aquifers is considered to be 25 times the thickness of the seam.

- *Amount of coal – Use of UCG product gas.* This criterion considers the final use of the UCG product gas. The final use of the produced gas needs to be decided at the design stage of UCG in order to choose accordingly the UCG site and the operating parameters (e.g. type of gasifying agents). If the UCG product gas is planned to be used as chemical feedstock for liquid fuels then $H_2$ and CO contents are beneficial and as a result high operating pressure (i.e. increased $CH_4$ content) is not advantageous. On the other hand, the capacity or the scale of the planned UCG syngas production has to be in accordance with the available coal resource.

The drilling concepts can be categorised into *shaft* and *shaftless* methods. The shaft methods involve the construction of subsurface galleries. This requires underground labour work and due to economical and safety concerns are not considered nowadays and might only be utilised when UCG is considered in abandoned coal mines. The focus has moved to *shaftless* methods. *Shaftless* methods involve directional drilling and no underground labour work (Khadse et al., 2007; Self et al., 2012). Linked Vertical Wells (LVW) and Continuous Retracting Injection Point (CRIP) are the most common techniques.

### 3.3.1 Linked Vertical Wells (LVW)

According to this design, two boreholes are drilled into the coal reserves and an accessible path has to be formed inside the seam in order to enable the gas migration from the injection to the production well.

The coal formation naturally allows limited gas movement through it, which is reduced as the coal particles change during oxidation (Gregg and Edgar, 1978). The following four techniques are the most commonly employed for facilitating the gas streams to flow towards the outflowing well through the coal seam:

- *Directional drilling*. This technique does not rely on physicochemical processes alone. Directional drilling is used to approach the coal seam from different angles and create boreholes that enable gas movement. This type of drilling is formulated though downhole electric motors.

A horizontal in-seam borehole (Figure 3.3) is created at the bottom of the coal seam in order to facilitate the gas flow from the injection to the production well. According to De Crombrugghe (1959), a borehole diameter of approximately 0.3m enables stream flow (3 m/s -10 m/s) through it.

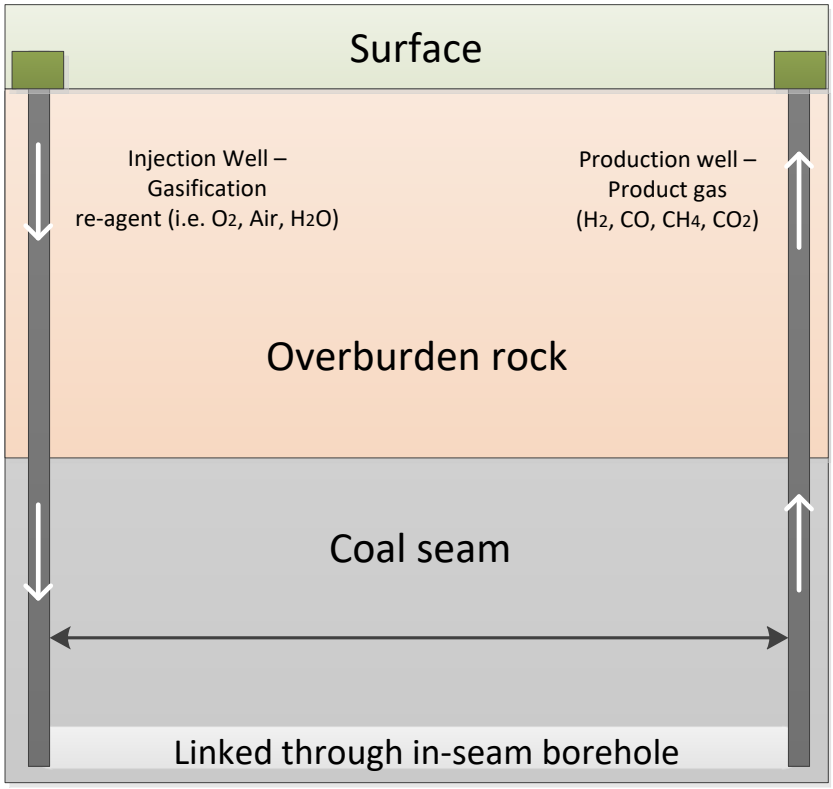


**Figure 3.3:** Linked vertical wells (LVW) subsurface layout with dedicated in-seam borehole (after Couch, 2009).

- *Counter/co current combustion*. This linkage scenario involves gasification propagation at one end and flow of the oxidising agents towards the other. At this point, if the gasification moves along with the inserted agents then the linkage process is called *co-current*; while if the gasification starts at one end and moves reversely to the inserted agents, then the process is called *counter-current*. The direction determinant in both cases is the oxygen concentration. There are certain advantages and disadvantages for both scenarios and although the counter-current technique is very efficient during the early-stage gasification of the coal seam, it must be followed by further processes to reach desired gas yields. On the other hand, although the co-current technique achieves high coal resource utilisation levels, the lower temperatures closer to the outflowing borehole, slow down the gas flow, due to plugging of the permeable path (Blinderman et al., 2008).

- *Electrolinking*. This process is based on electrical signal transfer between the two edges of the UCG panel. However, this technique cannot be considered as a reliable plan for gas movement inside the seam since it has as a prerequisite the development of a path between edges in order to diminish the length of coal seam that the electric signals have to cross. The uncertainty of whether the electric signals sent from both ends will ever meet (forming a canal) is the most significant drawback of this method (Gregg and Edgar, 1978).

- *Hydrofracking*. This technique relies on fluxing water inside the cavity widening the existing fractured pathways in the coal structure and creating new ones. Following the initial water injection, the fracture openings may return to their original size, thus sand is included in the initial fluid flux to sustain the created path. Similarly to electrolinking, the inadequate controllability of the process is considered its main drawback (Kreinin and Revva, 1974).

A comparative analysis of the above would reveal that coal features are determinedly important for which of the above methods would be employed. For instance, high rank coals have low (compared to lower rank varieties) initial natural permeability and as a result counter-current combustion technique may not be appropriate due to the fact that after initiation the injected gases have to pass through the seam in order to reach the combustion front (Blinderman and Klimenko, 2007). On the same pattern, if the coal's admittance to electric signals is quite low then electrolinking would also be inefficient. On the other hand directional drilling is not affected by the different coal attributes although its application might seem too refined for certain cases (Gregg and Edgar, 1978). Figure 3.4 can provide an overview of an increased permeability channel within a coal seam through the a) counter/co – current combustion b) electrolinking and c) hydrofracking methods.

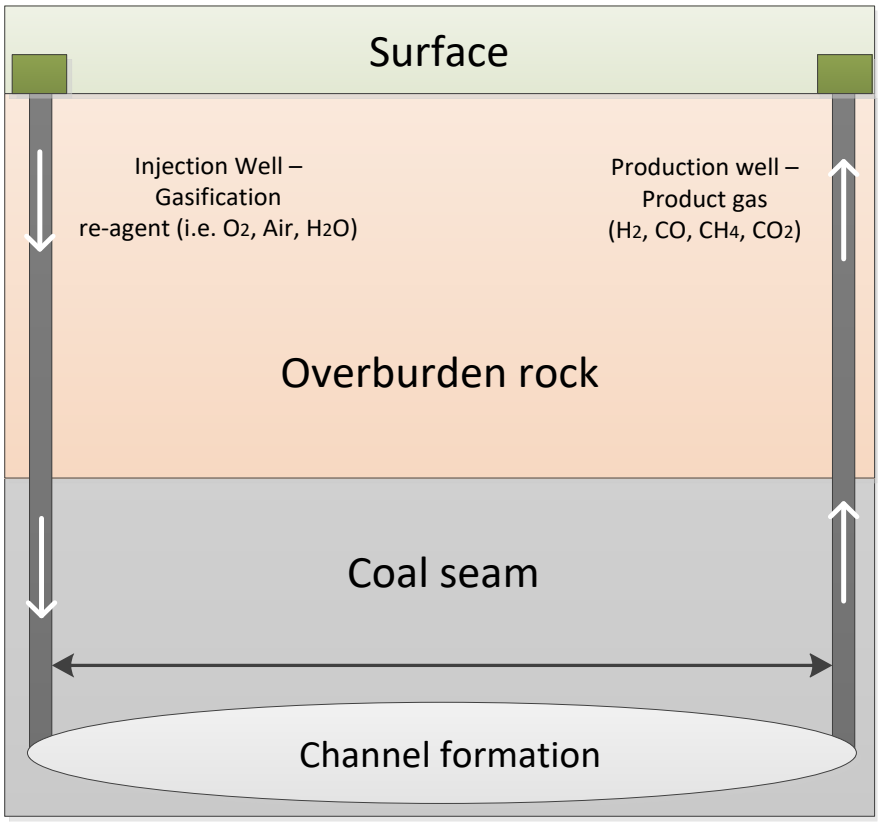


**Figure 3.4:** Linked vertical wells (LVW) subsurface layout with channel formation in the coal seam though a) counter/co – current combustion b) electrolinking c) hydrofracking (after Couch, 2009).

### 3.3.2 Controlled retracting injection point (CRIP)

The CRIP model consists of a well with a gradually detached final point. That detaching final point should continuously be found at the lower levels of the coal seam in order to initiate firing of fresh material. The whole process requires directional drilling. For horizontal coal beds, the injection well is drilled at an angle to the bottom of the coal seam. The gasification begins close to the meeting point between the curved injection and the vertical well. As the cavity from the consumed coal grows the directionally drilled well moves backwards in order to access fresh raw material and re-initiate the whole process (Nourozieh et al., 2010; Wang et al., 2009). The advantage of the CRIP practice relies on its high coal utilisation performance since it minimises the coal quantities unaffected by the process, increasing the coal conversion efficiency levels.

However, depending on the chosen CRIP design, there are two different scenarios (Couch, 2009):

- *The Linear CRIP*. As it can be seen in Figure 3.5, the production well is vertical to the coal seam and remain steady during the process. The initiation process starts at the end of the injection well where the coal gasification begins. As the coal is consumed and the cavity grows the injection well is retracted further away from the production well in order to restart the process. In contrast to the LVW configuration, the need for multiple pairs of injection and production wells into the coal in order to increase the control over the process does not exist. However, as the space between the injection and initial production well increases additional production wells might be required in order obtain the produced gas and minimise the losses (Self et al., 2012; Nourozieh et al., 2010;; Wang et al., 2009).

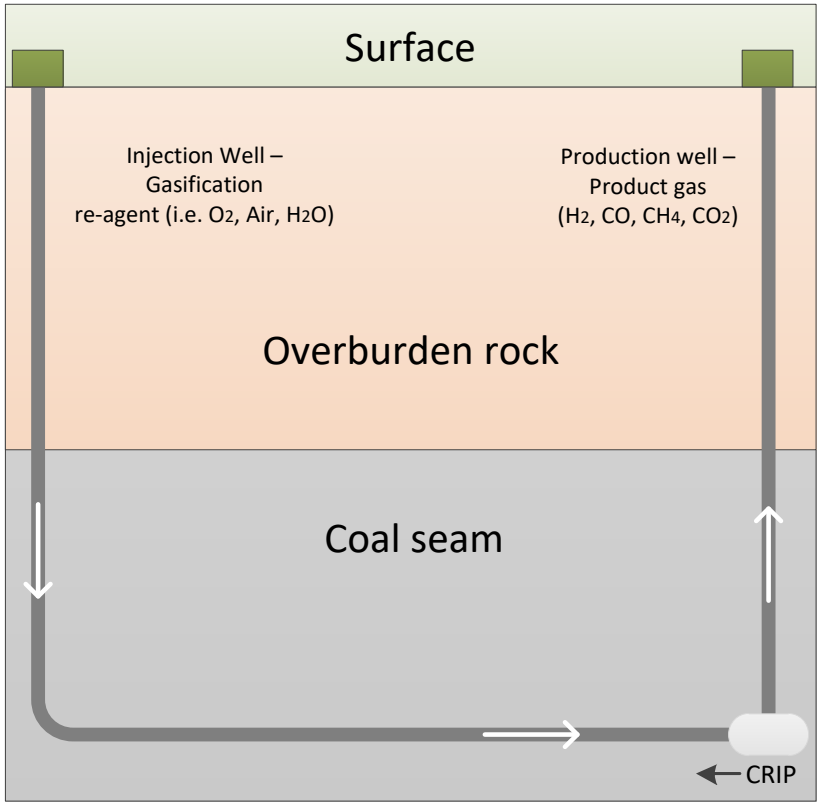


**Figure 3.5:** Linear CRIP formation (after Couch, 2009).

- *The parallel CRIP.* As it can be seen in Figure 3.6, this subsurface configuration involves directional drilling with vertical and horizontal sections for both the injection and the production well. A vertical ignition well is used in order to support the initiation process and a cavity starts developing at the end of the retracted wells. As coal is gasified and the developing cavity grows, the ignition well is retracted further away from the initial vertical well in order to access fresh coal. However, under *the parallel CRIP* the production well does not remain steady but it is also retracted closer to the ignition well. This layout increases the controllability over the process by controlling both where the gasification takes place and the collection point of the product gas (Couch, 2009; Perkins, 2005).

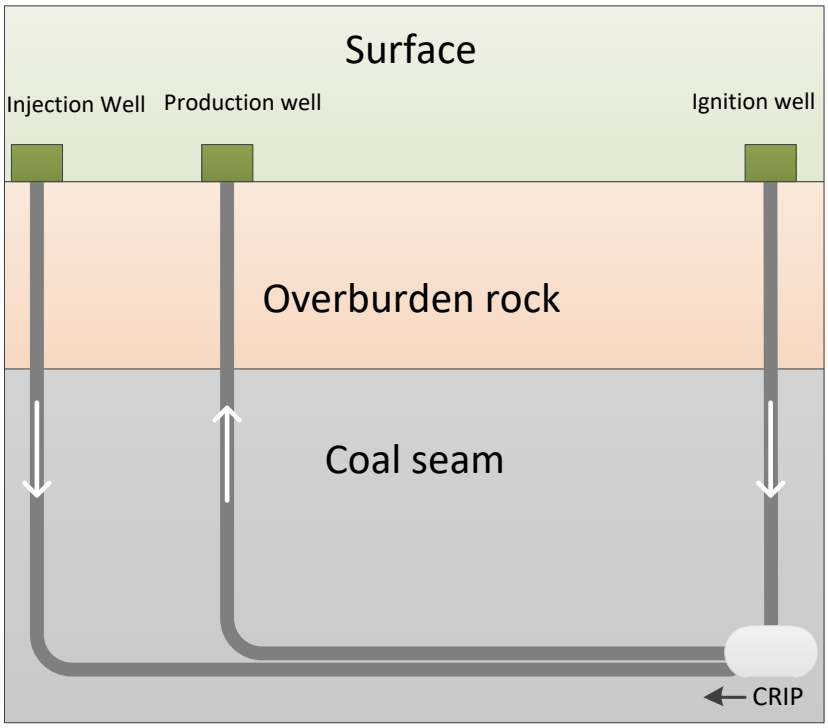


**Figure 3.6:** Parallel CRIP formation (after Couch, 2009).

### 3.3.3 Steeply dipping coal seams

This implementation considers coal seams whose inclination is so sharp that special handling is required to avoid safety and ecological problems, as well as maximise the raw material utilisation (Yang et al., 2003). For this type of coal deposits, UCG could be reasonably compared with the "updraft" fixed-bed gasifiers.

Similar to fixed-bed gasifiers, in steeply dipping coal bedrocks, the highest temperatures are developed at the lowest level and the gas-product follows an upwards route before it gets collected (Dossey, 1976; Perkins, 2005). However, the scarcity of such sites in combination with their geological features, that may not allow their exploitation, led to underdevelopment of this kind of designs; although, in contrast to traditional mining methods, UCG can create benefit from previously inaccessible sites.

Another exploitation technique for coal deposits with a sharp inclination is the stream method. This method relies on accessing the coal through two wells intercepting the seam at different depths. They become connected through an in-seam inclined channel along the seam direction. The injection of the usual gasification (i.e. $O_2$, air) agents takes places from the well at the lower depth. As the gasification process proceeds, coal parts detach and fall into the lower part of the cavity, feeding sequentially the gasification and combustion sections. Finally, the high temperature (low-density) generated gases flow upwards to the top of the seam where the production well is located (Gregg and Edgar, 1978; Self et al., 2012). Moreover, an added challenge is to maintain the flow from the injection well to the seam due to the ash, tar and rubbles cumulated at its bottom. For this reason, numerous injection wells are employed at different angles for increased accessibility (Dossey, 1976; Perkins, 2005).

## 3.4 *Experimental and Modelling work in UCG*

The main difficulty when studying the UCG process is the lack of field data, especially from deep UCG operations (>300m). For this reason, the need for experimental and simulation studies becomes critical. The experimental studies can be classified into in-situ (Kapusta et al., 2013; Mocek et al., 2016; Wang et al., 2009; Wiatowski et al., 2015; Wiatowski et al., 2012; Yang et al., 2008) and ex-situ trials (Daggupati et al., 2010; Daggupati et al., 2011b; Kapusta and Stańczyk, 2011; Kapusta et al., 2016; Liu et al., 2009; Porada et al., 2015; Prabu and Jayanti, 2011; Stańczyk et al., 2011; Stańczyk et al., 2012; Stańczyk et al., 2010; Yang, 2004; Yang et al., 2010). On the other hand, simulation studies play a vital role in understanding the UCG process and ultimately increasing its control.

Modelling efforts can be classified into two main groups. The first group includes the studies that investigate the chemical reactions combined with the heat and mass transfer phenomena involved in UCG without considering the occurring thermo-mechanical effects (Biezen et al., 1995; Britten and Thorsness, 1989; Daggupati et al., 2011a; Dinsmoor et al., 1978; Eftekhari et al., 2015; Kariznovi et al., 2013; Magnani and Ali, 1975; Nourozieh et al., 2010; Park and Edgar, 1987; Perkins and Sahajwalla, 2005; Perkins and Sahajwalla, 2007; Sarraf Shirazi et al., 2011; Seifi et al., 2011; Thorsness et al., 1978; Żogała and Janoszek, 2015). The second group includes the modelling studies that either consider the thermo-mechanical phenomena of UCG operation in a coupled process (Biezen et al., 1995; Britten, 1986; Daggupati et al., 2012; Perkins and Sahajwalla, 2008) or independently (Hettema et al. 1998; Yang et al., 2003; Wolf and Bruining, 2007; Tian and Ziegler, 2013; Najafi et al., 2014; Yang et al., 2014; Otto and Kempka, 2015).

### 3.4.1 Experimental work

#### 3.4.1.1 In-situ trials

Wang et al. (2009) conducted an in-situ trial for UCG in an abandoned coal mine in China by testing the Enhanced UCG (EUCG) application. This application is formulated though a combination of the CRIP design and the remaining infrastructure from the abandoned coal mine galleries. The trial lasted for three months and the introduced gasifying agents were steam ($H_2O$), steam ($H_2O$) mixed with air and oxygen ($O_2$). The highest temperature did not exceed the 1250°C with the highest value to be noticed during the oxygen ($O_2$) injection. In addition, the results from the trial proved that CRIP can benefit both the efficiency of the process and the composition of the produced gas.

Wiatowski et al. (2012) performed an in-situ trial in the experimental Mine “Barbara”. The in-situ trial took place in an actual coal deposit (1.5m thick) 30m below the surface. At the bottom of this coal bed, a circular channel (0.15m diameter) was drilled. The purpose of the channel was to facilitate the flow of the reactant and product gas inside the seam. Through the drilled borehole at the bottom of the seam, an injecting steel pipe was introducing the gasifying agents ($O_2$, air). At the other end of the channel, a production pipeline was collecting the product gas from the bottom of the seam.

The experiment took place at atmospheric pressures while the temperatures and the composition of product gases were constantly evaluated. The experiment lasted for 355h with the initiation process to last 2h although the operation of the reactor did not stabilise before the 190$^{th}$ hour. A material balance analysis was also performed while the environmental outcomes of the experiment were analysed by Kapusta et al. (2013). The main conclusions highlighted the concerns over the operating problems.

More specifically, although it was confirmed that product gas with high hydrogen ($H_2$) content is feasible to be produced, the loss of reactor tightness lead to gas leakage to the surrounding strata with groundwater contamination to take place. In addition, excessive water influx to the coal seam was noticed from the surrounding strata. Additional more recent studies (Wiatowski et al., 2015; Mocek et al., 2016) confirmed the feasibility of UCG application in abandoned or active coal mines. However, in contrast to the experimental studies conducted at "Barbara" experimental mine (Wiatowski et al., 2012; Wiatowski et al., 2015) where UCG operation was tested at shallow depths, the 60-days in-situ trial in "Wieszorek" coal mine (Mocek et al., 2016) proved the UCG feasibility also at higher depths (~ 460m).

#### 3.4.1.2 Ex-situ trials

Liu et al. (2009) developed an ex-situ laboratory test replicating an artificial coal seam through a surface gasifier. Lignite coal was used during the experiment and the focus was on the generation of syngas product rich in hydrogen ($H_2$) content. The effect of the operating conditions (injected oxygen/steam ratio, temperature profiles) on the product gas composition was also assessed.

Regarding the ex-situ trials, extensive work has been conducted by Stańczyk et al. (2010), Kapusta and Stańczyk (2011) and Stańczyk et al. (2012). In particular, Stanczyk et al. in both their research studies (i.e. 2010 and 2012) focused on producing UCG syngas with high hydrogen ($H_2$) content. Lignite coal was used in their research study in 2010 while hard coal was gasified during the corresponding one in 2012. In both cases the same gasifier was utilised with dimensions 3.0m x 1.5m x 1.5m. The lignite trial lasted 55h at atmospheric pressures with the ignition to last 3h and the subsequent oxygen ($O_2$) injection stages to get interrupted by an intermediate steam injection stage which lasted less than 1h.

The outcome from the lignite trial was product gas with an average heating value of 7.8MJ/$m^3$ and 46% hydrogen ($H_2$) content. However, the rapid heat losses when steam was introduced indicated that steam injection cannot be sustained during lignite gasification and high oxygen ($O_2$) injecting rates were required. On the other hand, the hard coal trial lasted for 7 days and in this case alternating oxygen ($O_2$) and steam ($H_2O$) injections were taking place periodically every 2h.

Finally, Kapusta and Stańczyk (2011) developed a comparative study between the two different coal types (i.e. hard coal and lignite). Different mixtures of oxygen to air were used as gasifying agents during the trials. Interesting conclusions were raised with the product gas from the hard coal trial to have the highest heating value (8.58 MJ/$m^3$) during the pure oxygen ($O_2$) injection. In addition, the corresponding product gas with the highest heating value from the lignite trial was 4.18 MJ/$m^3$.

Another interesting conclusion was that in the hard coal trial stable operation was achieved with an $O_2$/air ratio of 2:3 mixtures while the corresponding ratio for the ignite trial was 4:2. The above results show the high requirements for oxygen under the lignite trial in order to maintain high temperatures. Further discussion over the results of the two trials can be found in Kapusta and Stańczyk (2011).

Daggupati et al. (2010) and Daggupati et al. (2011b) conducted extensive work on analysing the cavity growth during UCG. They conducted their trials by developing a surface gasifier with a horizontally drilled borehole at its bottom. Their structure can reasonably be compared with the one used by Stańczyk et al. (2010) Stańczyk et al. (2011) and Stańczyk et al. (2012) in their trials. During their first study in 2010, they analysed how the cavity growth can be affected by different operating parameters such as the oxygen ($O_2$) feed rate, the operational time and distance between the injection and production wells. Interesting conclusions arose by assessing these parameters and in particular, by increasing the feed flow rate or the operational time the volume of the cavity increases while by increasing the distance between the two wells the volume decreases. These facts prove the higher coal consumption rates when the CRIP layout is used where the distance between the two wells is not fixed in contrast to the LVW process design. Furthermore, the increase of the feed flow rate increased the cavity growth speed mainly due to the increase of the mass transfer rate inside the cavity.

Due to the increased mass transfer, the injected $O_2$ can bypass the resistance of the ash layer and the product gas (that exist in the cavity) and reach the surface of the coal. The above conclusion was highlighted by Daggupati et al. (2010) as well as by Prabu and Jayanti (2011). During their second study Daggupati et al. (2011b) continued to investigate the evolution of the UCG cavity although in this effort they used a mixture of oxygen and steam as injected gasifying agents compared with the pure oxygen injection during their first study in 2010. The results indicated the generation of product gas with high hydrogen ($H_2$) content although the most interesting conclusion came from the post-process cavity inspection. On the floor of the cavity, large pieces of coal were found which proves that coal blocks were breaking off the roof and were dropping to the bottom of the cavity (i.e. coal spalling). One possible reason for this coal spalling can be either the thermal shocks that the coal experiences between the different temperature stages and cause its fracture and failure. Another reason could be the fact that the lower density of the steam allows its easier (compared to oxygen) flow to the roof causing the heterogeneity of the coal and ultimately its spalling (Hettema et al., 1998; Hill and Thorsness, 1983a). As a result, the rate of cavity growth can be attributed to both the coal consumption at its surface and to thermo-mechanical phenomena resulting to coal spalling.

Prabu and Jayanti (2011) developed laboratory tests in order to investigate the UCG cavity growth by conducting three different trials. A different material was tested in each trial (i.e. coal, wood and camphor). The authors argued that although coal is the primary resource of UCG the trials with the other two materials could possibly replicate more realistically the coal characteristics when this is lying in an underground coal seam. In all cases, the tested materials were shaped in a cylindrical format and a borehole was drilled horizontally along the two ends of their cylindrical shape. This borehole was acting as the connecting channel between the two ends of the structure. The injection of the reactants was taking place at one end while the product gases were being collected from the other.

Porada et al. (2015) investigated the chemical reactions' kinetics by replicating the UCG subsurface conditions through surface equipment. Bituminous coal was used and the experiments were conducted at high pressures (~ 4 MPa).

A range of temperatures (800°C – 1,000°C) was analysed in order to identify the composition of the product gas under different conditions and additional focus was placed on the kinetic parameters of carbon monoxide (CO) and hydrogen ($H_2$).

### 3.4.2 Modelling work

#### 3.4.2.1 Thermo-chemical phenomena

The gasification modelling studies can be classified into two categories. The first category (Biezen et al., 1995; Britten and Thorsness, 1989; Magnani and Ali, 1975; Thorsness et al., 1978) assumes the coal seam as a packed bed where the gasification takes place in a permeable coal bed while the second category (Dinsmoor et al., 1978; Kariznovi et al., 2013; Nourozieh et al., 2010; Park and Edgar, 1987; Perkins and Sahajwalla, 2005; Sarraf Shirazi et al., 2011; Seifi et al., 2011) assumes an already developed cavity-channel into the coal seam which expands and progresses with time.

Perkins and Sahajwalla (2005) developed an one-dimensional UCG model. The model assumes a pre-developed cavity which is neighbouring with the unconsumed coal. The unconsumed coal is classified into zones depending on its distance from the cavity face. On the boundary between the cavity and the coal seam the "dry-zone" exists while deeper inside the coal seam the "wet-zone" starts. The conservation of energy, mass and momentum was taken into account through the respective balance equations. In addition, the diffusion in the boundary between the developed cavity and the "dry-zone" was studied through the Stefan-Maxwell equations. The changes to the coal pore structure and permeability during the process were also considered. An additional study, by Perkins and Sahajwalla (2006), worked on conducting a sensitivity analysis on the operating parameters of the model. The temperature, the pressure and the oxygen to steam ratio participating in the process had the highest effect. It is important to highlight that the simulations were conducted at high pressures (10 MPa) while the ash layer on the face of the dry –zone was not considered. This omission comes in contrast to the modelling work of Park and Edgar (1987) which does consider an ash layer on the surface of the dry zone although this study was conducted at atmospheric pressures.

This assumption of atmospheric pressures reduces the accuracy of the simulation since UCG takes place in a reducing environment at high depths with the operating pressure to be compared with the hydrostatic.

Sarraf Shirazi et al. (2011) developed a 2-dimensional model for cavity growth during UCG by using the COMSOL software tool. The main objective was to model the fluid flow by approaching the coal seam as a porous media and emphasizing on the heterogeneous reactions that take place. They followed a similar methodology with Perkins and Sahajwalla (2005) regarding the modelling of the microprore and macropore structure of the coal. As both studies (Perkins and Sahajwalla, 2005; Sarraf Shirazi et al., 2011) highlighted the macropores are benefitted from coal pyrolysis and provide the necessary surface area for mass transfer while the micropore surface serves the heat transfer through the heterogeneous chemical reactions. However, in contrast to the work of Perkins and Sahajwalla (2005), Sarraf Shirazi et al. (2011) modelled the diffusion at the coal face where the combustion front exists using the Fickian diffusion which Perkins and Sahajwalla (2005) disregarded as inappropriate for UCG due to its requirement for homogeneous mixtures.

Nourozieh et al. (2010) and Seifi et al. (2011) developed 3-dimensional models following of the pattern of the expanding cavity-channel in the coal seam. They both implemented their 3-dimsnional models by using the STAR software as developed by the Computer Modelling Group (CMG). This software tool is a reservoir simulator that can model heat and transport phenomena coupled with chemical reactions. Nourozieh et al. (2010) also considered the geological structure around the coal seam. Both studies simulated the cavity growth by investigating the chemical reactions' rate, the heat and mass transport phenomena. The energy and mass conservation equations were considered combined with the Darcy's law for fluid flow in porous media. Furthermore, only convection and conduction were considered as heat transfer mechanisms which comes in contrast with other literature studies (Britten, 1986; Daggupati et al., 2012; Perkins and Sahajwalla, 2007) which argue that radiation is either the dominant or at least a significant heat transfer mechanism. The permeability, porosity and thermal parameters of both the coal seam and its surrounding structure (in the case of (Nourozieh et al., 2010)) were taken into account. Both simulation studies were conducted at high pressures (11.5 MPa).

Further work was conducted by Kariznovi et al. (2013) who based on the work of Nourozieh et al. (2010) published a specific analysis on how the kinetic parameters for the UCG reactions under high pressure conditions can be estimated. The extrapolation of the recorded kinetic parameters from low pressure UCG trials was investigated (Kariznovi et al., 2013). In addition, Seifi et al. (2011) highlighted that the kinetics of the heterogeneous reactions regulate the cavity growth and coal consumption at the face of the cavity while the homogeneous reactions have the greatest effect on the product gas composition. Further results indicated that the product gas had a high $CH_4$ content while the different regions within the cavity were classified through a temperature profile which revealed higher temperatures (~ 995°C) at the combustion front, temperatures varying from 341°C to 621°C in the pyrolysis region and lower temperatures were recorded deeper in the coal seam (Seifi et al., 2011).

Eftekhari et al. (2015) do not focus on cavity growth. However, they aim on developing a dynamic UCG model that can simulate the UCG processes when oxygen and steam are injected to the seam in alternating time periods. The focus is on modelling how the heat produced during the exothermic reactions of combustion stage can subsequently be used during the endothermic gasification reactions. Eftekhari et al. (2015) also compared their results with the ex-situ experimental trial of Stańczyk et al. (2012) where the alternating oxygen/steam injection was tested.

Furthermore, additional research studies (Daggupati et al., 2011a; Perkins and Sahajwalla, 2007; Żogała and Janoszek, 2015) employ computational fluid dynamics (CFD) techniques in order to model the UCG processes during the cavity growth. Perkins and Sahajwalla (2007) investigated the fluid flow inside the growing cavity through a 2-dimensional model. The dominance of natural convection over forced convection was highlighted. Furthermore, the double diffusive natural convection for the fluid flow inside the cavity was considered. The double diffusive natural convection was considered though the Grashof number that shows the mass transfer rate from the bulk fluid flow to the cavity boundary. This rate is influenced by the density differences of the gas-product inside the cavity. These density differences are in turn caused by both the different compositions of the gas at different locations inside the cavity and the temperature gradient within it.

However, as Perkins and Sahajwalla (2007) concluded, the temperature difference has the dominant effect on the density differences and the composition gradient does not affect the final Grashof number. Furthermore, sensitivity analyses were conducted referring to the location of the injected $O_2$, the height of the ash bed at the bottom of the cavity, the height of the cavity roof and lastly the oxygen ($O_2$) injection rate. It was revealed that that an increasing oxygen ($O_2$) can have a reducing impact on the $CO/CO_2$ ratio of the product gas. This means that at low injection rates the produced carbon dioxide ($CO_2$) at the combustion stage located at the bottom of the cavity is reduced to carbon monoxide (CO) at the roof of the cavity where lower temperatures exist. On the other hand, as the oxygen rate increases more gas escapes into the cavity without reacting at its bottom. As a result, the temperature distribution becomes more uniform inside the cavity with combustion to also accommodated at the roof and the $CO/CO_2$ balance ratio to reduce. Daggupati et al. (2011a) analysed the fluid flow patterns within the growing cavity, focusing on the velocity distribution within it. The ultimate task was to couple this CFD analysis with compartment modelling (using the Aspen Plus software tool) through residence time distribution (RTD) studies. This means that the CFD helped to quantify into steps the non-ideal flow pattern within the cavity and as a result that steps to be later modelled through a sequence of ideal reactors within Aspen Plus software tool. However, they considered an isothermal temperature profile within the cavity and in that way omitting the effect of the temperature gradient on the fluid flow. Żogała and Janoszek (2015) investigated the effect of different steam proportions to the UCG product gas through CFD techniques. They concluded that the steam participation into the UCG reactions can lead to a stable UCG operation although excess steam can rapidly deteriorate the operating results. However, the simulations were conducted at atmospheric pressures which are relatively uncommon for actual in-situ UCG operations.

The opportunity for the coupled operation of UCG and Carbon Capture and Storage (CCS) has been discussed in the literature (Roddy and Younger, 2010; Self et al., 2012). However detailed analyses (Chen F, 2013; Irfan et al., 2011; Mandapati et al., 2012; Marcourt et al., 1983; Prabu and Geeta, 2015) have been conducted over the role that carbon dioxide ($CO_2$) injection can play as gasifying re-agent either on its own or as a mixture with oxygen ($O_2$).

In addition, Prabu and Geeta (2015) analysed how the UCG-CCS coupled operation can become part of conventional surface power generation plants. The investigated power generation designs were the combined cycle (CC) and the steam turbine (ST) systems. The conclusions showed that $CO_2$ could act beneficially to the UCG process improving the $CO/H_2$ ratio while the CCS energy penalty could be avoided due to the fact that heating the injected post-combustion $CO_2$ was requiring less energy compared to the injection of superheated steam. Furthermore, a financial analysis by Nakaten et al. (2014) proved the economic viability of the combined UCG-CCS processes when coupled with a CC power plant. Furthermore, simulation studies focused on UCG syngas production with high $H_2$ proportions and this production was either coupled with CCS (Olateju and Kumar, 2013; Rogut, 2008) or not (Verma et al., 2015). Verma et al. (2015), compared the energy efficiencies with and without CCS in order to quantify the energy penalty during the CCS case. In order to facilitate the CCS process, the selected coal seam was located 1400m deep with high operating pressures (~12 MPa). Furthermore, the work of Verma et al. (2015) highlight the similarities – from a chemical perspective – between surface coal gasification processes and UCG operation and as a result the Aspen Plus software tool was employed for the simulation of the product gas composition by following the Gibbs free energy minimization principle (Teh and Rangaiah, 2002).

All the simulation studies discussed under this section do not include the effect of the thermo-mechanical phenomena (i.e. coal spalling) in their modelling efforts. However, many of these studies (Daggupati et al., 2011a; Dinsmoor et al., 1978; Eftekhari et al., 2015; Park and Edgar, 1987; Perkins and Sahajwalla, 2007; Seifi et al., 2011) clearly highlight and recognise the importance of these phenomena to the cavity growth rate or product gas composition but decided not to include them in order to reduce the complexity of their models.

#### 3.4.2.2 Thermo-mechanical failure

The simulation studies included in this section can be categorised into two groups. The first group includes studies (Daggupati et al., 2012; Perkins and Sahajwalla, 2008; Biezen et al., 1995; Britten, 1986) that consider the thermo-mechanical effects through simplifications in a combined modelling process.

Their focus is on the heat and mass transport phenomena and the participating chemical reactions during UCG cavity growth. On the other hand, there are studies that fully focus on the thermo-mechanical effects of UCG cavity growth and investigate these effects through dedicated analysis and not as part of a coupled process.

Stephens et al. (1985) developed an one-dimensional model that aims to couple the thermo-chemical and thermo-mechanical phenomena of UCG. The approach for the modelling of the thermo-chemical phenomena was similar to the one followed by Kariznovi et al. (2013), Seifi et al. (2011), Perkins and Sahajwalla (2005), Park and Edgar (1987) where cavity was handled as an expanding permeable channel and different zones (i.e. dry and wet) were identified inside the coal seam depending on the distance from the cavity boundaries. On the other hand, the thermo-mechanical phenomena that drive the cavity growth were considered through the assumption of a temperature benchmark and a failure length inside the coal seam. More specifically, a coal block was assumed to spall and fall at the bottom of the cavity if this exceeded the temperature benchmark value and was within the arbitrarily defined failure length. Both steam and oxygen were considered as gasifying re-agents at the bottom of the seam where a high temperature char bed was formed. Furthermore, the convection and radiation transfer mechanisms were considered with the results to prove that radiation was the dominant heat transfer mechanism.

Biezen et al. (1995) developed a 3-dimensional model that aimed to simulate both the thermo-chemical and the thermo-mechanical phenomena during UCG cavity growth. The authors argued that the model can simulate both the early-stages of UCG where no cavity is assumed to exist and the subsequent stages where a permeable channel (cavity) has already been developed and expands. They identified that during the early stage when no cavity has been developed permeable bed gasification is the dominant process while as a cavity is developed surface gasification driven by natural convection becomes the dominant mechanism. However, radiative heat transfer was not considered in this study. The spalling effect was considered by setting a temperature benchmark (500°C) above which a coal block could spall and become gasified at the bottom of the cavity.

The spalling rates were arbitrarily defined and remained steady throughout the process while the location where spalling could occur was determined through random probability methods.

Perkins and Sahajwalla (2008) developed a pseudo-one dimensional model by further developing their existing work (Perkins and Sahajwalla, 2007). Their already developed CFD model (Perkins and Sahajwalla, 2007) was not considering the thermo-mechanical failure during the cavity growth and as a result they decided to incorporate the "fragmentation factor". This factor represented how complete was the char to syngas conversion process. The lower this factor the more incomplete was the process due to spalling char that was not fully gasified. However, as authors recognised this is not the case in in-situ UCG projects because the spalling coal is also gasified at the bottom of the developing cavity. Furthermore, this factor was investigated by arbitrarily assigning three different values to it and without these values to be related with the thermo-mechanical properties of coal or the thermo-mechanical stress distribution.

Daggupati et al. (2012) built on their previous work (Daggupati et al., 2011a) by expanding the capability of their previous CFD model. Their previous work had assumed an isothermal temperature distribution within the developing cavity while in their updated study they argued that spalling of coal was also considered by assigning different temperature zones within the cavity. They argued that if spalling takes place then higher temperatures (combustion zone) would be developed at the bottom of the cavity (where they also assigned the higher temperature) while if there is no spalling then the combustion takes place on the roof (where they also assigned the higher temperature) and the floor-bottom of the cavity remains at low temperature.

On the other hand, studies that focused purely on the thermo-mechanical effects of UCG identified the effect of the permeability changes to the coal and surrounding strata as an important factor for controlling the in-flow or out-flow from the UCG reactor. Permeability changes can be caused by the re-distribution of the mechanical stresses as the UCG cavity expands and in addition, by the thermally induced stresses (Yang et al., 2003).

An additional study (Otto and Kempka, 2015) considered the temperature effect on the mechanical and thermal parameters of coal and its surrounding strata (i.e. sandstone) for the calculation of stress, displacement and permeability changes during the UCG process.

Furthermore, Wolf and Bruining (2007) highlighted that the exposure of the cavity roof rocks to high temperatures can have an effect to the combustion process itself apart from permeability changes. Hettema et al. (1998) investigated the coal spalling phenomena during the cavity growth concluding that these can be caused either due to steam pressure alone or by the combined effect of steam pressure and thermally induced compressive stresses. While additional simulation studies (Najafi et al., 2014; Tian and Ziegler, 2013; Yang et al., 2014) focused on reactor stability and ground subsidence. Tian and Ziegler (2013) incorporated the thermal effect into the Hoek Brown and the Mohr Coulomb failure criteria while Najafi et al. (2014) analysed the stress distribution profiles at the boundaries of the UCG panels in order to estimate the size of the required protection pillar during UCG operation. Finally, additional studies (Sarhosis et al., 2013; Younger, 2011) analysed the hydrogeological effect either for the reactor cool down at the end of the UCG process or for investigating the feasibility of a coupled UCG-CCS project.

Each of the above studies serves its task independently; however, modelling the UCG operation is a complex task which requires the integration of its diverse processes. In this thesis, the focus is on the development of a robust UCG model. The objective is to allow the dynamic interaction of the Thermo-Mechanical-Chemical (TMC) processes in an integrated model and investigate how these processes affect the quality of the generated syngas.

# Chapter 4 Chemical Process Modelling and Simulation of the Laboratory UCG Experiments

## 4.1 *Introduction*

This section aims to highlight the similarities and differences between surface gasification processes and UCG practices. Data available on the product-gas composition for surface and sub-surface gasification processes used in this comparison is shown in Table 4.1. Gregg and Edgar (1978) as well as Perkins (2005) also referred to this comparison between surface and sub-surface operations.

Considering the relative differences in syngas composition between the surface and the UCG Chinchilla gasification data shown in Table 4.1, it is evident that the carbon monoxide (CO) and hydrogen ($H_2$) composition of the fixed bed gasifier design are the closest to the UCG values. This is in agreement with the work of Gregg and Edgar (1978), who also indicate that fixed bed gasifier designs seem to be the most comparable surface processes to UCG. However, the similarities between the two concepts are not restricted only to the syngas components, and also extend to negligible pre-handling requirements for combustion materials, as well as the long-time scale of the processes which occur in both cases (Gregg and Edgar, 1978; Roberts, 2000).

**Table 4.1**: Comparison of syngas composition for surface and sub-surface coal gasification processes (Krevelen, 1993; Liu, 1999; Moulijn et al., 2013; Perkins, 2005).

| | Surface gasifiers | | | UCG |
|---|---|---|---|---|
| | Entrained | Fluidised | Fixed | Chinchilla |
| Components (%) | | | | |
| $H_2$ | 30.9 | 24.9 | 23 | 18 |
| CO | 64.4 | 32.7 | 11.1 | 6 |
| $CH_4$ | - | 4.3 | 6.7 | 7 |
| $CO_2$ | 2.4 | 16.6 | 17.6 | 16 |
| $H_2O$ | 1.4 | 20.8 | 41 | 16.5 |
| $N_2$ | - | 0 | 0 | 35.6 |
| Other | 0.9 | 0.7 | 0.6 | 0.9 |
| Temperature range ($^oC$) | 1,600 – 2,200 | 1,250 – 1,400 | 1,100 – 1,350 | 1,000 – 1,700 |
| Pressure (MPa) | 4.5 | 2.8 | 2.4 | 1 |
| $O_2$/MAF coal feed | 0.9 | 0.7 | 0.5 | - |
| $O_2$/Air feed | - | - | - | 0.21 |

After a review of the processes involved in the operation of different surface gasifier designs, a chemical process model, which was synthesised and developed as part of the current PhD work, was used to simulate the laboratory UCG experiments (described in Section 4.5.1). The model application analyses the laboratory data in order the validate the UCG modelling approach, as well as providing further knowledge and understanding of the processes involved at each UCG stage.

## 4.2 *Surface gasifiers*

### 4.2.1 Fixed bed gasifier

A fixed bed reactor – also known as moving bed – is named due to its characteristic of including fixed different process layers (Bhattacharya, 1985; Mandl et al., 2010; Okuga, 2007; Visagie, 2009). However, according to Okuga (2007), although the particles in every layer seem to be fixed, there is notion for movement between them but this notion is not enough in order to disperse the layer. Thus, the characterisation as moving bed gasifiers is also reasonable. There are three criteria according to which fixed bed reactors could be categorised. These are the following:

1. The flow direction of the gasification agents compared to the feedstock stream. This criterion involves the three following choices (Bhattacharya, 1985; Okuga, 2007; Visagie, 2009):
    a. Counter – current gasifier ("updraft") – Figure 4.1
    b. Co – current gasifier ("downdraft") – Figure 4.2
    c. Cross – draft gasifier
2. The number of the product gas collection points. This criterion mainly applies to the "up-draft" gasifiers and includes the following two choices (Visagie, 2009):

    a. The one exit gasifier – also known as one-stage – whose gas output is sourced from the top of the gasifier. The upwards flowing gas passes some of its heat to the incoming feedstock and as a result leaves the tank at low temperatures (e.g. Lurgi reactor - (Hartman et al., 1978; Visagie, 2009).

    b. The double exit gasifier – also known as two-stage – which is designed with two points for gas collection with one located just above the gasification zone and the other at the top, similarly to the one stage case.

       The advantage of this design is the better temperature control of the gas at the highest exit. This is possible since by controlling the gas quantity sourced from the lower exit, it is possible to determine the amount of heat passed to the incoming feedstock before the remaining gas is collected from the upper exit (e.g. Woodall-Duckham reactor - (Hartman et al., 1978; Visagie, 2009).

       However, the gas collected from the two exits differs in quality, namely the lower exit gas is purer since it is collected before mixing with the devolatilised feedstock components.

3. The temperature level in the lowest part of the gasifier (ash deposit) which determines the physical structure of the ash. The temperature level at that point decides if the gasifier is characterised as slagging or not.

   More specifically as more heat is released from the combustion zone, ash starts melting and the gasifier is classified as slagging. The above ash dissolution is feasible for zone temperatures above 1,377°C (Bhattacharya, 1985; Okuga, 2007; Visagie, 2009).

As the fuel is introduced at the top of the gasifier, it gets across certain fixed layers where different phenomena occur. In both designs (up & down draft), the stages of drying and pyrolysis (or devolatilisation) are found at the top.

However, the difference is on how the necessary heat for these two stages becomes available in each design. In the "up-draft" design (Figure 4.1) the gasification agents are introduced at the bottom (where also the combustion zone exists) and as the gas product flows upwards – passing also through the gasification stage – it reduces its temperature by providing the necessary heat to the drying and pyrolysis stages.

The advantage of this design is its high thermal efficiency combined with the reduced temperature of the output product-gas (Bhattacharya, 1985; Mandl et al., 2010; Okuga, 2007). Nevertheless, the interaction of the product-gas with the raw input is responsible for product-gas of low purity with increased tars and moisture proportions (Beenackers, 1999; Bhattacharya, 1985; Hobbs et al., 1992; Okuga, 2007).

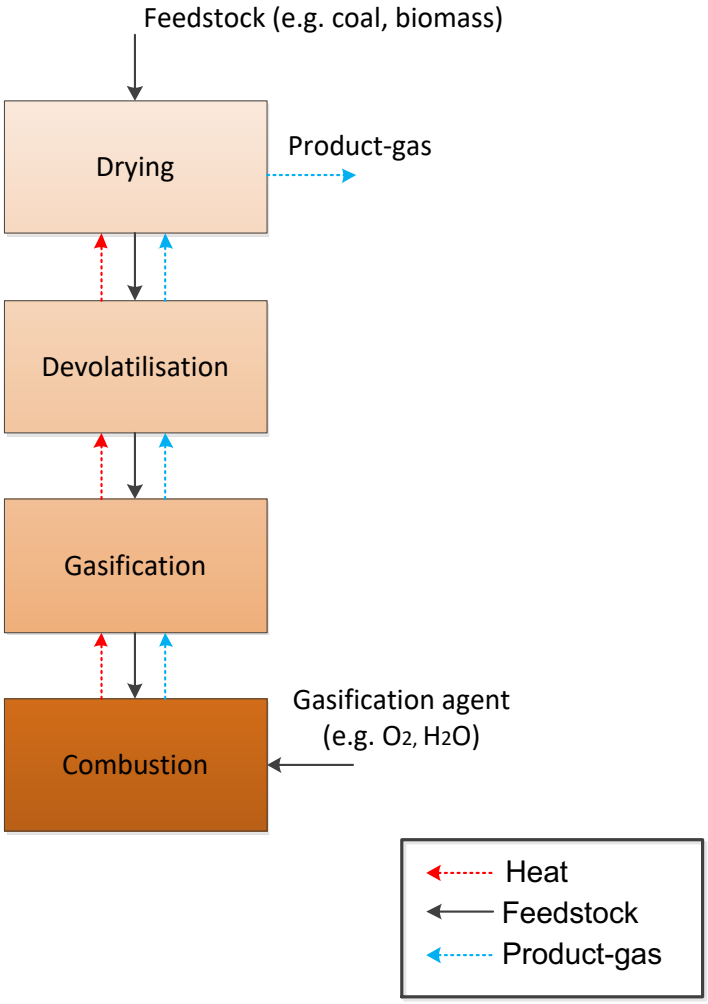


**Figure 4.1:** Up-draft fixed bed gasifier (after Mandl et al., 2010).

This drawback is not met in the "down-draft" design where the product-gas is collected from the bottom. The gasification layer – before product-gas exit – convert the tars from primary to secondary, easing their handling in the output gas (Bhattacharya, 1985; Okuga, 2007; Reed and Das, 1988).

This purity difference between the output gases of the two designs could also determine their end use with high purity gas required for combustion engines, while low purity is adequate for heating purposes (Okuga, 2007).

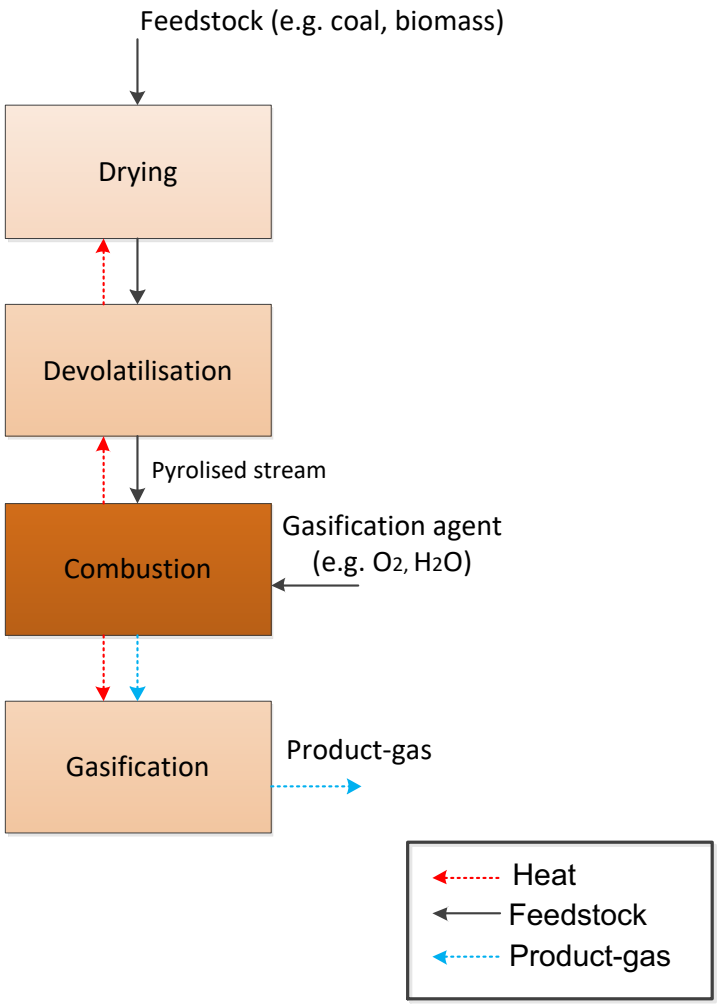


**Figure 4.2:** Down-draft fixed bed gasifier (after Okuga, 2007).

Another important characteristic especially for the "up-draft" designs is permeability (Bhattacharya, 1985; Okuga, 2007). This property highlights how easily or not the product-gas can flow through the gasifier's layers before reaching its exit. Various coal varieties develop different characteristics at different temperatures.

For instance, devolatilizing bituminous coals which are considered as greatly volatile – a characteristic which favours ignition but decreases the amount of released energy during burning (Visagie, 2009) – expand; while devolatilising sub-bituminous coals are converted to fragile structures (Bhattacharya, 1985).

Caking materials cause handling difficulties during the gasifier operation, thus anthracitic (non-caking fuel) is considered as suitable for fixed-bed designs (Bhattacharya, 1985; Okuga, 2007; Visagie, 2009). Table 4.2 indicates a quantitative overview of the operational characteristics of a Lurgi fixed bed gasifier.

**Table 4.2**: Indicative operational characteristics of a Lurgi fixed-bed reactor.

| **Parameter** | **Limitations** | **Source** |
|---|---|---|
| Gasification temperature | 620 °C – 815 °C | (Visagie, 2009) |
| Combustion temperature | 980 °C – 1370 °C | (Visagie, 2009) |
| Pressure | 24 bar – 31 bar | (Visagie, 2009)<br>(Elliott, 1981) |
| Oxygen/MAF coal ratio | 0.6 on average<br>0.45 on average | (Visagie, 2009)<br>(Elliott, 1981) |
| Steam/MAF coal ratio | 3.2 | (Visagie, 2009) |
| Outlet gas temperatures | 370 °C – 590 °C | (Visagie, 2009) |

In contrast to the previous designs discussed above (Figure 4.1 - Figure 4.2) in the cross-draft gasification design the layers – zones of the gasifier are asymmetrically distributed. At first, the oxidant is injected through a control valve causing the ignition of the coal material, which comes in contact with the oxidant. The temperatures that develop at that point are significantly high (at least 1,500 °C). Then, as the distance from the ignition stage increases and the oxygen concentrations decrease, gasification takes place. The importance of the ash and the unburned coal around the injection point is crucial since it acts as a protective "pillow" not allowing the excessive heat to pass to the surrounding environment (Hartman et al., 1978). Thus, in cross-draft gasification design slagging must be avoided in order to maintain that "pillow" protection. This is feasible by using as feedstock coal varieties with limited ash content (Kaupp and Goss, 1981; Okuga, 2007).

Another important characteristic of cross-draft gasifiers is the limited pyrolysis (or devolatilisation) stage taking place (Kaupp and Goss, 1981; Okuga, 2007). The inadequate pyrolysis stage leads to increased tar proportions in the product gas. That effect is caused by the rapid and also constrained hearth zone, where very high temperatures are hastily developed enabling only minimum material to participate and thus affecting the pyrolysis process.

The concerns increase if the movement of the material towards the hearth zone inside the gasifier is not continuous. Then there is not proper absorption of the released heat, leading to sudden increase of the material temperature when it finally enters the hearth zone. Since the temperature increase is so rapid, there is not enough time to reduce adequately the tar load of the outflowing gas, offsetting for the limited pyrolysis effect. Thus, coal varieties with minimum tar characteristics are required and applications of such gasifiers are found in lower than 10 kWe generation plants in emerging economies (Kaupp and Goss, 1981).

### 4.2.2 Fluidised bed gasifier

The operation of a fluidised bed gasifier relies on dragging the coal particles which lie on the bed of the gasifier (together with the inert elements, also present there) by the accelerated fluid (e.g. gasification agents) which enters. The high velocity of the incoming agents is responsible for the drag of the fuel particles to the surface of the gasifier, making the whole gasifier content to look like a "uniform" fluid mixture. However, the conversion efficiency of the initially solid material to a component of the final mixture depends on the velocity level of the incoming fluid. Thus, if the velocity remains at low levels, then it is not enough energy to drag the material lying at the bottom of the gasifier. However, as the velocity levels increase, adequate forces to withstand material load also increase (Bridgwater, 1995; Howard, 1989; Siedlecki et al., 2011; Visagie, 2009). With respect to velocity levels, fluidised reactors are classified to bubbling and circulating.

The bubbling reactors are characterised by lower incoming fluid velocities compared to the circulating ones (1m/s$^3$ compared to 3-10 m/s$^3$, respectively) (Bridgwater, 1995; Siedlecki et al., 2011). Moreover, fluidised bed reactors (including both above categories) run at reasonably low temperatures (800 °C – 900 °C) compared to fixed bed cases and in combination with their inadequate available time for the necessary reactions, their outflowing gas is characterised by increased tar and methane proportions.

However, although the tar load of the outflowing gas is high, it cannot be considered higher than the tar levels found in the gas-product of the "updraft" fixed bed designs (Siedlecki et al., 2011).

The low temperature levels do not ease reactions rates and as a result the utilised fuel (e.g. coal) must offset this disadvantage with high reactivity; thus, low-grade coal is considered as more suitable (Kaupp and Goss, 1981; Siedlecki et al., 2011; Visagie, 2009). In comparison with the fixed bed, fluidised reactors can process higher coal quantities within the same time unit (Visagie, 2009).

### 4.2.3 Entrained flow bed

The operation of this reactor type has several similarities with the fluidised bed design discussed above (Siedlecki et al., 2011). The main similarity is that incoming agents enter the tank at high speed and drag the fuel components, enabling the start of the conversion process. However, in the entrained flow bed gasifiers, the gasification agents are introduced with higher speed than in the fluidised bed resulting to the entrainment of coal elements. The second difference is that the coal elements' size which must be even smaller than the ones used in the fluidised bed. This size restriction necessitates pre-treatment of the fuel, introducing an extra cost requirement. Moreover, the temperatures developed in this gasifier type are the highest across all gasifier categories. Similar to the observations made for the other two gasifier designs (i.e. fixed-bed, fluidised bed), high temperatures favour carbon monoxide (CO) and hydrogen ($H_2$) proportions, while they reduce methane ($CH_4$) and tar contents in the output gas (Benyon, 2002; Siedlecki et al., 2011).

An interesting consideration is whether an increase of the oxygen input can benefit the gasification process. The answer depends on design priorities, since high oxygen concentrations require smaller tank size, resulting in lower initial cost investment requirements, while the requirement for pure oxygen leads to the need for oxygen separation unit and higher operational costs. Moreover, high oxygen concentrations improve chemical reactions rates and as a result more carbon is converted to useful gas fuel, reducing cleaning requirements after its collection. The coal feedstock in entrained flow bed gasifiers may be introduced in either dry or slurry form. A critical view to the advantages and disadvantages of the two forms would reveal that the slurry form favours the cost and reliability aspects; however it is followed by reduced energy efficiency compared to the dry form (Benyon, 2002).

Overall, entrained flow bed gasifiers could be classified into several different sub-categories according to the following criteria (Benyon, 2002):

- type of the introduced gasification agents (e.g. air, oxygen etc.),
- condition of the used feedstock (e.g. slurry, dry),
- number of the feeding stages.

Table 4.3 presents a summary of the gasifiers discussed in this chapter, allowing to compare the operational parameters for the different designs.

**Table 4.3**: Comparative overview of the different gasifier designs (Perkins, 2005; Van Heek, 2000; Van Heek and Mühlen, 1991)

| Parameter | Fixed Bed | Fluidised Bed | Entrained Flow |
|---|---|---|---|
| Feed size (mm) | 5-80 | 0.1-6 | 0-0.1 |
| Residence time (s) | High | Medium | Low |
| Ash character | | | |
| Dry | ✓ | ✓ | × |
| Slagging | ✓ | × | ✓ |
| Agglomerating | × | ✓ | × |
| Ash fusion temperature | Low and High | High | Low |
| Feedstock conversion | High | Medium | High - Medium |

## 4.3 *Aspen Simulations*

According to Begum et al. (2013), various software packages (e.g. Aspen One©, ChemCAD etc.) are available to simulate and investigate the sensitivity of chemical processes, as well as to replicate the optimum operating conditions. Aspen One© is the general label for a "family" of products (Bose, 2012) and Aspen Plus© is the specific software product that is relevant for the current research on UCG.

The Aspen Plus© manuals (Aspen Plus, 2009) offer useful understanding since they describe how models for handling solids should be developed. Earlier studies (Begum et al., 2013; Chen et al., 2010; Corbetta et al., 2014; Kim and Kim, 2011; Preciado et al., 2012; Ramzan et al., 2011), which employed Aspen Plus© in developing fixed bed gasifier models are the best examples which have guided model development in the present research.

The models developed by Corbetta et al. (2014), Begum et al. (2013) and Chen et al. (2010) simulated the operation of fixed bed reactors. On the other hand, Kim and Kim (2011) and Preciado et al. (2012) employed the Aspen Plus© software tool for the simulation of entrained-flow gasifiers, while Shehzad et al. (2016) used the software for the simulation of fluidised bed gasifiers. Moreover, since Preciado et al. (2012) used oxygen as the input agent, they incorporated an Air Separation Unit (ASU) as well as further process stages needed to handle the product-gas stream. Although these studies followed the same basic concept, they differ, firstly, in terms of the number and location of the injected inputs, as well as on the routes of the discharged products.

In addition, different feedstock streams were tested by different studies, with some of them utilising food waste (Chen et al., 2010; Ramzan et al., 2011), coal (Corbetta et al., 2014; Kim and Kim, 2011; Preciado et al., 2012) and biomass (Begum et al., 2013; Corbetta et al., 2014) in the gasification process.

Furthermore, the sensitivity analyses included in the above studies were conducted based on criteria and performance indicators. The following list provides an insightful view to the analysis criteria:

- the ratio between the injected agents ($O_2$, $N_2$ and $H_2O$) and the feedstock quantities (coal, biomass, solid waste etc.);
- the quality of the product-gas based on its composition under different operating conditions (i.e. pressure, injection rate, gasification temperature)
- the energy content of the product-gas ($MJ/Nm^3$) - specifically, how product-gas (LHV) is affected by varying operating conditions.
- the volumetric flow rate of the produced gas ($Nm^3$).
- the carbon efficiency with the comparison of the carbon content between the inflowing and outflowing streams.
- the energy efficiency, which is the ratio of the energy contained in the product-gas to the original energy input through the raw material used.

Regarding the results of the sensitivity studies there were differences between the reported absolute numbers, although some increasing/decreasing tendencies by modifying selected parameters were common.

For instance, Begum et al. (2013) and Chen et al. (2010) investigated how an increase of the air input effects composition of the product-gas, and the results indicated that higher air supply – with steady gasification temperature – leads to decreased hydrogen ($H_2$) and methane ($CH_4$) contents and, subsequently to reduced LHV. On the other hand, Preciado et al. (2012) identified that, by increasing the oxygen supply, the gasification temperature increases and, as a result, higher carbon monoxide (CO) and hydrogen ($H_2$) quantities lead to increased energy content for the outflowing gas.

## 4.4 *UCG model development*

The model synthesised and developed as part of the current PhD work was used in simulating and analysing the large laboratory reactor UCG experiments described in Section 4.5.1. It was inspired by the Aspen Plus gasification studies discussed in Section 4.3 and the UCG modelling studies discussed in Section 3.4.2.1. The UCG modelling studies provided the necessary background knowledge and foundations on the UCG thermo-chemical processes while the Aspen Plus simulation studies provided some examples on how such thermo-chemical processes can be replicated in the Aspen Plus simulation environment.

The geometry of the subsurface Linked Vertical Wells (LVW) UCG layout presented in Figure 4.3) forms the framework for the development of the Aspen Plus UCG process model, and particularly for the modelling of the laboratory experiments.

The Aspen Plus model simulates the chemical processes taking place in the coal seam and focuses on the thermodynamic, mass and heat transfer modelling components in order to calculate the amount of produced gas under restricted Gibbs minimisation and equilibrium conditions.

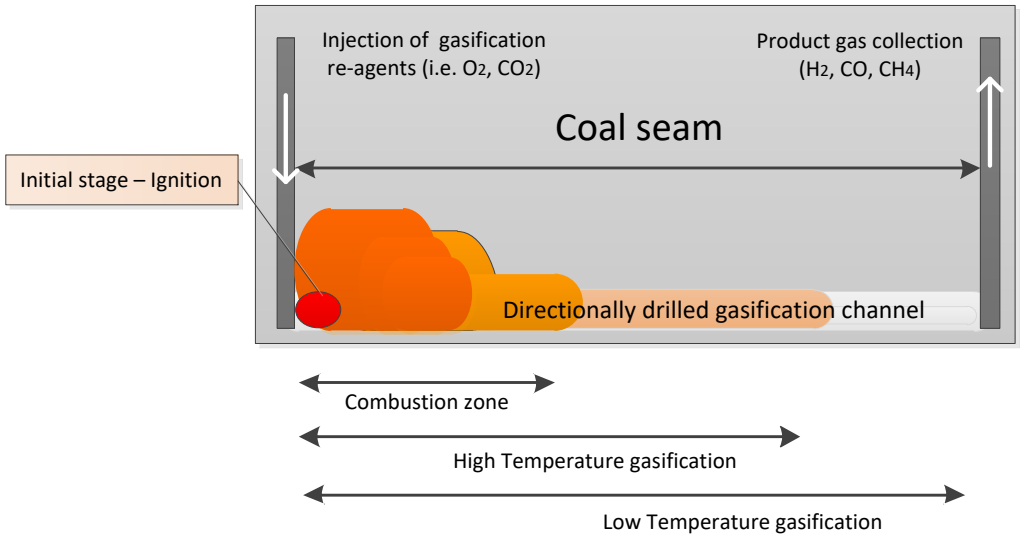


**Figure 4.3:** Linked Vertical Wells (LVW) subsurface UCG layout (after Couch, 2009).

As it can be seen in Figure 4.3, the process is initiated at the one end of the seam and propagates towards the other end. At the bottom of the seam a directionally drilled channel is formed in order to facilitate the flow of the produced gas to the production well (Couch, 2009). Further description of this UCG subsurface layout and its comparison with other existing designs can be found in Chapter 3, Section 3.3 of the thesis.

A key factor in identifying and modelling the UCG thermochemical processes is to understand where the different temperatures zones are developed within the coal seam and how the one follows the other. This is also the reason that any given UCG process model would not be adequate to represent every in-situ UCG subsurface layout. Figure 4.4 presents the different coal to syngas conversion stages as they are simulated in the Aspen Plus UCG process model in this research.

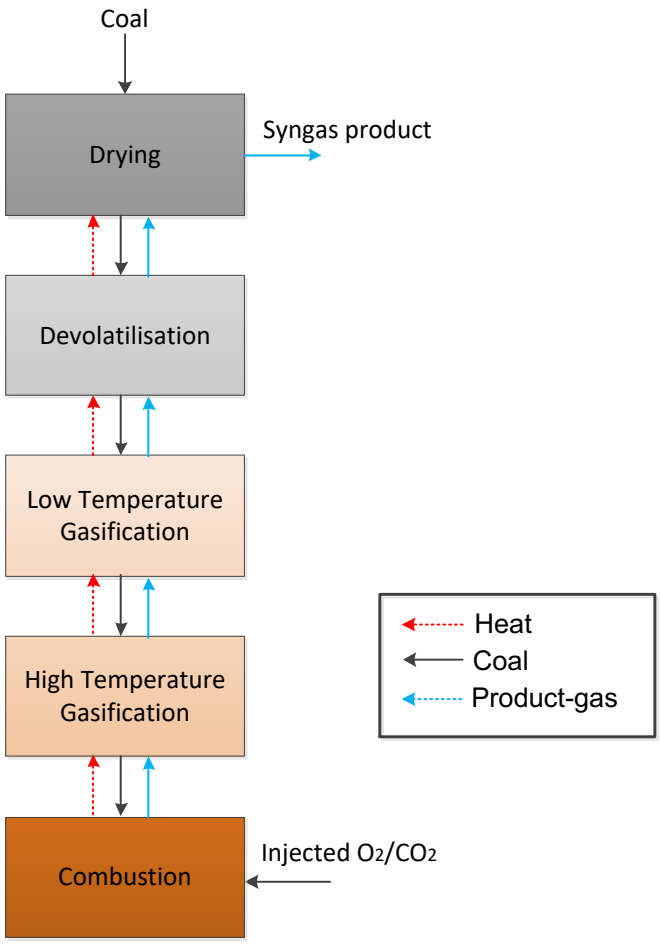


**Figure 4.4:** Conceptual approach to the UCG process model developed in this research.

A correlation between the high/low temperature gasification stages of the UCG process model (Figure 4.4) with the in-situ UCG subsurface layout would reveal the way that the UCG chemical processes drive the coal to syngas conversion process. Firstly, a combustion front is developed within the coal seam close to the ignition well. This combustion front encounters fresh coal as it proceeds from the ignition to the production well. However, the fresh coal resource before reaching the combustion front goes through the drying and devolatilisation stages (Figure 4.4). During these stages, the produced heat from the combustion stage is utilised to reduce the moisture content of the coal and devolatilise it, facilitating the subsequent gasification and combustion stages.

As it can also be seen, the UCG process model coal to syngas conversion stages (Figure 4.4) have inherent similarities to the operation of the up-draft fixed bed gasifier (Figure 4.1).

It is clear that, in both cases, there is flow of gas and heat towards one direction and flow of mass towards the other. The exposure of the devolatilised and partially gasified coal to the oxidising agents (e.g. $O_2$, $CO_2$) triggers the combustion reaction ($C + O_2 \rightarrow CO_2$), while during the flow of the product-gas towards the exit, the gasification takes place where mainly the produced carbon dioxide ($CO_2$) reduces to carbon monoxide (CO) (*Boudouard reaction:* $CO_2 + C \rightarrow 2CO$).

Depending on the distance the combustible gas has to cover before reaching the collection point, the gasification can be simulated through different decreasing temperature zones. In the present work, two temperature zones were considered as a good approximation for the simulated process as the comparison with the experimental results will later reveal. The conceptual modelling approach that was followed in this research work regarding the sequential coal to syngas conversion stages (i.e. drying, devolatilisation, combustion and gasification) is in accordance with the UCG literature (Kariznovi et al., 2013; Park and Edgar, 1987; Perkins and Sahajwalla, 2005; Seifi et al., 2011). Although Figure 4.4 presents a simple overview of the developed process model, the actual Aspen Plus configuration that replicates the UCG process in this research is significantly more complex (Figure 4.5).

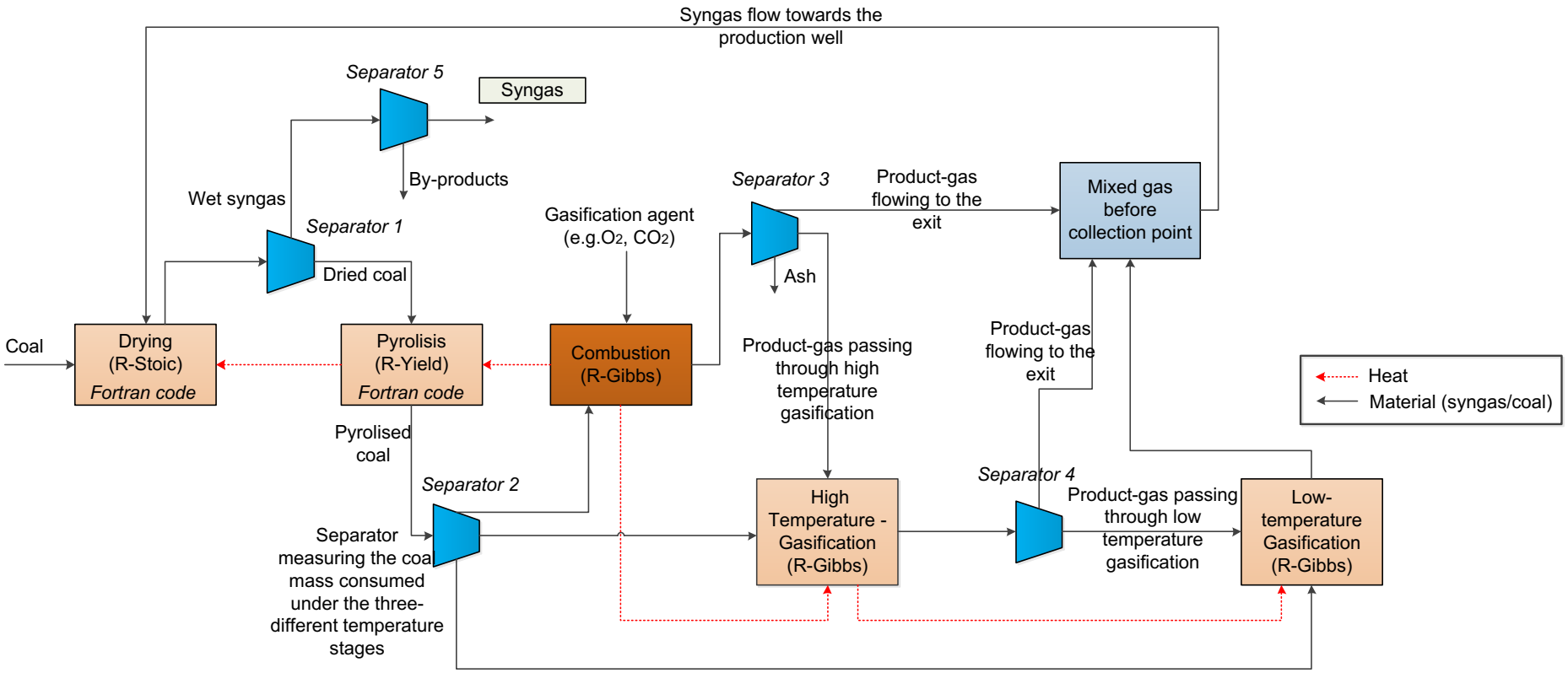


**Figure 4.5:** Aspen Plus configuration designed to replicate the LVW UCG sub-surface layout which has been used in modelling the laboratory UCG trials.

As can be seen in Figure 4.5, the fed coal mass flows through the drying and devolatilisation stages before reaching the combustion stage and the different temperature gasification stages. On the other hand, the produced gas is initially produced in the combustion stage before passing through the different temperature (high-low) gasification stages. As it can be seen, the high temperature gasification stage is neighbouring with the combustion stage. The produced gas finally finds its way out of the process through the drying stage. During its flow, the product-gas stream carries the necessary heat for the endothermic reactions of the gasification, devolatilisation and drying stages. The heat flow, which starts from the combustion stage and eventually reaches all the other stages is indicative.

This process model configuration showcases the advantages of the LVW UCG subsurface layout, which is higher thermal efficiency combined with the reduced temperature of the output product-gas. Nevertheless, the interaction of the product-gas with fresh coal is responsible for product-gas of low purity with increased tars and moisture proportions similar to up-draft fixed bed reactors (Beenackers, 1999; Bhattacharya, 1985; Hobbs et al., 1992; Okuga, 2007).

This drawback is not faced in the down-draft design, where the product-gas is collected from the bottom of the gasifier closer to the combustion stage. As a result, in the UCG context, the location of the product-gas collection point is of specific importance. In the LVW UCG design, the product gas has to flow through the coal seam before its collection, and thus its similarity with the up-draft designs. In contrast, the produced gas collection point is closer to the combustion stage in the CRIP design, therefore, a different process model configuration is required for its simulation. The route that the collected gas will follow before its collection also affects its composition and handling processes, and ultimately leading to its different end-uses.

Before proceeding into explaining the different components of the model, it is important to clarify the assumptions made in the model design. The most important are: steady-state conditions, pressure balance across the process and that chemical equilibrium is reached by the reactions.

In addition, although there is heat transfer between the UCG stages, each stage is assumed to preserve the same temperature (isothermal).

Finally, ash is considered as inert, remaining unaffected after the reactions. These assumptions were also explicitly mentioned by Chen et al. (2010), Preciado et al. (2012) and Begum et al. (2013) in their studies. The four stages of the designed process-model are discussed in more detail in the following sections.

### 4.4.1 Drying

The drying section consists of an R-Stoic reactor (Figure 4.5), which is used to convert part of the moisture of the fresh coal entering the process into steam. This conversion is regulated by a calculator module where the user can pre-define the moisture percentage of the coal after the drying stage and, as a result, the fraction of coal that would participate in the stoichiometric reaction of the R-Stoic reactor. The calculator block (module) is written in FORTRAN code. The necessary heat for the moisture conversion is sourced from the high temperature gas received from the hot bottom stages. Moreover, an SSplit block (i.e. Separator 1) is used to separate the wet product from the dried feedstock that passes to the pyrolysis/decomposition stage. The wet product gas goes through additional purification/dehumidification process through another SSplit block (i.e. Separator 5).

### 4.4.2 Pyrolysis

The pyrolysis section consists of an R-Yield reactor and the aim of this stage is to prepare the dried coal-input for the subsequent gasification and combustion stages. This preparation stage is crucial for the process since the upcoming R-Gibbs reactors (i.e. Combustion, High/Low Temperature Gasification) can only handle "*conventional*" elements and, as a result, coal – which is declared as "*non-conventional*"- has to be disintegrated to its constituents. This decay is controlled by a second calculator block. The coal components are assigned to their fractions based on the coal's ultimate analysis using a code written in Fortran for this calculator block. The necessary heat for the reactions is supplied through a heat stream. Additionally, an SSplit block (i.e. Separator 2) was added in order to analyse how much pyrolysed coal is consumed in each of the three subsequent UCG stages (i.e. Combustion, High/Low Temperature Gasification).

The SSplit blocks were preferred among the other separators provided in the Aspen Plus simulation environment as it can handle all the available stream classes (Table 4.4).

During the gasification stages, the devolatilised coal reacts under less oxidising conditions (compared to the combustion stage) with the product gas during its flows towards the collection stage.

### 4.4.3 Gasification

The gasification section consists of two stages: the high and low temperature gasification reactions. Both stages are simulated through R-Gibbs reactors. These reactor blocks have the advantage of being able to achieve three phase chemical equilibrium (Ramzan et al., 2011). At a steady temperature and pressure, equilibrium conditions can be achieved based on the minimisation of Gibbs free energy (Rossi et al., 2009; Teh and Rangaiah, 2002). The Gibbs free energy of a system can be given by the following equation:

$$G = \sum_{k=1}^{KP}\sum_{n=1}^{NC} n_i^k \mu_i^k \tag{4.1}$$

Where,

*KP*: represents the number of phases

*NC*: represents the number of components

$n_i^k$: represents the number of moles of the *i* component in the *k* phase

$\mu_i^k$: represents the chemical potential of the *i* component in the *k* phase

At standard conditions, the change in the Gibbs free energy can also be expressed by the following equation:

$$\Delta G = \sum \Delta G_{f_{products}} - \sum \Delta G_{f_{reactats}} \tag{4.2}$$

Where,

*ΔG*: represents the change in the Gibbs free energy of the system

$G_{fproducts}$: represents the change in the Gibbs free energy of the products

$G_{freactants}$: represents the change in the Gibbs free of the reactants

As ΔG values change from positive to negative, the spontaneity of the reactions changes as well. Positive ΔG values characterise non-spontaneous reactions while the reverse takes place for reaction with negative ΔG values.

However, equilibrium conditions are reached if ΔG approaches a zero value. As a result, the requirement for minimisation of the Gibbs free energy of the system is a way to reassure that equilibrium condition are satisfied. Furthermore, the R-Gibbs reactor in the Aspen Plus simulation environment provides the user the opportunity to define which products are generated, but not their proportions. Therefore, in the current model, the R-Gibbs reactors were modelled in order to provide results across the whole range of the stream classes (Table 4.4). All the product gases were declared as a *mixed* stream class, while the carbon content (C) was declared as pure solid (CIPSD). Table 4.4 presents an overview of the stream classes that were considered as well as the elements that were included in each (Aspen Plus, 2009).

**Table 4.4**: Considered steam classes and their elements.

| Stream Class | Elements |
|---|---|
| MIXED | Gas, Steam |
| NCSOLID | Coal, Ash (inert) |
| CISOLID | Carbon content of coal (C) |

An additional SSplit block (i.e. Separator 3) (Figure 4.5) has been added between the two different gasification stages in order to identify the proportion of the high-temperature gasification product gas that passes through the low-temperature gasification stage as well. This will allow another observation to be made as not all the high temperature gasification product-gas reacts with the devolatilised coal under the low temperature gasification conditions. A proportion of this gas takes advantage of the permeable path at the bottom of the coal seam and finds its way directly to the production well. This configuration of multiple gasification stages provides the advantage of analysing how the composition of the product gas changes under gradually reducing temperature conditions as it reacts with the devolatilised coal.

### 4.4.4 Combustion

The combustion stage consists of an R-Gibbs reactor and an SSplit block (i.e. Separator 4). The high temperatures reached during this stage also provide sufficient heat for the whole process. This is the stage where the injection of the gasification agents takes place.

Furthermore, the SSplit block (i.e. Separator 4) placed after the combustion R-Gibbs reactor helps to identify the proportion of the combustion product gas that flows through either of the two gasification stages or finds its way directly towards the product gas collection point. Additionally, it discretises the ash component from the remaining stream that flows towards the gasification stages.

## 4.5 *Laboratory Experiments and Model Results*

### 4.5.1 Description of the experiments

The experimental work presented in this section was carried out as part of the European Commission Seventh Framework Programme project TOPS (Technology Options for Coupled Underground Coal Gasification and $CO_2$ Capture and Storage). The experiments were conducted by one of the project partners, the Central Mining Institute (GIG) in Poland (Kapusta et al., 2015; Kapusta et al., 2017) .

The objective of the experiments was to identify the parameters that affected the composition of the UCG product gas and evaluate its suitability for different end-purposes, namely for electricity generation, hydrogen ($H_2$) production or as chemical feedstock. The particular focus of the experiments was the composition of the injected re-agent gas (i.e. $O_2/CO_2/H_2$) which would support the gasification, and the pressure and temperature conditions under which the process takes place. These laboratory scale experiments ultimately aim to increase the controllability and the understanding of the UCG processes. A high-pressure laboratory installation enabled the simulation of the underground coal gasification process in the laboratory (ex-situ) (Figure 4.6).

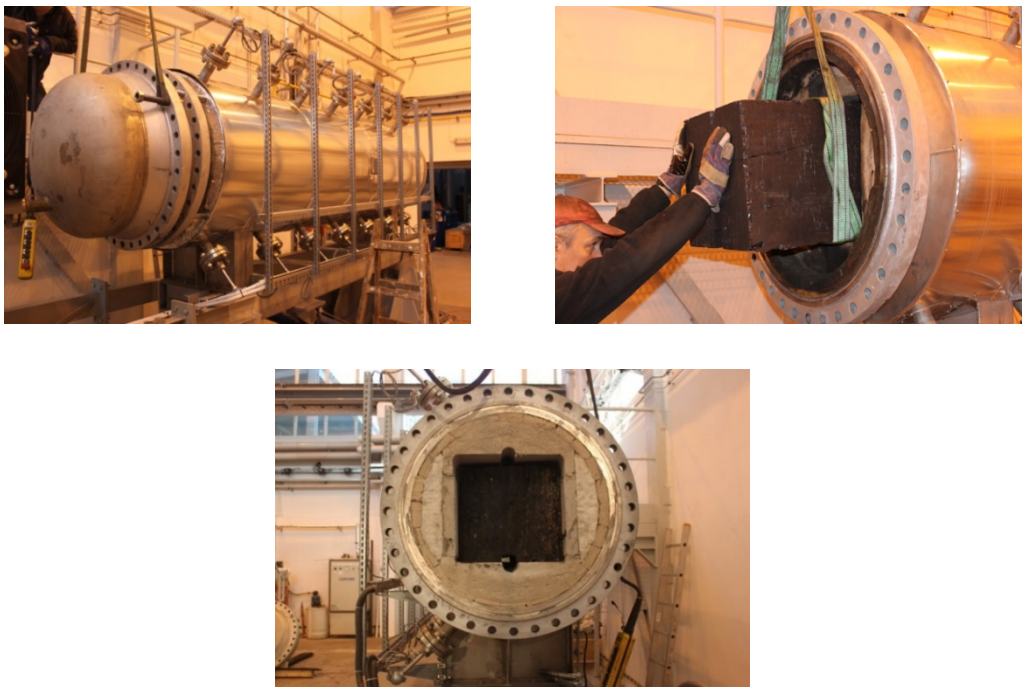

**Figure 4.6:** GIG's high pressure UCG reactor and the coal samples used in the experiments (Kapusta et al., 2015).

The total length of the simulated coal seam in the ex-situ reactor is 3.5 m (Figure 4.7), the cross-section of the coal sample used is 0.4 x 0.4 m (Figure 4.8). UCG simulations in the experimental unit can be carried out at temperatures up to 1,600°C and pressures up to 50 bar. The operating pressure of the conducted experiments were between 10 to 40 bars. The coal seam inside the ex-situ reactor (3.5 x 0.4 x 0.4) was built by a number of block samples and, in some experiments, an additional roof rock (0.1. m) (Figure 4.8a) was prepared for the initial 1.5 m length (Figure 4.7) out the total 3.5 m length of the reactor.

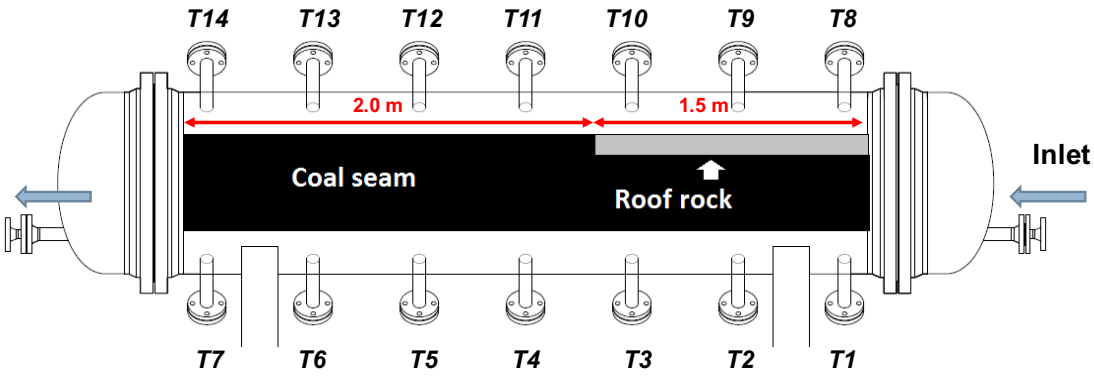


**Figure 4.7:** Side cross-section of GIG's high pressure UCG reactor (Kapusta et al., 2015).

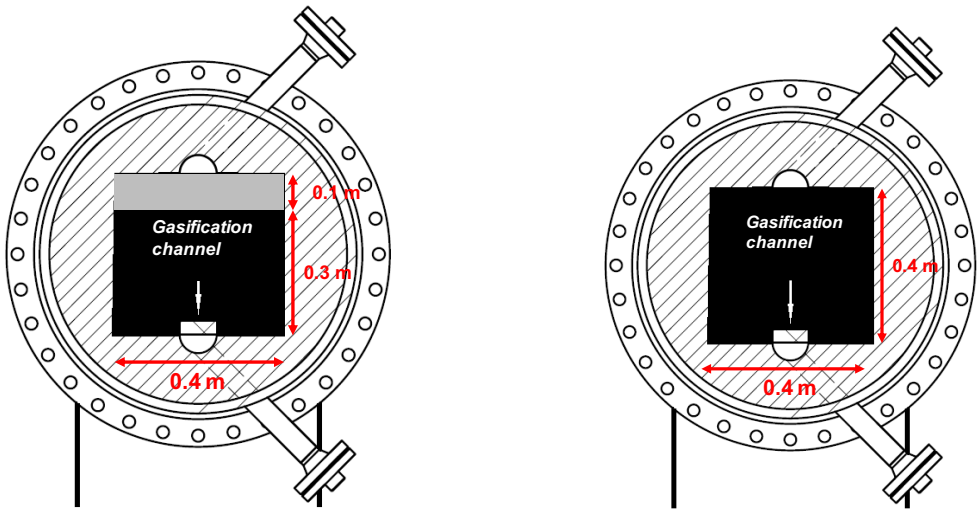


(a) (b)

**Figure 4.8:** Vertical cross-section of – (a) inlet (b) outlet – GIG's high pressure UCG reactor (Kapusta et al., 2015).

A bottom channel (0.07 m diameter) was drilled at the bottom of the simulated coal seam along its length (Figure 4.8) before the start of the experimental UCG process.

Thermocouples were also placed along the length of the coal seam at different places (T1 – T14 in Figure 4.7). The first seven (T1 – T7) were placed at the bottom of the seam within the gasification channel while the remaining seven at the top of the reactor. The initiation of the coal seam takes place at one end of the coal seam (Figure 4.8a) while the product gas is collected at the other (Figure 4.8b), similar to the process taking places in LVW UCG designs.

The product gas after its collection is subject to purification in a gas separation unit while after its dehumidification and filtering the composition of the product-gas is analysed through chromatography. Additional details on the experimental equipment supporting the ex-situ reactor can be found in the literature (Wiatowski et al., 2016).

The ultimate and proximate analyses of the coal samples that were used for the building of the simulated coal seam in the experiments are presented in Table 4.5. Two different coal types were used in the experiments, with one coal type to be used in each experiment. The bituminous coal was provided by Kapusta et al. (2015) from the Murcki – Staszic coal mine in Poland and the lignite coal type by Zavsek et al. (2015) from Coal Mine Velenje in Slovenia.

**Table 4.5**: Proximate and ultimate analysis of coal used in the experiments (Kapusta et al., 2015; Zavsek et al.,2015)

| *Proximate analysis ( % w/w, dry basis)* | Murcki – Staszic Bituminous | Velenje Lignite |
|---|---|---|
| Fixed carbon | 62.74 | 29.71 |
| Volatile material | 32.58 | 64.43 |
| Ash(g) | 4.68 | 5.86 |
| *Ultimate analysis (% w/w, dry basis)* | | |
| Carbon | 79.51 | 56.10 |
| Hydrogen | 4.27 | 5.25 |
| Nitrogen | 1.26 | 0.72 |
| Sulphur | 0.31 | 0.74 |
| Ash | 4.68 | 5.86 |
| Oxygen | 9.97 | 31.33 |
| High Heating Value (dry basis, kJ/kg) | 30.97 | 19.73 |
| Moisture (% w/w) | 4.93 | 31.00 |

**Table 4.6** Experimental conditions for the laboratory gasification experiments (Kapusta et al., 2015; Kapusta et al., 2017).

| Parameter | Experiment No. | | | | |
|---|---|---|---|---|---|
| | 1 | 2 | 3 | 4 | 5 |
| Coal | Murcki - Staszic (Bituminous) | Velenje (Lignite) | Velenje (Lignite) | Murcki - Staszic (Bituminous) | Murcki - Staszic (Bituminous) |
| Gasification reagent | $O_2/CO_2$ | $O_2/CO_2$ | $O_2/CO_2$ | $H_2$ | $H_2$ |
| Gasification pressure, bar | 10 | 10 | 40 | 10 | 40 |

Oxygen ($O_2$), carbon dioxide ($CO_2$) and hydrogen ($H_2$) were used independently and under different proportions in combined mixtures as injected gasification re-agents in different experiments. The experimental conditions set during the modelled gasification tests in the laboratory of GIG are presented in Table 4.6. The experimental data and the results of modelling work carried out using the same conditions as those set for the first two experiments in the laboratory will be presented in detail in the following pages. Building upon the experienced gained during these modelling work, experiments 3, 4 and 5 (Table 4.6) were also modelled and results presented briefly.

### 4.5.2 Modelling and discussions on Oxygen/Carbon dioxide blown gasification experiments

This section presents the results and analysis of the data obtained through the implementation of the developed chemical process model using the conditions set during the first three gasification experiments (Kapusta et al., 2015; Kapusta et al., 2017) in the laboratory. The first two low pressure (10 bar) experiments and model simulations with the bituminous and lignite coal samples are discussed in detail as well as presenting a brief review of the high pressure (40 bar) lignite gasification experiment and modelling studies. As presented in Table 4.7 and Figure 4.9, the 10 bar gasification experiments started with the injection of oxygen ($O_2$) in the initial stages (~ 42 hours) with a mixture of oxygen ($O_2$) and carbon dioxide ($CO_2$) injection taking place in the subsequent stages before the final gasification stage.

**Table 4.7**: Timeline of the experiments conducted using a) the bituminous and b) the lignite coals at 10 bar gasification pressure (Kapusta et al., 2015).

(a)

| Stage no. | Injected reagent | Duration (h) |
|---|---|---|
| 1 | $O_2$ | 0 – 42.5 |
| 2 | $O_2/CO_2$ | 42.5 – 145 |
| 3 | $CO_2$ | 145 – 150.5 |
| **Total** | | **150.5** |

(b)

| Stage no. | Injected reagent | Duration (h) |
|---|---|---|
| 1 | $O_2$ | 0 – 42 |
| 2 | $O_2/CO_2$ | 42 – 89 |
| 3 | $O_2$ | 89 – 95 |
| **Total** | | **95** |

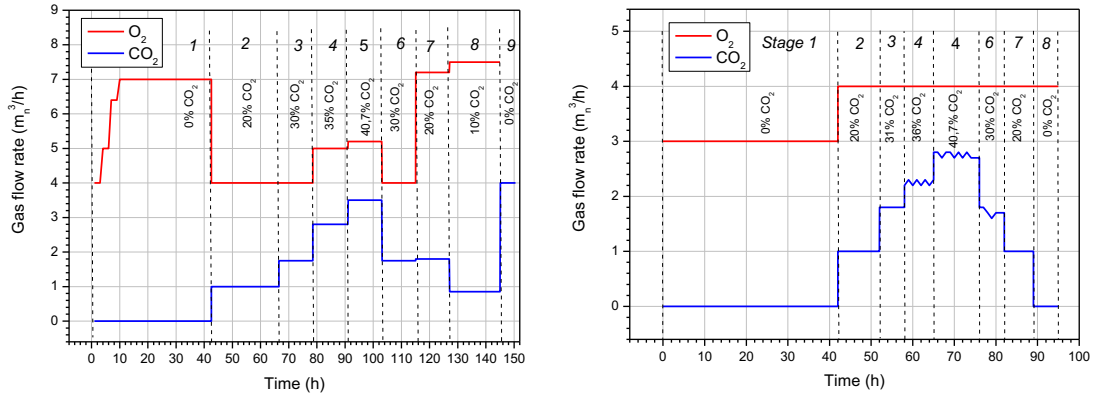


(a) (b)

**Figure 4.9:** Reagent supply rates over the course of the 10 bar laboratory gasification experiments: (a) Murcki - Staszic vosl at 10 bar, (b) Velenje coal at 10 bar (Kapusta et al., 2015).

The final stage includes significant differences between the two experiments. In the bituminous coal experiment during the last stage (145$^{th}$ to 150$^{th}$ hour) only carbon dioxide ($CO_2$) was injected while during the corresponding stage (89$^{th}$ to 95$^{th}$ hour) in the lignite experiment only oxygen ($O_2$) was injected.

As a result, it could be assumed that the experiments were organised into three stages with the second stage being sub-divided into additional sub-stages. During the 2$^{nd}$ stage, the injected oxygen ($O_2$) concentration gradually decreased and then it started increasing again. The proportion of carbon dioxide ($CO_2$) in the injected gas mixture reached its highest point (40%) on the 103$^{rd}$ hour of the bituminous coal experiment while the corresponding ratio in the lignite coal experiment reached approximately the same fraction (~ 40.7%) on the 76$^{th}$ hour. In both experiments, after the afore mentioned time points (103$^{rd}$ and 76$^{th}$ hour) the oxygen ($O_2$) concentration in the injected gas mixtures started increasing until the end of the second stages (Table 4.7 and Figure 4.9).

**Table 4.8**: Gas compositions in the 10 bar oxygen-blown stage.

| **Coal rank** | **Source** | **Duration (h)** | **$O_2/CO_2$, %** | **Composition, $\%_{vol.}$** | | | | **Calorific value (MJ/Nm$^3$)** |
|---|---|---|---|---|---|---|---|---|
| | | | | **$CO_2$** | **CO** | **$H_2$** | **$CH_4$** | |
| Bituminous | Experimental | 12-36 | 100/0 | 44.0 | 30.0 | 18.0 | 4.0 | 7.10 |
| | Modelling | - | 100/0 | 49.0 | 33.0 | 13.0 | 3.0 | 6.90 |
| Lignite | Experimental | 0-42 | 100/0 | 77.2 | 4.0 | 9.0 | 6.2 | 4.22 |
| | Modelling | - | 100/0 | 74.9 | 3. 9 | 9.3 | 6.5 | 4.34 |

Table 4.8 presents an overview of the comparison between the experimental and modelling gasification results for the two coal types at 10 bar pressure. It also presents a comparison of model results against the experimental data for the first stage of both experiments. In particular, the comparison applies to the 12$^{th}$ to 36$^{th}$ hours of the experiment for the bituminous coal and for the full first stage of the lignite experiment. During these periods, the injected gasification agent was oxygen. These time periods were carefully selected since the operation inside the ex-situ reactor stabilises and approaches steady-state conditions in this period.

Therefore, the modelling assumptions for steady state conditions were believed to have been fulfilled. Comparison of the product gas compositions (Table 4.8) between the experimental and modelling results shows that they are in good agreement. Specifically, high carbon dioxide content ($CO_2$) can be seen in both cases due to the abundance of oxygen ($O_2$) during this period. Especially in the case of the bituminous coal experiment, high carbon monoxide content (CO) is also evident through the above comparison. This can be attributed to the relatively long distance that the product gas has to cover from the one end of the reactor, where the initial combustion front resided, to the other end of the reactor where the gas is collected. During this flow, the developed carbon dioxide ($CO_2$) reduces to carbon monoxide (CO) mainly through the *Boudouard reaction* ($CO_2 + C \rightarrow 2CO$).

Regarding the hydrogen ($H_2$) content in the product gas, the modelling results estimate it a little lower than the experimental output in the case of the bituminous coal experiment. The reason may be that, in general, the hydrogen ($H_2$) content in the UCG product gas is linked with the moisture content of the coal or steam injection (if it exists). In both experiments, no steam injection took place and the only source of steam was the moisture content of coal that remained in the gasifier after the drying stage. This lack of steam injection may have caused the model to slightly underestimate (due to increased presence of natural moisture within the laboratory gasifier) the performance of the *water-gas shift reaction* ($C + H_2O \rightarrow CO + H_2$) in the case of bituminous coal. However, during the lignite experiment, its inherently higher moisture content facilitated a better correlation of the hydrogen ($H_2$) content between the experimental and modelling results.

In addition, a cross-comparison between the (experimental and modelling) results of the two experiments shows the higher methane ($CH_4$) content in the case of lignite trial due to the lower temperatures developed there and the high-pressure conditions of both experiments. Furthermore, the lower hydrogen ($H_2$) content observed during the lignite experiment indicates that the methanation reaction ($C + 2H_2 \rightarrow CH_4$) plays a significant role on converting hydrogen ($H_2$) to methane ($CH_4$).

The experimental and modelling results regarding the calorific values of the product gases were also compared.

In the case of the bituminous coal experiment, the modelling study estimated 6.9 MJ/Nm$^3$ (Table 4.7) which is in close agreement with the experimental average (7.1 MJ/Nm$^3$) as presented in Figure 4.10 for the period between the 12$^{th}$ and 36$^{th}$ hour of the experiment.

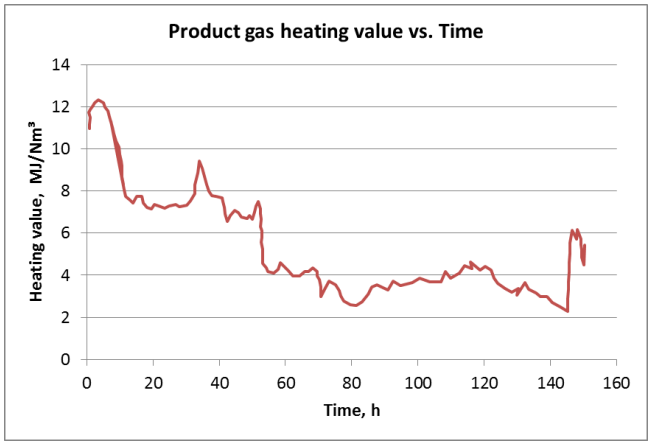


**Figure 4.10:** Calorific value of the collected product-gas during the 10 bar bituminous coal experiment (Kapusta et al., 2015).

As Figure 4.10 illustrates, the product gas maintains its calorific value above 6 MJ/Nm$^3$ during the oxygen blown stage. This value is significantly higher than the caloric values recorded in the subsequent stage (< 5 MJ/Nm$^3$) when carbon dioxide ($CO_2$) was included in the injected gas mixture. This rapid drop is associated with the rapid increase of the carbon dioxide ($CO_2$) content in the product gas and the rapid drop in the concentrations of carbon monoxide (CO) and hydrogen ($H_2$) in it. In addition, even when the oxygen content in the injected gas mixture was increasing (103$^{rd}$ to 145$^{th}$ hours) the calorific value of the product gas did not increase as one would have expected. This unstable performance during the last two stages of the experiment was also the reason why further comparison of the model results with the experimental results was not attempted. Additionally, the continuous change (every 10 minutes) in the injected gas mixture concentration did not help the development of operating conditions that could be characterised as steady state and help the modelling effort.

In the case of lignite experiment, the model estimated 4.34 MJ/Nm$^3$ calorific value for the product gas, which is in close agreement with the 4.22 MJ/Nm$^3$ obtained from the experimental studies.

Similar to the bituminous coal experiment, the heating value drops considerably when carbon dioxide ($CO_2$) is also injected. The slightly higher modelling estimate compared to the experimental value (4.34 vs. 4.22 MJ/Nm$^3$) can be attributed to the higher methane ($CH_4$) content. Literature (Gregg and Edgar, 1978) has already commented on why equilibrium studies can overestimate the methane proportions as the reaction rate of methane formation is slow (at low temperatures) and the formation rate is determined by the kinetic rates rather than the equilibrium conditions.

Figure 4.11 presents how the compositions of the product gases changed during the experiments. During the bituminous coal experiment, up to the 42$^{nd}$ hour of the experiment, there was steady oxygen injection. As it can be seen from the figure, during the 12$^{th}$ to 36$^{th}$ hours of the experiment the gas concentration stabilises, confirming that assuming steady state conditions for the model simulations was reasonable.

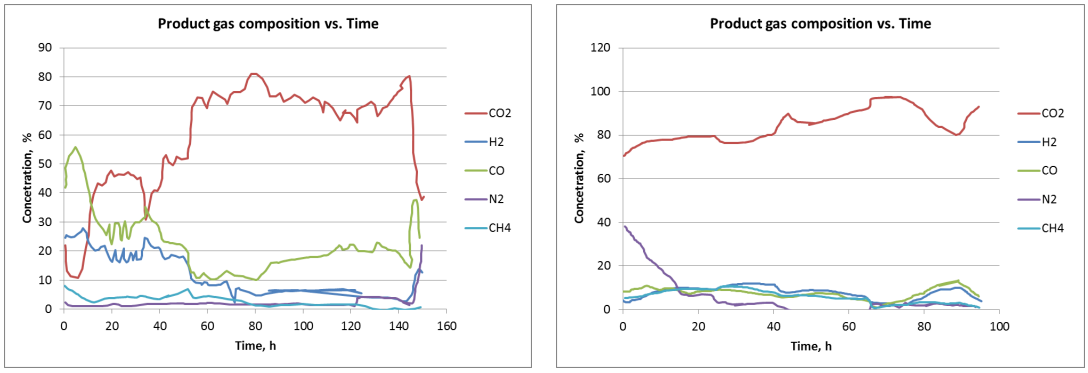


(a) (b)

**Figure 4.11:** Composition of the collected product-gases during a) the bituminous b) the lignite coal laboratory gasification experiments at 10 bar (Kapusta et al., 2015).

As Figure 4.11a illustrates, during the oxygen blown stage the carbon dioxide ($CO_2$) concentration is maintained below 50%. As the oxygen injection ($O_2$) is gradually replaced by carbon dioxide ($CO_2$), the $CO_2$ concentration in the product-gases increases to values above 50%. On the other hand, the lower temperatures developed during the lignite gasification experiment maintained the carbon dioxide ($CO_2$) fraction above 70% throughout (Figure 4.11b).

The results presented in Figure 4.11 also lead to the conclusion that, during the increased the carbon dioxide ($CO_2$) injection stages (91$^{st}$ to 103$^{rd}$ hour of the bituminous coal experiment and 65$^{th}$ to 76$^{th}$ hour of the lignite experiment), the thermodynamic conditions (pressure and temperature) did not facilitate its conversion to carbon monoxide (CO). As a result, the carbon monoxide (CO) content decreased during these stages in both experiments.

Table 4.9 compares the coal consumption (conversion to syngas) and product-gas yield rates obtained from the experimental and modelling studies. During the bituminous coal simulations the oxygen ($O_2$) injection rate was fixed at 6.46 $Nm^3/h$ in the, which is equal to the average oxygen injection rate during the 12$^{th}$ to 36$^{th}$ hour of the experiment (Figure 4.9a). The ($O_2$) injection rate for the lignite model, on the other hand, was fixed at 3.00 $Nm^3/h$ (Figure 4.9b).

Regarding the bituminous coal experiment, the average coal consumption rate during the 1$^{st}$ stage of the experiment is 6.73 kg/hr. The model simulations estimated the corresponding rate as 6.89 kg/hr, which proves to be a reliable estimate when it is compared with the experimental one. The corresponding model estimate for the lignite experiment was 6.2 (kg/hr), which again was in a reasonably good agreement with the experimental result (6.42 kg/hr).

**Table 4.9**: Comparison of coal consumption (conversion to syngas) and product-gas yield rates obtained in the experimental and modelling studies during the oxygen-blown stage.

| Coal rank | Source | Pressure (bar) | $O_2$ injection rate ($Nm^3/h$) | Coal consumption rate kg/h | Product gas volume ($Nm^3/h$) |
|---|---|---|---|---|---|
| Bituminous | Experimental | 10 | 6.46 | 6.73 | 9.7 |
| | Modelling | 10 | 6.46 | 6.89 | 9.6 |
| Lignite | Experimental | 10 | 3.00 | 6.42 | 5.3 |
| | Modelling | 10 | 3.00 | 6.20 | 5.1 |

As identical oxidant injection rates are used for both the experiment and model simulations of the experiments, the product gas flow rates can be consistently compared.

Table 4.9 shows that the experimental and modelling results are in good agreement. During the lignite experiment, the product gas flow rate was significantly lower than that observed for the bituminous coal experiment. However, the corresponding coal consumption rates do not differ significantly. The reason for this can be attributed to the different moisture contents of the two coal types. The higher moisture content of the lignite implies that, for the same coal mass, the converted carbon (C) mass is significantly lower in the case of the lignite. As a result, a carbon balance analysis can reveal that significantly lower volume of product gas is produced during the lignite gasification experiment (Table 4.9).

Figure 4.12 presents the input and output flow rates of oxidant and product gas during both gasification experiments. During the oxygen blown stages of the experiments (~up to 42$^{nd}$ hour), the coal conversion processes are active and this element leads to high product gas flow rates. On the other hand, during the subsequent stages of the experiments when carbon dioxide ($CO_2$) is also injected, the volumetric flow rate of the product gas is almost equal to the corresponding oxidant supply rate. This raises some doubts over the vigorousness of the gasification process during these stages and, this was another reason why model simulations during these stages were not expected to yield consistent results. This conclusion further supported by the observation that high carbon dioxide ($CO_2$) injection period overlap with increased proportions of $CO_2$ in the product gases.

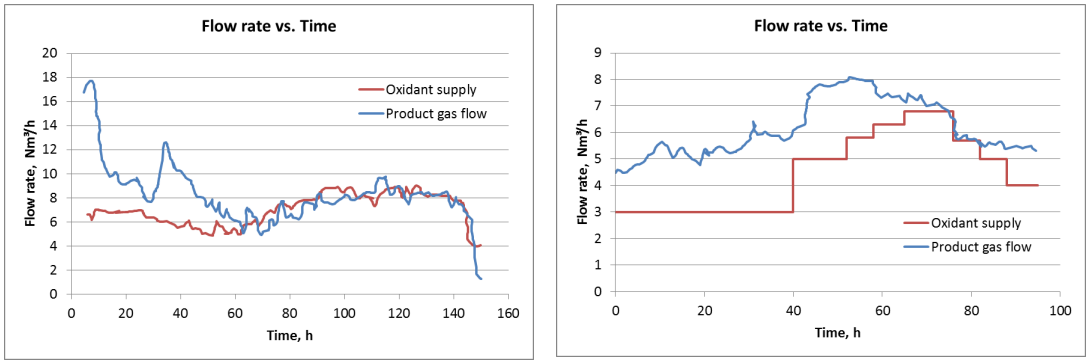


(a) (b)

**Figure 4.12:** Volumetric flow rate of injected and produced gases during (a) bituminous coal and (b) lignite gasification experiments at 10 bar (Kapusta et al., 2015)

The reason for the low conversion of the injected carbon dioxide ($CO_2$) to useful product gas (e.g. CO) can be attributed to both the temperature and pressure conditions. As also mentioned in the literature (Section 2.1.3), lower pressures increase the forward reaction rate of the *Boudouard* reaction and, as a result, the carbon monoxide (CO) output increases (Basu, 2006; Fischer et al., 1979b; Roddy, 2013).On the other hand, increased pressures (such as 10 bar) have the reverse effect. Additionally, the *Boudouard* reaction is an endothermic reaction which requires high temperature environments for an increased forward rate (Fischer et al., 1979b; Basu, 2006; Li et al., 2001; Roddy, 2013). For this reason, the temperature profile within the ex-situ reactor at different time periods and at different locations helps to identify under which conditions the combustion and the gasification takes place. The following series of figures (Figure 4.13 to Figure 4.15) present the temperature profiles at the roof and the bottom of the experimental reactor during these experiments.

Figure 4.13 presents the temperature variation at different times along the length of the reactor during the bituminous coal experiment. The maximum gasification temperature was about 1,500$^{o}$C and it was recorded in the roof strata close to the reactor inlet (oxidation zone). Another observation made form Figure 4.13 is that temperatures in the bottom strata (gasification channel) were about 200 to 400$^{o}$C lower than those at the top of the reactor. This phenomenon confirms that the post gasification ash/slag and molten roof may effectively insulate against heat conduction to the bottom strata during the field UCG operations.

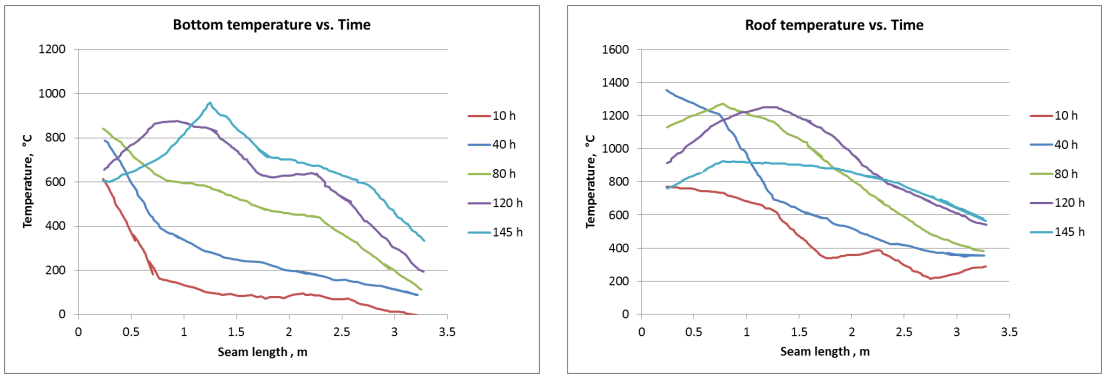


(a) b)

**Figure 4.13:** Temperatures at the (a) bottom and (b) roof within the 10 bar pressure UCG reactor during the bituminous coal gasification experiment (Kapusta et al., 2015).

Figure 4.14 presents the temperature distribution as they were recorded by the thermocouples placed at the roof (Figure 4.14a) and the bottom (Figure 4.14b) of the ex-situ UCG reactor in the bituminous coal experiment. The corresponding temperature distributions for the lignite experiment are presented in Figure 4.15.

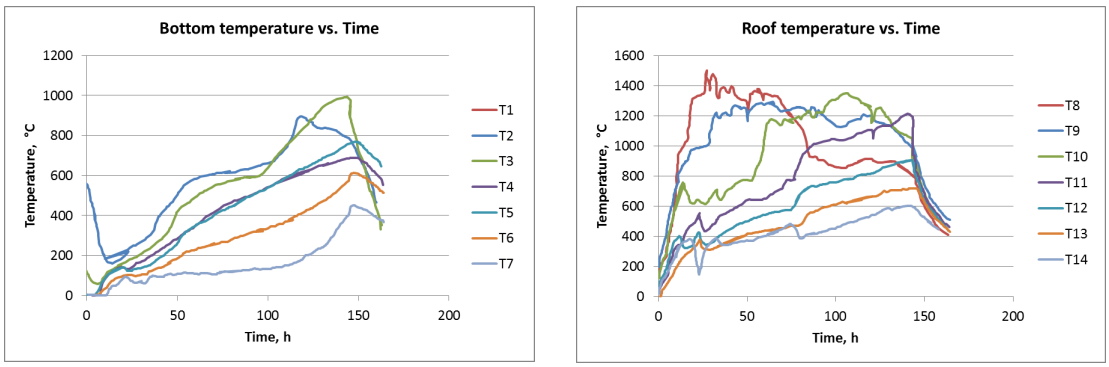


(a) (b)

**Figure 4.14:** Temperature profiles at the (a) bottom and (b) roof of the 10 bar pressure UCG reactor during the bituminous coal gasification experiment (Kapusta et al., 2015).

The location of the thermocouples (T1-14) within the ex-situ UCG reactor were illustrated in Figure 4.7. The temperature profiles help identifying where the combustion front is at different time periods. In addition, the thermocouples readings can help deciding the temperatures of the different coal-syngas conversion stages developed within the reactor as the product gas flows towards its end. For gasification modelling purposes in particular, these profiles form a useful tool for the decision of the temperature conditions at different gasification stages.

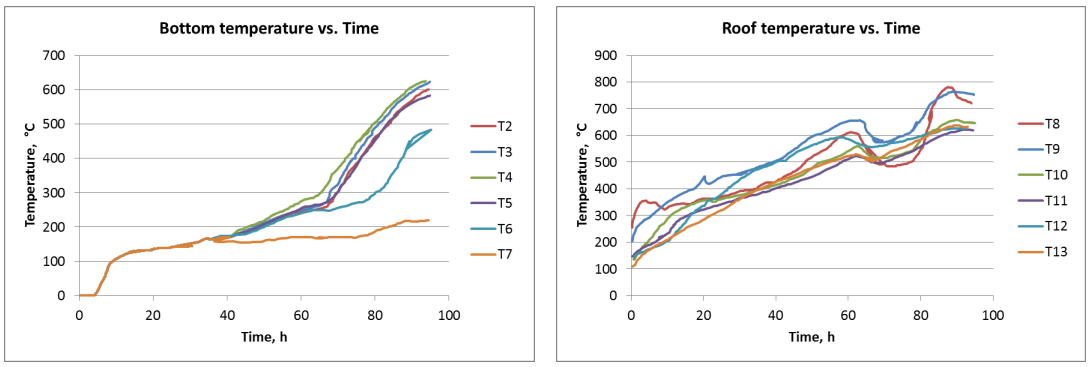


(a) (b)

**Figure 4.15:** Temperatures at the (a) bottom and (b) roof of the 10 bar pressure UCG reactor during the lignite gasification experiment (Kapusta et al., 2015).

Table 4.10 provides an overview of the temperatures assigned to the combustion, high temperature and low temperature gasification stages of the simulation models developed (Figure 4.5) for the two different coal types. As the modelling studies presented here simulated the initial oxygen injection stages of the experiments, representative sets of temperature conditions had to be selected to offer a good representation of the in-situ conditions as Aspen Plus software does not have spatial capabilities and assumes steady state conditions.

**Table 4.10**: Temperature across the different stages in the 10 bar gasification model.

| Coal rank | Combustion temperature ($^oC$) | High Temperature Gasification ($^oC$) | Low temperature Gasification ($^oC$) |
|---|---|---|---|
| Bituminous | 1,250 | 650 | 400 |
| Lignite | 525 | 400 | 350 |

Regarding the bituminous coal experiment, the temperatures selected for the model simulations were taken from the thermocouples located at the roof during the 36$^{th}$ hour of the experiment (Figure 4.14b). It is believed that, at this point in time the combustion stage was taking place close to the T9 thermocouple, while the high and low temperature gasification stages were taking place near the T10 and T12 thermocouples respectively. Figure 4.13b (in particular the 40$^{th}$ hour plot) shows that the combustion temperature (1,250$^o$C) was reached between the initial 0.25m – 1.0m length of the reactor. The high temperature zone was assumed to take place between the initial 1.0m – 1.75m length of the reactor and, for this reason, 650$^o$C selected was assumed to be representative. Finally, the low temperature zone was observed to be extending between the last 1.75m – 3.25m of the reactor, where the product gas was collected.

Consistent with the choice made for the bituminous coal experiment, the corresponding simulation temperatures (Table 4.10) for the lignite gasification model were selected by observing the temperatures recorded by the different thermocouples located at the roof of the reactor during the 36$^{th}$ hour of the experiment (Figure 4.15b). During this period (36$^{th}$ hour), the combustion stage was taking place where the T9 the thermocouple is located.

The subsequent high and low temperature gasification stages were taking place around T10 and T11 thermocouples respectively (Figure 4.15b). However, a cross-comparison between the bituminous coal and the lignite experiments reveals that, during the second case the temperature difference between the combustion and the subsequent gasification stages is neither significant, nor completely apparent.

Therefore, by utilising the actual experimental temperature measurements in the model simulations, the degree of freedom regarding the independent variables of the model were restricted and, at the same time, the modelling accuracy was increased. Furthermore, the model configuration (Figure 4.5), which uses a number of separators to intervene between the different stages (i.e. combustion, high temperature gasification, low temperature gasification) allows for reliable estimates on the stage the coal consumption takes place. Specifically, the model simulations can show how much carbon was converted into gas in each stage. Table 4.11 presents the data available. As it can be seen, the conversion rates could be correlated with the temperatures developed in each stage. The higher carbon conversion rates (4.13 kg and 1.58 kg respectively) were achieved in the combustion zone where the oxygen concentrations were higher.

A cross-comparison between the bituminous coal and lignite gasification experimental results presented in Table 4.11 display the lower carbon (C) quantities converted during the lignite experiment. This observation is reasonable considering the lower temperatures existing under the lignite experiment. In addition, despite the lower carbon (C) quantities converted during the lignite experiment, the corresponding difference in the coal conversion rates (Table 4.9) between the two experiments is not as significant. This is reasonable since the weight fraction (w/w%) of carbon (C) in lignite is significantly lower than the corresponding fraction in bituminous coal.

The gasification zones also contribute to the carbon conversion through the *steam gasification reaction* ($C + H_2O \rightarrow CO + H_2$). However, in the models, the steam concentration was constrained to the moisture content of the coal (the laboratory experiments did not include steam injection) and, as a result, it could be assumed that higher conversion rates would have been achieved if substantial steam proportions were present.

The low temperature gasification stage contributes to the carbon consumption through the *methanation reaction* ($C + 2H_2 \rightarrow CH_4$), which is favoured at high pressures and supports the methane content of the product gas.

**Table 4.11**:Carbon (C) balance calculations for the oxygen-blown stage at 10 bar.

| Coal rank | Combustion (kg) | High Temperature Gasification (kg) | Low temperature Gasification (kg) |
|---|---|---|---|
| Bituminous | 4.13 | 2.06 | 0.69 |
| Lignite | 1.58 | 0.51 | 0.25 |

As discussed in the above paragraphs, the model simulation results for both the temperatures developed during different stages and the carbon conversion rates are in agreement with those reported in the UCG literature (Gregg and Edgar, 1978); (Blinderman et al., 2008) and earlier experimental observations (Stańczyk et al., 2012). As Table 4.12 shows, additional analysis of the modelling results reveals how much product gas yielded after each stage has actually reacted in the subsequent gasification stages.

**Table 4.12**: Product-gas balance calculations for the oxygen-blown stage at 10 bar.

| Coal rank | Stage *To/From* | High Temperature Gasification (%) | Low temperature Gasification (%) |
|---|---|---|---|
| Bituminous | **Combustion (%)** | 60 | - |
| | **High temperature gasification (%)** | - | 80 |
| Lignite | **Combustion (%)** | 10 | - |
| | **High temperature gasification (%)** | - | 25 |

As presented in Table 4.12, in the case of bituminous coal experiment the percentage of combustion stage product gas that goes through the high temperature gasification stage is only 60 %. This means that remaining 40% manages to find its way to the end of the reactor through the channel drilled at the bottom of the reactor.

However, vast majority (80%) of the high temperature stage product gas also passes through the low temperature gasification stage. This percentage highlights the author's earlier conclusion that, if the combustion product gas does not manage to find its way through the bottom channel, then it flows through a permeable path within the coal body and, as a result, it reacts with the devolatilised coal in both the high and low temperature gasification stages.

On the other hand, the process has been considerably different in the lignite experiment. The low temperatures that exist in the gasification stages subsequent to the combustion stage do not support as much the reactions with the combustion stage product gas while passing through the gasification stages. For this reason, only 10% of the combustion stage product gas reacts at the high temperature gasification stage in the lignite experiment.

Additionally, as the high and low temperature gasification stages have a low temperature difference, a higher percentage (25%) of the high temperature gasification stage product gas also passes through the corresponding low temperature stage. Finally, the low percentage (10%) of the combustion stage product gas that passes through the subsequent gasification stages is also evidenced by the increased carbon dioxide $CO_2$ content in the final product gas (>70%).

Furthermore, Figure 4.16 presents the data collected over the course of the high pressure (40 bar) $O_2/CO_2$ blown gasification experiment carried out with the Velenje lignite in detail. Figure 4.16a which illustrates the increasing $CO_2$ injection rate during the course of the experiment drives the key observations presented in the related Figures 4.16a-c. In particular, the highest gas production rate (Figure 4.16b) takes place (during the 25th -30th hour of the experiment) with an $CO_2/O_2$ injection ratio of 1:3 while during that stage the $CH_4$ reaches its peak content (Figure 4.16c) leading to a peak value for the corresponding calorific value (Figure 4.16d).

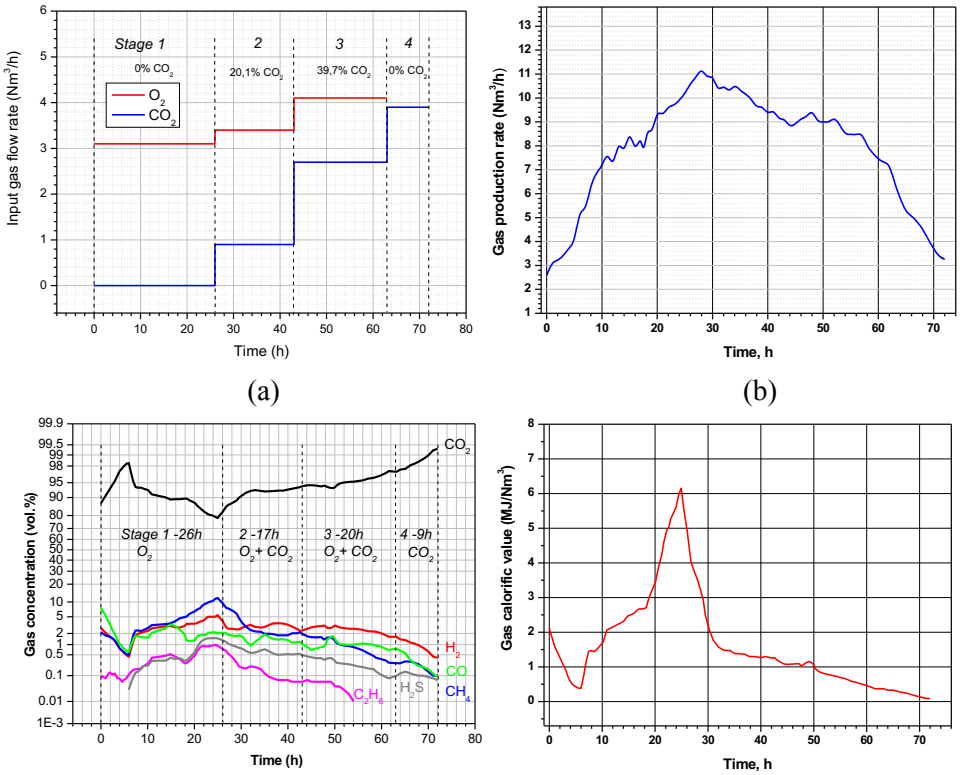


**Figure 4.16:** Changes in (a) oxidants supply and (b) gas production rates, (c) gas composition and (d) calorific value over the course of the experiments for the 40 bar $O_2/CO_2$ blown gasification experiments with the Velenje lignite (Kapusta et al., 2017) .

**Table 4.13**: Average gas compositions in the 40 bar oxygen-blown stage for the Velenje lignite gasification case study.

| Coal rank | Source | Pressure (bar) | $O_2/CO_2$, % | Composition, $\%_{vol.}$ | | | | Calorific value ($MJ/Nm^3$) |
|---|---|---|---|---|---|---|---|---|
| | | | | $CO_2$ | CO | $H_2$ | $CH_4$ | |
| Lignite | Experimental | 40 | - | 92.4 | 1.2 | 2.7 | 2.1 | 1.3 |
| | Modelling | 40 | 53/47 | 92.1 | 1.7 | 2.0 | 3.3 | 1.6 |

Table 4.13 presents a summary of the experimental and model simulation conditions and the product gas composition obtained for the same case study. As discussed before, simultaneous injection of carbon dioxide ($CO_2$) and oxygen ($O_2$) lead to high carbon dioxide ($CO_2$) in the product gas in both the modelling and the experimental results. Consequently, the high carbon dioxide contents ($CO_2$) lead to low calorific values.

The *Boudouard reaction* ($C + CO_2 \rightarrow 2CO$), which was targeted in order to increase the carbon monoxide (CO) content in the product gas, requires a high temperature environment in order to have increased reaction rates. The high carbon dioxide ($CO_2$) content observed in both the experimental and modelling results suggests that most of the injected carbon dioxide ($CO_2$) has bypassed the reaction zone and collected in the product gas.

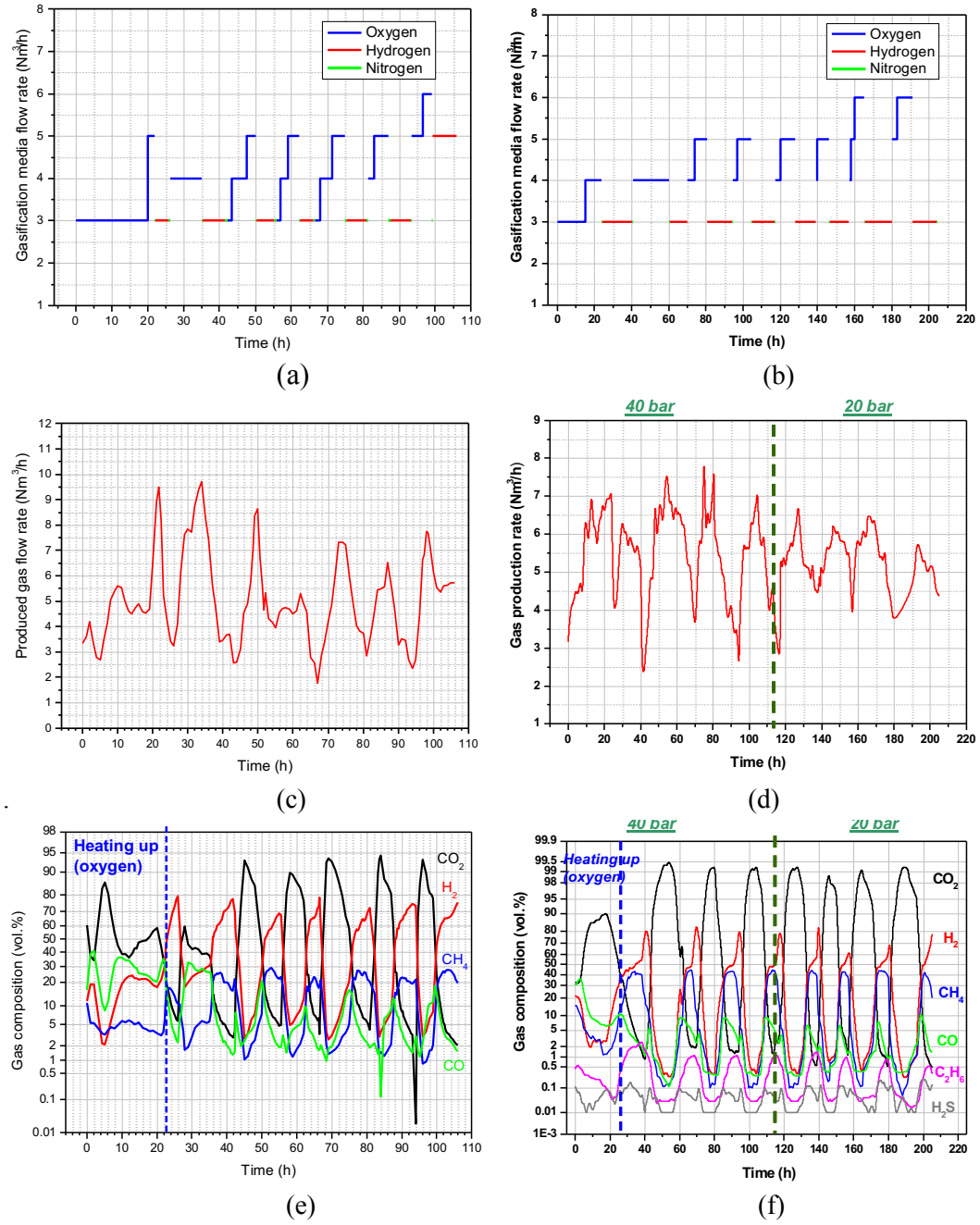


**Figure 4.17:** Changes in the rates of the gasifying media at (a) 10 bar and (b) 20 and 40 bar the product gas yield rates at (a) 10 bar and (d) 20 and 40 bar and product gas compositions at (e) 10 bar and (f) 20 and 40 bar for the Murcki - Staszic bituminous coal over the course of the experiments (Kapusta et al., 2017).

### 4.5.3 Modelling and discussions on hydrogasification experiments

Further to the detailed review of the $O_2/CO_2$ blown laboratory reactor experiments and the gasification performance analysis presented above, this section presents a brief review of the results of model simulations carried out after the completion of two hydrogasification experiments (Kapusta et al., 2017) using the Murcki-Staszic bituminous coal at GIG. Furthermore, Figures 4.17a-c-e present an overview of the experimental results during the 10 bar hydrogasification experiment while Figures 4.17b-d-f present the corresponding data for the coupled 20-40 bar experiment.

As initially planned during the experimental design stages of research, the hydrogasification experiments aimed at improving the product gas calorific value significantly through increased methane ($CH_4$) formation. Table 4.14 presents the details of both the experimental and modelled gas compositions and calorific values for the product gas in these experiments. As Figure 4.17a-b illustrate, the hydrogasification experiments were carried out by sequential injections of hydrogen ($H_2$) and oxygen ($O_2$) throughout the experimental process. This was modelled by injecting a mixture of $H_2$ and $O_2$ at a ratio of 3/7 during the numerical modelling studies. As the hydrogasification experiment on the Velenje lignite at 10 bar yielded very disappointing results, no further experiments and analysis were considered with this coal and focus diverted to the bituminous coal samples.

**Table 4.14**: Average gas compositions in the 10 and 40 bar hydrogasification case studies with the Murcki-Staszic bituminous coal.

| **Coal rank** | **Source** | **Pressure (bar)** | **$H_2/O_2$, %** | **Composition, $\%_{vol.}$** | | | | **Calorific value ($MJ/Nm^3$)** |
|---|---|---|---|---|---|---|---|---|
| | | | | **$CO_2$** | **CO** | **$H_2$** | **$CH_4$** | |
| Bituminous | Experimental | 10 | - | 11 | 5.5 | 61.1 | 21.1 | 15.4 |
| | Modelling | 10 | 30/70 | 8.9 | 7.1 | 60.9 | 22.0 | 15.9 |
| Bituminous | Experimental | 40 | - | 20.5 | 5.3 | 44.1 | 29.2 | 16.40 |
| | Modelling | 40 | 30/70 | 16.8 | 6.9 | 48.6 | 27.0 | 16.24 |

Table 4.14 presents a summary of the experimental and model simulation conditions and the product gas composition obtained for the same case study. The coupled 40-20 bar experiment was simulated solely at 40 bar pressure conditions across the whole experiment. The reason was that as the 20 bar experiment followed the 40 bar one there is an extensive sequential effect over the 20 bar case which cannot be captured. In addition, the aim was to highlight the effect of elevated pressure conditions during hydro-gasification.

At higher pressures (40 bar vs. 10 bar), the hydrogen ($H_2$) content in the product gas is reduced in both the experimental and model results while the corresponding carbon dioxide ($CO_2$) increases. The above results are realistic as the higher pressures allow for higher carbon (C) consumption rates, which at low temperatures lead to higher carbon dioxide ($CO_2$) (due to reduced effect of the *Boudouard reaction*: $C + CO_2 \rightarrow 2CO$) and lower hydrogen ($H_2$) contents (due to the reduced effect of the endothermic *reverse methanation reaction* ($CH_4 + H_2O \rightarrow CO + 3H_2$)). As the data reported confirm, higher operating pressures help even higher concentrations of methane ($CH_4$) to be formed. These results are in agreement with the literature and highlight that low temperature and high pressure environments benefit the formation of methane ($CH_4$) and increase, significantly, the product gas calorific value. The main reaction that supports the methane ($CH_4$) formation is $C + 2H_2 \rightarrow CH_4$. This is an exothermic reaction, where the reaction rate is improved at lower temperatures.

Furthermore, as Figure 4.18b illustrates, the gasification temperatures remain at low levels in both the roof and the bottom of the reactor (Figure 4.7).

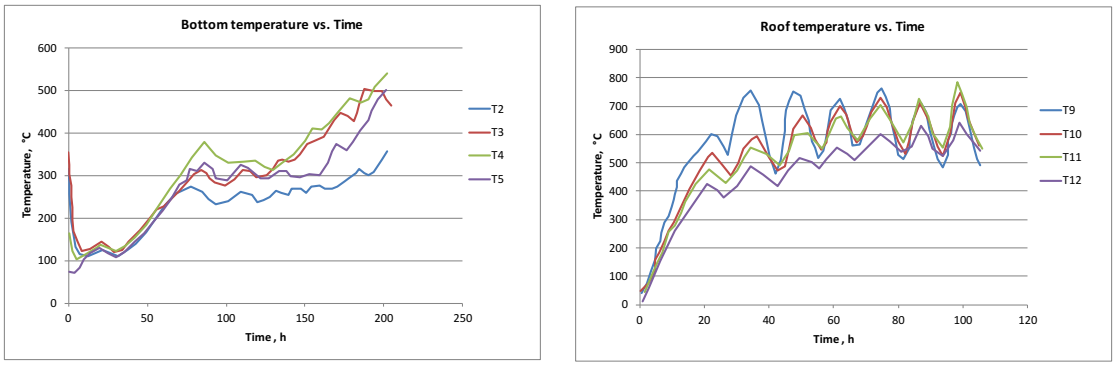


(a) (b)

**Figure 4.18:** Distribution of temperatures recorded in the roof and bottom level thermocouples during Murcki-Staszic 10 bar gasification experiment (Kapusta et al., 2017) .

It can be seen that the corresponding temperatures during the $O_2/CO_2$ experiment (Figure 4.14) at 10 bar are highly elevated compared to the temperatures reached during the hydrogasification experiment (Figure 4.18). As for hydrogasification, the targeted temperature region within the UCG cavity is found between $600^0$C and $700^0$C.

The numerical model developed was used to carry out a number of sensitivity analysis, investigating the effects of gasification temperature, pressure and reagent composition on the product gas quality and its corresponding heating value. These results are presented in Figure 4.19 to Figure 4.21.

As Figure 4.19 illustrates, a range of gasification temperatures has been cross-checked ($500^0$C - $800^0$C) against the product gas compositions yielded at each gasification temperature.

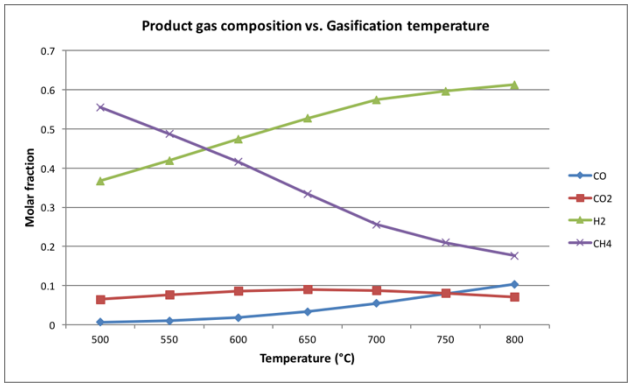


(a)

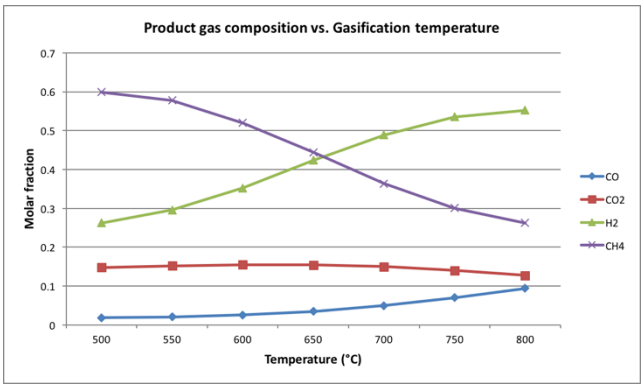


(b)

**Figure 4.19:** Sensitivity analysis for the hydro-gasification bituminous coal experiment - Distribution of the product gas molar composition during increasing gasification temperatures at (a) 10 bar and (b) 40 bar operating pressures.

As Figure 4.19 illustrates, higher gasification temperatures increase the hydrogen ($H_2$) formation in the product gas. This effect can be explained due to the increased influence of the endothermic *reverse methanation reaction* ($CH_4 + H_2O \rightarrow CO + 3H_2$) which is favoured by the higher temperatures. In addition, the reduced effect of the exothermic *methanation reaction* which is ($C + 2H_2 \rightarrow CH_4$) prevents the conversion of hydrogen ($H_2$) to methane ($CH_4$). Also, the reduced conversion rate of the endothermic *Boudouard reaction* ($C + CO_2 \rightarrow 2CO$) is also observed with the slight increase of the carbon monoxide (CO) and the corresponding decrease of the carbon dioxide ($CO_2$) above the $750^0$C.

Furthermore, as Figure 4.20 presents higher pressure (40 bar vs. 10 bar) consistently leads to product gases with higher heating values across the whole range of gasification temperatures. Moreover, as Figure 4.19 points out, increasing gasification temperatures result in decreasing methane ($CH_4$) concentrations in the product gas. This decreasing trend of the methane ($CH_4$) content is predominantly responsible for the also decreasing heating value of the product gas as the gasification temperature increases. The decreasing methane ($CH_4$) content is gradually converted to hydrogen ($H_2$) as the gasification temperature increases (*reverse methanation reaction* $CH_4 + H_2O \rightarrow CO + 3H_2$) while the positive correlation between the methane ($CH_4$) content and the heating value can be understood through the equation $CO: 0.85\ H_2: 2.85\ CH_4$, (Perkins, 2005; Littlewood, 1977) initially presented in Chapter 2.1.3.

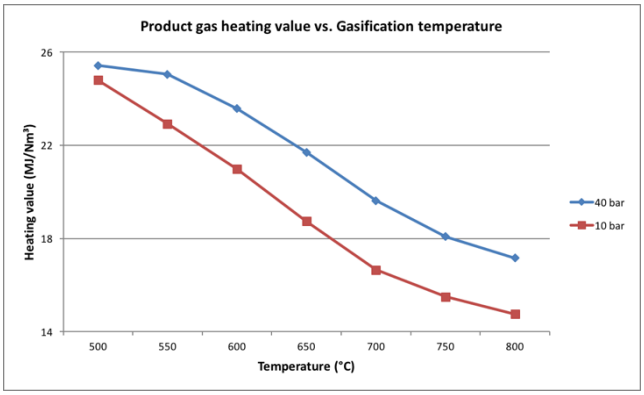


**Figure 4.20:** Sensitivity analysis for the hydro-gasification bituminous coal experiment - Distribution of the product gas heating values at 40 bar and 10 bar operating pressures during increasing gasification temperatures.

As Figure 4.21a-b show, higher $O_2/H_2$ feed ratios lead to lower hydrogen ($H_2$) contents in the product gas. In addition, higher ratios lead to higher carbon dioxide ($CO_2$) as the abundance of oxygen ($O_2$) increases the reaction rate of the heterogeneous char combustion reaction ($C + O_2 \rightarrow CO_2$). Furthermore, it is interesting to highlight that the methane ($CH_4$) contents of the product gases at both 10 and 40 bar pressures achieve their highest values at $O_2/H_2$ ratio equal to 0.6/0.4. This observation demonstrates that the hydrogen content ($H_2$) within the injected re-agent can have a positive impact on methane ($CH_4$) formation (and subsequently to the corresponding gas heating value) if it exists at moderate levels. Furthermore, a cross-comparison between Figure 4.21a and Figure 4.21b indicates a similar trend of the molar compositions at increasing $O_2/H_2$ feeding ratios although a more prompt effect is rather evident at higher pressure.

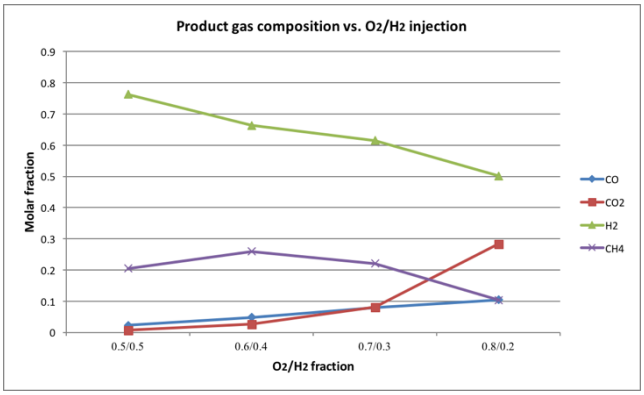


(a)

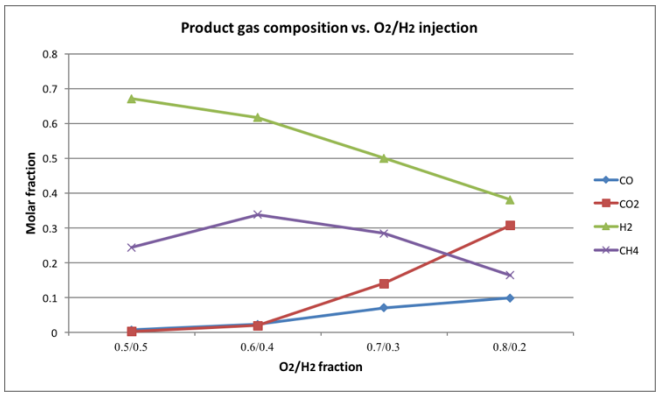


(b)

**Figure 4.21:** Sensitivity analysis for the hydro-gasification bituminous coal experiment - Distribution of product gas molar composition for different $O_2/H_2$ feed ratios at (a) 10 bar (b) 40 bar operating pressures.

## 4.6 *Conclusions*

During the $O_2/CO_2$ blown experiments, the maximum coal consumption rate, power output and energy efficiency were obtained during the oxygen-blown gasification stage. Due to unfavourable thermodynamic conditions (elevated pressure and decrease in temperature), all process performance parameters were significantly smaller for the $O_2/CO_2$ gasification stage. The phenomenon of carbon dioxide ($CO_2$) by-passing the reaction zone and collected in the product gas was also observed. In addition, the lack of steam ($H_2O$) injection affected the hydrogen ($H_2$) content of the product gas leaving the only source of steam to be the moisture content of coal that remained in the gasifier after the drying stage. This effect was more evident during the bituminous coal experiment compared to the lignite case whose higher moisture content offset that effect. Hence, one of the most relevant conclusions that can be drawn from the studies carried out is that UCG using solely recirculation of carbon dioxide ($CO_2$) may not be feasible in locations where elevated gasification pressure is necessary due to operational and environmental constraints, i.e. deep coal seams with a relatively high hydrostatic pressure of the test site aquifer.

A cross-comparison between the bituminous coal and lignite gasification experimental and modelling results displayed the lower gasification temperatures consistently developed during the lignite experiments. This observation has driven differences on both the carbon conversion rates and the product gases compositions. As the experimental data confirmed, hydrogasification experiments with bituminous coal resulted in much higher methane ($CH_4$) yields. Average methane ($CH_4$) concentrations during the bituminous coal experiments were: 21.1%vol and 29.2%vol at 10 and 40 bar respectively, so the effect of gasification pressure on the methane ($CH_4$) yields was clear. Changes in the gas calorific value during the bituminous coal hydrogasification experiments indicate that the process was stable and conditions conducive for the methane formation were reproducible in each hydrogen stage. Hydrogasification tests with lignite were discarded, as they resulted in very low methane efficiencies and the process was not stable with poor thermodynamic conditions for methane ($CH_4$) formation.

# Chapter 5 Coupled Thermo-Mechanical-Chemical (TMC) Model – Methodology

## 5.1 *Introduction*

This chapter aims to present the details of the methodology of the coupled Thermo-Mechanical-Chemical (TMC) process developed as part of the current PhD work for modelling UCG cavity growth. The coupled TMC model consists of three interacting modules: a) *the Aspen Plus module* b) *the FLAC$^{3D}$ module* c) and the *Gasification Support module*. Each module has a number of tasks to accomplish by accepting input data from the remaining two modules as well as providing updated input data to these modules. Besides the coupling of two commercial models, the gasification support module developed by the author acts as the interface between the two software environments. The Advanced System for Process ENgineering (Aspen) Plus software, a standard tool for the simulation of complex processes in the chemical industry, is used for the thermo-chemical simulation of coal gasification. On the other hand, the FLAC$^{3D}$ software tool, which is a numerical modelling tool for conducting advanced geomechanical analysis encountered in geotechnical engineering applications (FLAC$^{3D}$-Itasca, 2012), is used for the thermo-mechanical simulation of the UCG process. The coupling of the two simulation tools is achieved through sequential interchange of data. Figure 5.1 illustrates the coupling process between the two simulators schematically.

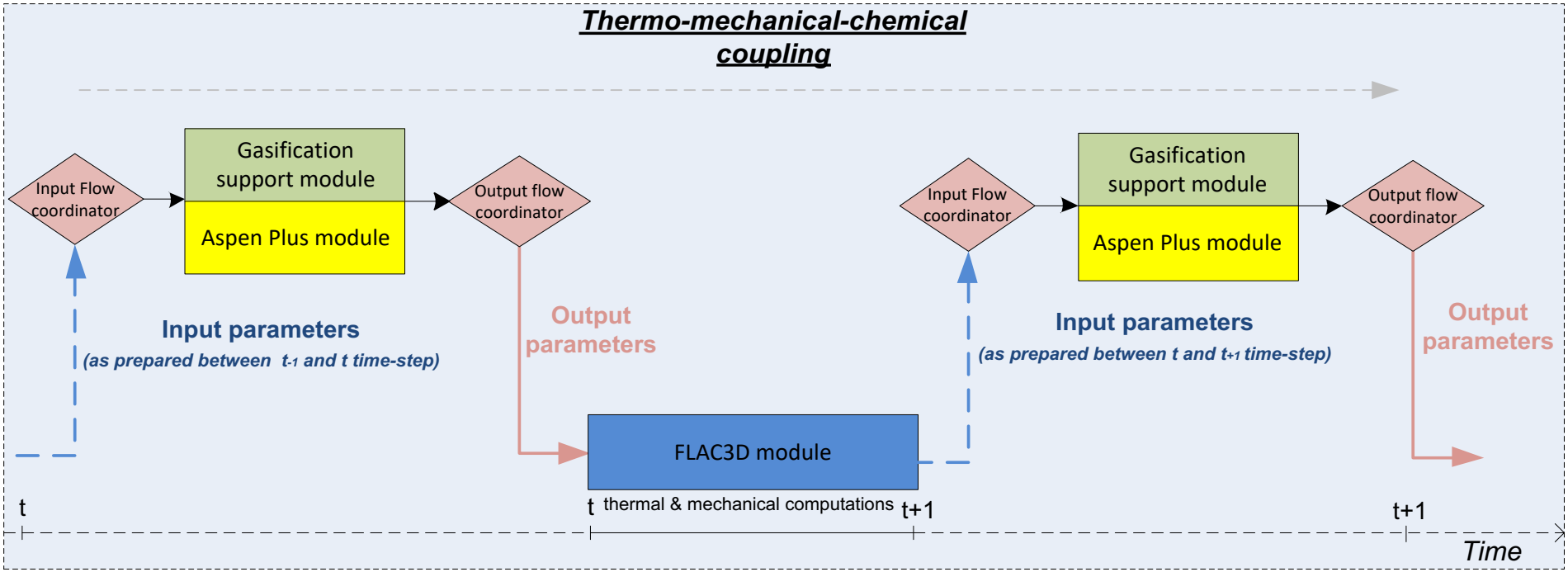


**Figure 5.1:** Overview of the modelling framework depicting the coupling process between the Aspen Plus and the FLAC$^{3D}$ software tools.

However, the operational concept on which each module relies upon is quite different when it is cross-compared. The exchanged parameters among the different modules are discussed in detail always in combination with the underlying assumptions. The aim of the coupled study is to consider the complexity of the developed Thermo-Mechanical-Chemical (TMC) process model as well as to analyse how this coupled scheme is necessary for realistic UCG simulation efforts. Targeted parameters through the TMC process model are the UCG cavity growth rate, the gasification temperatures and the quality of the generated syngas.

The ultimate purpose of this chapter is to facilitate and equip the reader with the necessary understanding regarding the results that should be expected from each module. This understanding will form the backbone of the conclusions and will help analysing the advantages and limitations of the developed coupled UCG process.

The Chapter is organised in four sections. Sections 5.2-5.4 focus on describing every operational element of the three participating modules. Section 5.5 addresses how the three coupled modules interact with each other.

## 5.2 *Thermo-Chemical modelling of UCG: The Aspen Plus module*

The geometry of the Continuous Retracting Injection Point (CRIP) subsurface layout used for UCG (Figure 5.2) is utilised to design the thermo-chemical process modelling framework in the Aspen Plus simulation environment (Figure 5.3).

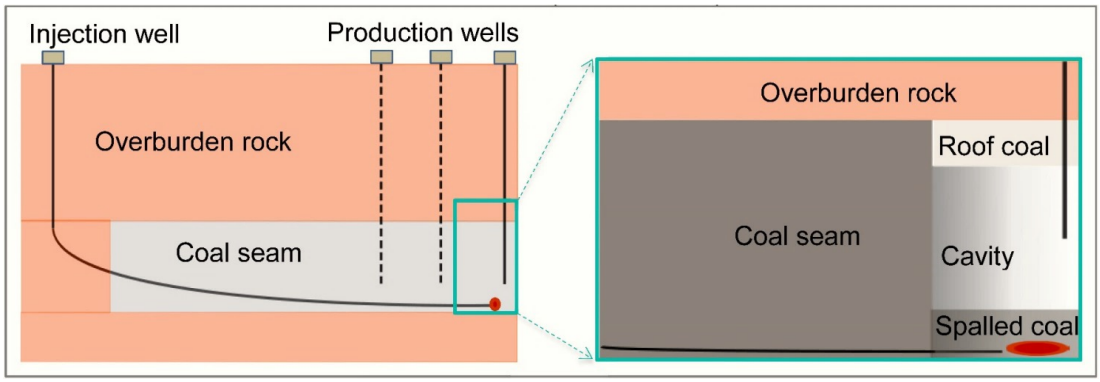


**Figure 5.2:** The subsurface gasifier layout used in the continuous retracting injection point (CRIP) UCG method

Although the principles of the CRIP UCG methodology have been in detail discussed in Section 3.3.2, Figure 5.2 helps to further understand how this UCG layout can be replicated in the Aspen Plus simulation environment. It offers a qualitative overview of how the bottom of the cavity, where combustion takes place, is separated from the roof layer through the growing cavity between them. As described by previous researchers (Britten and Thorsness, 1989; Perkins and Sahajwalla, 2008) and experimentally validated by Daggupati et al. (2011b), both spalled coal and char coming from the coal that has already gone through gasification at the cavity surface are collected at the bottom of the developing cavity.

As Daggupati et al. (2011a, 2011b) highlighted, the spalling phenomenon, which consists of the detachment of ungasified coal blocks from the roof of the growing cavity, depends on both the coal composition and other parameters such the depth and the temperature gradient within the coal body. However, it was also highlighted that high ash content coals are more probable to develop spalling behaviour compared to those with a lower ash content. A possible reason for this distinction among coal ranks based on their ash content is linked with the thickness of the ash layer that can be developed on the surface of the gasified roof. As this ash layer becomes thicker, the roof surface gasification is delayed while the temperature of the dried coal gradually increases. At some stage, a fraction of coal detaches from the rest of the roof and collapses to the bottom of the developing cavity. To add to this phenomenon, the heterogeneity of coal is an additional factor, especially as water influx takes place within the growing cavity as $H_2O$ changes the density and the uniformity of properties within the dried coal (Daggupati et al., 2011b).

As a result, the need for a thermo-chemical model which should have the ability to take into account how coal is gasified during UCG cavity growth under heterogeneous coal conditions (as opposed to globally uniform conditions) is essential. Additionally, it is further challenging to couple this detailed simulation of the UCG thermo-chemical process with the thermo-mechanical and fluid flow processes that takes place simultaneously.

The Aspen Plus model simulates the chemical processes taking place in the coal seam and focuses on the thermodynamic, mass and heat transfer modelling components in order to calculate the amount of produced gas under restricted Gibbs minimisation and equilibrium conditions. Similar to the Aspen Plus process model described in Chapter 4 simulating the LVW subsurface layout (Figure 4.5) used in representing the laboratory UCG reactor experiments, the corresponding process model simulating the CRIP UCG layout (Figure 5.3) is structured based on the same operating principles. Specifically, the developed Aspen Plus process configuration represents a zero-dimensional model under steady-state conditions. Pressure balance exists across the process and, although there is heat transfer between the UCG stages (e.g. between drying and pyrolysis stage), each UCG stage preserves the same temperature (isothermal). Furthermore, ash content is considered inert and all the three stream classes (Table 4.4) available in the Aspen Plus simulation environment are used in the model.

The chemical reactors that constitute the drying (R-Stoic reactor) and pyrolysis (R-Yield reactor) stages of the Aspen Plus model include calculator blocks written in Fortran code in order to regulate the model performance. However, these two initial UCG stages are not identically the same for the LVW and CRIP subsurface layouts (Figure 4.5). In the LVW layout, the necessary heat addition for the endothermic reactions of these two stages was being supplied by both the heat stream originating from the combustion stage, and through the flow of combustion and gasification product gases towards the production well. On the other hand, in the CRIP layout (Figure 5.3), the product gas stream flows towards the production well without coming in direct contact with the dried coal.

Nevertheless, in both subsurface layouts (i.e. LVW - Figure 4.3 and CRIP - Figure 5.2), their corresponding Aspen Plus process models (LVW - Figure 4.5, CRIP - Figure 5.3) aim to reduce the moisture content of the coal in the drying stage, while the pyrolysis stage discretises the coal to its volatiles facilitating the subsequent gasification stages.

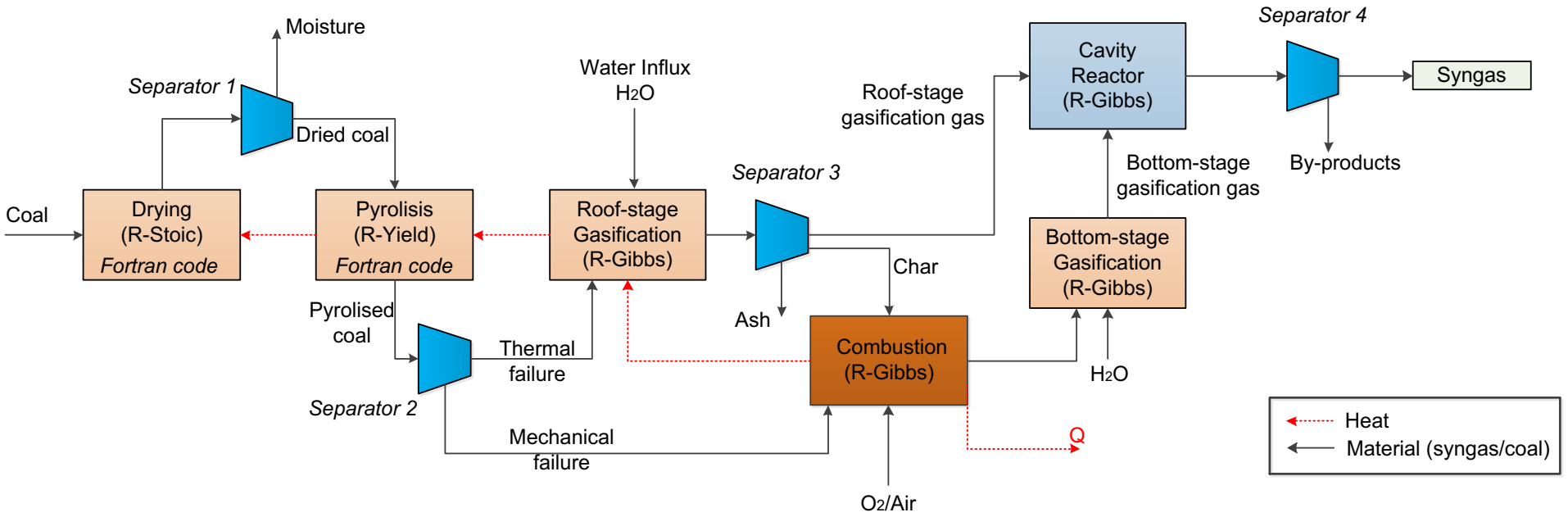


**Figure 5.3:** The Aspen Plus chemical process model developed for the simulation of CRIP subsurface layout.

Therefore, the Aspen Plus process model (Figure 5.3) incorporates two different stages of gasification, as well as a combustion stage inside the UCG cavity. Based on the temperature and stress distributions calculated in FLAC$^{3D}$ on the coal seam surrounding the developing cavity, the model assigns a fraction of the pyrolised coal to the roof-stage gasification process and, the remainder, which is calculated as spalled coal due to thermo-mechanically induced stresses, is assigned to the bottom combustion stage.

The "Separator 2" (Figure 5.3) performs this classification. The total mass of coal together with the ratio of the roof-gasified to spalled coal is passed on to Aspen Plus. The thermal failure stream represents the coal fraction that is gasified at the roof of the cavity.

On the other hand, the mechanical failure stream represents the mass of coal that spalls and is directly combusted at the bottom of the cavity. This also is the distinct difference between the two streams; the thermal failure coal stream is gasified while still at the roof of the cavity and only the remaining char (if there is any) is assumed to drop to the bottom where the combustion stage exists. The mechanical failure coal stream assumes that dried coal blocks are directly fed to the combustion stage after detaching from the roof, without being (partially) gasified first.

Furthermore, apart from the combustion stage where the reagent ($O_2$/air) injection takes place, gasification also occurs at the bottom of the cavity. As a result, the location of each gasification stage within the reactor is the first and principle difference among them. This location difference implies further disparities among the gasification stages related to:

- *Temperature.* The bottom-stage gasification is located closer to the combustion stage (at the bottom of the reactor) where higher temperatures are developed compared to the corresponding roof-stage gasification. By taking into account, the steady pressure conditions during the simulation process, the temperature differentiation leads to considerably different results regarding the efficiency in the carbon conversion process and the composition of the product gases coming from the two different sources.

- *$H_2O$ concentration.* The $H_2O$ concentration is highly influenced by the location of the gasification stage within the reactor. As literature (Gregg and Edgar, 1978) and in-situ experimental studies (Wiatowski et al., 2012) have highlighted, although steam presence might be beneficial (due to the fact that it increases the heating value of the product gas) its injection may not be necessary during the UCG process due to the water influx into the UCG cavity from the surrounding strata. As a result, the roof-stage gasification, which takes place at the borders of the growing cavity, is expected to be exposed to higher $H_2O$ concentrations than the corresponding bottom stage. Although extensive water influx can have a detrimental effect on the energy efficiency and can even terminate the UCG process, the current research assumes that $H_2O$ to coal ratio is close to 2:3, which is in line with the laboratory experimental observations (Daggupati et al., 2010) and previous UCG field trials (Wiatowski et al., 2012).

- *Carbon (C) content.* The bottom-stage gasification follows the combustion stage and, as a result, its carbon (C) concentration is expected to remain at low levels as most of the carbon content is expected to be consumed in the prior combustion stage. However, this is not the case for the roof-stage gasification, where devolatilised coal – including (C) carbon – participates in that stage. This parameter affects the ratio between the homogeneous and heterogeneous reactions taking place at each gasification stage.

Both the roof and bottom stage gasification product gases are mixed and react in the cavity-reactor (Figure 5.3) stage. This stage aims to replicate and provide an insight into the homogeneous gas reactions that take place as the product gas is accommodated in the developed cavity. This is assumed to be the last stage before the final product gas is collected through the production well.

The cavity reactor stage (Figure 5.3) helps understanding the temperature conditions and the product gas composition within the growing cavity. Both these parameters are fed into the gasification support module as they are important to understand the fluid flow phenomena that take place within the growing cavity.

In addition, as it can be seen in Figure 5.3, the heat flow (Q) that leaves the combustion stage represents the heat flux that is radiated to the surrounding surface of the cavity. This heat flux is provided as input to the FLAC$^{3D}$ module. An overview of the exchanged parameters between the Aspen Plus process model and the other two modules (i.e. FLAC$^{3D}$ module and the Gasification support module) is presented in Table 5.1 - Table 5.2.

Table 5.1 details the input parameters that are provided to the Aspen Plus model together with the module that offers that input. The first two parameters of Table 5.1 come directly from the FLAC$^{3D}$ module, while the remaining four (although originally sourced at some form from the FLAC$^{3D}$ module) reach the Aspen Plus module through further calculations within the gasification support module.

**Table 5.1**: Presentation of the input parameters provided to the Aspen Plus module.

| Sourced from | Parameter Identity | Unit |
|---|---|---|
| FLAC$^{3D}$ module | Roof-stage gasification temperature | $^{o}$C |
| FLAC$^{3D}$ module | Bottom-stage gasification temperature | $^{o}$C |
| Gasification support module | Ratio of roof-gasified to spalled coal | ~ |
| Gasification support module | Total mass of coal | kg/hr |
| Gasification support module | Mass of gasification reagent ($O_2$/air) injected | kg/hr |
| Gasification support module | Mass of water ($H_2O$) influx | kg/hr |

The *total mass of coal* is fed at the drying stage of the Aspen Plus process model (Figure 5.3) while the *ratio of roof-gasified to spalled coal* is passed to the "Separator 2" located after the pyrolysis stage. Furthermore, the *mass of the injected gasification reagents ($O_2$/air)* as well as the *mass of water ($H_2O$) influx* into the growing cavity are calculated within the gasification support module and are subsequently offered to the Aspen Plus module.

**Table 5.2**: Description of the output parameters from the Aspen Plus module

| Parameter Identity | Provided to | Unit |
|---|---|---|
| Product gas composition | Gasification support module | Mole fraction |
| Cavity reactor temperature | Gasification support module | $^{o}$C |
| Radiative heat flux | FLAC$^{3D}$ module | W (Watts) |

Table 5.2 presents the parameters that are calculated within the Aspen Plus module and provided as inputs to the other two modules. The first two parameters are offered as input to the gasification support module.

The *product gas composition* and the *cavity reactor temperature* are necessary components for the convective heat transfer calculations. In addition, the *radiative heat flux*, which is diffused from the high temperature combustion stage, is offered to the FLAC$^{3D}$ module.

### 5.2.1 An example run for the presentation of Aspen Plus module results

The purpose of this section is to clarify the questions that may arise from the complex structure of the Aspen Plus module. In this section, an example run is provided together with its input and output variables. Table 5.3 presents the proximate and ultimate analysis of coal used as input to the model presented in Figure 5.3.

**Table 5.3**: Proximate and ultimate analysis of the Velenje lignite (Zavsek et al., 2015).

| *Proximate analysis (% w/w, dry basis)* | Velenje Lignite |
|---|---|
| Fixed carbon | 29.71 |
| Volatile material | 64.43 |
| Ash | 5.86 |
| *Ultimate analysis (% w/w, dry basis)* | |
| Carbon | 56.10 |
| Hydrogen | 5.25 |
| Nitrogen | 0.72 |
| Sulphur | 0.74 |
| Ash | 5.86 |
| Oxygen | 31.33 |
| High Heating Value (dry basis, MJ/kg) | 19.73 |
| Moisture (% w/w) | 31.00 |

The roof and bottom stage gasification temperatures (Figure 5.3), as explained in Table 5.1, are provided to the Aspen Plus module by the FLAC$^{3D}$ module. Figure 5.4 presents the corresponding temperatures during the UCG simulation for the Velenje lignite (Table 5.3) where the simulation assumes that the bottom of the coal seam lies at 400m depth and an operating pressure of 40 bar is used.

As the CRIP process involves the retraction of the injector, the results are also classified as to whether this has taken place or not.

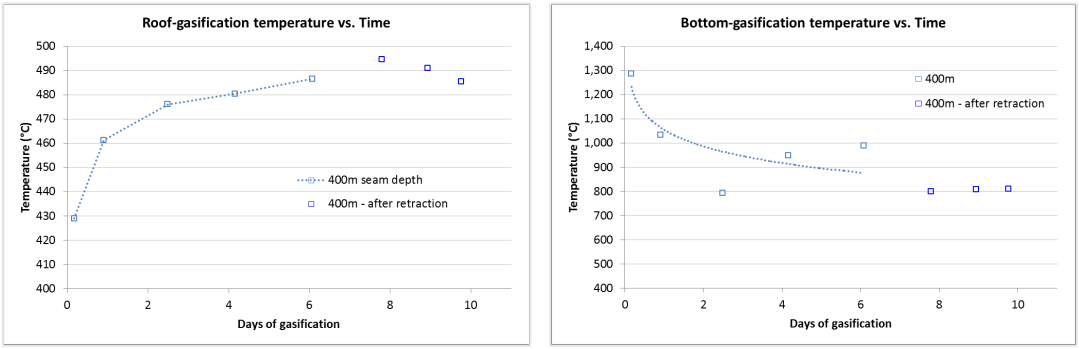


(a) (b)

**Figure 5.4:** The temperatures for (a) the roof and (b) bottom gasification stages during the UCG simulation of the Velenje lignite at 400m depth and 40 bar gasification pressure.

In addition, the composition and the heating value of the product gas are presented in Figure 5.5. Both output parameters are generated through the Aspen Plus module and Figure 5.5 presents their variation with time.

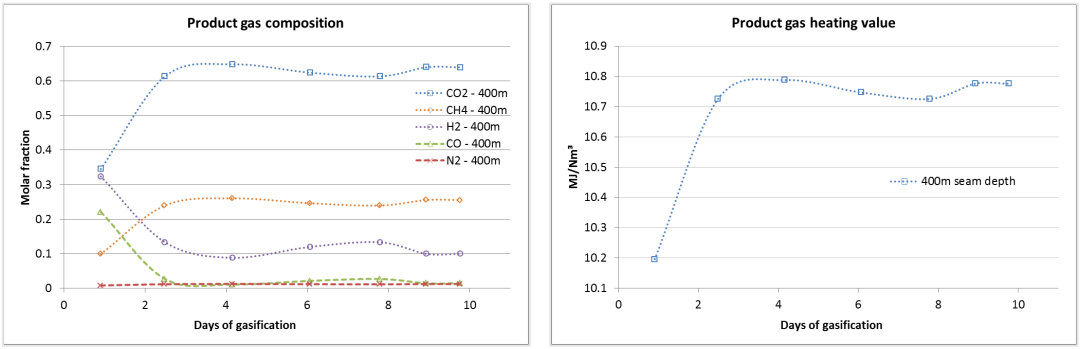


(a) (b)

**Figure 5.5:** The product gas (a) composition and (b) heating value during the UCG simulation of the Velenje lignite at 400m depth and 40 bar gasification pressure.

As the UCG CRIP layout is simulated in this example, the stage when the retraction of the oxidant injection point takes place has also been taken into account as this has an impact on the corresponding temperatures (Figure 5.4).

## 5.3 *Thermo-Mechanical modelling of UCG: The FLAC$^{3D}$ module*

The FLAC$^{3D}$ module is designed to reflect realistically the 3D spatial features of an underground coal seam. The thermo-mechanical modelling procedure involves a number of sequential processes/functions. In particular, eight consecutive functions containing several sub-functions were written in the FISH language supported by the FLAC$^{3D}$ simulation environment.

Figure 5.6 depicts an operational diagram illustrating the tasks taking place within the FLAC$^{3D}$ module. The FLAC$^{3D}$ module has eight principle functions which will be discussed in detail later in this Section. It can also be seen in Figure 5.6 that there are certain tasks which are performed only once and exist outside the developed loop. The loop consists of functions which are executed multiple times periodically within every TMC scenario. When the loop starts again, one step of the simulated TMC scenario is completed. Each of the TMC scenarios discussed under this study requires 9 to 10 steps in order to be completed.

The three FLAC$^{3D}$ module functions associated with the tasks that are performed only once outside the loop are the following:

***Development and construction of the model domain***

This FLAC$^{3D}$ module function aims to construct the model domain. The model domain consists of different layers of rock with different properties assigned to each layer. It consists of consecutive blocks, however, the blocks within each layer do not have uniform size. As the task is to replicate a 3-dimensional coal seam, the size of each block need to be defined in all three dimensions (x,y,z).

Figure 5.7 presents the three-dimensional model domain within the FLAC$^{3D}$ module, with the base of the coal seam at 400m or 600m depth depending on the model scenario considered.

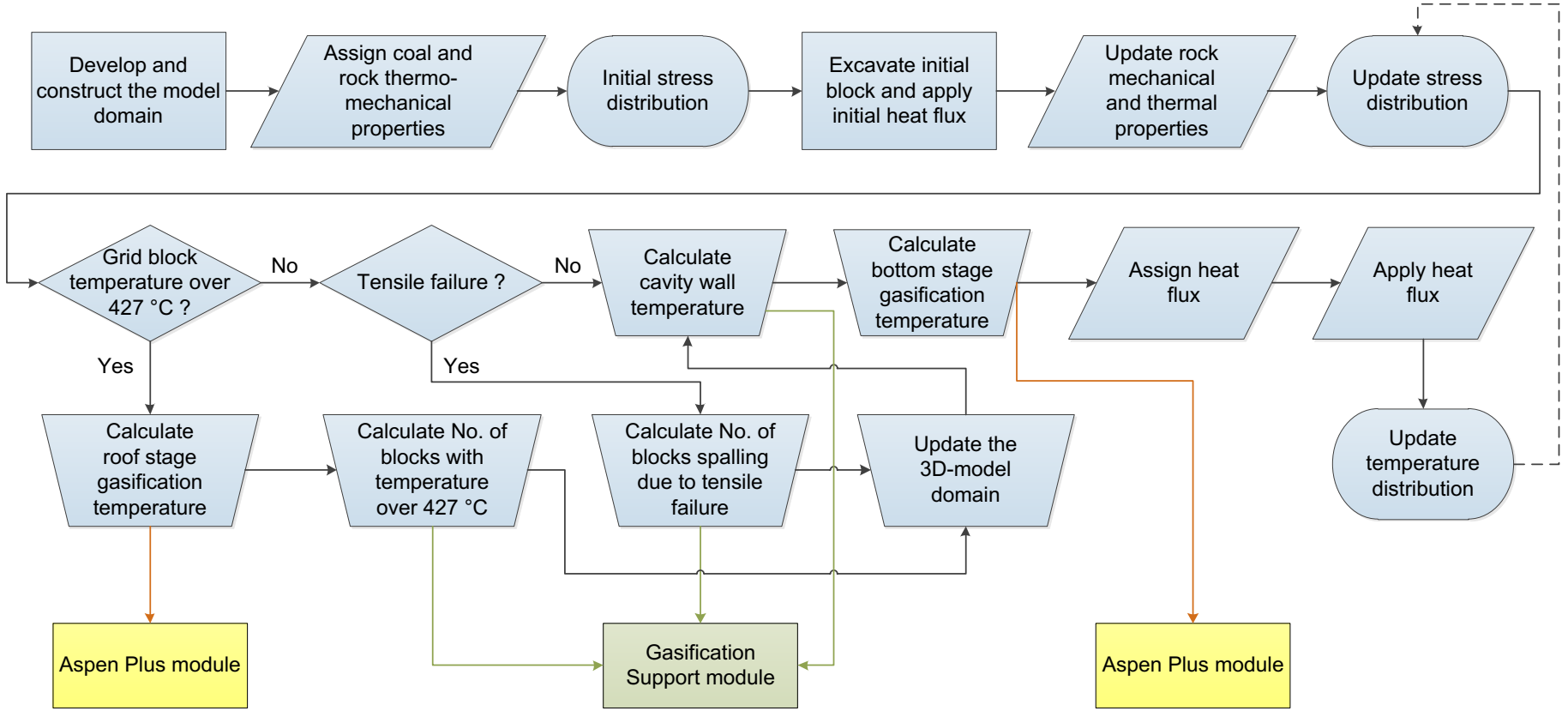


**Figure 5.6:** Schematic operational diagram of the FLAC$^{3D}$ module as part of the coupled Thermo-Mechanical-Chemical model

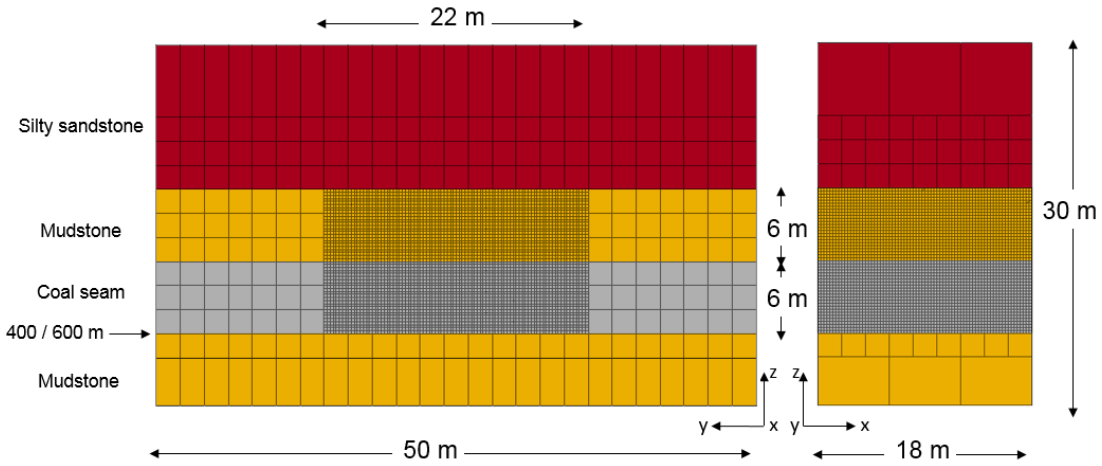


**Figure 5.7:** Vertical cross sections (y-z plane and x-z plane) representing the initial model domain developed within the FLAC$^{3D}$ module.

The coal seam is surrounded by 6m thick mudstone layers above and below, while the upper layer mudstone borders with 12m thick silty sandstone layer. The grid blocks that constitute each rock layer have a different size. Table 5.4 presents how block size are defined within each layer of the model domain, with some grid refinement implemented at data critical parts of the model.

**Table 5.4**: Classification of the different grid-block sizes according to the layers they belong

| Layer identity | Grid-block size (x,y,z) (m) |
|---|---|
| Silty sandstone | 6x2x6 |
| Silty sandstone (refined zone) | 2x2x2 |
| Mudstone above the coal seam | 2x2x2 |
| Mudstone above the coal seam (refined zone) | 0.25x0.25x0.25 |
| Coal seam | 2x2x2 |
| Coal seam (refined zone) | 0.25x0.25x0.25 |
| Mudstone below the coal seam (refined zone) | 2x2x2 |
| Mudstone below the coal seam | 6x2x4 |

The grid refinement within the coal seam was set at 0.25m x 0.25m x 0.25m, which provided the optimum combination of data accuracy and computational times. Furthermore, literature studies (Otto and Kempka, 2015; Nourozieh et al., 2010) that employed grid refinement techniques used similar grid sizes for their highly refined areas.

***Assigning initial thermo-mechanical properties and initial stress calculations***

This second FLAC$^{3D}$ module function builds on the model domain supplied by the first function. As the model grids are not uniformly refined and sized, the assignment of the corresponding thermo-mechanical properties is achieved by grouping the different type of layers.

The established groups are subsequently used for the assignment of the thermo-mechanical properties. The grid blocks within each of the established groups have the same initial thermo-mechanical properties. These groups are the following:

*a) silty sandstone.*
*b) mudstone.*
*c) coal seam*.

Table 5.5 offers an overview of the initial mechanical and elastic properties assigned through this function to the model domain. Especially, the Young's modulus (E) combined with the Poisson's ratio (ν) helps determine the calculation of the shear (G) and bulk moduli (K) assigned to the model.

**Table 5.5**: Average initial mechanical and elastic properties assigned to the different layers of 3D-domain in the FLAC$^{3D}$ module (Hettema, 1996; Tan et al., 2008).

| | Unit | Mudstone | Silty Sandstone | Coal (Bituminous) | Coal (Lignite) |
|---|---|---|---|---|---|
| *Mechanical Properties* | | | | | |
| Young's modulus (E) | GPa | 3.60 | 30 | 2.30 | 0.85 |
| Tensile strength ($\sigma_i$) | MPa | 1.8 | 4.8 | 1.3 | 0.86 |
| Friction angle ($\gamma$) | ° | 30 | 40 | 28 | 22 |
| Cohesion (c) | MPa | 5.20 | 18.68 | 4 | 2.90 |
| Poisson's ratio ($\nu$) | - | 0.35 | 0.2 | 0.34 | 0.42 |
| Density ($\rho$) | kg/m$^3$ | 2,530 | 2,540 | 1,342 | 1,390 |

As explained in Section 2.2.2, two of the elastic moduli are sufficient for the definition of the rest of the properties listed in the table. Shear modulus (G) is calculated using:

$$G = \frac{E}{2(1+v)} \tag{E5.1}$$

while bulk modulus through

$$K = \frac{E}{3(1-2v)} \tag{E5.2}.$$

Where $E$ represents the Young's modulus, $v$ represents the Poisson's ratio, $G$ represents the shear modulus and $K$ represents the bulk modulus.

Furthermore, this FLAC$^{3D}$ module function also defines the initial stress conditions applied at the top and the bottom boundaries. The current research work was carried out assuming that the vertical overburden stress ($\sigma_v$) is higher in magnitude compared to the principal horizontal stresses ($\sigma_{Hmax}$, $\sigma_{Hmin}$). The vertical stresses at the top and the bottom of the domain are calculated according to:

$$\sigma_v = \rho g z \tag{E5.3}$$

by considering a uniform layer with a density of 2,360 kg/m$^3$ for the overburden which lies at the top of the domain. Finally, the lateral stresses are calculated based on the vertical stresses according to:

$$\sigma_{H\max} = \sigma_{H\min} = \rho g z \frac{v}{1-v} \tag{E5.4}$$

The initial stress equilibrium is established before assigning the relevant thermal properties to different rock formations within the model domain. Stress equilibrium is assumed to be reached when the unbalanced forces are less than 1e-4 Pa. Table 5.6 presents the initial thermal properties assigned to the three rock formations. As presented in the table, the coal thermal properties are assumed to be the same for both coal ranks (lignite and bituminous), whereas their mechanical and elastic properties differ as presented in Table 5.5 before.

**Table 5.6**: Average initial thermal properties values assigned to the different layers of 3D-domain in the FLAC$^{3D}$ module (Eppelbaum et al., 2014; Gilliam and Morgan, 1987; Midttømme et al., 1998; Min, 1983; Robertson, 1988; Tan et al., 2008; Waples and Waples, 2004)

| Thermal properties | Unit | Mudstone | Silty Sandstone | Coal |
|---|---|---|---|---|
| Linear thermal expansion coefficient ($\alpha$) | °C$^{-1}$ | $0.873\times10^{-5}$ | $0.55\times10^{-5}$ | $0.65\times10^{-5}$ |
| Specific heat ($C_p$) | J/(kg °C) | 985 | 852 | 1066 |
| Thermal conductivity ($\lambda$) | W/(m °C) | 1.76 | 2.4 | 0.28 |

***Excavating initial block and applying initial heat flux***

This FLAC$^{3D}$ module function is responsible for the initial coal block excavation. The aim of this first excavation is to create adequate space within the coal seam for the initiation/ignition process. In the case of in situ UCG trials, this space is located at the start of the UCG cavity between the injection and the production wells. In the model simulations this space is assumed to be located at the bottom of the coal seam, centrally located within the model (y-direction), and 4m along the x-direction of the seam. The total excavated volume is 1m$^3$ (Figure 5.8).

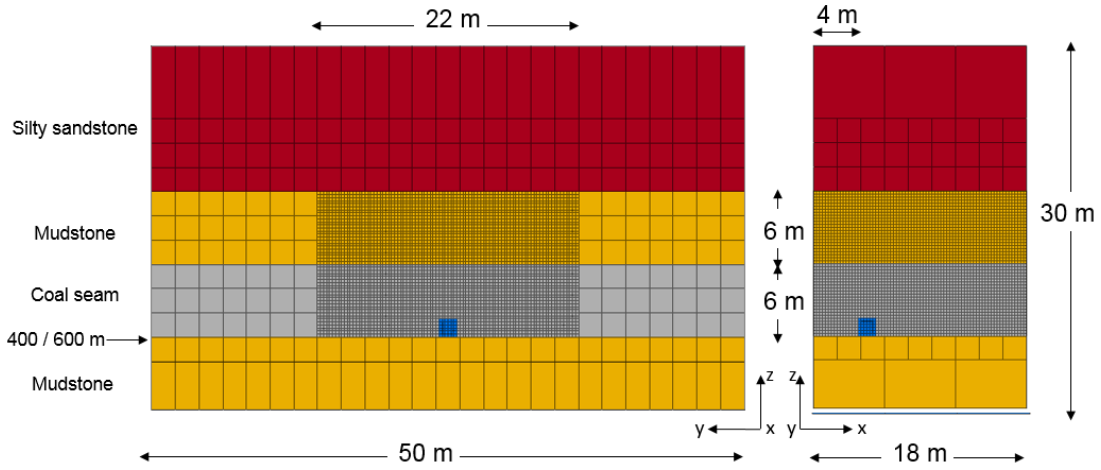


**Figure 5.8:** Vertical cross sections (y-z plane and x-z plane) locating the initial cavity developed within the model domain of the FLAC$^{3D}$ module.

The calculation for the initial heat flux, which will initiate the process it is also conducted within this function. For this reason, it is necessary to specify the surface boundaries between the excavated coal and the rest of the coal seam. These boundaries consist the surface where the initial heat flux ($W/m^2$) is assigned.

To specify the surface boundaries two loops were built in FISH language. The first loop groups the grid points of the blocks that exist around the excavated surface under a "label" name. As a result, this label name contains the grid points that consist the boundaries of that surface.

The second loop goes through all the grid points under that label and group the surfaces which these grid points form under a different "label". In that way, the new "label" name includes the surface area where the assignment of the initial heat flux should take place.

A heat flux of 5,333 $W/m^2$ is assigned to the initial surface boundaries. The aim of this initial heat flux is to develop approximately 400$^oC$ temperature in the surrounding structure (Stańczyk et al., 2011). For the development of this temperature, a combination of heat flux ($W/m^2$) and exposure time (s) is required. Therefore, the running-time clock is also set, which eventually allows FLAC$^{3D}$ simulator to combine the above two pieces of information and calculate the temperature profile of the surrounding structure. In the model runs, the running-time clock for the initial heat flux was set at 14,400 sec (~ 4 hours). The heat flux exposure time used in this research is in line with experimental ex-situ efforts, where the early stage initiation process lasted for either 1 hour (Stańczyk et al., 2012), 3 hours (Stańczyk et al., 2010) or 4 hours (Stańczyk et al., 2011).

Furthermore, this FLAC$^{3D}$ module function also prepares the updated domain structure for the next module functions. Specifically, as it will be further described within the *identifying failed coal blocks* function, the mechanical failure of a coal block is decided if it has gone through tensile failure as well as its exposed surface being in physical contact with the growing cavity. This means that the relevant surface boundary of the block needs to be "labelled" under a different name in order to specify the blocks that fulfil both the above mechanical failure criteria, compared to those blocks which do not.

For this reason, a complex loop was developed within the FLAC$^{3D}$ environment. The developed pointer loops through all the surface boundaries of the blocks neighbouring the growing cavity and identifies if a surface of the coal blocks in the model are in contact with the growing cavity. FLAC$^{3D}$ simulating environment facilitates this process as each of the 6 surfaces of a coal block is labelled with an identification number. As it can be seen in Figure 5.6, the FLAC$^{3D}$ functions already discussed so far prepare the model before activating the looping process, which starts with the *update of the rock mechanical and thermal properties* function. The operational diagram also presents the stages within every loop iteration where the remaining two modules (i.e. the Aspen and the Gasification support modules) are involved. It will be further detailed how the FLAC$^{3D}$ module interacts with the other two modules as the functions included in the loop stage are explicitly discussed.

***Update of rock mechanical and thermal properties.***

The *update rock mechanical and thermal properties* functions consist of the first phase within the loop stage of the FLAC$^{3D}$ module. It builds upon the previous functions that calculate the temperature profile of the domain. As a result, by knowing the average temperature at each grid point of every block, it is feasible to calculate an average temperature for that block. The temperature for every grid block is determined by averaging the temperature values of its 8 grid points. Once the temperature of every grid block has been identified, the function can fulfil its main purpose, which is to update their thermo-mechanical properties. The thermo-mechanical properties of every grid block depend on both the lithological group where it belongs and the temperature of that block. Further details on thermo-mechanical properties of rocks were discussed in Sections 2.2.3 - 2.2.4 of this thesis.

In the model, the thermo-mechanical properties for both the roof-rock materials and the coal are updated as a function of temperature through the use of regression models. These models were developed based on the literature data presented in Section 2.2.3 - 2.2.4. Specifically, Figure 2.6 - Figure 2.17 present literature data of how thermo-mechanical properties of rocks and coal change as a function of temperature. In this research, one concern was to increase the accuracy of the developed model without significantly increasing its already high computational runtime.

In order to change the thermo-mechanical properties of every block multiple loops were required. Specifically, three different loops, each accessing the grid blocks of each different lithological group were set up.

As every grid block is retrieved by a pointer – that is moving across all the grid blocks of one particular lithological group – the temperature of this block is entered in the relevant regression model. Furthermore, the new thermo-mechanical properties assigned to the grid blocks are determined by multiplying the initial value of the particular thermo-mechanical property (Table 5.5-5.6) with the relevant value taken from the regression models. The new value for the relevant thermo-mechanical property is also represented as the percentage difference multiplied by the initial value. Therefore, the vertical axes across all the middle graphs in Figure 5.9 - Figure 5.14 are in unit scale, representing the corresponding normalised change of the initial value of the thermo-mechanical property.

Table 5.7 presents how the thermo-mechanical properties change when temperature increases. The decisions are based on the available literature data (Sections 2.2.3 - 2.2.4) for each thermo-mechanical property as well as on how relevant literature studies (Hettema, 1996; Min, 1983; Otto and Kempka, 2015; Tian and Ziegler, 2013) addressed that issue. Specifically, the density (ρ) and the Poisson's ratio (v) remains stable as the temperature changes (Gercek, 2007; Somerton, 1975), while the other thermo-mechanical properties are updated as a function of temperature at this within every loop and iteration.

**Table 5.7:** Classification of roof/floor rock thermo-mechanical parameters into stable (×) and varying (✓) as a function of temperature.

| | Unit | Mudstone | Silty Sandstone |
|---|---|---|---|
| *Mechanical Parameters* | | | |
| Elastic modulus (E) | GPa | ✓ | ✓ |
| Tensile strength ($\sigma_i$) | MPa | ✓ | ✓ |
| Friction angle (γ) | ° | × | × |
| Cohesion (c) | MPa | × | × |
| *Thermal parameters* | | | |
| Linear thermal expansion coefficient (a) | $°C^{-1}$ | ✓ | ✓ |
| Specific heat ($C_p$) | J/(kg °C) | ✓ | ✓ |
| Thermal conductivity (λ) | W/(m °C) | ✓ | ✓ |

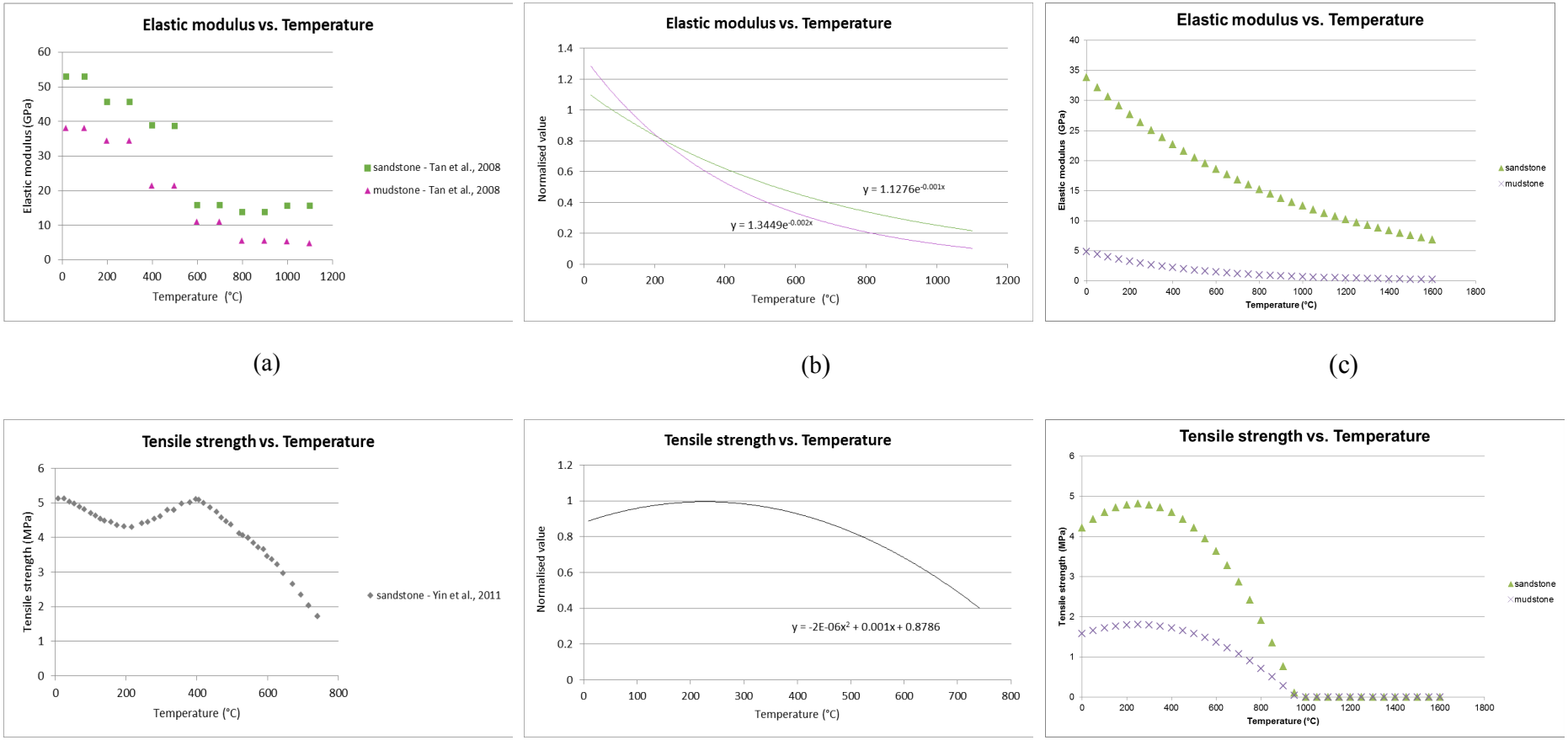


**Figure 5.9:** Variation of the elastic modulus and tensile strength of sandstone and mudstone as temperature increases (a) literature data; (b) normalised regression model; (c) variation within the FLAC$^{3D}$ module of the coupled Thermo-Mechanical-Chemical model.

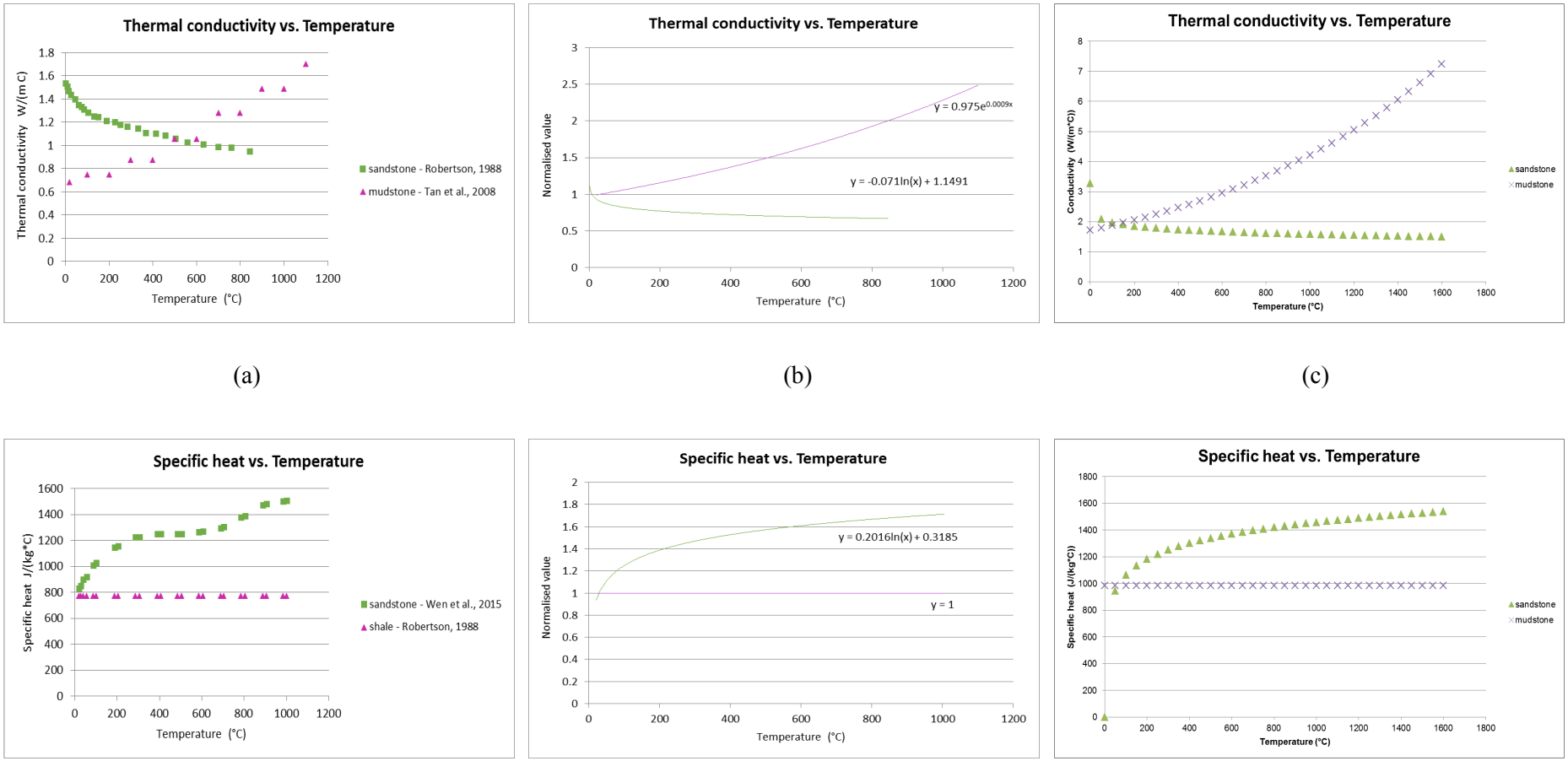


**Figure 5.10:** Variation of the thermal conductivity and specific heat of sandstone and mudstone as temperature increases (a) literature data; (b) normalised regression model; (c) variation within the FLAC$^{3D}$ module of the coupled Thermo-Mechanical-Chemical model.

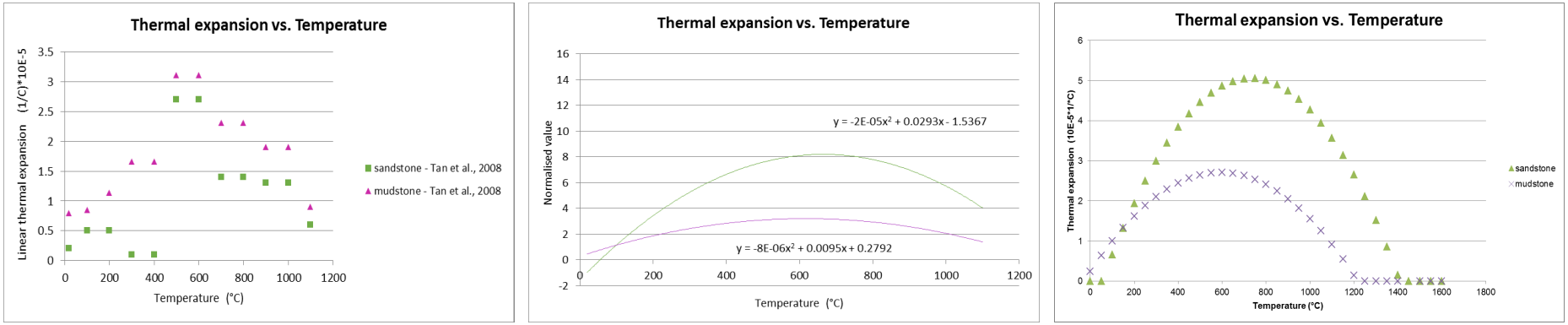


(a) (b) (c)

**Figure 5.11:** Variation of the thermal expansion coefficient for sandstone and mudstone as temperature increases (a) literature data; (b) normalised regression model; (c) variation within the FLAC$^{3D}$ module of the coupled Thermo-Mechanical-Chemical model.

Figure 5.9 - Figure 5.11 are organised in order to equip the reader with an overview of how the roof/floor rock (i.e. sandstone, mudstone) thermo-mechanical properties change as a function of temperature within the developed model. For each thermo-mechanical property, the left-hand side figure presents the literature data (as already presented in Section 2.2.3), the middle figure presents the regression model that was built based on the literature data, and the right-hand side figure shows how the initial roof/floor rock thermo-mechanical. The unsteady properties (Table 5.7 and Table 5.8) of the current model vary with temperature. It should be noted that the literature data (left-hand side figures) presented in this section highlight only the specific literature sources on which the regression models were based on. For this reason, the left-hand side graphs (Figure 5.9 - Figure 5.11) include only the relevant literature data for sandstone and mudstone.

Similar to Figure 5.9 - Figure 5.11, the following graphs (Figure 5.12 - Figure 5.14) present how the corresponding thermo-mechanical properties of coal vary with temperature. In both set of figures (Figure 5.9 - Figure 5.14), the middle charts include the mathematical equations that describe the formulated regression curves.

**Table 5.8**: Classification of coal thermo-mechanical parameters into stable (✗) and varying (✓) as temperature changes.

| | Unit | Coal |
|---|---|---|
| *Mechanical Parameters* | | |
| Elastic modulus (E) | GPa | ✓ |
| Tensile strength ($\sigma_i$) | MPa | ✓ |
| Friction angle (g) | ° | ✓ |
| Cohesion (c) | MPa | ✓ |
| *Thermal parameters* | | |
| Linear thermal expansion coefficient (a) | $°C^{-1}$ | ✓ |
| Specific heat ($C_p$) | J/(kg °C) | ✓ |
| Thermal conductivity ($\lambda$) | W/(m °C) | ✓ |

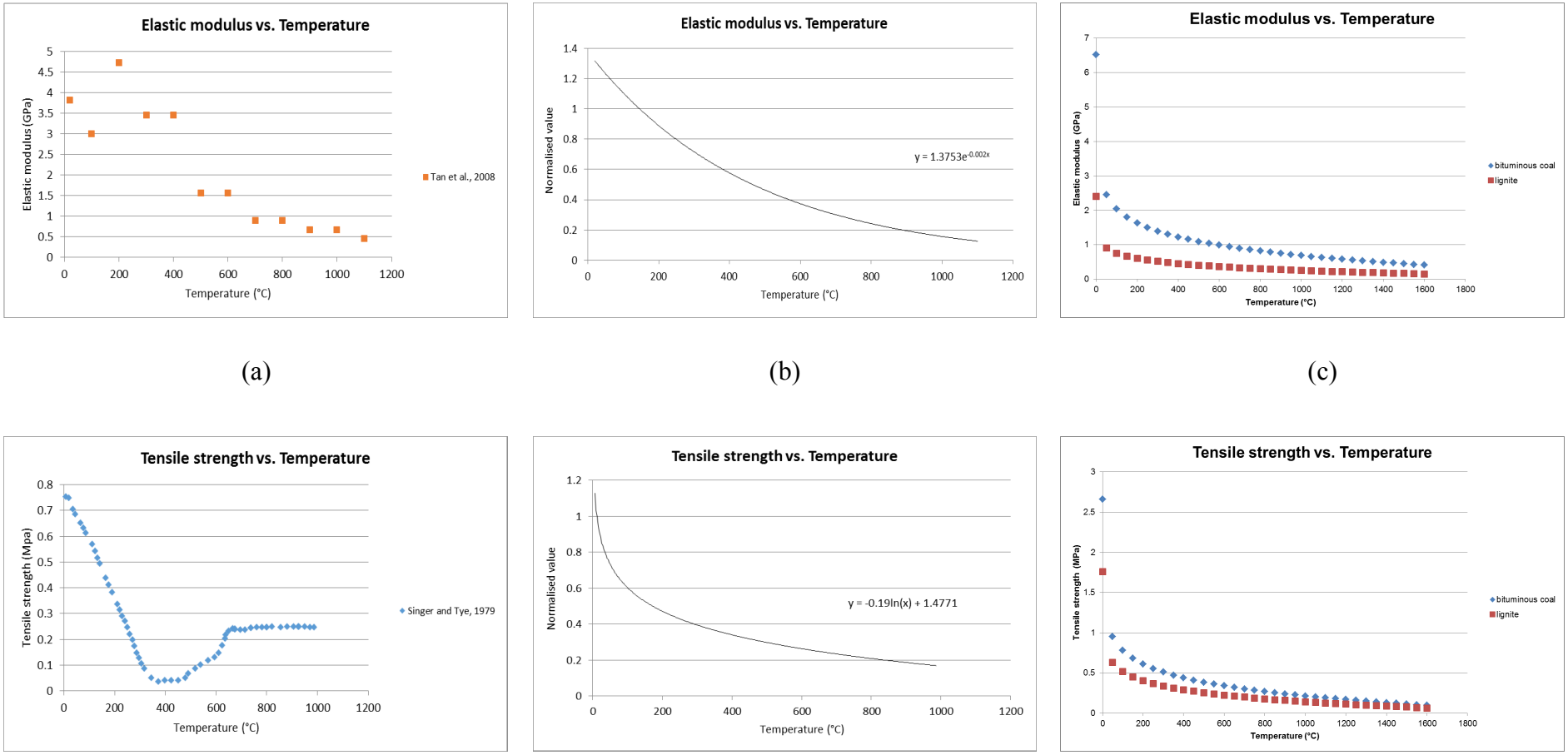


**Figure 5.12:** Variation of the elastic modulus and tensile strength of coal as temperature increases (a) literature data; (b) normalised regression model; (c) variation within the FLAC$^{3D}$ module of the coupled Thermo-Mechanical-Chemical model.

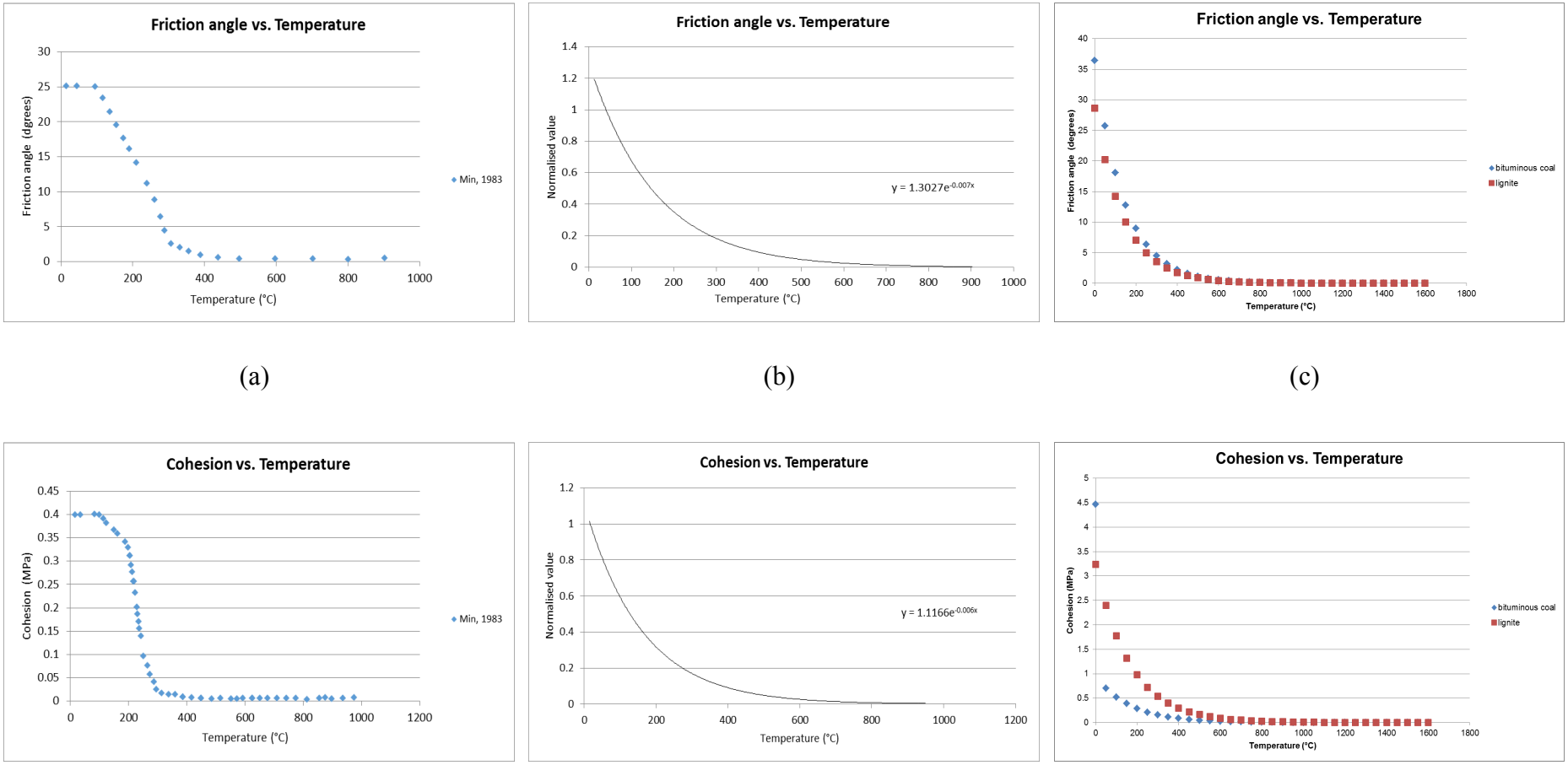


**Figure 5.13:** Variation of the friction angle and cohesion of coal as temperature increases (a) literature data; (b) normalised regression model; (c) variation within the FLAC$^{3D}$ module of the coupled Thermo-Mechanical-Chemical model.

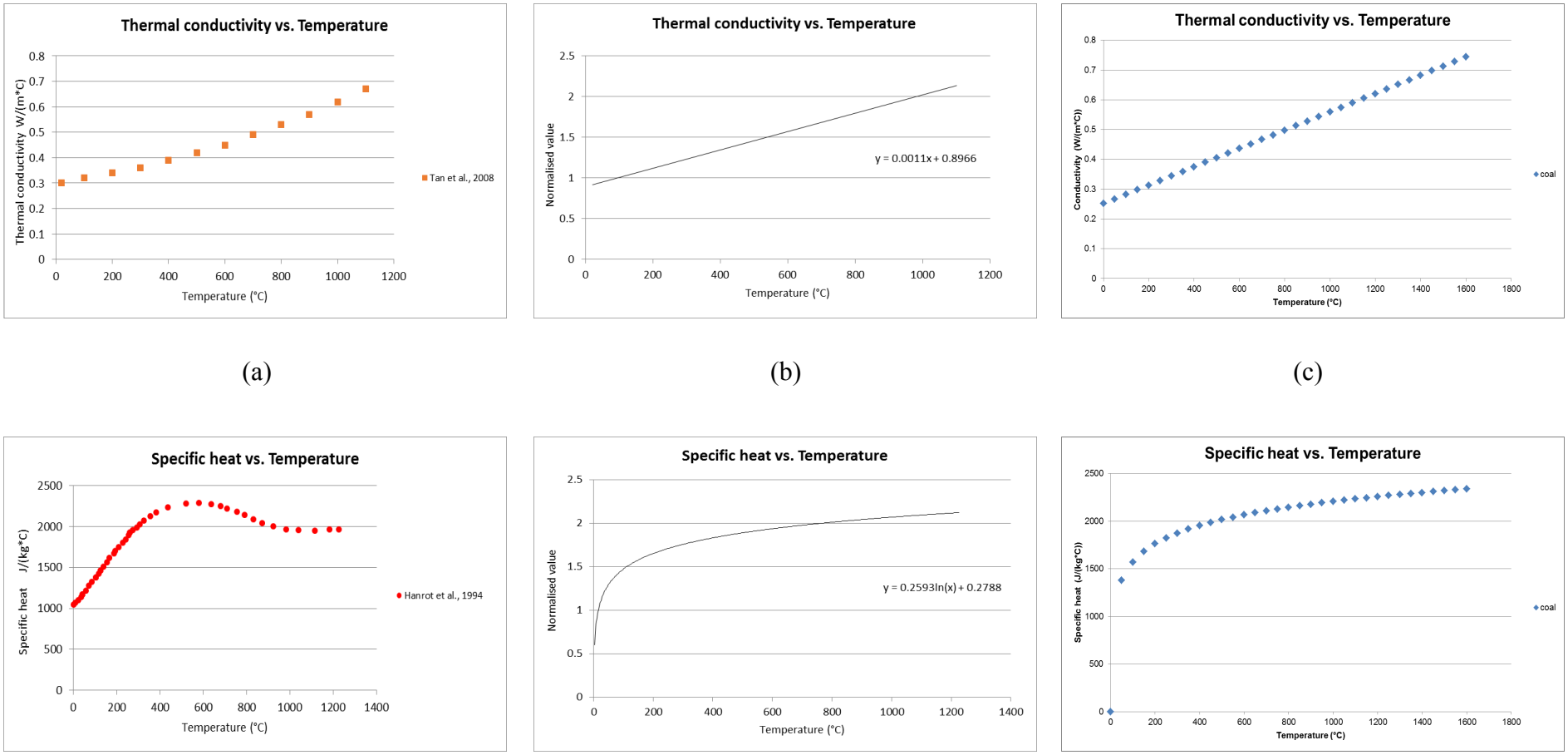


**Figure 5.14:** Variation of the thermal conductivity and specific heat capacity of coal as temperature increases (a) literature data; (b) normalised regression model; (c) variation within the FLAC$^{3D}$ module of the coupled Thermo-Mechanical-Chemical model.

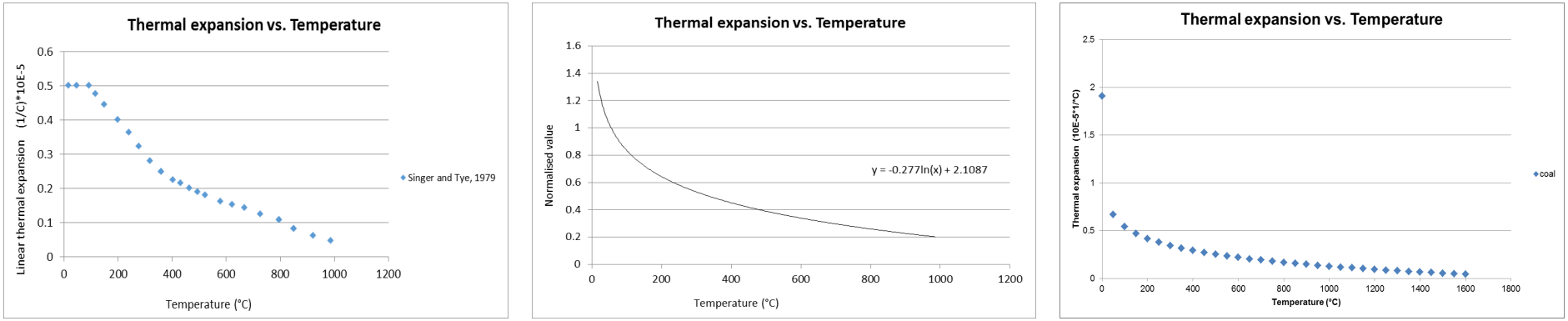


(a) (b) (c)

**Figure 5.15:** Variation of the thermal expansion coefficient of coal as temperature increases (a) literature data; (b) normalised regression model; (c) variation within the FLAC$^{3D}$ module of the coupled Thermo-Mechanical-Chemical model.

A cross-comparison between Table 5.7 and Table 5.8 would reveal that, in the case of coal, all its thermo-mechanical properties (including its friction angle (γ) and cohesion (c)) are updated as temperature changes. This is in contrast to roof/floor rocks whose only mechanical properties affected by temperature is the elastic modulus and the tensile strength. However, relevant literature (Otto and Kempka, 2015; Tian and Ziegler, 2013) highlighted that, although the cohesion (c) and friction angle (γ) of roof/floor rocks can remain stable against temperature changes, the thermal behaviour of rocks depends highly on the rock's mineral composition.

Finally, this FLAC$^{3D}$ module function also includes the stress calculations based on the updated thermo-mechanical properties of both the rocks and coal. These updated stress calculations decide whether every grid block of the domain has already failed or not. A grid block fails if it experiences either *tensile* failure or *shear* failure. The type of failure each grid-block (if any) experiences is labelled with an identification number describing its state. Consequently, the stress calculations update the state identification number of every grid block facilitating the operation of the *identifying failed grid blocks* function.

***Identifying the failed grid blocks.***

This FLAC$^{3D}$ module function forms the backbone of the coupled process model. It is the function where the failed grid blocks are removed from the domain. It is also where the interaction between the FLAC$^{3D}$ and the remaining two modules takes place. As it can be seen in the operational diagram (Figure 5.6), two decision criteria determine whether a coal block has gone through thermal or tensile failure. As the operation of this function is rather complex, it would be helpful to classify its tasks into sub-groups. These sub-groups follow a logic and include several sub-functions that exist within the larger function block.

Firstly, the grid blocks that experience thermal failure are identified. For this reason, one loop function whose pointer accesses all the grid blocks of the domain and checks if the average block temperature is above 427$^{o}$C. A minimum temperature of 427$^{o}$C (Britten, 1986) is used as the criterion for identifying the gasified grid blocks of coal within the model structure.

Grid blocks whose temperature exceeds this benchmark value are considered to be (partially) gasified at the roof of the growing cavity and are removed from the model domain. To ensure this, the developed loop includes multiple *IF* conditions in order to check whether the thermally failed grid block is mudstone or coal. These *IF* conditions are particularly relevant when the roof of the growing UCG cavity comes in contact with the mudstone layers above. This sub-function group, therefore, feeds the number of the thermally failed grid blocks (both in as coal and mudstone) to the gasification support module as well as feeding the average temperature of these grid blocks to the Aspen Plus module Figure 5.6.

A second group of functions aim to identify the grid blocks that have mechanically failed. The tensile failure criterion is used to identify the grid blocks that fail (spall) and fall to the bottom of the UCG cavity without going through roof stage gasification. The failure criterion requires that every mechanically failed grid block has to go through both tensile failure as well as its exposed surface bring in contact with the growing UCG cavity.

Therefore, an iterative loop was developed with a couple of *IF* conditions in it. The first *IF* condition checks the state identification number – which reveals if this grid block has been through shear failure, tensile failure or none – as this was expected to have been updated after the stress calculations within the *update rock mechanical and thermal properties* function. The second *IF* condition checks whether the exposed surface of the particular grid block is in contact with the growing cavity. In case both the first and the second *IF* conditions are met, that particular grid block is identified as mechanically failed (spalled) and is removed from the model domain. This second *IF* condition ensures that, after each iteration, every exposed grid block is checked against both mechanical failure criteria and the total number of mechanically failed grid-blocks are fed to the Gasification Support module, as well as feeding the bottom stage gasification temperature to the Aspen Plus module (Figure 5.3). The bottom stage gasification temperature is taken as the average temperature at the bottom of the growing cavity. Finally, both the roof gasified and thermo-mechanically failed coal are removed from the 3D-structure leading to an updated cavity boundary.

The third group of sub-functions is associated with the modelling of the pilling rubble at the bottom of the growing cavity. The rubble also includes the ash content from the failed coal blocks. This is necessary as the pile is treated as the heat source from which the radiative heat is acting upon the surface of the growing cavity. The accumulating rubble is assumed to take a conical shape at the bottom of the growing cavity. The centre of the conical shape of the piling rubble is assumed to be at the bottom of the growing cavity at equal distanced from its side walls (y-z coordinates). For every grid blocks that fails, its x-coordinate is saved. When all the x-coordinates of the mechanically failed grid blocks are saved, they are summed up and divided by the number of the failed grid blocks. In this way, the calculated x-coordinate point defines where the highest concentration of rubble would exist. By considering the rubble volume and the coordinates of the cone's bottom centre as known, the building of the rubble pile becomes a process of constructing consecutive rubble layers of reducing radius, one on top of the other.

Finally, an additional task is to calculate the available cavity wall surface as well as classifying the accumulated rubble. As a result, the failed grid blocks forming the *rubble surface*, which can radiate heat to the cavity wall surface depending on their angle and their distance from the cavity surface grid block are identified. Nevertheless, this is the main task of the *Assigning updated heat flux* function that will be discussed later in this Chapter.

The main objective of this function is to group the accumulated rubble into two different zones after calculating the available cavity wall surface. The cavity wall surface available is required for the calculation of the convective heat transfer as it will be provided by the gasification support module. This requires two loop processes. The pointer of the first loop accesses all the domain grid blocks (either coal or mudstone) that are located at the boundaries of the developed cavity and groups the grid-points of the cavity wall-surface under a certain "label". This "label" helps in identifying and counting the relevant grid block surfaces during the second loop. In that way, the number of the grid block surface is calculated and it is provided to the Gasification Support module.

***Assigning the updated heat flux***

This is the function where the calculation and assignment of radiative and convective heat transfer values takes place. The radiative heat transfer is received as an input to this stage of the FLAC$^{3D}$ module from the corresponding Aspen Plus module, while the convective heat transfer is also provided as an input to this stage by the Gasification Support module.

This function can be split into two stages. The first stage incorporates an iterative loop. Within this loop two counters exist. The first counter counts the number of the rubble grid blocks under the "label" *rubble surface*. As explained earlier, these blocks constitute the outer surface of the rubble pile that can radiate heat to the wall-surfaces of the growing cavity. By knowing the number of grid blocks within this rubble group and the total amount of radiative heat power (W) it can be assumed that this heat power is uniformly shared by the grid blocks forming the *rubble surface* group before it is radiated to the cavity wall-surfaces.

The second counter counts the number of grid blocks neighbouring the growing cavity. These grid blocks are located on the boundaries where the cavity ends and the coal seam (or roof) starts. The convective heat transfer power is assumed to be uniformly distributed over the surface of the growing cavity. Therefore, by knowing the volume of every grid block, as well as its share of the total available convective heat power, the corresponding convective heat flux (W/m$^3$) can be calculated.

The second stage is rather more complex as it conducts the main task of this function which is the actual assignment of the radiative and conductive heat fluxes (W/m$^3$) to every grid block located at the boundaries of the growing cavity. For this purpose, two integrated loops were constructed. The outer loop iterates across all the grid blocks located on the boundaries of the growing cavity (i.e. "boundary blocks"), while the inner loop iterates over the grid blocks that form the *rubble surface*.

The objective is to calculate the radiative heat flux (W/m$^3$) that every boundary grid block attracts from every grid block that forms the *rubble surface* and add to this value the corresponding convective heat flux (W/m$^3$) that every boundary block also receives. For example, if the pointer of the outer loop has accessed one boundary block, the inner loop passes through every grid block forming *the rubble surface*.

Every grid block forming *the rubble surface* is assigned a heat value (a task that was performed by the first stage of this function) and, using a view factor as discussed in Section 2.3.3

$$Fij = \frac{1}{A_i} \iint_{A_i A_j} \frac{\cos\theta_i \cos\theta_j}{\pi R^2} dA_i dA_j \tag{E5.5}$$

a fraction of that value is assigned to the boundary grid block at which the outer loop points. In addition, the absorptivity of the medium within the growing cavity is also considered through

$$\frac{I_{\lambda,L}}{I_{\lambda,0}} = e^{-\kappa_\lambda L} \tag{E5.6}$$

with the absorption coefficient ($\kappa$ = 0.12) being sourced from the literature (Perkins and Sahajwalla, 2007).

An extra variable (SUM) is initialised outside the inner loop and sums the radiative heat flux (W/m$^3$) radiated from every grid block of *the rubble surface* group to the particular boundary grid block where the pointer of the outer loop points. When the inner loop ends the SUM variable contains the total radiative heat flux (W/m$^3$) that should be assigned to the boundary grid block of the outer loop. After the end of the inner loop and before the end of the outer loop the corresponding convective heat flux (W/m$^3$) is also added to the SUM value. As a result, before the end of the outer loop the SUM value contains the total heat flux (W/m$^3$) for this boundary grid block and this final value can be assigned to it. As one iteration of the outer loop ends the whole process is repeated for the next boundary grid block, and so on.

Due to the fact that this function has the responsibility to assign the correct heat flux value to every grid block lying at the boundaries of the growing cavity, it has also the ability to exclude certain grid blocks from being assigned a specific heat flux value. A model assumption was made such that heat flux values are assigned only to the grid blocks that lie at the boundaries of the growing cavity in one direction. This is controlled by implementing the retraction of the injection point in this function, if/when it is required. However, this restriction does not necessary imply that the UCG cavity cannot grow in the opposite direction.

A much slower cavity growth in the opposite direction can still take place due to the conduction of heat as a result of thermal conductivity of coal.

***Applying the updated heat flux***

This function is the second necessary component in the process of updating the temperature profile of the model domain. It consists of an iterative loop whose pointer accesses all the grid blocks located on the cavity surface. In order to define the time period over which the heat flux value assigned to each cavity surface grid block is applied, a time step has to be established.

A running-time clock forms the time component of the whole coupled process as the FLAC$^{3D}$ module is the only module where a run time can be defined (since the other two modules are steady-state models). Each boundary grid block has already been assigned a particular heat flux value (W/m$^3$) and the pointer of the aforementioned loop links this heat flux value with the running-time clock. As a result, by the end of the loop all the grid blocks of the cavity surface have been accessed and their heat flux values have been linked with the running-time clock. The value of the time step is provided as an input to this stage of the FLAC$^{3D}$ module by the Gasification Support module.

***Preparing the model for the next time step***

This function aims to re-initialise the model domain for the next iteration of the FLAC$^{3D}$ module. Specifically, this function consists of an additional loop which accesses all the grid blocks of the structure (across all layers, i.e. coal, mudstone, sandstone) and turns to zero the already assigned heat flux values making sure that only the updated heat flux values will participate during the next execution of the *Applying the updated heat flux* function.

This is the final function implemented during one iteration within the FLAC$^{3D}$ module. The next iteration is expected to start with the execution of the *update rock mechanical and thermal properties* function which, based on the updated temperature profile of the domain, re-calculates the values of the relevant thermo-mechanical properties (Figure 5.6).

### 5.3.1 An example run for the presentation of FLAC$^{3D}$ module results

The case study parameters presented under this section refer to the same simulation study given in Section 5.2.1. The initial model domain developed within the FLAC$^{3D}$ module is presented in Figure 5.16.

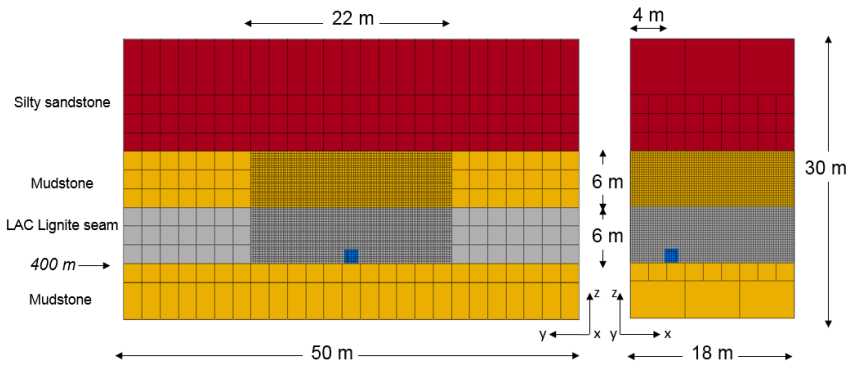


**Figure 5.16:** Initial model domain developed within the FLAC$^{3D}$ module during the Low Ash Content (LAC) Velenje lignite simulation study.

Here, the objective was to maintain consistency and showcase how the coupled results of one simulation study can be correlated with the three individual modules constituting the coupled model. The base of the lignite coal panel is located at 400 m below the earth's surface and its proximate and ultimate analysis data was presented earlier in Table 5.3. The model parameters are presented in order to equip the reader with the necessary understanding for the case study comparisons in Chapters 6 and 7. The thermo-mechanical parameters of the Velenje lignite and its surrounding strata were presented in Table 5.5 and Table 5.6 earlier in this Chapter.

Figure 5.17 presents a summary of the results for cavity growth and vertical stress distribution around the cavity in a sequence from the start of gasification (model run) to approximately ten days after the ignition/initiation stage. This figure also shows that, in the case of vertical stress distributions, compliance mismatches between the adjacent sandstone and coal layers and sudden changes in grid block sizes affect model results visibly.

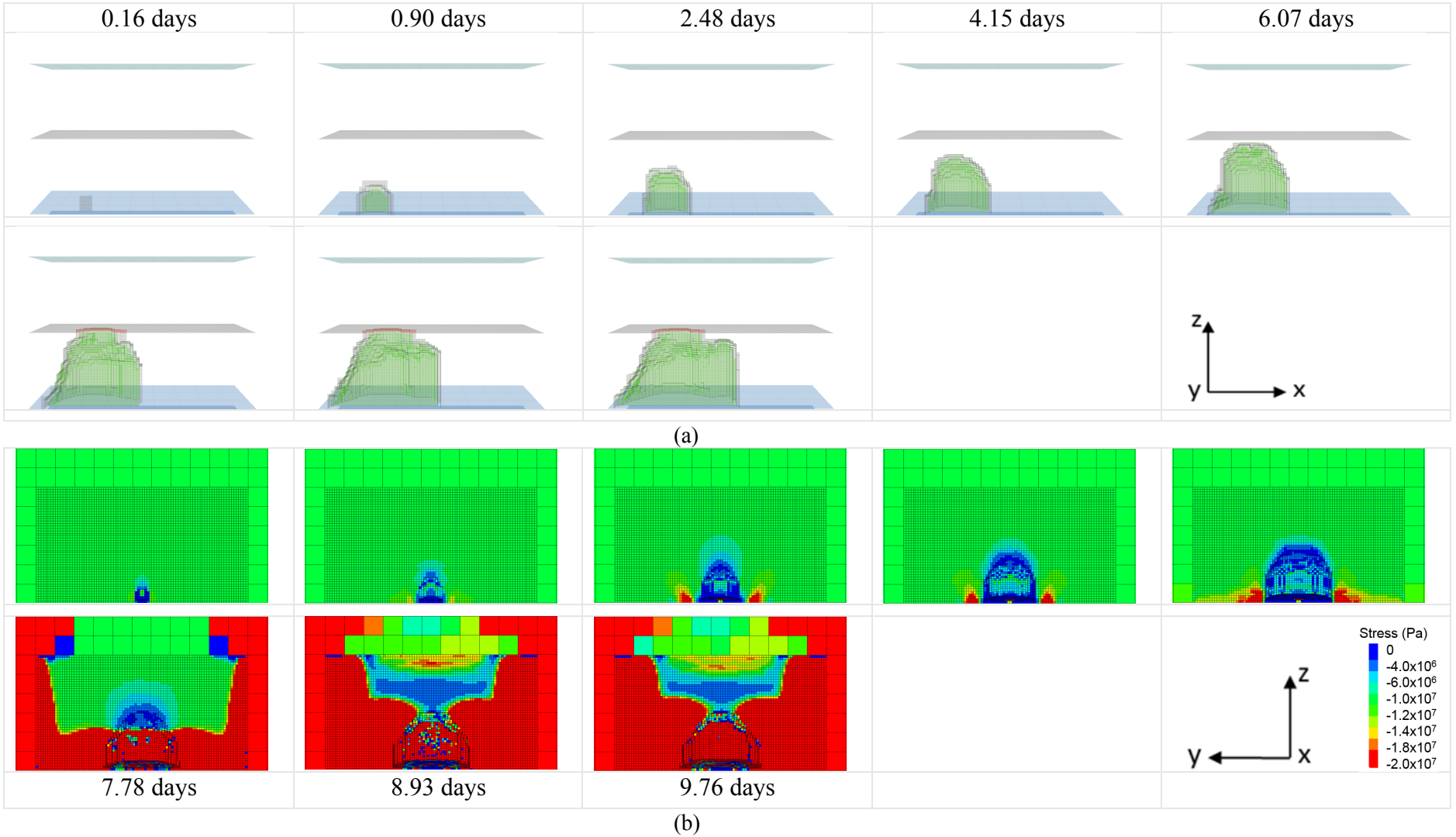


**Figure 5.17:** Representation of the (a) cavity growth (x-z plane) and (b) vertical stress distribution (y-z plane) around the UCG cavity in different time periods during a 6m thick Velenje lignite seam gasification model run at 400m depth (Sections taken from Figure 5.16).

## 5.4 *The Gasification Support module*

The coupling between the Aspen Plus and FLAC$^{3D}$ modules requires the development of a third module, which was developed to calculate the convective heat transfer between the product gas and the cavity boundaries, as well as facilitating the exchange of data between the remaining two modules. The role of the gasification support module is to source the output data from one module and transform them for use as input for the relevant module. Figure 5.18 describes the main tasks of this module under two operational groups as:

- The *Dimensional Data* block has as its main role to prepare the necessary input for the Aspen Plus module. It sources the necessary input data from the *Identifying failed grid- blocks* function of the FLAC$^{3D}$ module and subsequently converts this data into a format acceptable by the Aspen Plus module. Specifically, the sourced data include the number of grid blocks experiencing thermal failure and the corresponding number of grid blocks undergoing mechanical failure (spalling).

  The data sourced from the FLAC$^{3D}$ module cannot be directly provided as input to the Aspen Plus module. For this reason, the number of grid blocks are converted to their equivalent mass (kg) as input to the Aspen Plus module. The conversion process requires the knowledge of the corresponding density value (kg/m$^3$) and the grid block's volume (m$^3$). By converting the number of grid blocks to their equivalent volume and subsequently multiplying this value with the corresponding density value the final mass is obtained. As the FLAC$^{3D}$ module provides the numbers of grid blocks that have failed due to either thermal or mechanical causes the corresponding mass balance ratio for the two failure types can be calculated. This ratio is also provided to the Aspen Plus module, and particularly to the "Separator 2" (Figure 5.3). According to the given ratio, Separator 2 decides the proportion of the total coal mass that will pass through the roof gasification stage (*thermal failure* route) or will spall reaching directly the combustion stage (*mechanical failure* route).

Furthermore, the number of the grid block faces (side-surfaces) sourced from the FLAC$^{3D}$ module should be converted into the corresponding surface area. This conversion facilitates the knowledge of the surface area at every time step as the UCG cavity grows within the coal seam. By combining this cavity surface area information with the corresponding cavity volume size at every time step, the surface/volume ratio can be calculated and assessed throughout the UCG cavity development.

- The *Convective Heat Calculation* block, as its title reveals, is responsible for calculating the amount of heat transferred to the wall surface area of the cavity due to the convection phenomenon. This operational block is based on the heat and mass transport theory detailed in Section 2.3. This module requires data provision by external sources such as the Aspen Plus module, the FLAC$^{3D}$ module and the literature, as well as by internal sources such the *Dimensional Data* operational block. This process starts with the calculation of the Reynolds number (*Re*) from

$$\mathrm{Re} = \frac{\rho u L}{\mu} \tag{E5.7}$$

which requires the computation of dynamic viscosity ($\mu$) through (Perkins and Sahajwalla, 2008):

$$\mu = 1.98 \times 10^{-5} \left(\frac{T}{300}\right)^{0.66} \tag{E5.8}$$

Where $\mu$ is the dynamic viscosity (kg/ms) and $T$ is the temperature within the growing cavity (K).

The calculation of the dynamic viscosity requires the knowledge of the gas temperature within the growing cavity. This information is provided by the Aspen Plus module. Specifically, this is the temperature of the cavity reactor stage (Figure 5.3). Therefore, the running of the Aspen Plus module should be completed after the *Dimensional Data* block and before the *Convective Heat Calculation* block.

After the calculation of the Reynolds number, the calculation of the Grashof number is also performed through

$$Gr_L = \frac{g\beta\Delta TL^3}{v^2} \tag{E5.9}$$

which requires a knowledge of the temperature of the cavity wall surface, which is temperature after the thermally or mechanically failed blocks have been removed from the cavity walls. This value is offered by the FLAC$^{3D}$ module and calculation of this value takes place within the *Identifying failed grid blocks* function. In addition, the calculation of the Grashof number also requires the definition of the kinematic viscosity ($v$), which is the ratio between the dynamic viscosity (μ) and the density (ρ) of the product gas within the growing cavity. The composition of the product gas is provided by the Aspen Plus module. As both the Reynolds and Grashof numbers have been calculated, the Archimedes ratio can be derived from

$$Ar = \frac{Gr}{\mathrm{Re}^2} \tag{E5.10}$$

which defines if natural or forced convection is the dominant convective heat transfer mechanism. Furthermore, the Rayleigh number is also calculated through:

$$Ra_L = Gr_L \,\mathrm{Pr} \tag{E5.11}$$

Here, the Prandtl number ($Pr$) is taken as 0.71 from the literature (Perkins and Sahajwalla, 2007). Finally, in order to establish the convective heat transfer coefficient, the Nusselt number ($Nu$) is calculated through (Harloff, 1983):

$$Nu = 0.023\mathrm{Re}_D^{0.8}\,\mathrm{Pr}^{0.4} \tag{E5.12}$$

In addition, the convective heat transfer coefficient ($h$) is then calculated using

$$Nu = \frac{hL}{k} \tag{E5.13}$$

where the thermal conductivity ($k$) of the gas mixture flowing through the growing cavity is assumed as 0.0805 W/ms, as sourced from the literature (Perkins and Sahajwalla, 2007)

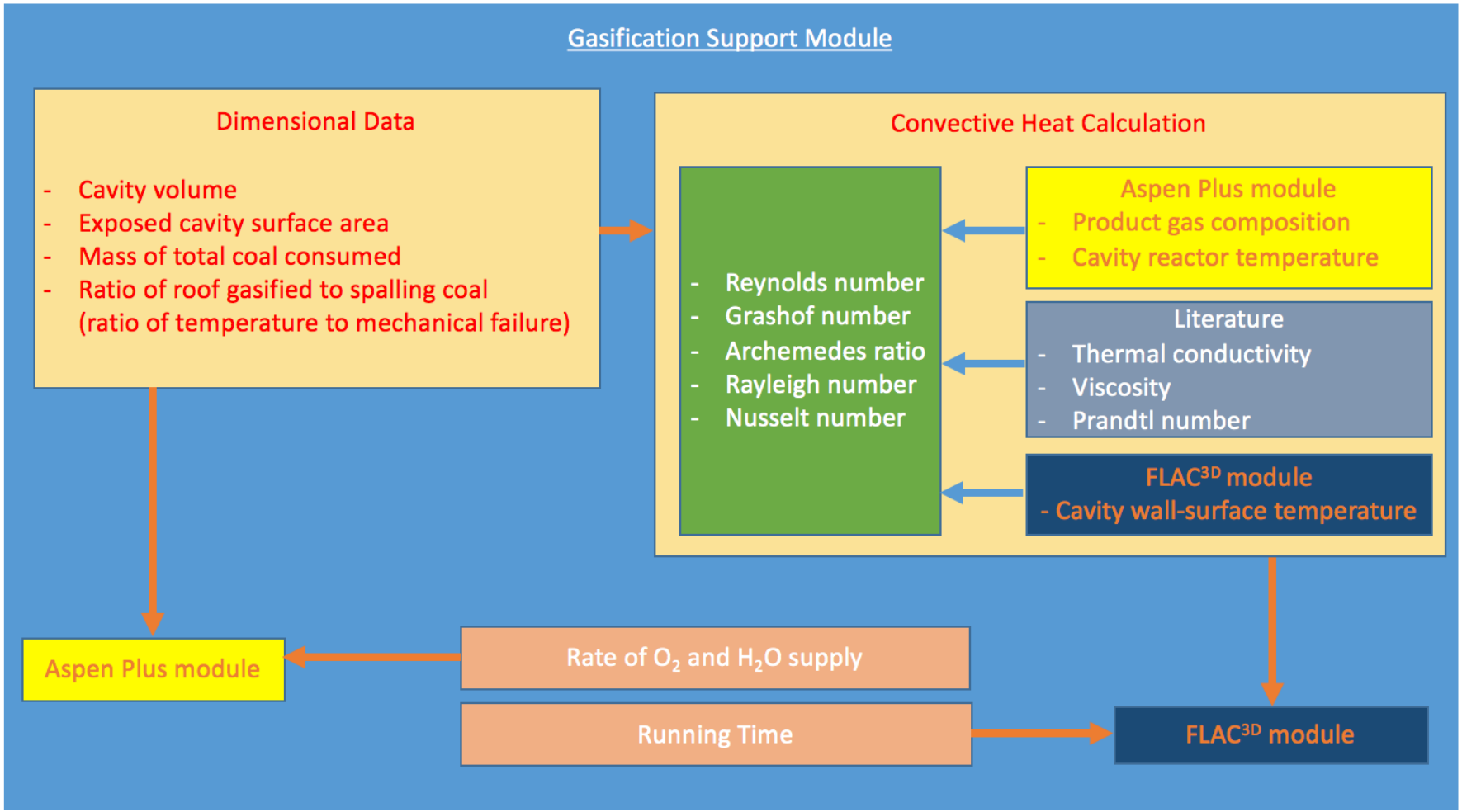


**Figure 5.18:** Schematic overview of the gasification support module developed as part of the coupled Thermo-Mechanical-Chemical model

This leads to the calculation of the resulting convective heat transfer (Lienhard (2013):

$$Q = h \times A \times \left(T_{fluid} - T_{surface}\right) \tag{5.14}$$

Where, $Q$ is the convective heat transfer (W), $h$: is the convective heat transfer coefficient (W/m$^2$ K), $A$ is the exposed cavity wall surface area (m$^2$), $T_{fluid}$ is the temperature of the fluid within the growing cavity (K) and $T_{surface}$ is the temperature of the cavity wall surface (K).

Finally, the rates of oxygen ($O_2$) injection and water ($H_2O$) influx are also calculated within the Gasification Support module and are provided as input to the Aspen Plus module. These rates are highly correlated with the coal consumption rate. This coal consumption rate facilitates the running-time step (should be provided to the *Applying the updated heat flux* function of the FLAC$^{3D}$ module) which is also calculated within the Gasification Support module. The calculation of the coal consumption rate is conducted through:

$$Cr = rec \times \rho \tag{5.15}$$

Where $Cr$ is the coal consumption rate (kg/s), $rec$ is the volumetric cavity expansion rate (m$^3$/s) and $\rho$ is the density of coal (kg/m$^3$). The running-time step, which is fed to the FLAC$^{3D}$ module is then defined by:

$$Rt = \frac{Cm}{Cr} \tag{5.16}$$

Where $Rt$ is the running-time step (s), $Cm$ is the coal mass (kg) - equivalent to the mass value of the failed grid-blocks, and $Cr$ is the coal consumption rate (kg/s).

Finally, the running-time step ($Rt$), in combination with the reagent flux rate ($gf$) form the necessary components for the calculation of the mass for the participating reagents (i.e. $O_2$/Air or $H_2O$). The mass values of the participating reagents are calculated through:

$$Rs_i = gf \times Rt \times A \times mw_i \quad (5.17)$$

Where $Rt$ is the running time step (s), $gf$ is the reagent flux rate (mol/m$^2$s) and $mw_i$ is the molar weight of the $i$ reagent (kg/mol). Here, the reagent mass flux rate ($gf$), which also affects the volumetric cavity expansion rate ($rec$), is taken from the UCG literature (Britten, 1986).

In conclusion, the gasification support module enables the operation of the other two modules and facilitates the development of the coupled process. Figure 5.18 provides an overview of how different tasks within the module are organised. It also provides an indication on how the calculated parameters are spread among the remaining two modules.

Sections 5.2 – 5.4 aimed mainly on explaining how the tasks in each module within the coupled Thermo-Mechanical-Chemical UCG model are performed. However, a more detailed understanding regarding the interaction between the different modules is offered in Section 5.5.

### 5.4.1 An example run for the presentation of Gasification Support Module results

The case study parameters used under this section refer to the same simulation study as in Sections 5.2.1 and 5.3.1. The aim is to present how the calculation blocks within the Gasification Support Module can facilitate the computation of different performance indicators. These performance indicators have a critical role in the comparison of different simulation scenarios presented in Chapters 6 and7. Figure 5.19 illustrates how the Dimensional Data block of the Gasification Support module facilitates the calculation of both the cumulative coal mass consumed (Figure 5.19a) and the measurement of the cavity expansion along the three dimensions (Figure 5.19b). The iterative nature of the coupled process allows the Gasification Support module to store the data and plot them against the UCG operating time.

The *Convective Heat Calculation* block allows the computation of the convective hear transfer and its comparison with the corresponding radiative heat mechanism (Figure 5.20a).

In addition, as the UCG CRIP layout is simulated, the stage when the retraction of the oxidant injection point takes place is taken into account, as this has an impact on the corresponding ratio.

Furthermore, the combination of the radiative heat transfer mechanism with the surface area of the growing cavity allows the calculation of the radiative heat flux ($W/m^2$) (Figure 5.20b).

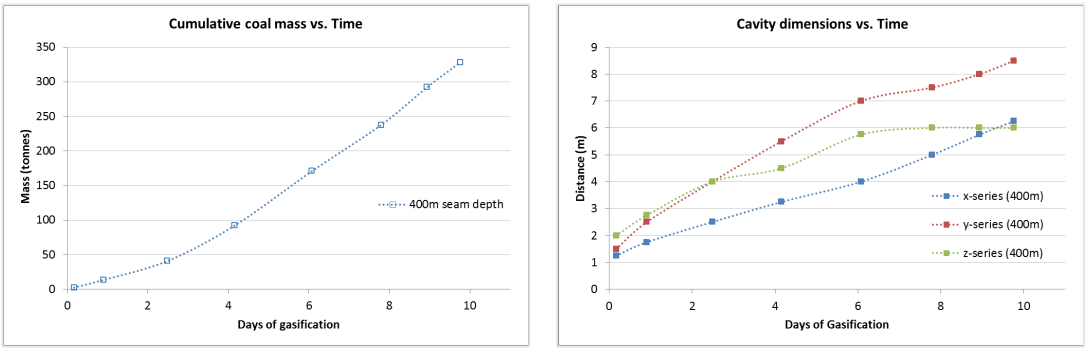


(a) (b)

**Figure 5.19:** (a) The cumulative consumed coal mass; (b) The dimensions of the growing cavity during the UCG simulation of the Velenje lignite at 400. depth.

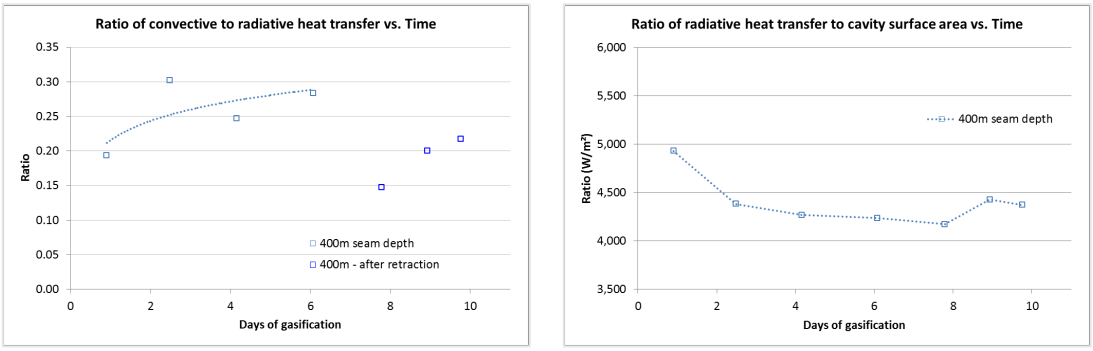


(a) (b)

**Figure 5.20:** (a) The ratio of convective to radiative heat transfer; (b) The radiative heat flux ($W/m^2$) during the UCG simulation of Velenje lignite at 400m depth.

In addition, Figure 5.21a presents the comparison of thermal to mechanical failure at different time stages. Particularly, Figure 5.21a indicates that, at least in the early stages of UCG process, the ratio of roof-gasified to totally consumed coal is approximately 80% with the remaining 20% occurring due to mechanically failure. On the other hand, Figure 5.21b describes in absolute mass of coal consumed due to thermal and mechanical failure at different time stages of the UCG process.

Further analysis of these data will be presented in Chapters 6 and 7 where different UCG scenarios are discussed in detail.

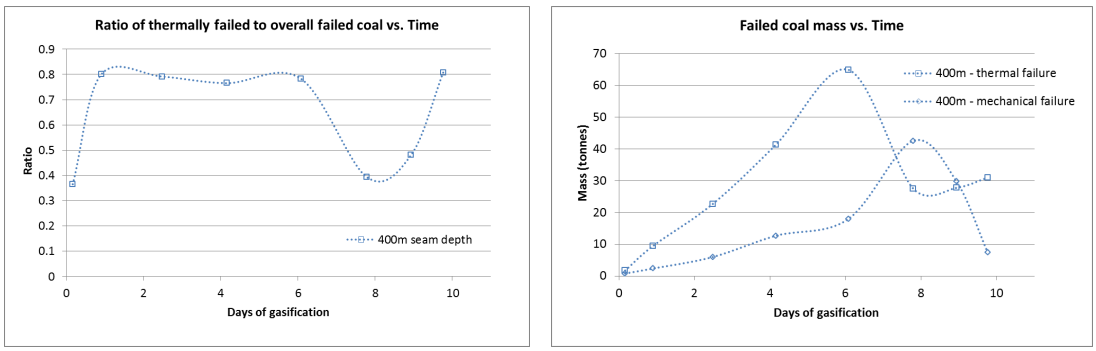


(a) (b)

**Figure 5.21:** (a) The ratio of thermally failed to overall consumed coal; (b) The failed coal mass at different stages during the UCG simulation of Velenje lignite at 400m depth.

## 5.5 *The coupled Thermo-Mechanical-Chemical process model*

The main objective of this section is to describe the complex interaction between different modules of the coupled thermo-mechanical-chemical UCG model as it is illustrated in Figure 5.22. The three participating modules have been organised into three operational blocks. In contrast to Figure 5.3, Figure 5.6 and Figure 5.18 where the different components of each participating module were presented, the focus of Figure 5.22 is on the exchanged parameters between the three modules. For this reason, specific emphasis has been placed on particular components of the FLAC$^{3D}$ module, which interact with the Gasification Support and the Aspen Plus modules.

Specifically, when the first criterion, which assesses the temperature dependent failure of a grid block is addressed within the FLAC$^{3D}$ module, a negative or a positive result might be obtained. In the case of a positive outcome (that is the temperature of the grid block exceeds the gasification temperature benchmark set as 427$^{o}$C), the temperatures of all the grid blocks of the domain that exceed the 427$^{o}$C are averaged and the roof stage gasification temperature is calculated. Subsequently, this temperature is fed to the Aspen Plus module (green line in Figure 5.22). Furthermore, the number of the grid blocks that have thermally failed is counted and this number is added to the *Dimensional data* block of the Gasification support module (yellow line in Figure 5.22). When both these tasks are completed, the thermally failed grid blocks are removed and the 3D-model domain is updated.

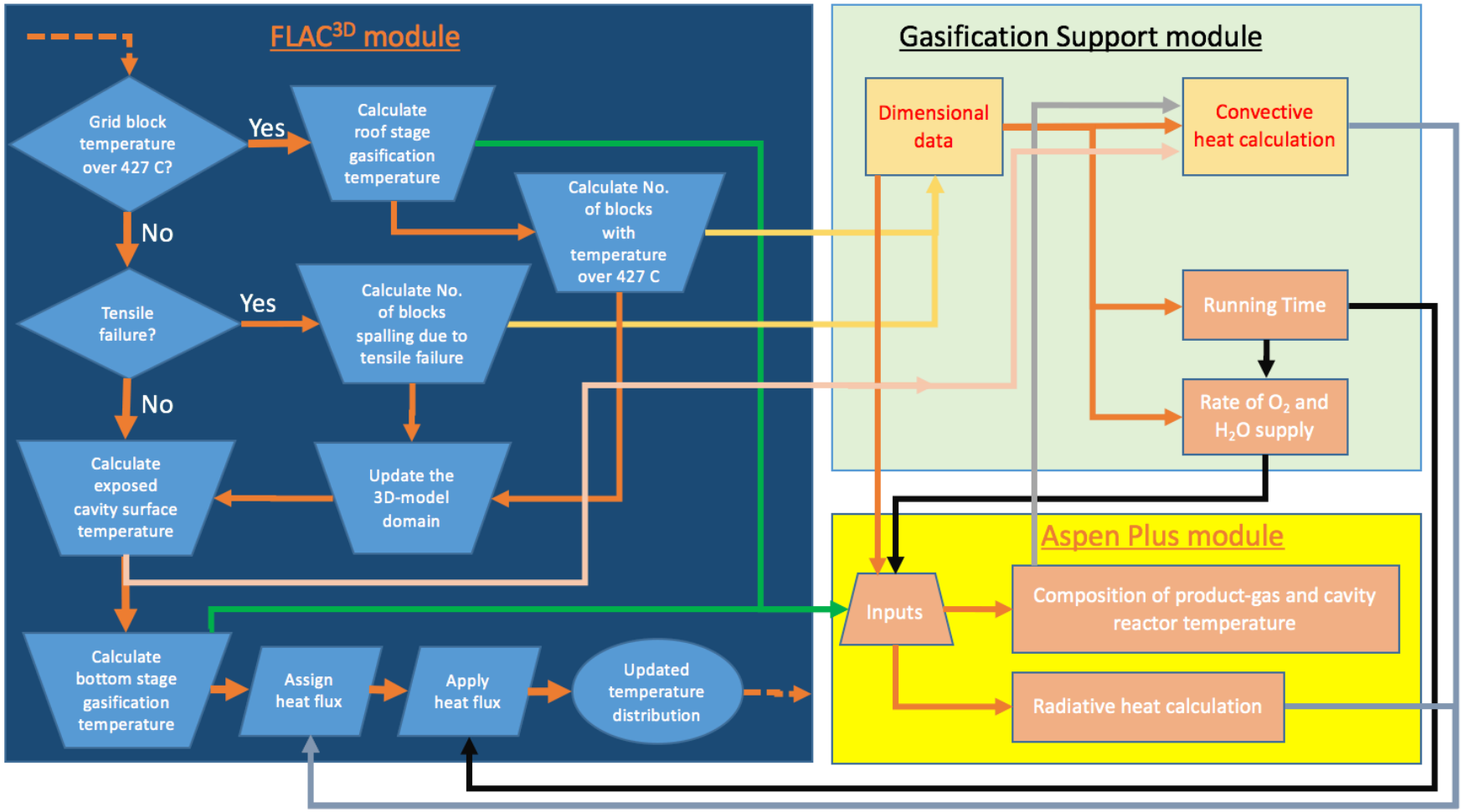


**Figure 5.22:** Schematic representation of the exchanged parameters between the three modules of the developed Thermo-Mechanical-Chemical model

If the outcome of the first criterion is negative (that is no temperature failure), the process continues in order to identify the grid blocks that have experienced mechanical failure (tensile failure). The mechanically failed grid blocks are counted and the result is offered to the *Dimensional data* block of the Gasification support module (yellow line in Figure 5.22). The mechanically failed grid blocks are removed and the 3D-model domain is updated.

When the 3D-model domain is updated, or in the case when none of the two failure criteria is met, the cavity surface temperature is measured by averaging the individual temperatures of the grid blocks that are located on the boundaries of the growing cavity. This temperature value is supplied to the *Convective heat calculation* block of the Gasification Support module (pink line in Figure 5.22). Also, the bottom stage gasification temperature is calculated and its value is fed to the Aspen Plus module (green line in Figure 5.22).

The *Dimensional data* block within the Gasification Support module accepts the number of failed (both mechanically and thermally) grid blocks from the FLAC$^{3D}$ module. The exposed cavity surface area is offered to the convective heat calculation block and it is also used in the calculation of the $O_2$ and $H_2O$ reagents' supply. The volumetric cavity expansion rate is also provided for the calculation of the running-time step (orange lines in Figure 5.22). The convective heat transfer rate (grey line) and the running-time step (black line) are directly supplied to the *Assign heat flux* and *Apply heat flux* functions of the FLAC$^{3D}$ module respectively (Figure 5.22).

The running-time step facilitates the calculation of the $O_2$ and $H_2O$ reagent supply. The resulting masses of the reagents combined with the coal mass data (from the *Dimensional data* block) are supplied to the Aspen Plus module. In this module, these data inputs combine with the roof-stage and bottom-stage gasification temperatures supplied by the FLAC$^{3D}$ module. The resulting parameters of this module are either fed to the *Convective heat calculation* block (product gas composition and cavity reactor temperature) or fed directly to the *Assign heat flux* function of the FLAC$^{3D}$ module (radiative heat) (grey lines in Figure 5.22). Once the *Assign heat flux* and *Apply heat flux* functions of the FLAC$^{3D}$ module are executed, a new temperature distribution profile is developed within the 3D-model domain and one iteration of the coupled TMC model has been completed.

# Chapter 6 UCG Performance Analysis for Different Operational Conditions

## 6.1 *Introduction*

This Chapter presents the results when the methodology presented in Chapter 5 is employed. Different scenarios were structured and simulated through the coupled TMC process model, which cases served two objectives. The first objective was to assess the robustness of the developed model with different input parameters. The second objective was to evaluate and draw conclusions based on the outputs of the developed model.

Therefore, the Chapter discusses how tailored and "flexible" the developed model is and if can meet the needs of its users. In addition, the degree of reliability or accuracy of the model is discussed through the comparison of the results with data from experimental and in-situ trials. Furthermore, modelling studies sourced from the literature provided an additional comparison mechanism.

Different performance indicators facilitate the cross-comparison between the results of the different scenarios. In addition, the size of the growing cavity along with the vertical stress and temperature distribution around it was monitored at different stages during the evolving UCG process.

Table 6.1 presents six different UCG scenarios. One bituminous and two lignite coals are included in these scenarios. The two lignite coals are identified by their widely different ash content. The Low Ash Content (LAC) Velenje lignite from Slovenia and the bituminous coal sourced from the Murcki – Staszic Colliery in Poland were also used in the ex-situ reactor experiments discussed in Chapter 4. These scenarios aimed at identifying the effect of depth (therefore the operating pressure) on the performance of the UCG process for different coals. Therefore, the seam thickness and the reagent used were kept as constant at 6m and as oxygen respectively.

Table 6.2 presents two additional scenarios, which were designed to investigate how seam thickness and the type of the injected reagent influences the UCG process.

**Table 6.1**: UCG scenarios investigating the effect of seam depth on performance.

| Coal type | Seam depth | Seam thickness | Reagent |
|---|---|---|---|
| Velenje Lignite - LAC | 400 m | 6 m | Oxygen |
| | 600 m | | |
| YiHe Lignite - HAC | 400 m | | |
| | 600 m | | |
| Murcki – Staszic Bituminous coal | 400 m | | |
| | 600 m | | |

**Table 6.2**: UCG scenarios investigating the effect of seam thickness and injected reagent on performance.

| Coal type | Seam depth | Seam thickness | Reagent |
|---|---|---|---|
| Velenje Lignite - LAC | 600 m | 10 m | Oxygen |
| Murcki – Staszic Bituminous coal | 600 m | 6 m | Air |

The proximate and ultimate analyses of the coal types used in these scenarios are presented in Table 6.3. The volatile material content, as well as the ash content significantly differs between the two lignite coals. The High-Ash-Content (HAC) YiHe lignite from China was provided to the research by Seamwell International Limited, while the corresponding Low-Ash-Content (LAC) Velenje lignite was provided by Coal Mine Velenje in Slovenia.

**Table 6.3**: Proximate and ultimate analysis of coals used in the UCG model scenarios.

| *Proximate analysis ( % w/w, dry basis)* | Murcki – Staszic Bituminous | YiHe Lignite | Velenje Lignite |
|---|---|---|---|
| Fixed carbon | 62.74 | 38.75 | 29.71 |
| Volatile material | 32.58 | 26.39 | 64.43 |
| Ash | 4.68 | 34.86 | 5.86 |
| *Ultimate analysis (% w/w, dry basis)* | | | |
| Carbon | 79.51 | 49.29 | 56.10 |
| Hydrogen | 4.27 | 2.85 | 5.25 |
| Nitrogen | 1.26 | 0.89 | 0.72 |
| Sulphur | 0.31 | 0.13 | 0.74 |
| Ash | 4.68 | 34.86 | 5.86 |
| Oxygen | 9.97 | 11.98 | 31.33 |
| High Heating Value (dry basis, kJ/kg) | 30.97 | 16.17 | 19.73 |
| Moisture (% w/w) | 4.93 | 28.00 | 31.00 |

Note that the same coals used in the model implementation in Chapters 4 and 5 were also used in these case studies in order to provide consistency and reliable conclusions from the chemical process modelling of Chapter 4 and from the coupled TMC process modelling of Chapter 5.

**Table 6.4**: The initial thermo-mechanical propertied for the coals and the surrounding strata used in the simulation scenarios (Eppelbaum et al., 2014; Gilliam and Morgan, 1987; Hettema, 1996; Midttømme et al., 1998; Min, 1983; Robertson, 1988; Tan et al., 2008; Waples and Waples, 2004).

| | Unit | Mudstone | Silty Sandstone | Bituminous | Lignites |
|---|---|---|---|---|---|
| *Mechanical Properties* | | | | | |
| Elastic modulus (E) | GPa | 3.6 | 30 | 2.3 | 0.85 |
| Tensile strength ($\sigma_i$) | MPa | 1.8 | 4.8 | 1.3 | 0.86 |
| Friction angle ($\gamma$) | ° | 30 | 40 | 28 | 22 |
| Poisson's ratio ($\nu$) | | 0.35 | 0.2 | 0.34 | 0.42 |
| Cohesion (c) | MPa | 5.2 | 18.68 | 4 | 2.9 |
| Density ($\rho$) | kg/m$^3$ | 2,530 | 2,540 | 1,342 | 1,390 |
| *Thermal Properties* | | | | | |
| Linear thermal expansion coefficient ($\alpha$) | °C$^{-1}$ | $0.873\times10^{-5}$ | $0.55\times10^{-5}$ | $0.65\times10^{-5}$ | |
| Specific heat ($C_p$) | J/(kg °C) | 985 | 852 | 1,066 | |
| Thermal conductivity ($\lambda$) | W/(m °C) | 1.76 | 2.4 | 0.28 | |

As Table 6.4 suggests, it was assumed that both lignite coals have the same mechanical properties. Therefore, the input properties to the FLAC$^{3D}$ module for both lignite coals will be the same, while the corresponding FLAC$^{3D}$ outputs and the inputs to the Aspen Plus module will be different. This further helps analyse the robustness of the coupled TMC model. In addition, while the mechanical properties of different ranks of coal change, the same thermal properties are considered for both ranks. The thermo-mechanical parameters have already been extensively discussed both in the literature review Chapter 2-3 and the methodology Chapter 5 before.

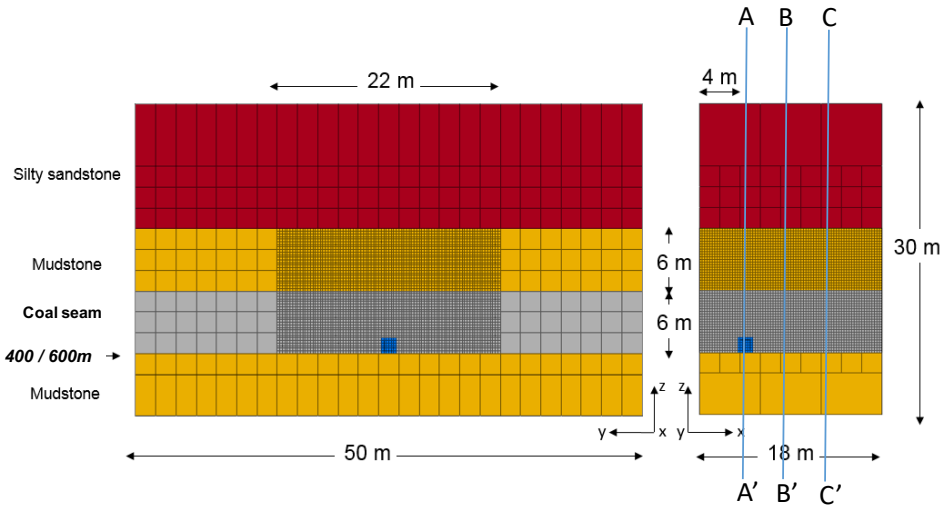


**Figure 6.1:** The model domain developed within the FLAC$^{3D}$ module for the 400m and 600m deep 6m thick bituminous coal and lignite UCG scenario analysis. The AA', BB' and CC' sections represent where the temperature profiles around the growing UCG cavity are taken.

## 6.2 *The UCG performance of Low Ash Content Velenje lignite*

The objective of the work described in this section is to investigate how the depth as well as thickness of the gasified coal seam influences the UCG process. Initially, the LAC Velenje lignite seam of fixed thickness (6m) at 400 and 600m depths was considered and its UCG performance compared. Next the same lignite was modelled as a 10m thick seam at 600m depth to facilitate thickness comparison. Figure 6.1 shows the model domain used for the 6m thick seam model scenarios (for both lignites and bituminous coal) at 400 and 600m depths. This is the same model domain used in Chapter 5 where different modules of the coupled TMC model were described.

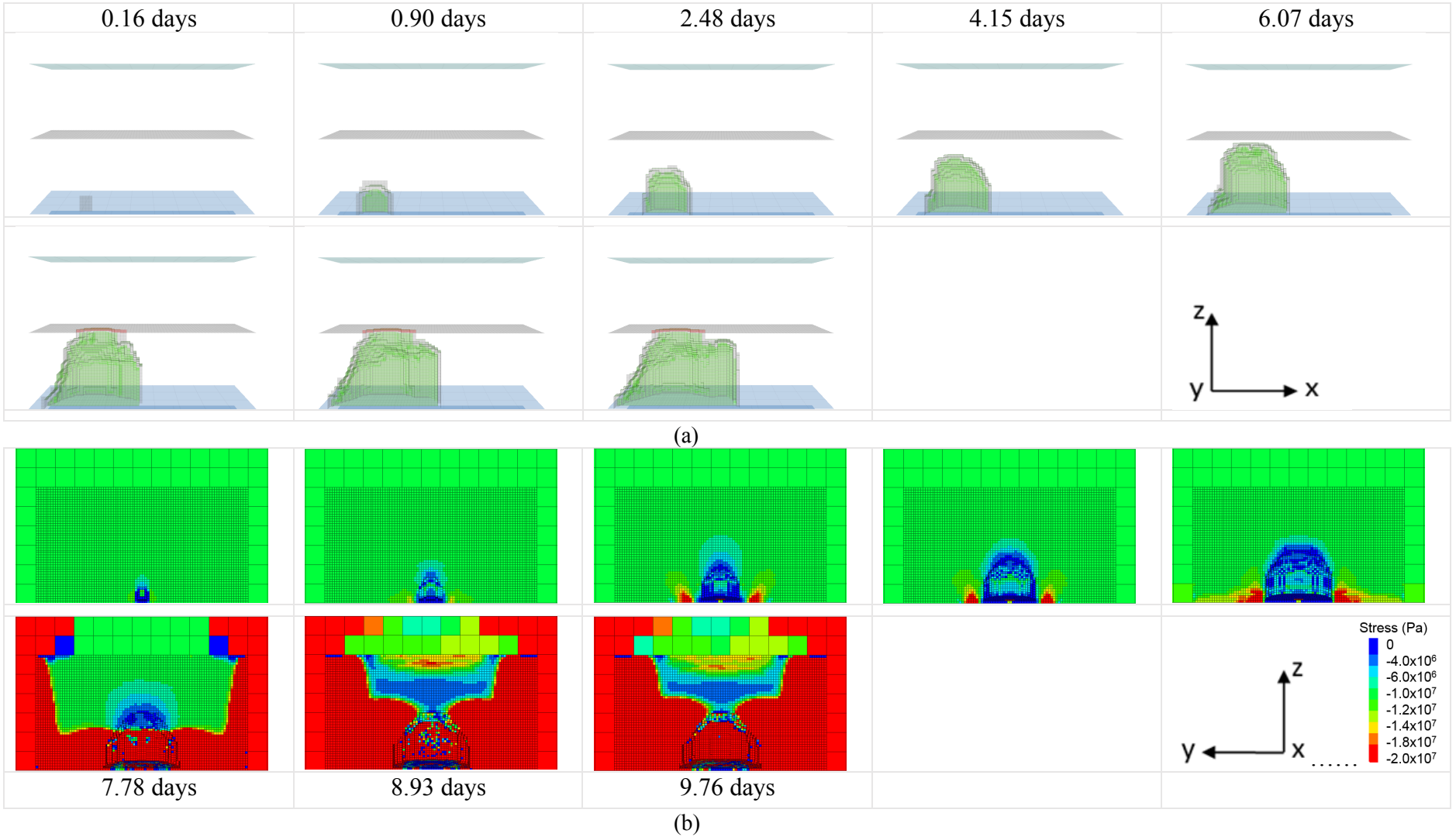


**Figure 6.2:** Representation of (a) cavity growth (x-z plane) and (b) vertical stress distribution (y-z plane) around the UCG cavity in different time periods during a 6m thick Velenje lignite seam gasification model run with oxygen at 400m depth (Sections taken from Figure 6.1).

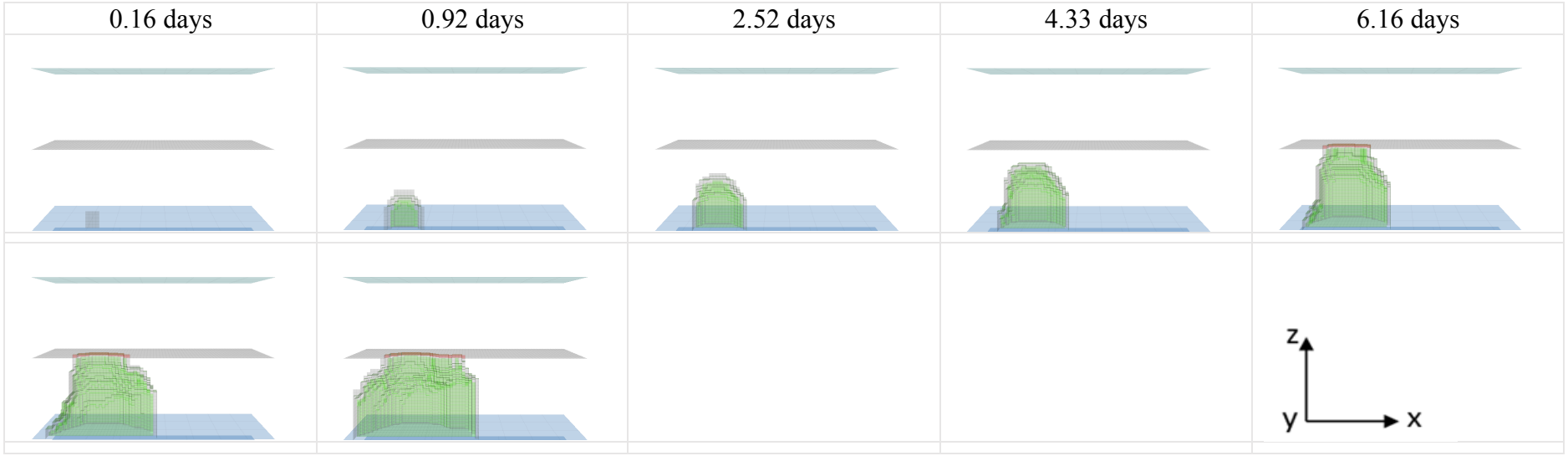


(a)

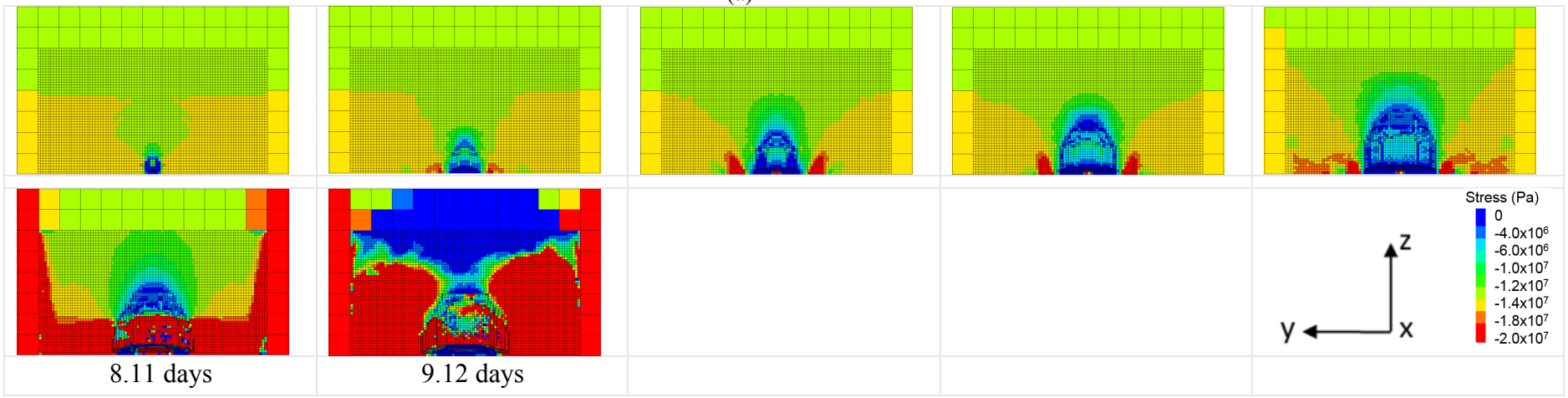


(b)

**Figure 6.3:** Representation of (a) cavity growth (x-z plane) and (b) vertical stress distribution (y-z plane) around the UCG cavity in different time periods during a 6m thick Velenje lignite seam gasification model run with oxygen at 600m depth (Sections taken from Figure 6.1).

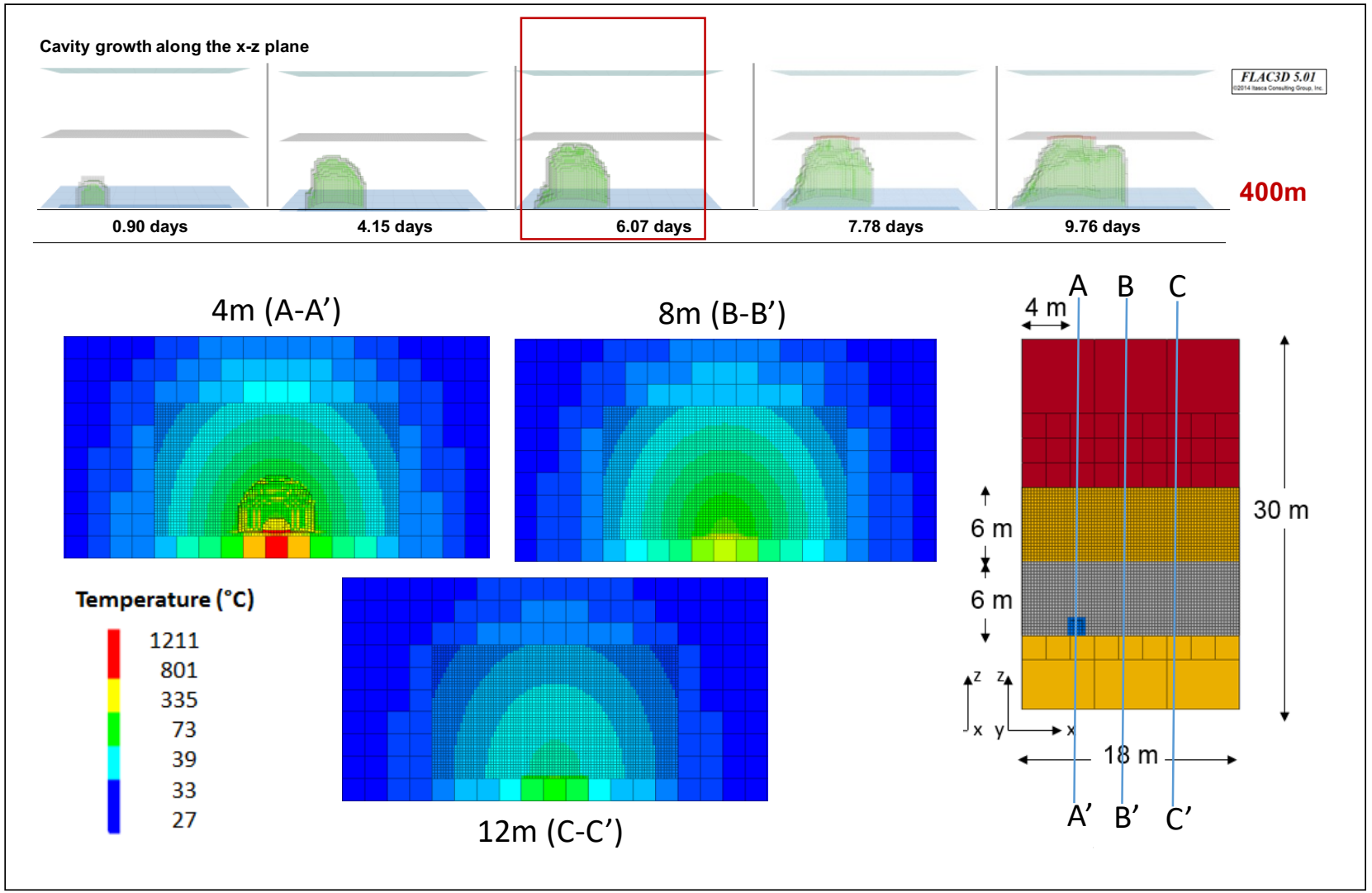


**Figure 6.4:** Temperature profiles along y-z plane across the UCG cavity and the coal seam ahead of the gasified zone after 6.07 days of cavity advance during a 6m thick Velenje lignite seam gasification model run with oxygen at 400m depth.

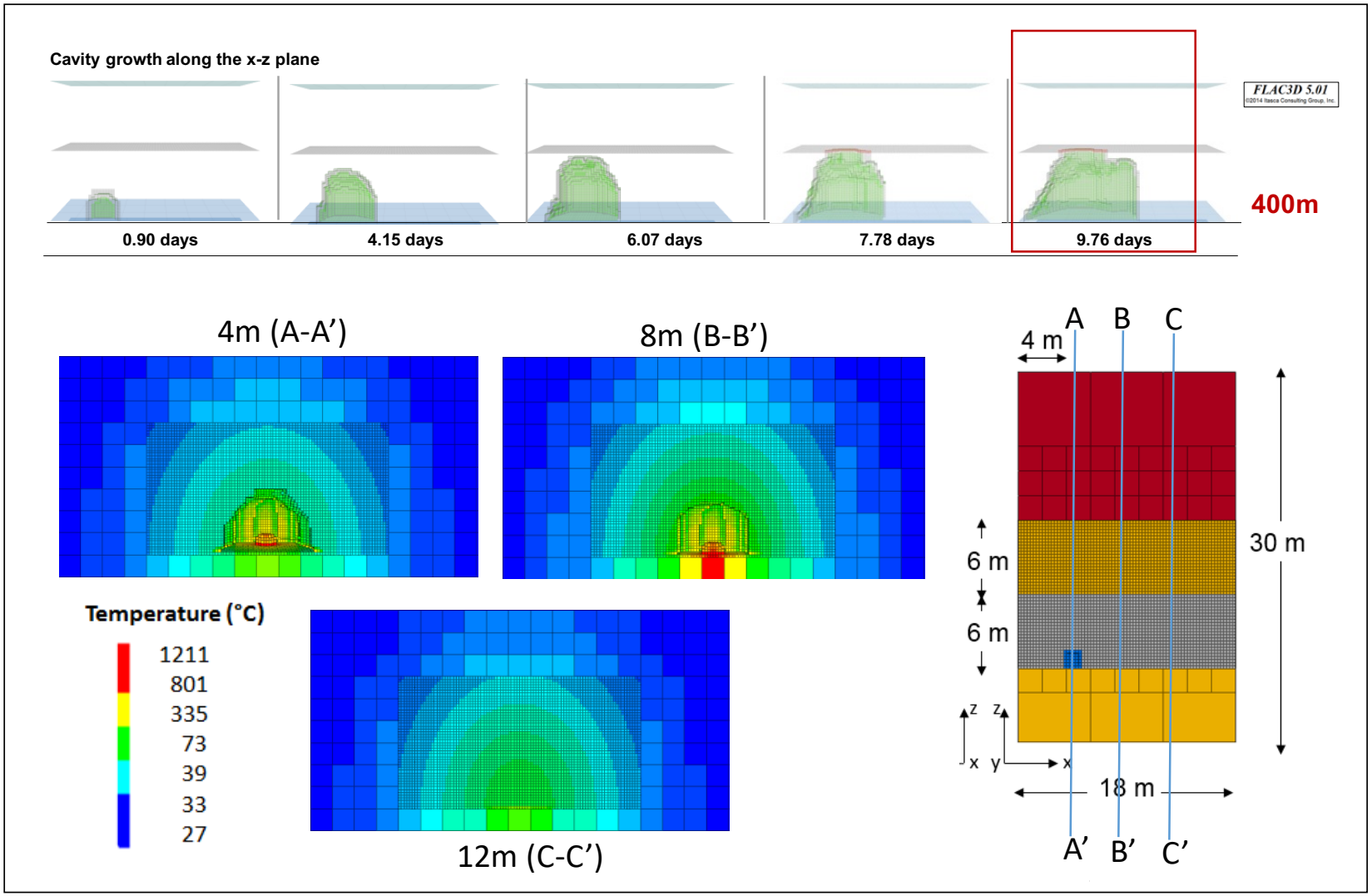


**Figure 6.5:** Temperature profiles along y-z plane across the UCG cavity and the coal seam ahead of the gasified zone after 9.76 days of cavity advance during a 6m thick Velenje lignite seam gasification model run with oxygen at 400m depth.

The evolution of the UCG cavity along with vertical stress distribution around it at two different depths are presented in Figure 6.2 - 6.3. Figure 6.2 repeats the data already presented in Chapter 5, while Figure 6.3 presents the corresponding results at 600m depth for comparison purposes. The temperature distribution around the UCG cavity at two different stages of cavity growth for 400m deep Velenje lignite UCG simulations are shown in Figure 6.4 - 6.5 (also in Appendix, Figures A.1 - A.2). It is clear that, due to low thermal conductivity of coal (and relatively low conductivities of the surrounding rocks), temperature around the UCG cavity drops significantly with distance.

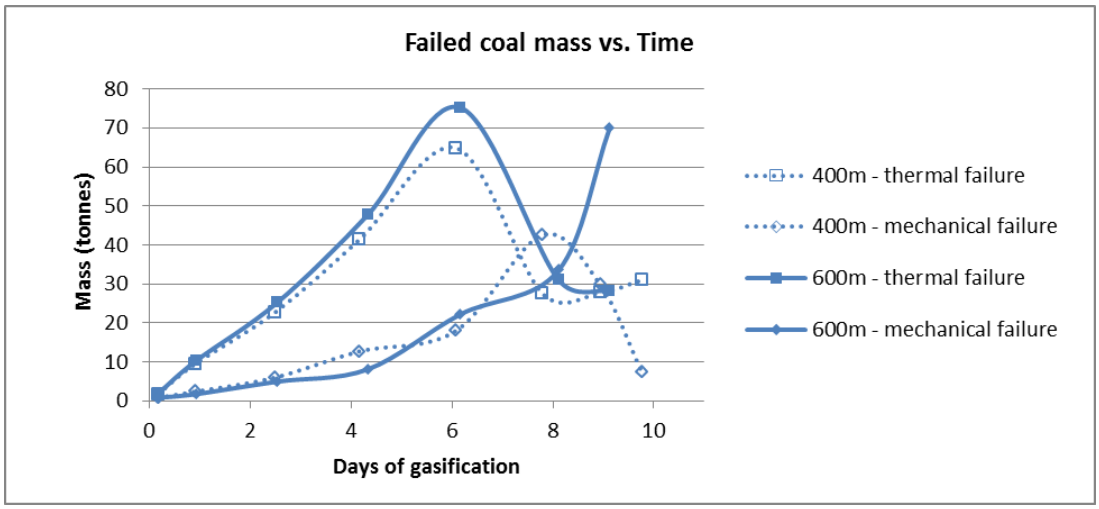


**Figure 6.6:** Failed coal due to thermal and mechanical failure at different stages of the UCG process during the Velenje lignite gasification simulations with oxygen at different depths.

Figure 6.6 presents the coal mass consumed through either thermal (roof-gasification) or mechanical failure (spalling effect) at different time stages of the UCG process at 400 and 600m seam depths. As it can be seen, in both cases at approximately 6 days from the beginning of the UCG process (6.07 days at 400m; 6.16 days at 600m) the coal mass consumed through thermal failure reaches its highest point. This represents the point in time when the growing cavity has reached the roof of the seam and the injection point needs to be retracted. However, the highest consumption rate is not the same for both depths. In the case of 600m depth, the largest coal consumption is equal to 75.2 tonnes while the corresponding value for the 400m depth is equal to 64.9 tonnes of coal.

On the other hand, while the thermally failed coal reaches a maximum and starts declining when the cavity approaches the roof of the seam, the mechanically failed coal/rock mass continues to increase.

This observation suggests that mechanically failed coal/rock mass is an indicator of the stability of the growing cavity. Figures 6.2b and 6.3b illustrate the differences between the vertical stress distribution around a 400m and 600m deep UCG cavity as it grows. It is clear that, at 600m depth, the stresses formed around the growing cavity are much higher. This explains why the mechanically failed (spalled) coal mass around a 600m deep cavity continues to increase after approximately 8 days, while the same for the 400m deep cavity starts to decline.

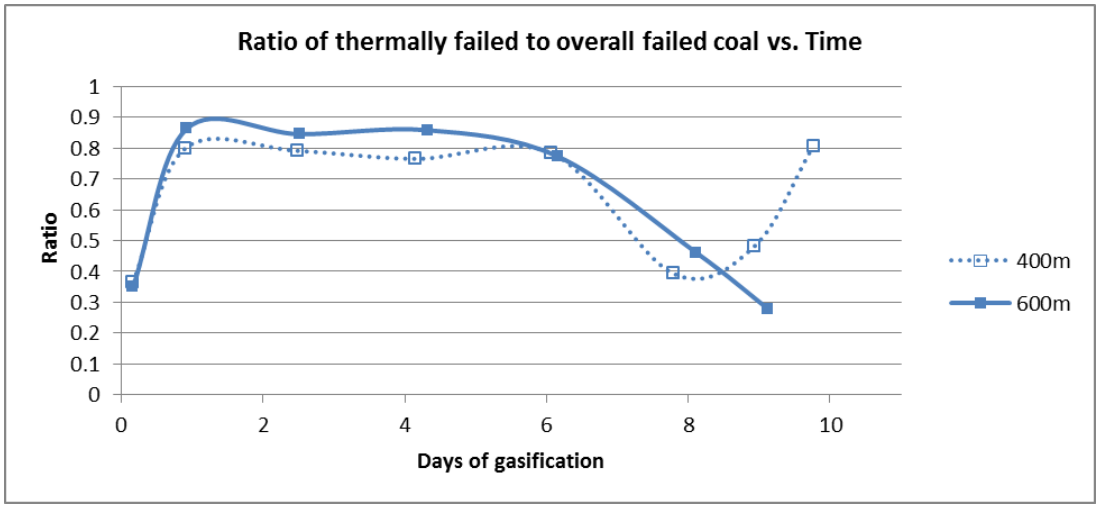


**Figure 6.7:** Ratio of thermally failed to total failed coal mass at different stages of the UCG process during 6m thick Velenje lignite gasification simulations with oxygen at different depths.

Figure 6.7 illustrates that the ratio of thermally failed to total coal consumed is higher for 600m deep UCG. This confirms that, as the UCG depth increases, increasing operating pressure (60 bar vs. 40 bar) leads to higher temperatures to be developed in deeper seams and, as a result, more coal is gasified on the roof of the cavity than that fails mechanically. Figure 6.4 also illustrates that, when the roof reaches a critical distance from the base of the cavity, the mass of the thermally failed coal starts to fall due to increased distance from the heat source on the floor of the cavity.

Figure 6.8 compares different UCG performance indicators for a 6m thick Velenje lignite gasified at two different depths. Figure 6.8a shows that, while it takes nearly 9.7 days to gasify 329 tonnes of coal at 400m depth, it takes 9.1 days to gasify 380 tonnes of coal at 600m depth.

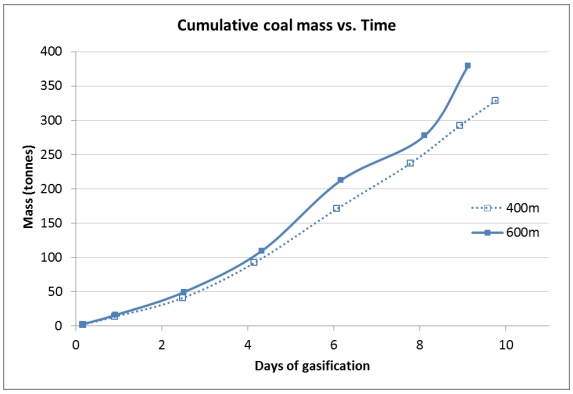


(a)

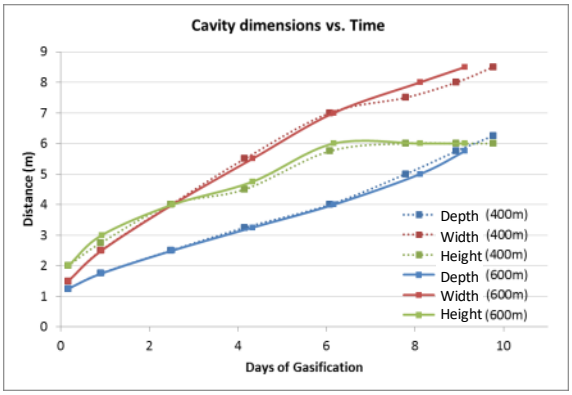


(b)

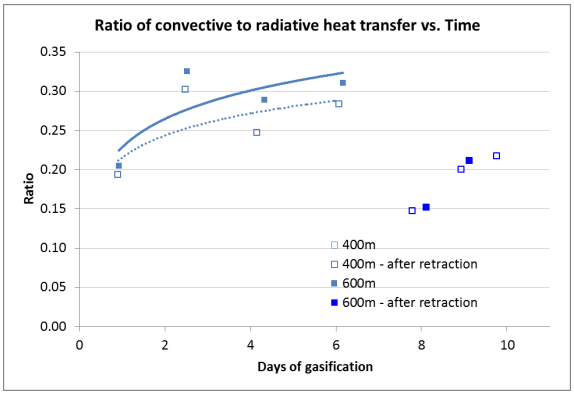


(c)

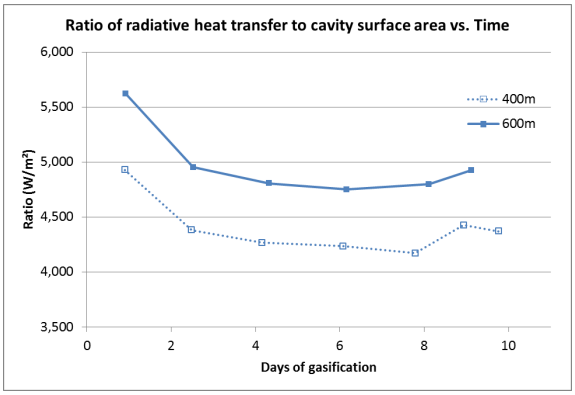


(d)

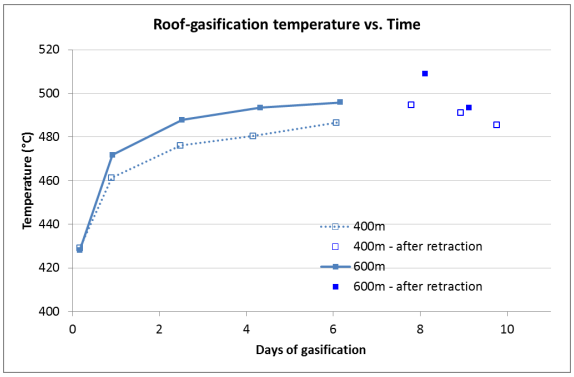


(e)

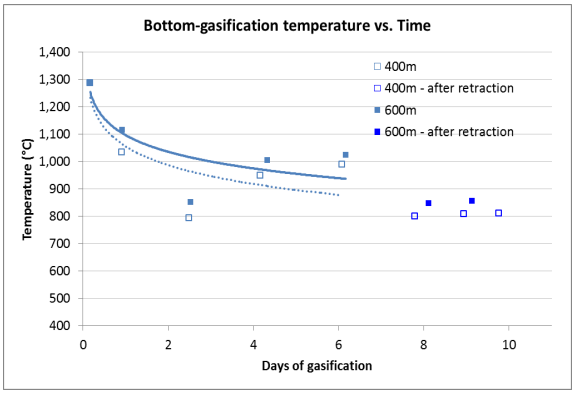


(f)

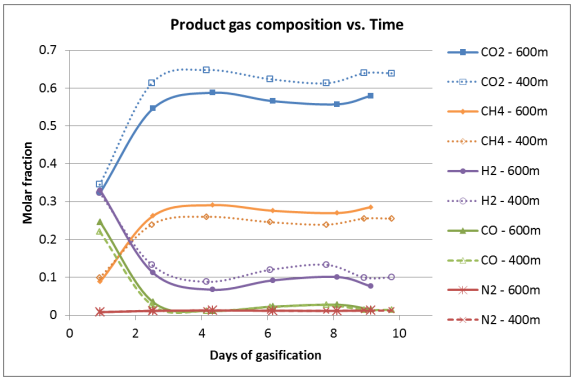


(g)

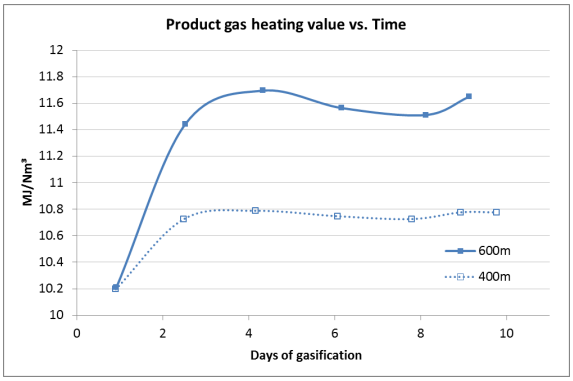


(h)

**Figure 6.8:** Comparison of different performance indicators plotted against UCG run time for the 6 m thick Velenje lignite gasification simulations with oxygen at 400m and 600m depth.

Figure 6.8b illustrates the dimensions of the growing UCG cavities at different stages of the gasification process. It can be seen that higher coal consumption rates lead to slightly larger UCG cavities at larger depths. Note that, in the case of 400m deep seam, retraction took place ~0.25m before the cavity reached the maximum seam thickness of 6m. This ensures to sustain the UCG process and avoid significant caving of the mudstone layer during the gasification process. Therefore, the growth of the cavity at different stages of gasification also depends on the retraction time in the two models.

Figure 6.8c and Figure 6.8d illustrate the heat transfer mechanisms involved in the UCG cavity growth. Figure 6.8c shows that the dominant heat transfer mechanism is radiative heat transfer. As the cavity grows the share of convective heat transfer increases due both to increased volume of gas flowing through the cavity as well as the growing distance of the cavity boundaries from the rubble. However, when the retraction takes place and the distance between the new injection point and the cavity boundaries decreases, the radiative heat transfer mechanism revives and the ratio of the convective to radiative heat transfer mechanism drops again. Figure 6.8d shows that, as the UCG process advances, radiative heat flux decreases significantly, indicating that the injection point should be retracted periodically for the cavity boundaries to attract significant heat quantities and sustain the advancement of the UCG cavity.

Figure 6.8e and Figure 6.8f present the change in the roof-stage and bottom-stage gasification temperatures as the UCG process evolves, and also compares these for the two different gasification depths. In both cases, the roof-stage gasification temperature increases until the retraction takes place. On the other hand, the bottom-stage gasification temperatures decrease as the UCG cavity grows and the low temperature rubble collecting at the bottom of the cavity starts acting as an insulating pillar over the floor. Finally, the product gas compositions and heating values are presented in Figure 6.8g and Figure 6.8h. As the figures illustrate, the slightly lower roof and bottom-stage gasification temperatures for the 400m depth scenario leads to increased $CO_2$ and $H_2$ contents in the product gas. In contrast, the higher operating pressure of the 600m depth scenario leads to a higher methane ($CH_4$) content in the product gas.

As discussed before, the LAC Velenje lignite was also used in an additional model run for a 10m thick seam at 600m depth to assess the effect of seam thickness on UCG performance. The site lithology was kept the same, but the thickness of the mudstone layer above the coal seam was reduced to 2m to achieve this. Oxygen was used as the injected gasification agent to ensure consistency. Figure 6.9 illustrates the model domain for the updated seam thickness (10m).

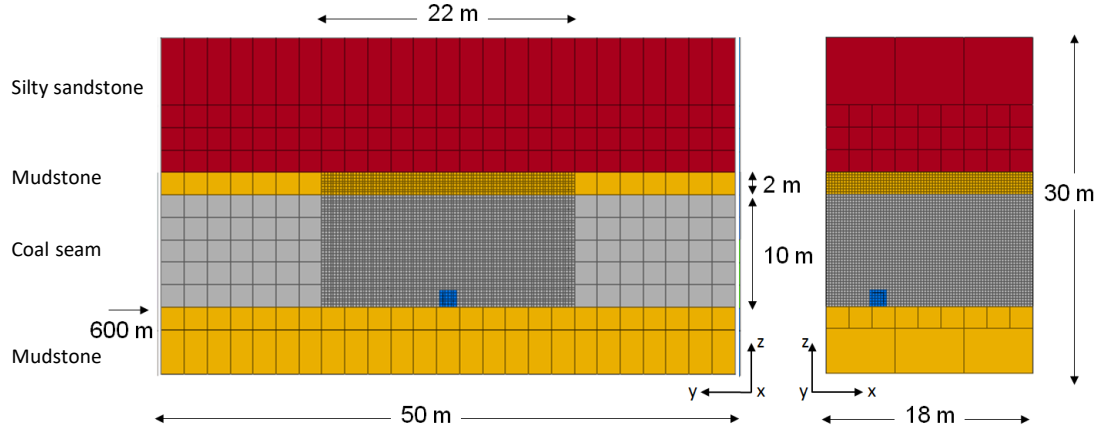


**Figure 6.9:** The model domain developed within the FLAC$^{3D}$ module depicting the10m thick seam scenario used during the Velenje lignite simulations at 600m depth.

Figure 6.10a-b presents the cavity growth along with vertical stress distribution around it at different stages of the UCG process. Figure 6.10a displays the higher cavity size developed under the increased seam thickness scenario compared to the corresponding cavity size in Figure 6.10a. Additionally, the comparison of the stress distributions around the growing cavities (Figure 6.10b vs. Figure 6.3b) reveal the change in load acting on the area depending on seam thickness and the size of the cavity. The increase in the load applied to the surrounding structure in the case of a higher seam thickness occurs more gradually and less rapidly compared to the lower seam thickness case due to less frequent retraction of the injection point.

Figure 6.11 compares the UCG performance of 6m and 10m thick Velenje lignite at 400m and 600m depths respectively. The cross-comparison of Figure 6.10a with Figure 6.11b relates the cavity growth screenshots to the actual dimensions at different time periods. As Figure 6.11b illustrates, in the case of 10m thick seam, the UCG cavity reaches the roof (10m height) after approximately 12 days. At this point in time, the cavity is approximately 7.5m deep and 11.8m wide.

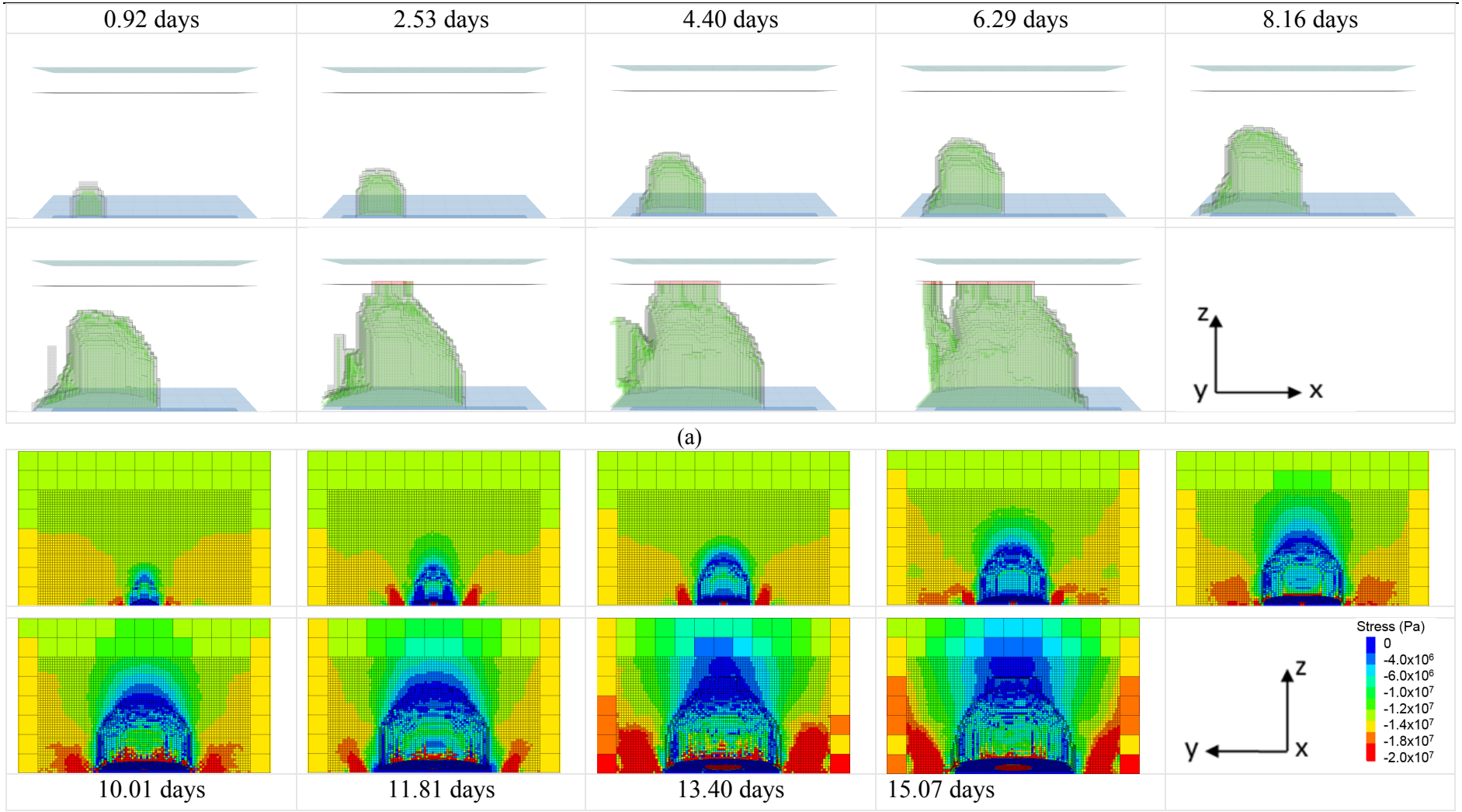


**Figure 6.10:** Representation of (a) cavity growth (x-z plane) and (b) vertical stress distribution (y-z plane) around the UCG cavity in different time periods during a 10m thick Velenje lignite seam gasification model run with oxygen at 600m depth (Sections taken from Figure 6.1).

The retraction of the injection point, which takes place when the growing cavity comes in contact with the roof of the coal seam, restricts its expansion along its height, as the objective is to expose fresh coal and protect the roof strata from unnecessary heat exposure. Upon retraction, the cavity height remains constant for some time yet it advances further to reach 10m depth and 13m width after approximately 15 days. The thickness of a layer of coal which needs to be established between the new injection point and the roof was established as 2m or above through sensitivity analysis.

As Figure 6.11a illustrates, since retraction of the injection point is less frequent in the case of a thicker seam, the mass of coal consumed by the time retraction takes place is much larger. Furthermore, the seam thickness affects considerably the role of different heat transfer mechanisms taking place. This is expected since a larger seam thickness leads to cavities of larger volumes and, as a result, the convective heat transfer mechanism has a more critical role. As Figure 6.11c illustrates, the ratio of convective to radiative heat transfer rates became as high as 0.5 when the UCG cavity in the 10m thick seam reached its largest size. Note that the growth in the ratio of convective to radiative heat transfer occurs in both cases before the retraction takes place, which of course is at different times as discussed above. The figure also shows that, in the case of a thicker coal seam, the role of convective heat transfer mechanism is relatively higher even after retraction of the injection point.

Figure 6.11d shows that the radiative heat flux ($W/m^2$) in the case of a thicker coal seam is consistently lower than that experienced by the lower thickness coal seam as a result of much larger surfaces being exposed. A slight increase in the radiated heat flux is observed after the retraction of the injection point. Moreover, the roof-stage and bottom-stage gasification temperatures both seam thicknesses do not experience significant differences during the UCG operation, apart from the fact that the higher seam thickness allows for the same temperatures to last for a longer period before retraction takes place. The figure also illustrates that the product gas composition and heating value does not change significantly for both seam thicknesses, considering that the same lignite is being gasified.

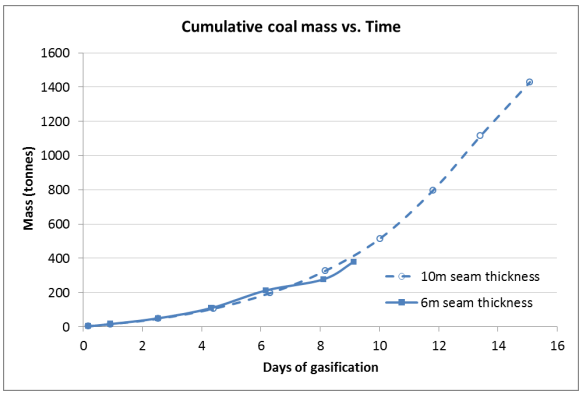


(a)

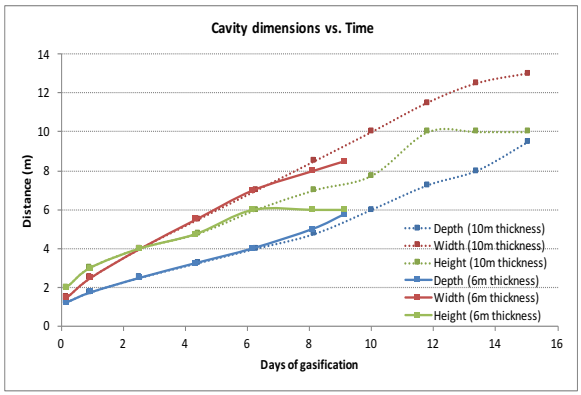


(b)

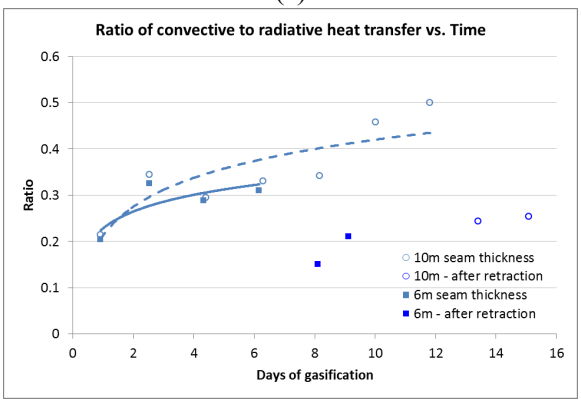


(c)

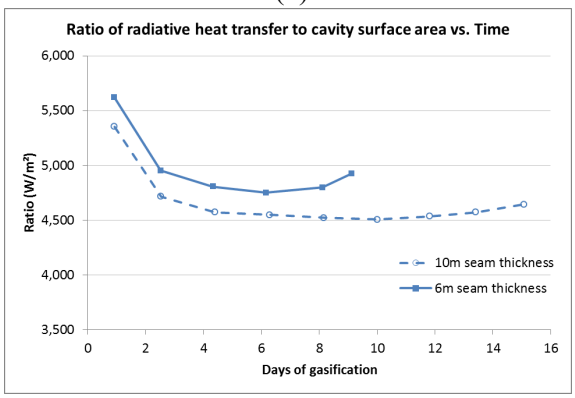


(d)

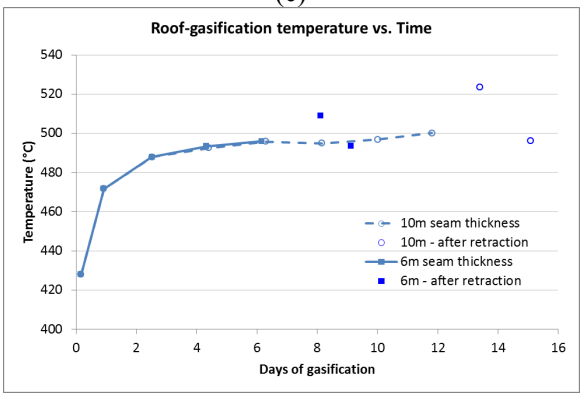


(e)

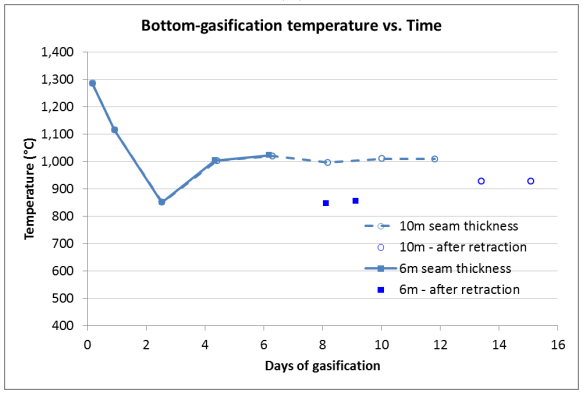


(f)

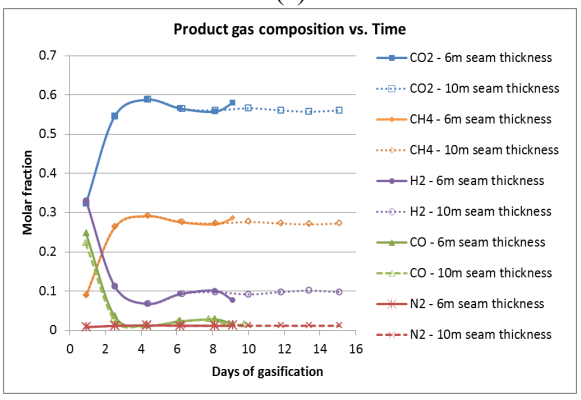


(g)

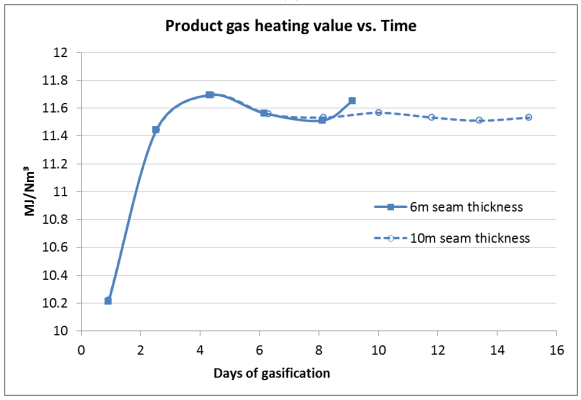


(h)

**Figure 6.11:** Comparison of different performance indicators plotted against UCG run time for the 6m and 10m thick Velenje lignite gasification simulations with oxygen at 600m depth.

## 6.3 *The UCG performance of High Ash Content YiHe lignite*

The High Ash Content (HAC) YiHe lignite was selected to compare the performance of two different lignites by rank, while keeping their thermo-mechanical properties the same in the UCG simulations performed. Figure 6.13 and Figure 6.14 and present UCG cavity progression along with vertical stress profiles around them for two different depths (400m vs. 600m) for a 6m thick YiHe lignite.

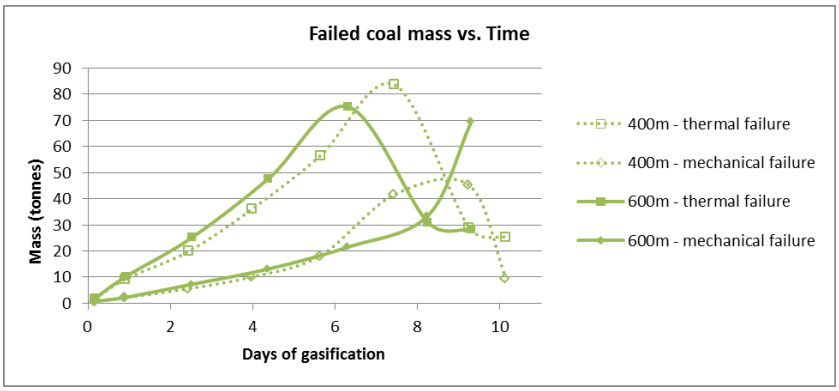


(a)

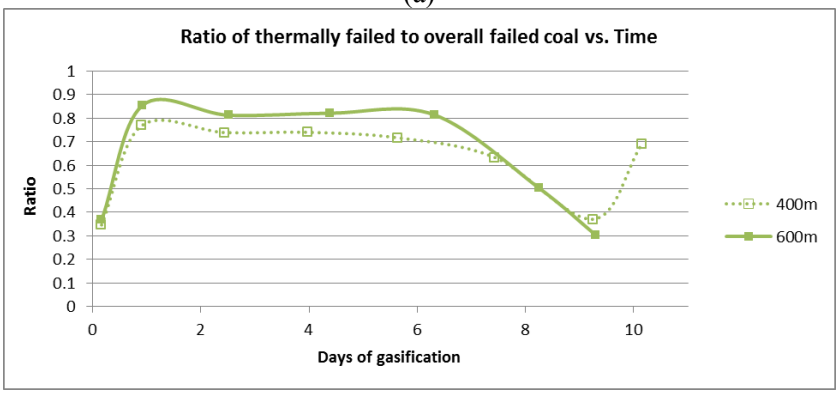


(b)

**Figure 6.12:** (a) Failed coal due to thermal and mechanical failure and (b) ratio of thermally failed to total failed coal mass at different stages of the UCG process during 6m thick YiHe lignite simulations with oxygen at different depths.

Figure 6.12a confirms that, at 600m depth, retraction of the injection point results in a significant reduction in the thermally failed coal mass, while mechanically failed coal mass continues to increase. Figure 6.12b shows that the ratio of thermally failed coal to total coal mass failed also follows the same trend as that observed for the Velenje Lignite (Figure 6.6 and Figure 6.7). The higher temperatures reached at 600m depth lead to more dried coal to be gasified at the boundaries of the cavity. Figure 6.15e and Figure 6.15f further confirm that both the roof and bottom-stage gasification temperatures are higher at greater depths.

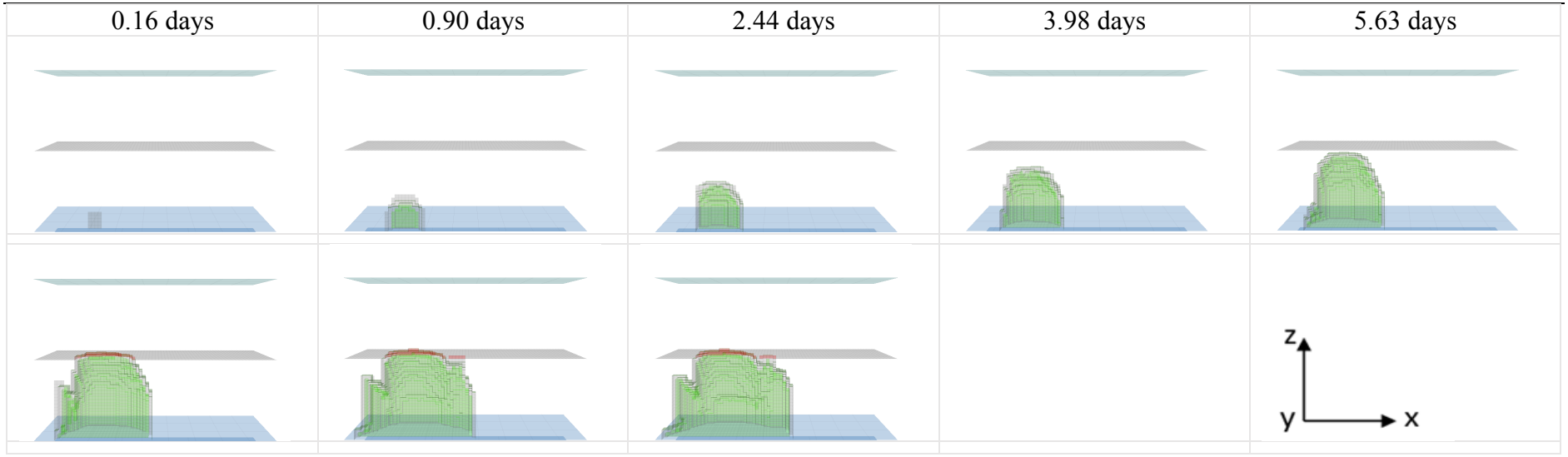


(a)

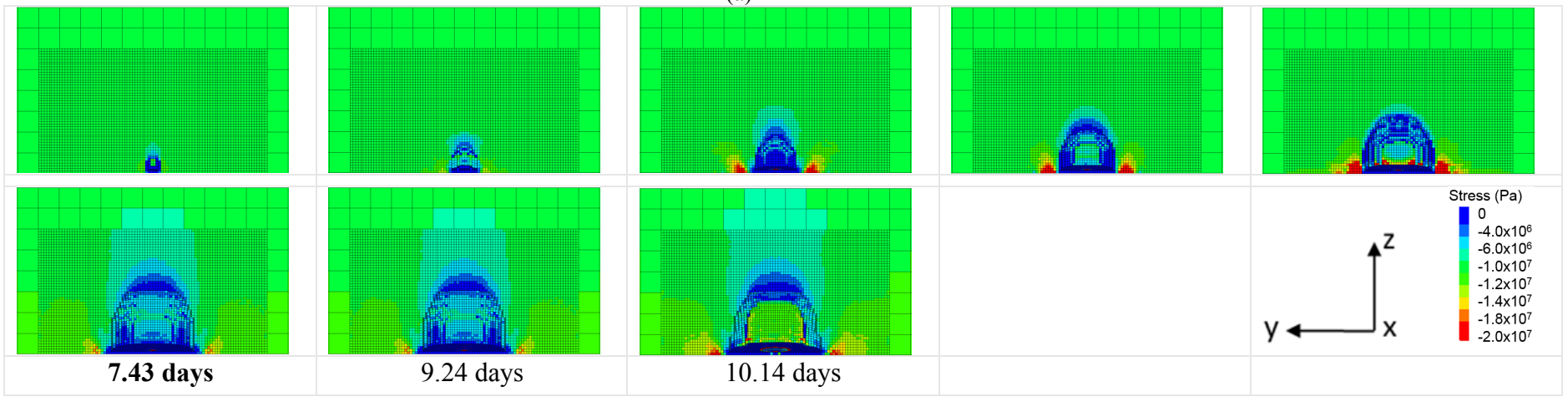


(b)

**Figure 6.13:** Representation of (a) cavity growth (x-z plane) and (b) vertical stress distribution (y-z plane) around the UCG cavity in different time periods during a 6m thick YiHe lignite seam gasification model run with oxygen at 400m depth (Sections taken from Figure 6.1).

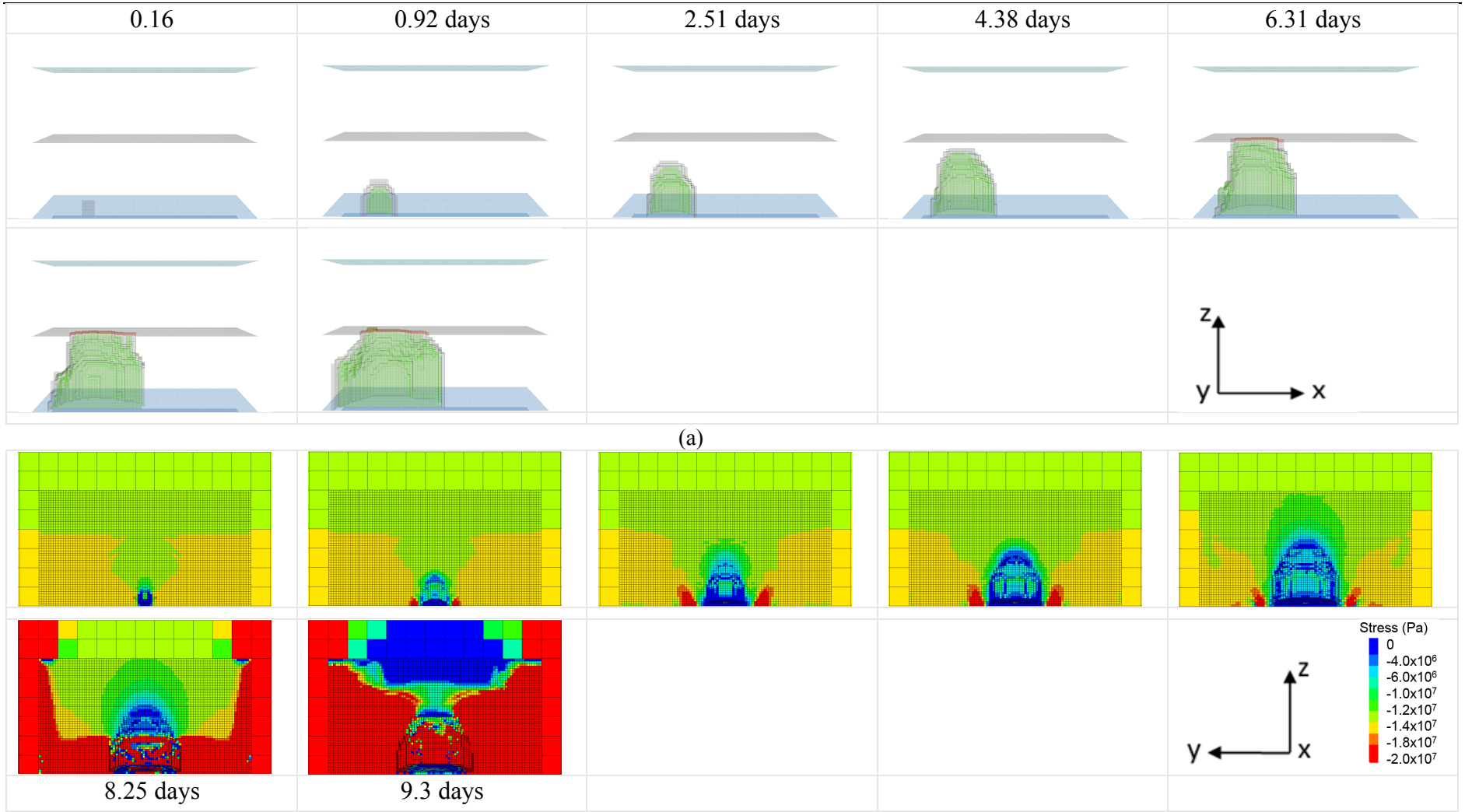


**Figure 6.14:** Representation of (a) cavity growth (x-z plane) and (b) vertical stress distribution (y-z plane) around the UCG cavity in different time periods during a 6m thick YiHe lignite seam gasification model run with oxygen at 600m depth (Sections taken from Figure 6.1)

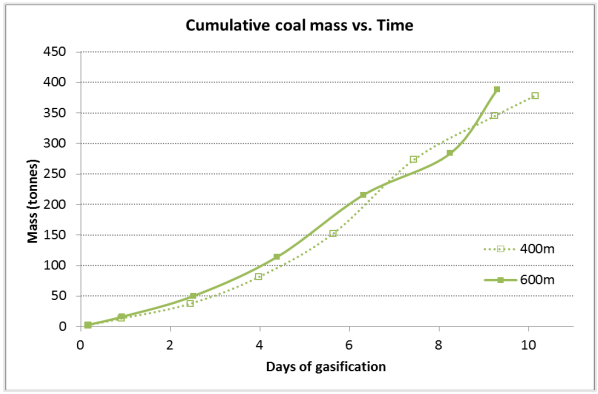


(a)

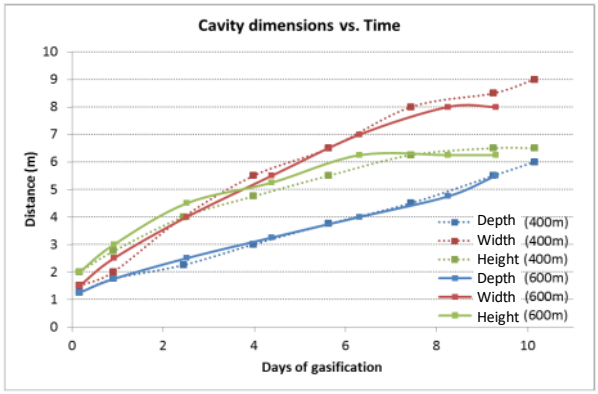


(b)

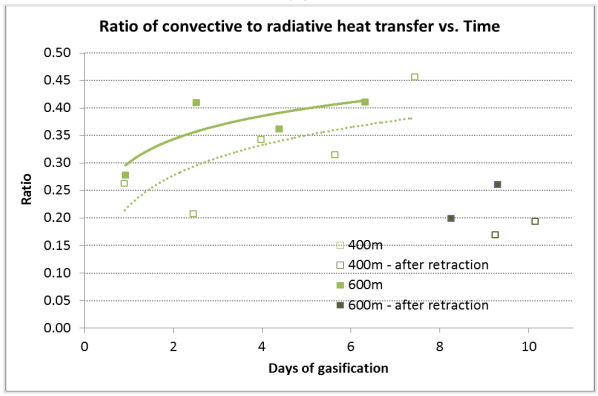


(c)

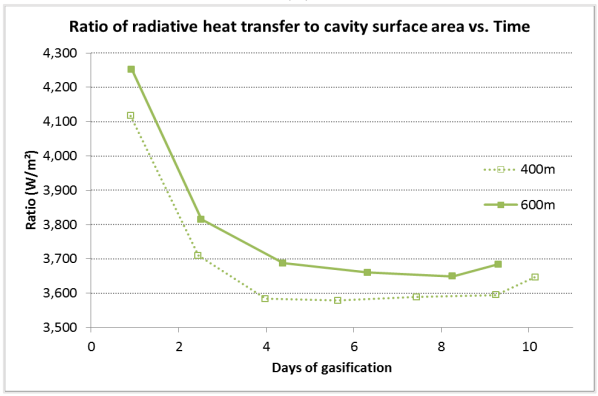


(d)

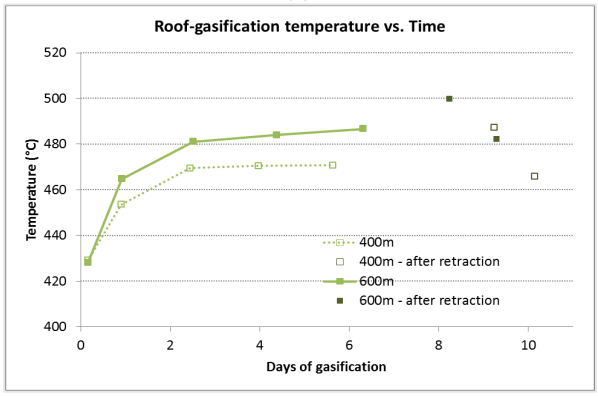


(e)

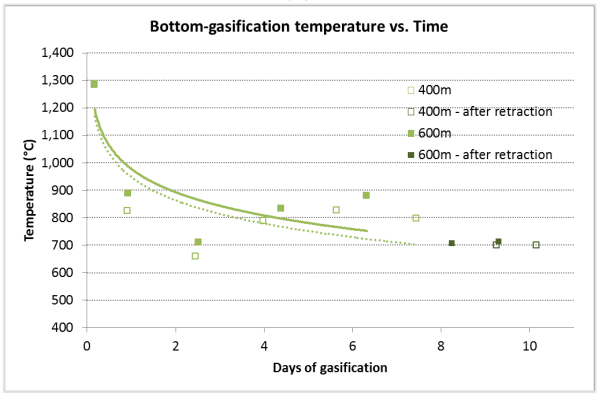


(f)

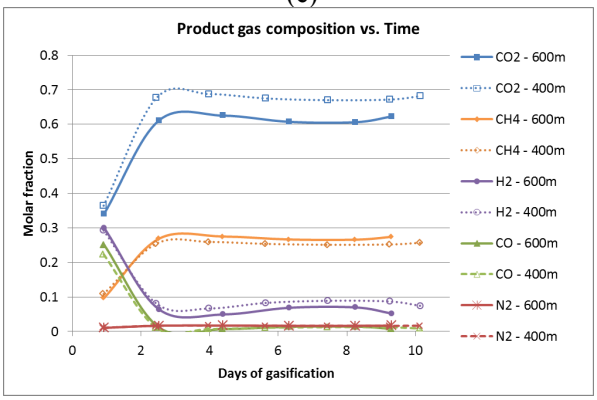


(g)

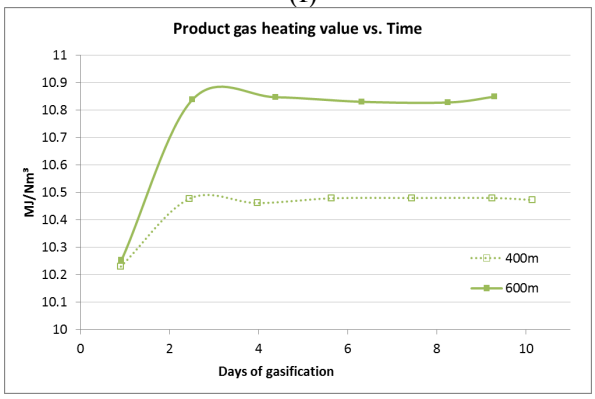


(h)

**Figure 6.15:** Comparison of different performance indicators plotted against UCG run time for the 6m thick YiHe lignite gasification simulations with oxygen at 400m and 600m depths.

Different performance indicators presented in Figure 6.15 confirm the same overall performance observed for the Velenje lignite. The mass of the consumed coal does not differ significantly between the different depth scenarios. As Figure 6.15a shows, in both cases approximately 380 tonnes of coal are consumed (388 tonnes at 600m and 378 tonnes at 400m). However, until retraction, the coal consumption rate is higher at 600m depth compared to 400m depth. Figure 6.15b illustrates that UCG cavity at 400m develops more gradually compared to that at 600m. As the volume of the cavity increases the effect of the convective heat transfer increases. When the retraction takes place the convective to radiative heat transfer ratio drops rapidly as the retraction stimulates the radiative heat transfer mechanism.

As Figure 6.15d illustrates, the higher radiative heat flux values at 600m depth is the reason for the higher roof and bottom stage gasification temperatures (Figure 6.15e-Figure 6.15f) as well as for the higher ratio of the thermally failed coal in Figure 6.14b. Finally, the effect of the depth on the product gas composition is consistent with that of the LAC Velenje lignite coal scenario.

## 6.4 *The UCG performance of Murcki – Staszic bituminous coal*

As Table 6.1 presented, a bituminous coal Murcki-Staszic was also selected for UCG simulation scenarios at different depths. Figure 6.16 and Figure 6.17 present cavity progression along with vertical stress distribution around the UCG cavity at different stages for 400m and 600m deep coal seam.

Figure 6.18a and Figure 6.18b confirm that thermal and mechanical failure processes acting upon the Murcki-Staszic bituminous coal at both depths are consistent with those observed and reported for the two lignites. However, the dimensions that the UCG cavities reach in equal number of days in the case of bituminous coal scenarios (Figure 6.19b) are significantly larger than those observed for the lignites. As a consequence, the thermo-mechanical properties of bituminous coal in combination with its high energy content facilitate a more combustible environment which is demonstrated through the development of larger volume cavities.

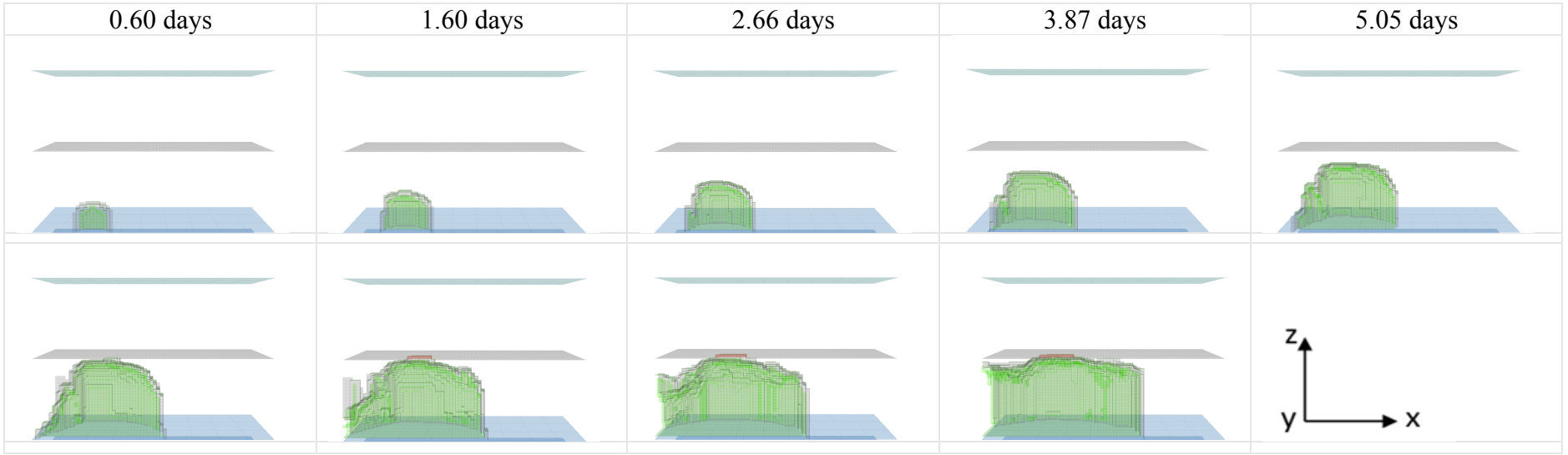


(a)

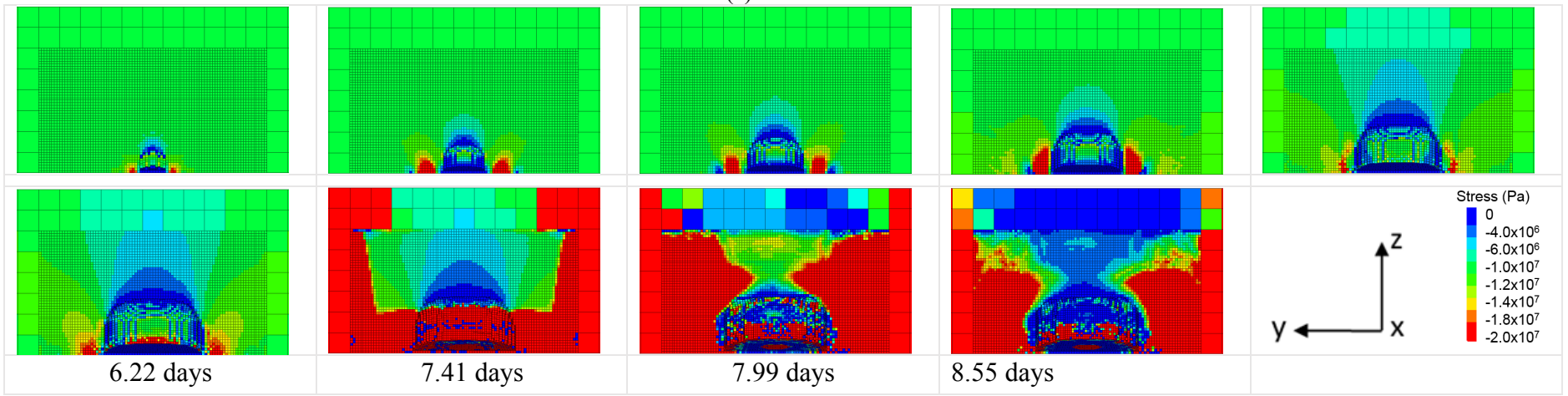


(b)

**Figure 6.16**: Representation of (a) cavity growth (x-z plane) and (b) vertical stress distribution (y-z plane) around the UCG cavity in different time periods during a 6m thick Murcki – Staszic bituminous coal seam gasification model run with oxygen at 400m depth (Sections taken from Figure 6.1).

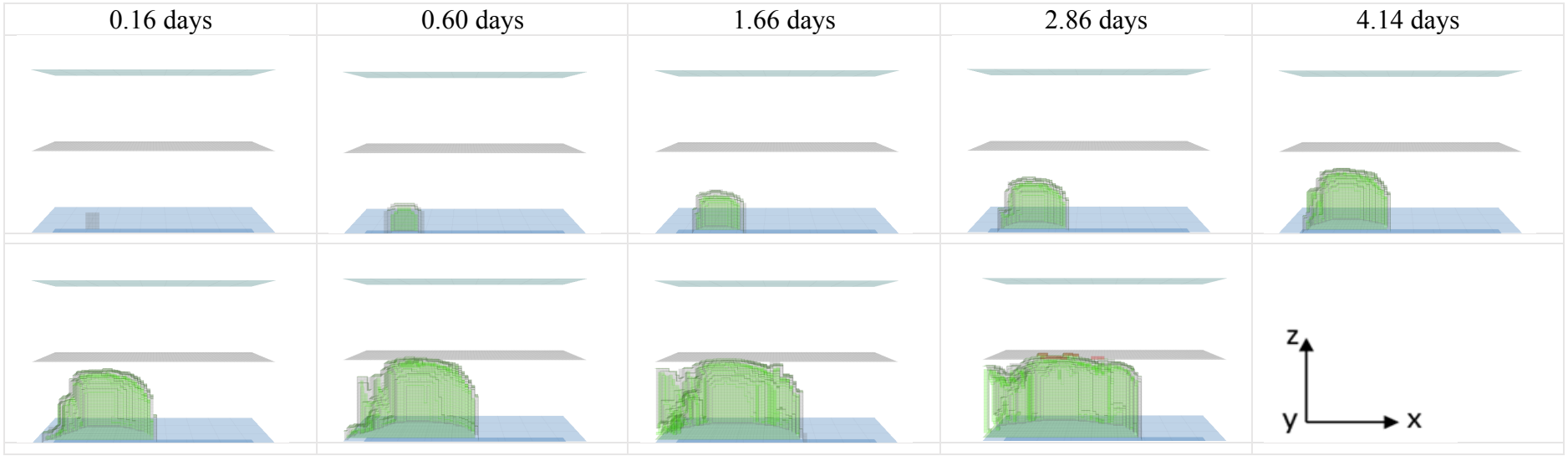


(a)

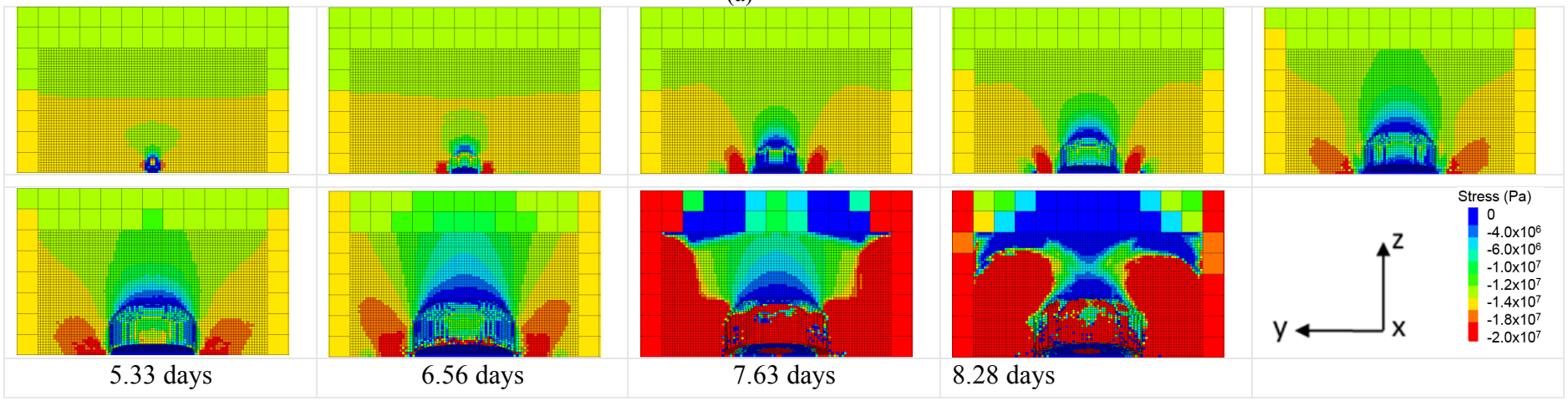


(b)

**Figure 6.17:** Representation cavity growth (x-z plane) and (b) vertical stress distribution (y-z plane) around the UCG cavity in different time periods during a 6m thick Murcki – Staszic bituminous coal seam gasification model run with oxygen at 600m depth (Sections taken from Figure 6.1).

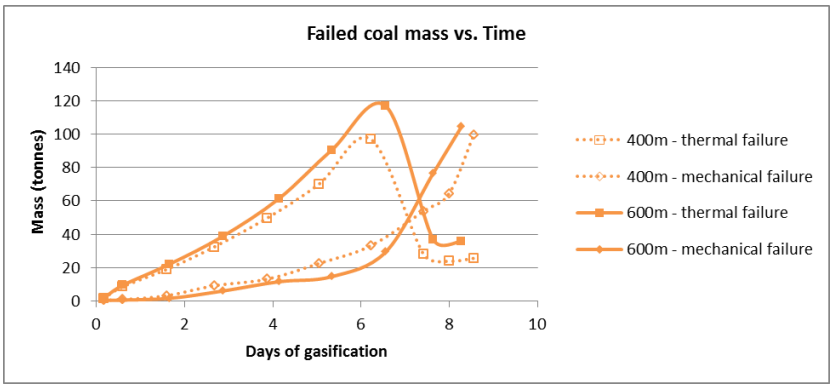


(a)

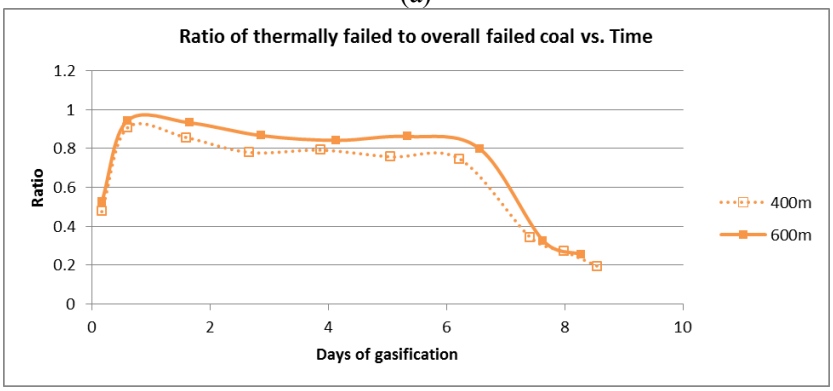


**Figure 6.18:** (a) Failed coal due to thermal and mechanical failure and (b) ratio of thermally failed to total failed coal mass at different stages of the UCG process during 6m thick Murcki – Staszic bituminous coal simulations with oxygen at different depths.

Compared to that observed for the lignites, the ratio of convective to radiative heat transfer rates for the Murcki – Staszic bituminous coal are relatively low, suggesting a rather restricted role of the convective heat transfer mechanism in the bituminous coal scenarios (Figure 6.19c).

As Table 6.5 presents, the high pressure in-situ trials conducted in El Tremedal in Spain (Nourozieh et al., 2010; Shafirovich and Varma, 2009) can be a reliable benchmark for the evaluation of the bituminous coal simulation results.

**Table 6.5**: Comparison of the product gas composition between the El Tremedal trial and the coupled TMC model simulation results for the Murcki – Staszic bituminous coal.

| Source | Depth | Pressure (bar) | $N_2$ (%) | CO (%) | $CO_2$ (%) | $H_2$ (%) | $CH_4$ (%) | Heating Value ($MJ/Nm^3$) |
|---|---|---|---|---|---|---|---|---|
| Simulation | 400m | 40 | 2 | 8.5 | 47 | 22 | 23.8 | 12.3 |
| El Tremedal | 550m | 50 | 1 | 8-14 | 35-44 | 24-25 | 15-26 | 10.9-11.0 |
| Simulation | 600m | 60 | 2 | 9 | 43 | 20 | 28 | 13.1 |

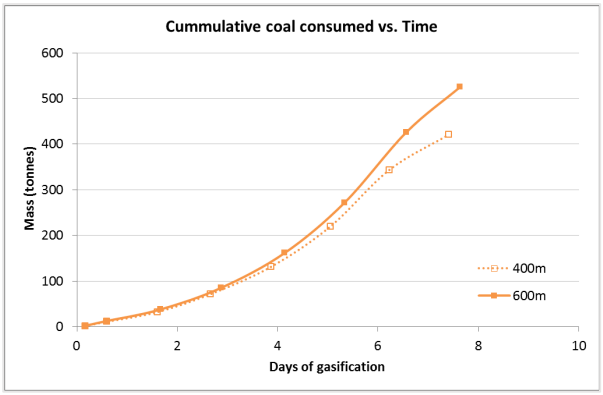


(a)

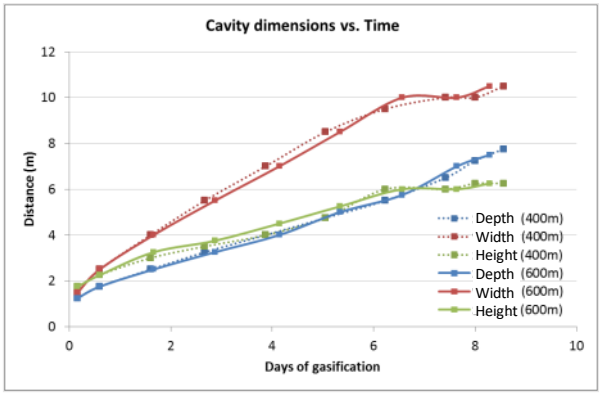


(b)

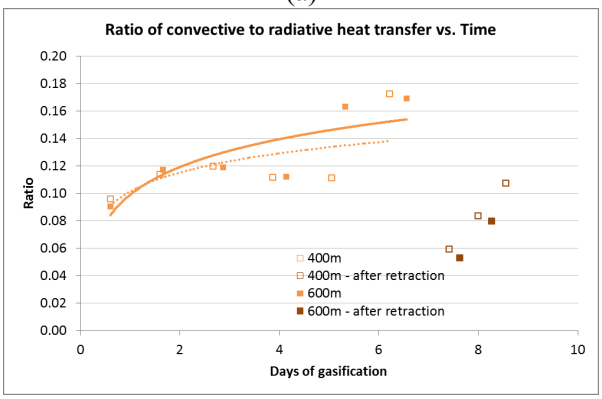


(c)

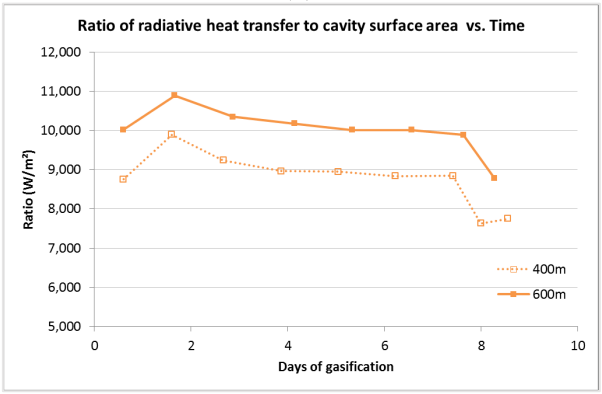


(d)

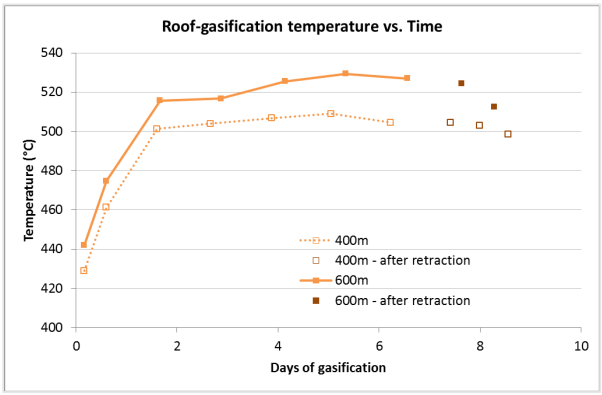


(e)

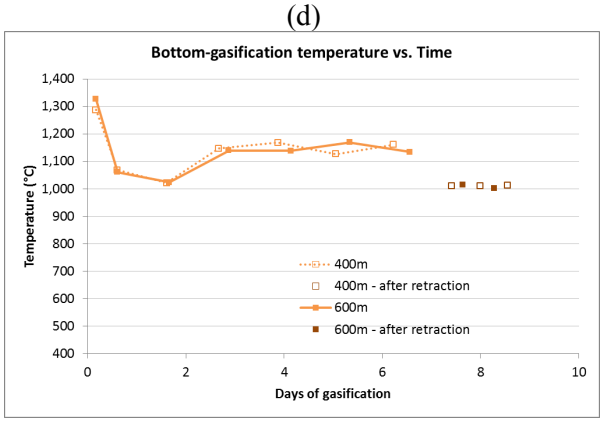


(f)

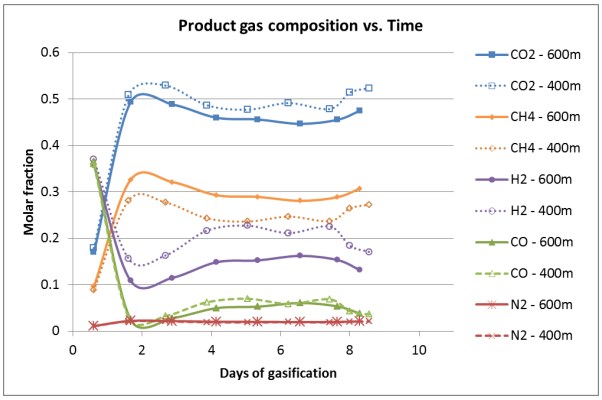


(g)

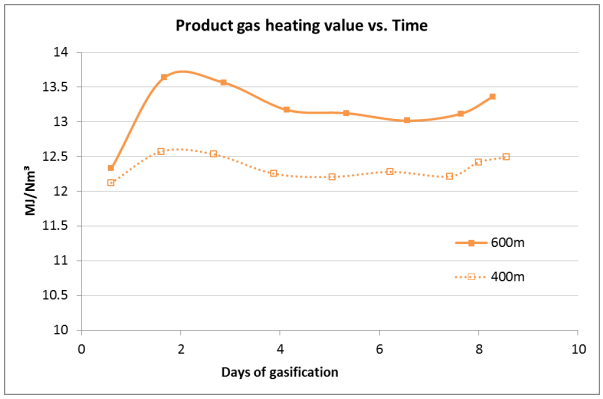


(h)

**Figure 6.19:** Comparison of different performance indicators plotted against UCG run time for the 6m thick Murcki – Staszic bituminous coal gasification simulations at with oxygen 400m and 600m depths.

High pressure in situ trials are quite scarce in the UCG literature and past high pressure simulation studies with bituminous coals (Kariznovi et al., 2013; Nourozieh et al., 2010) have all compared their findings with the El Tremedal results. However, the product gas composition comparisons can only be approximated against a range of values available for the El Tremedal trials (Table 6.5).

For the 400m depth simulation, the carbon dioxide ($CO_2$) content is slightly higher than the upper limit of the corresponding value for the El Tremedal trials. The reason for this difference could be the lower operating pressure which ultimately leads to the development of lower temperatures. In fact, in the case of 600m depth simulation, the operating pressure is higher and, as a result, the higher operating temperatures lead to reduced carbon dioxide ($CO_2$) content in the product gas. Furthermore, the 600m depth simulation shows that the methane ($CH_4$) content of the product gas is slightly higher than the upper limit value for the El Tremedal trials. In addition, the simulated hydrogen ($H_2$) content is slightly lower than the lower limit for the El Tremedal results. Both these differences can be explained by the effect of the methanation reaction ($C + 2H_2 \rightarrow CH_4$). Gregg and Edgar (1978) have already commented on why equilibrium modelling studies can overestimate the methane proportions. As the reaction rate of methane formation at low temperatures is slow, the formation rate is determined by the kinetic rates rather than the equilibrium conditions.

## 6.5 *Air vs oxygen injection as the gasification reagent*

As discussed earlier, an additional simulation scenario aiming to investigate the effect of the injected oxidant type on the UCG process performance was set up using a 6m thick Murcki – Staszic bituminous coal seam at 600m depth and using air as the injected reagent. The high energy content of bituminous coals can reduce the negative impact of air injection on the heating value of the produced gas (Shafirovich and Varma, 2009). In the case of oxygen injection scenarios, the ratio of injected $O_2$ over gasified coal was 1:3, while the corresponding $H_2O$/coal ratio was close to 2:3, which are in line with laboratory experimental observations (Daggupati et al., 2010) and field trials (Wiatowski et al., 2012).

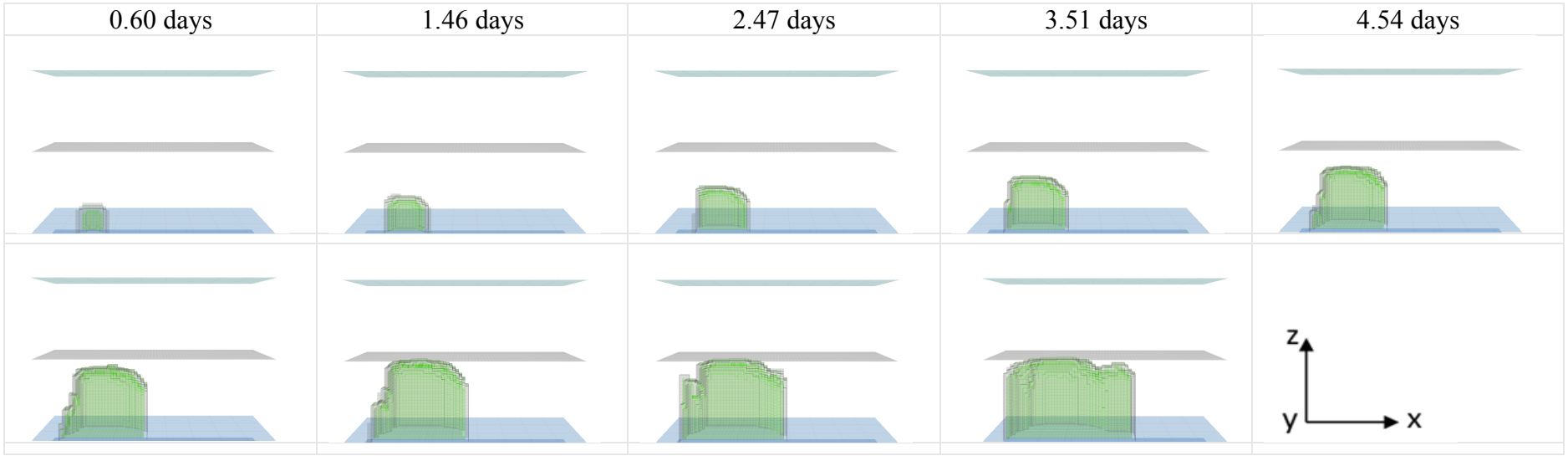


(a)

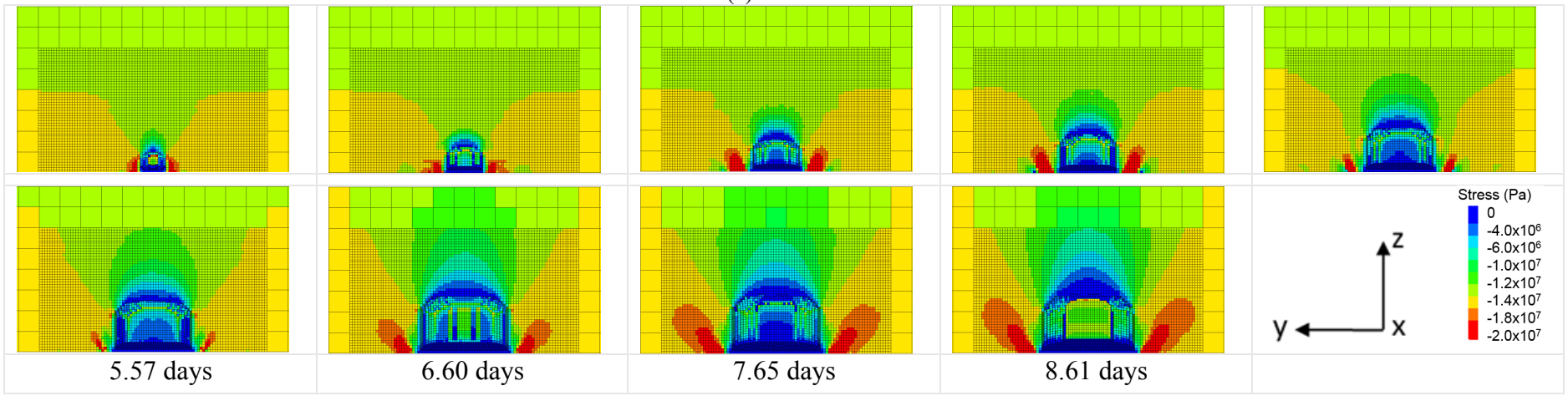


(b)

**Figure 6.20:** Representation of (a) cavity growth (x-z plane) and (b) vertical stress distribution (y-z plane) around the UCG cavity in different time periods during a 6m thick Murcki – Staszic bituminous coal seam gasification model run with air at 600m depth (Sections taken from Figure 6.1).

On the other hand, the ratio of the injected air over gasified coal was equal to 2:3 proving the higher requirement for air injection compared to oxygen during the different types of gasification. This was also confirmed by the ex-situ experiments conducted with bituminous coals by Stańczyk et al. (2011) that a stable operation was achieved with an $O_2$/air ratio of 2:3, while the corresponding ratio for the lignite experiments was 4:2, indicating that air injection is better suited to bituminous coals rather than lignites (Stańczyk et al., 2011). Figure 6.20 presents model results for cavity growth and vertical stress distribution around a 6m thick Murcki – Staszic bituminous coal seam at 600m depth and using air as the injected reagent.

As Figure 6.23b illustrates, the cavity dimensions under the oxygen injection are considerably larger than that observed under the air injection scenario. The largest difference is experienced along the width of the growing cavity. Under oxygen injection, cavity growth rates along its width and depth were found to be 1.27m/day and 0.91m/day, while the same under air injection were 1.05m/day and 0.81m/day respectively. However, the simulation results suggest that expansion of the growing cavity along its height is not largely affected by the type of the injected oxidant. In their review of different field trials, Perkins and Sahajwalla (2006) refer to the reduced cavity growth rates under air injection as well as the increased cavity expansion rates as the depth and the operating pressure increases.

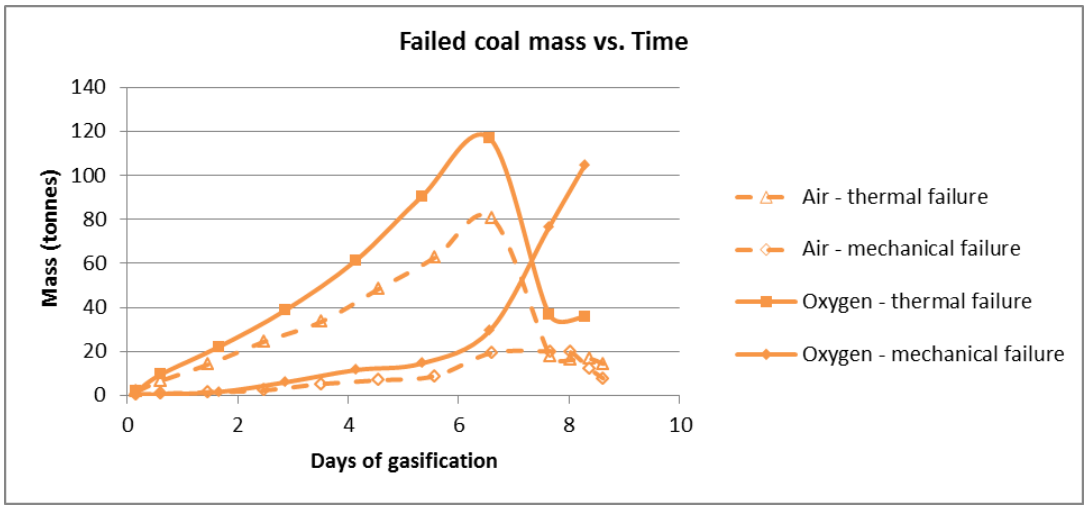


**Figure 6.21:** Failed coal mass due to thermal and mechanical failure at different stages of the UCG process during 6m thick Murcki – Staszic bituminous coal simulations under air and oxygen injection at 600m depth.

Perkins and Sahajwalla (2006) report an average cavity growth rate of 0.7m/day increasing to over 1m/day as the operating depth/pressure increases, which is in general agreement with the simulation results reported in this thesis. As Figure 6.21 illustrates, oxygen injection leads to higher coal consumption rates compared to air injection. In particular, the thermally failed coal mass consumed under the oxygen injection scenario is consistently higher than that for air injection. The mass of the thermally failed coal peaks at the time of cavity reaching the roof. Simulations suggest that the thermally failed coal mass can decrease by up to 33% when air instead of oxygen injection is employed.

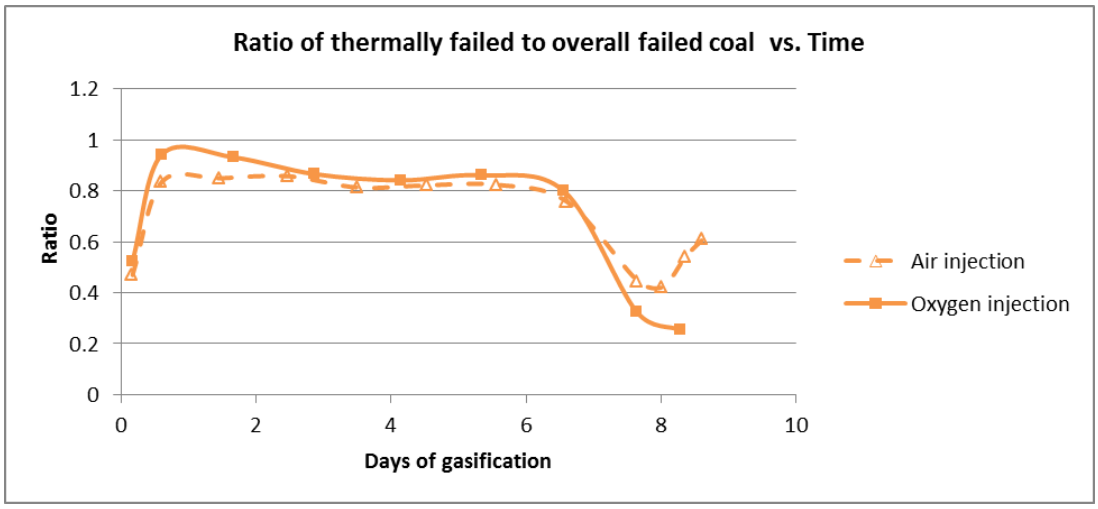


**Figure 6.22:** Ratio of thermal to overall failed coal at different stages of the UCG process during 6m thick Murcki – Staszic bituminous coal simulations studies under air and oxygen injection at 600m depth.

As Figure 6.17 and Figure 6.22 illustrate, faster lateral expansion of an oxygen injected cavity exerts larger vertical stresses on the rib side pillars and, in combination with the operating conditions, increases mechanical failure (spalling).

Figure 6.23c illustrates the significance of the role of the convective heat transfer mechanism during air injection. In addition, Figure 6.23d shows higher radiative heat flux values ($W/m^2$) experienced under the oxygen injection as compared to air injection. As a result, both roof- and bottom gasification temperatures are much higher under the oxygen injection (Figure 6.23e and Figure 6.23f), suggesting that radiative heat transfer mechanism is significantly more dominant under oxygen injection.

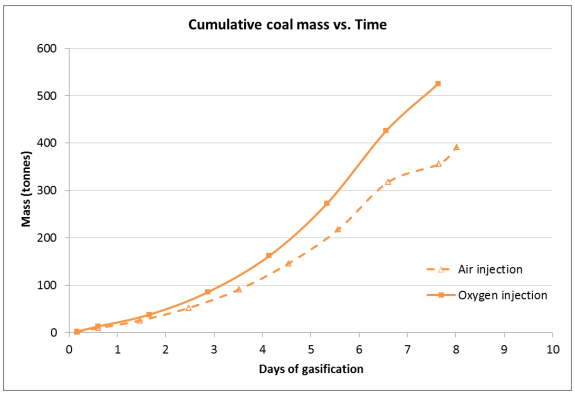


(a)

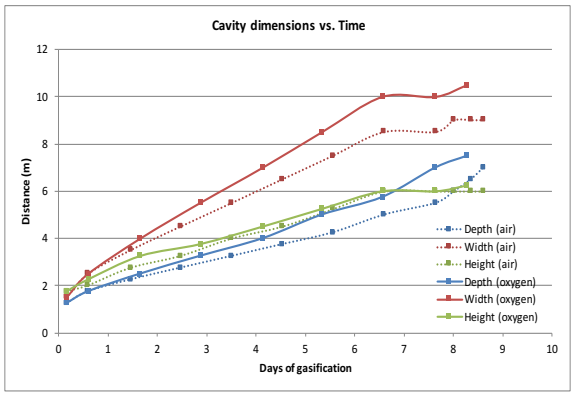


(b)

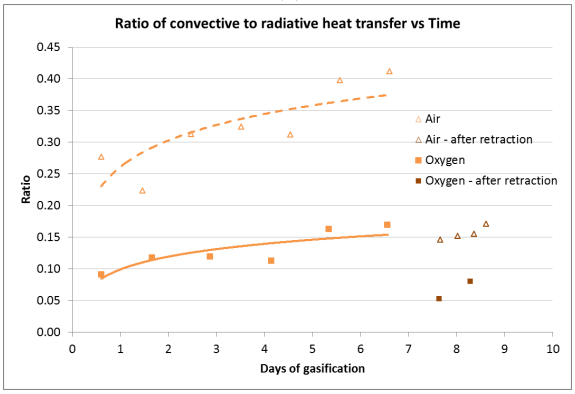


(c)

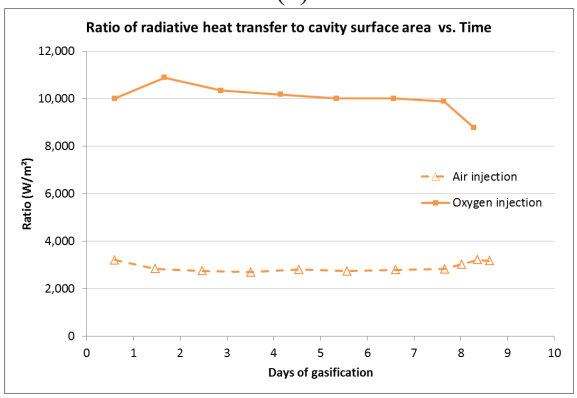


(d)

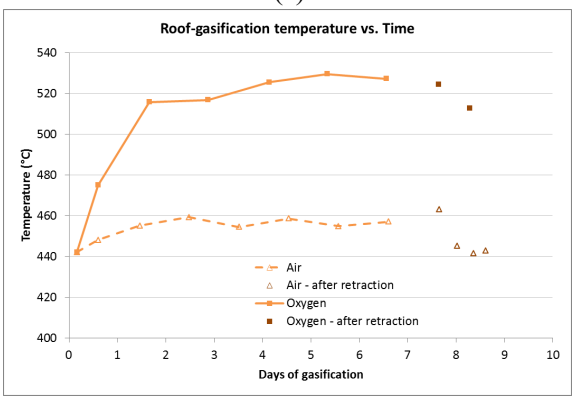


(e)

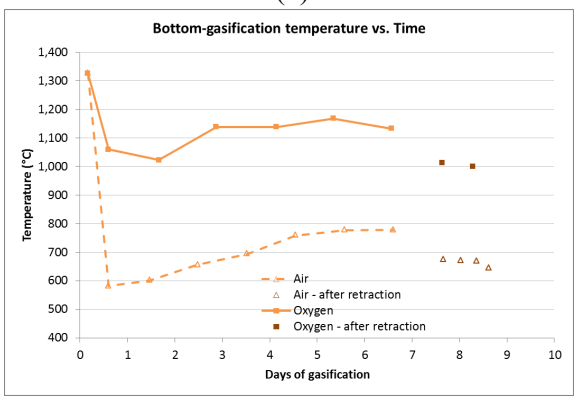


(f)

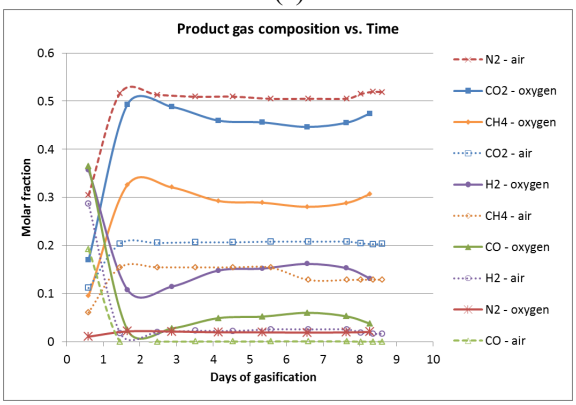


(g)

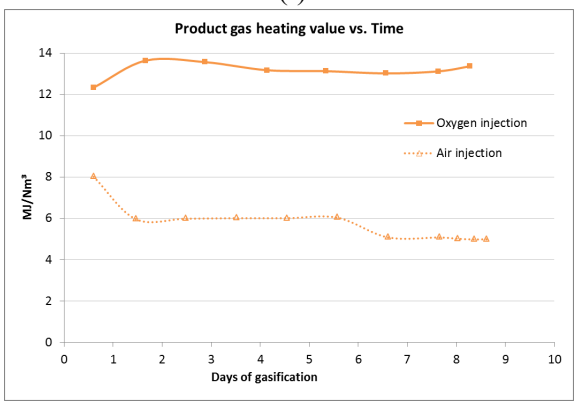


(h)

**Figure 6.23:** Comparison of different performance indicators plotted against UCG run time for the 6m thick Murcki – Staszic bituminous coal gasification under air and oxygen injection at 600m depth.

Finally, the compositions as well as the heating values of the product gases differ significantly between different oxidant injection scenarios (Figure 6.23e and Figure 6.23f). In the air injection scenario, the product gas molar fractions were determined as around 0.21 $CO_2$; 0.17 $CH_4$; 0.05 $H_2$; 0.02 CO; 0.52 $N_2$ when the oxygen injection based product gas yielded around 0.43$CO_2$; 0.28 $CH_4$; 0.20 $H_2$; 0.09 CO; 0.02 $N_2$ (Figure 6.23g). Especially, the lower methane ($CH_4$) and hydrogen ($H_2$) contents under the air injection scenarios lead inevitably to lower heating values for the product gas. As Figure 6.23h shows, under the oxygen injection scenario the product gas heating value varies around to 13.1 MJ/$Nm^3$ while the corresponding value under air injection scenario fluctuates around 5.7 MJ/$Nm^3$. These values are in agreement with literature data reported by Shafirovich and Varma (2009).

## 6.6 *Summary and Conclusions*

The applicability of the developed coupled UCG TMC process model was validated through the simulation of eight different scenarios. Three different coal types simulated at two different depths formed six out of the total eight scenarios. In addition, the type of injected reagent and the coal seam thickness were two parameters considered through the development of two further scenarios. The aim of this chapter was to understand the implications of operating parameters on UCG performance. For this reason, the simulation results were analysed on a coal type basis and results compared.

One bituminous coal and two lignites with different ash contents were simulated considering a seam thickness of 6m at 400m and 600m depths. Oxygen ($O_2$) injection was assumed across the first six simulation scenarios with a consistent seam thickness at 6m. In addition, the fracturing tendency of the lignite coals made evident the need for a higher seam thickness (10m vs. 6m) scenario.

Furthermore, the high heating value of the bituminous coal scenario facilitated the employment of air (79% $N_2$ – 21% $O_2$) instead of oxygen ($O_2$) injection. The results showed that the type of the injected oxidant affects significantly the heating value of the product gas. Air instead of oxygen ($O_2$) injection reduced the product gas heating values. As a result, air injection is particularly relevant for coal types with high heating value as they can balance the negative effect of air injection.

Deeper coal seams led to elevated operating pressures. As the results have shown, elevated pressures increase the coal consumption rate. Furthermore, the comparison of the radiative and convective heat transfer mechanisms among the different depth scenarios led to two conclusions. Firstly, the convective heat transfer mechanism has higher involvement in the heat distribution process as the cavity volume increases and secondly, the radiative heat transfer mechanism benefits from the high temperatures developed at the floor of the cavity (bottom stage gasification). The radiative heat transfer mechanism remained the dominant mechanism across all the simulated scenarios.

Moreover, the operational pressure and temperature conditions had a direct impact on the product-gas compositions. In 400m depth simulations higher carbon dioxide ($CO_2$) and lower methane ($CH_4$) contents were obtained compared to their values at 600m depth. Methane ($CH_4$) content was found to dominate the product-gas heating values. Therefore, the elevated pressure conditions at 600m depth led to higher methane ($CH_4$) contents across all simulated scenarios and finally to product gases with higher heating values.

# Chapter 7 Assessment of UCG Performance for Different Coals at Identical Operational Conditions

## 7.1 *Introduction*

This Chapter (Chapter 7) interprets and compares the results of all the UCG TMC model simulations for different coals and depths and oxidising reagents, characterising the most important properties that affect the UCG performance. First a comparison of some of the UCG processes is presented against seam depth. Next an overall comparison of properties such as cavity growth, product gas composition and heating value are compared for all the coals modelled under different depths.

The model results compared refer to the same scenarios described before where a 6m thick Velenje lignite, YiHe lignite and Murcki – Staszic bituminous coal at 400m and 600m depth were simulated with oxygen as the reagent. One further oxygen blown model was run for a 10m thick Velenje lignite at 600m depth. The final model was run with a 6m thick Murcki – Staszic bituminous coal at 600m depth and with air as the reagent.

Table 7.1 presents the parameters of the scenarios included within the subsequent comparisons (i.e. Chapters 7.2-7.3).

**Table 7.1**: Classification of the parameters for the simulation scenarios

| **Seam** | **Type of injected** | **Seam** | **Coal rank** |
|---|---|---|---|
| 6 m | Oxygen | 400 m | Velenje Lignite coal (LAC) |
| | | | Yihe Lignite coal (HAC) |
| | | | Murcki – Staszic bituminous coal |
| | | 600 m | Murcki – Staszic bituminous coal |
| | | | Velenje Lignite coal (LAC) |
| | | | Yihe Lignite coal (HAC) |
| | Air | 600 m | Murcki – Staszic bituminous coal |
| 10 m | Oxygen | 600 m | Velenje lignite coal |

For each depth scenario (i.e. 400m and 600m) a number of performance indicators are studied against the time duration of the UCG process in order to specify where the effect of the coal rank is more significantly met during the UCG process. Specifically, the studied performance indicators are the following:

- *Cumulative coal mass consumed*
- *Product gas heating value*
- *Ratio of convective to radiative heat transfer*
- *Ratio of radiative heat transfer to cavity surface area*
- *Roof-stage gasification temperature*
- *Bottom-stage gasification temperature*
- *Thermally failed coal*
- *Mechanically failed coal*
- *Grashof number*
- *Reynolds number*
- *Archimedes number*
- *Rayleigh number*

## 7.2 *Results and Conclusions of Coupled TMC Model Scenarios*

Figure 7.1 and Figure 7.2 demonstrate that both the roof and bottom gasification temperatures for all coals are higher at greater depth and higher rank Murcki – Staszic bituminous coal generate higher temperatures than those for the two lignites.

The figures (Figure 7.1 and Figure 7.2) also confirm that the ash content of coal plays a significant role on the levels of gasification temperatures developed and the low ash content Velenje lignite develop higher temperatures compared to high ash content YiHe lignite. For all coal types, the temperatures are lower at the boundaries of the growing cavity where more steam is participating in the reactions and higher at the bottom of the cavity which is closer to the combustion stage. These temperatures were found to be in agreement with ex-situ experiments by Daggupati et al. (2011b) and the modelling studies by Britten (1986).

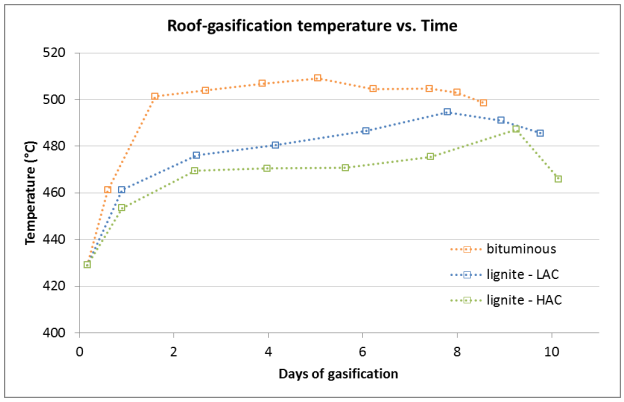


(a)

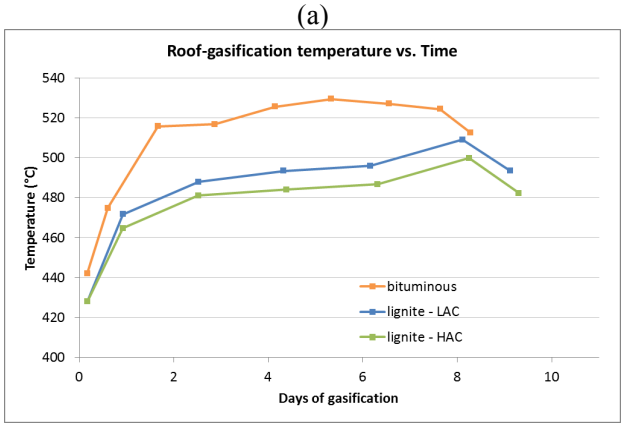


(b)

**Figure 7.1:** Roof gasification temperatures over model simulation time at (a) 400m and (b) 600m depth for 6m thick LAC Velenje lignite, HAC YiHe lignite and the Murcki – Staszic bituminous coal

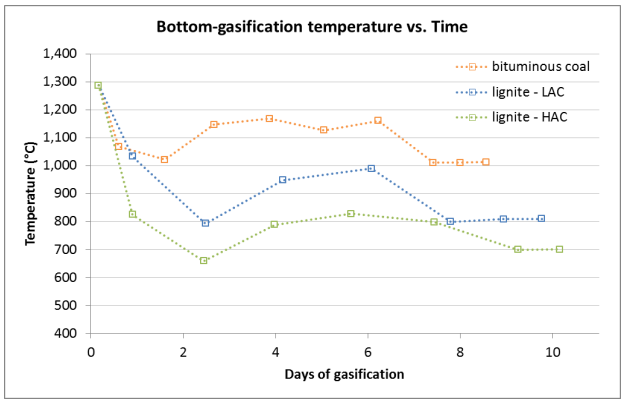


(a)

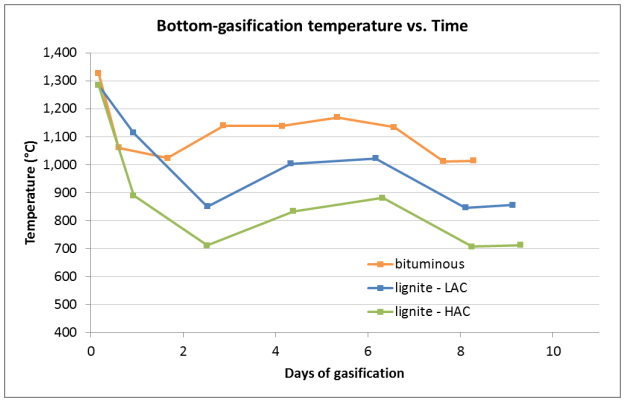


(b)

**Figure 7.2:** Bottom gasification temperatures over model simulation time at (a) 400m and (b) 600m depth for 6m thick LAC Velenje lignite, HAC YiHe lignite and the Murcki – Staszic bituminous coal.

Figure 7.3 illustrate that radiative heat flux acting upon the cavity surfaces will be significantly higher for the bituminous coals since high coal calorific value coals lead to the development of high temperatures, which eventually lead to higher radiative heat fluxes. Furthermore, increased depth, therefore the pressure, also leads to higher temperatures and radiative heat fluxes.

Figure 7.1 and Figure 7.5 confirm that coals which develop higher roof stage gasification temperatures lead to higher thermally failed (roof gasified) coal masses and, higher cavity operating pressures at depth lead to even higher roof gasification rate. However, a comparison between Figure 7.4b and Figure 7.5b also suggest that, depending on depth, coal rank also plays an important role on the rate of mechanical failure (spalling).

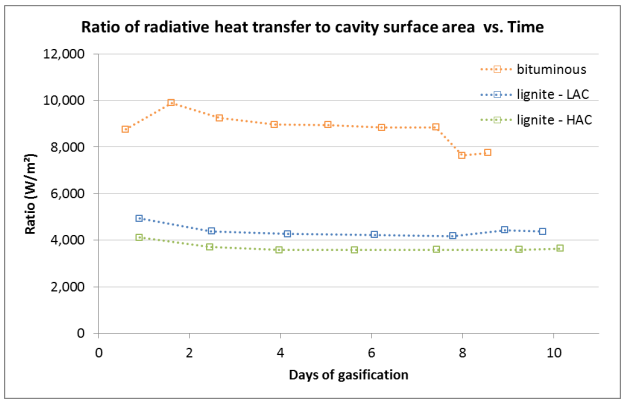


(a)

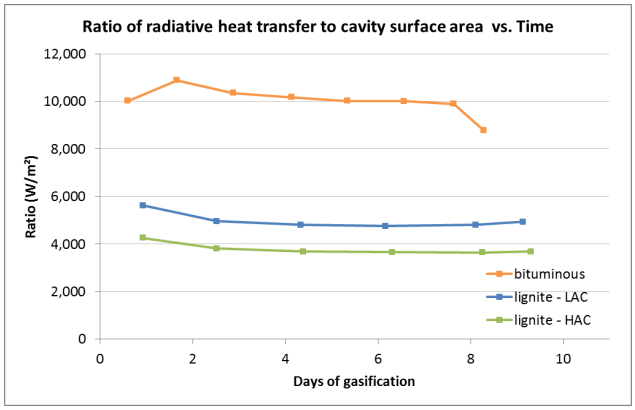


(b)

**Figure 7.3:** Ratio of radiative heat flux over model simulation time at (a) 400m and (b) 600m depth for 6m thick LAC Velenje lignite, HAC YiHe lignite and the Murcki – Staszic bituminous coal.

By observing the Figures 7.4 - 7.5 it is clear that the cavity growth rate controls the mechanical stresses developed around the cavity and, when the cavity growth rate reaches a critical value at a given depth, the rate of mechanical failure increases without being as much dependent on the rate or distance of retraction. The figures suggest that this growth rate is reached at much shallower depths for the bituminous coals. Furthermore, greater spalling rates developing at depth would further accelerate the cavity growth rates as highlighted by Perkins and Sahajwalla (2006).

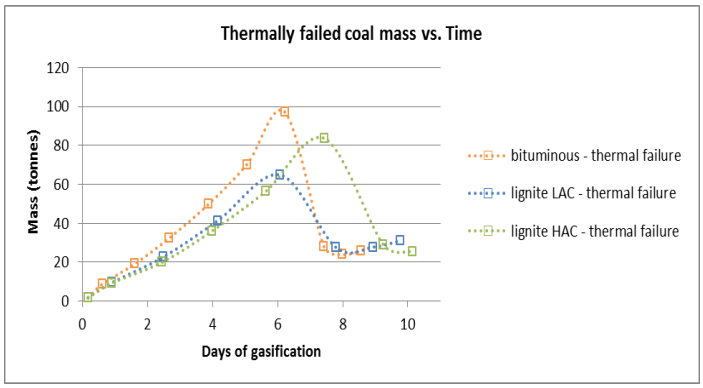


(a)

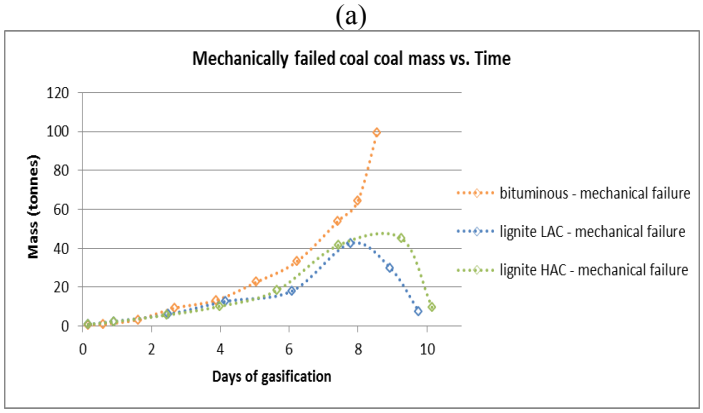


(b)

**Figure 7.4:** (a) Roof gasified (thermally failed) coal and (b) mechanically failed (spalled) coal for 6m thick LAC Velenje lignite, HAC YiHe lignite and the Murcki – Staszic bituminous coal during the simulations at 400m depth.

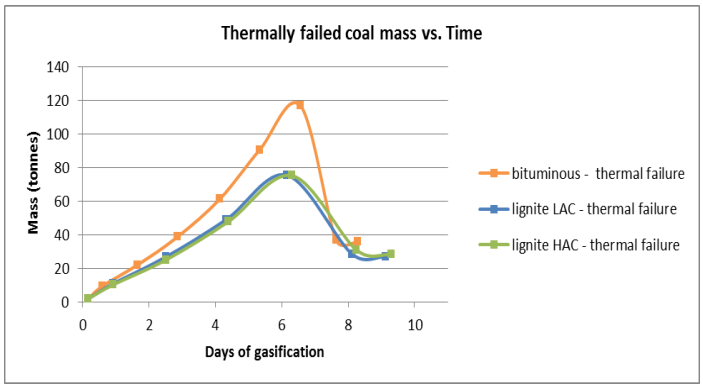


(a)

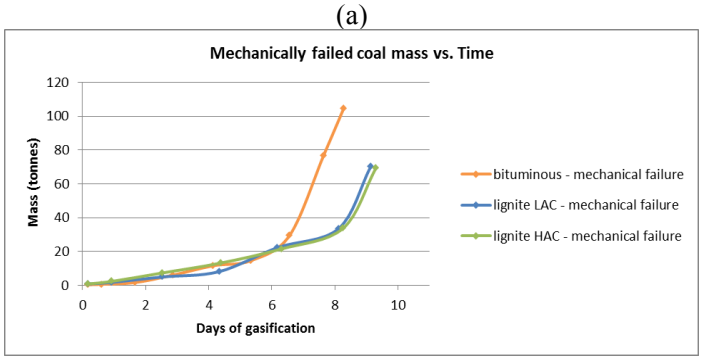


(b)

**Figure 7.5:** (a) Roof gasified (thermally failed) coal and (b) mechanically failed (spalled) coal for 6m thick LAC Velenje lignite, HAC YiHe lignite and the Murcki – Staszic bituminous coal during the simulations at 600m depth.

As Figure 7.6 illustrates, higher roof gasification temperatures, radiative heat fluxes and thermal/mechanical failure rates discussed earlier for the bituminous coals lead to significantly higher coal consumption rates during the UCG process. This necessarily leads to the development of higher volume of UCG cavities and, naturally, the coal consumption rates are higher for all coals as the UCG becomes deeper (Figure 7.6b).

In addition, if the retraction of the injection point is relatively late or delayed (as was the case for the HAC YiHe lignite during the 400m depth seam simulations presented in Figure 7.6a) this would also lead to the expansion of the UCG cavity, higher coal consumption rates and, potential roof failure if not addressed early enough.

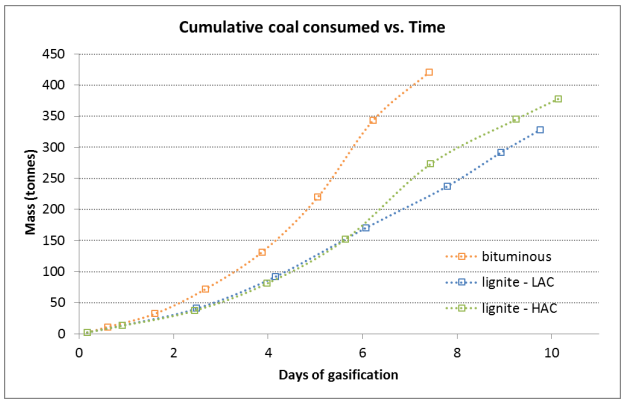


(a)

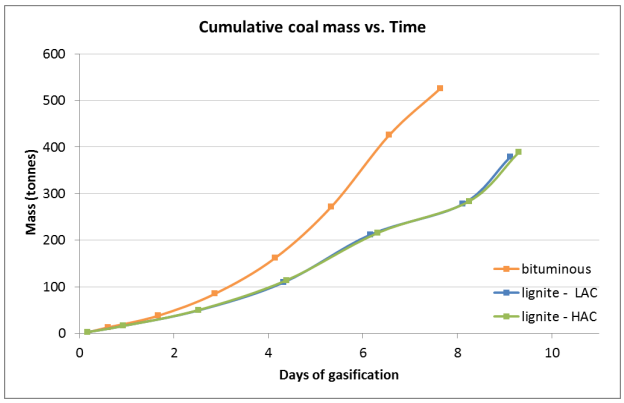


(b)

**Figure 7.6:** Cumulative coal mass consumed against UCG run time (a) at 400m depth and (b) at 600m depth for the 6m thick LAC Velenje lignite, HAC YiHe lignite and the Murcki – Staszic bituminous coal during the simulations.

As discussed in the above paragraphs, UCG at different depths and/or with different thicknesses of coal affect the gasification temperatures formed, the cavity growth rates and the mass of coal consumed during the process. Cavity and gasification temperatures, developed as a function of coal type/rank and depth, propagate within the strata and result in both the thermal and mechanical failure of the coal and rock depending on the thermo-mechanical properties of the rocks. Figure 7.7 compares the temperatures developed around an oxygen blown UCG cavity for 6m and 10m thick LAC Velenje lignite seam at equal depths (600m). The three temperature profiles taken from the model represent the strata temperatures through and ahead/above the cavity at equal model time steps for both model runs. As the figure demonstrates, in the case of thicker coal seams, the significantly lower thermal conductivities of coal seams slow down the rate of heat/temperature propagation through the strata surrounding the UCG cavity, and reduce/regulate the development of thermo-mechanical stresses as they are also illustrated in Figure 6.10b compared to Figure 6.3b.

The temperature profiles for all the time-stages during the UCG cavity growth and at different sections (AA', BB', CC' – as presented in Figure 6.1) can be found in the Appendix. In particular, the profiles for the Velenje LAC lignite coal at 600m depth and 6m seam thickness are shown in Figure A.3 and Figure A.4, while the corresponding profiles for 10m seam thickness are presented in Figure A.5 and Figure A.6.

Figure 7.8, on the other hand, compares the effects of oxidising agent used on the strata temperatures developed around the UCG cavity for 6m thick Murcki – Staszic bituminous coal at 600m depth. The three temperature profiles taken from the model represent the strata temperatures through and ahead/above the cavity at equal model time steps for both model runs (also in Appendix Figure A.13-Figure A.16). It is clear that, the lower gasification temperatures developed during air blown UCG also results in lower temperature gradients around the cavity, a much reduced rib side stresses as illustrated in Figure 6.20b and Figure 6.17b smaller masses of thermally and mechanically failed/consumed coal in the process.

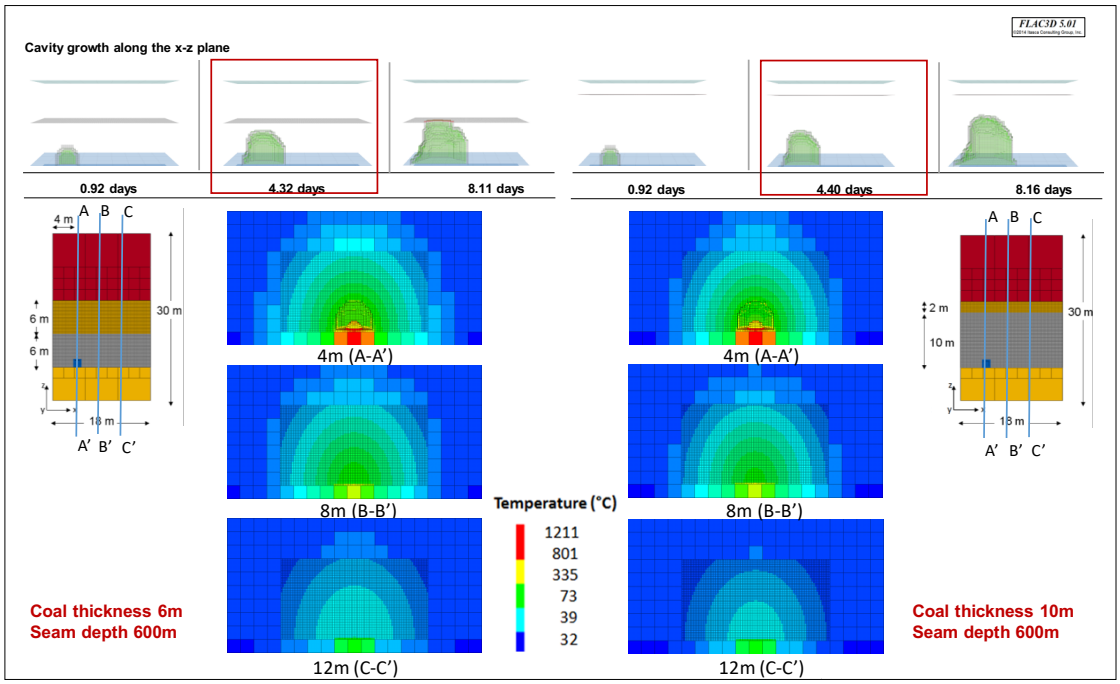


**Figure 7.7:** Comparison of the development of strata temperatures around the UCG cavity for 6m and 10m thick LAC Velenje lignite at 600m depth. Sections are taken on approximately 4.3-4.4 days after ignition at 4m, 8m and 12m into the model, through and ahead of the UCG cavity.

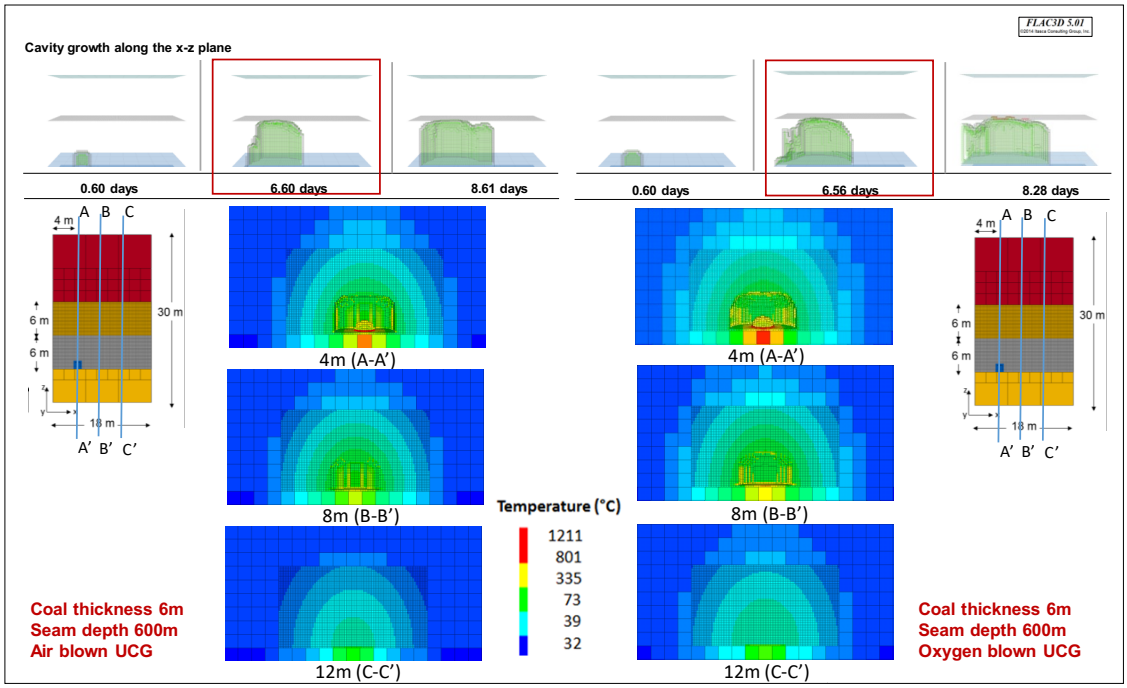


**Figure 7.8:** Comparison of the development of strata temperatures around the UCG cavity for 6m thick Murcki – Staszic bituminous coal at 600m depth. Sections are taken on approximately 6.5-6.6 days after ignition at 4m, 8m and 12m into the model, through and ahead of the UCG cavity.

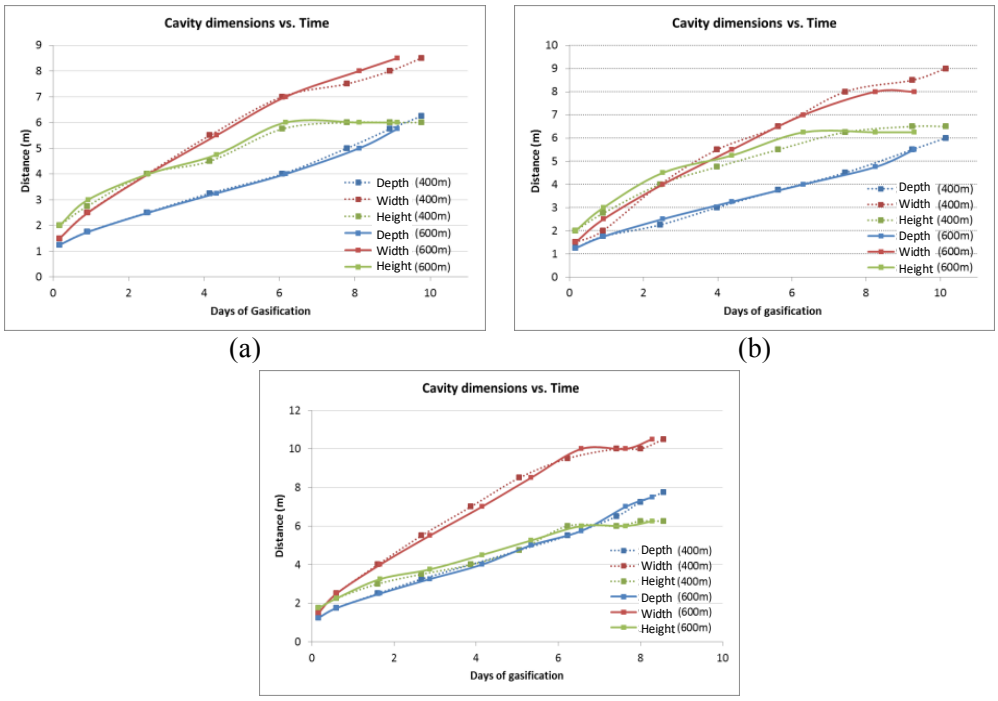


**Figure 7.9:** The development of cavity dimensions for 6m thick (a) LAC Velenje lignite, (b) HAC YiHe lignite and (c) Murcki – Staszic bituminous coal at 400 and 600m depths for oxygen blown UCG during the model runs.

Figure 7.9 compares the cavity growth rate for 6m thick two lignite and one bituminous coal seams at 400 m and 600m depths. As discussed in detail during the previous pages, the cavity growth trends for all the coals used in the scenarios are generally the same. The time of retraction of the injection point controls and steadies the growth of the cavity in its height, while its width and depth continue to grow. Slight differences in the timing of the retraction during different simulation runs were mainly due to slight differences in the cavity growth rate for different coals and at different depths, which may have resulted in slight deviations from the general trend. The figure also shows that, for equal coal thickness and depths, this rate will be relatively higher for the bituminous coals.

Figure 7.10 summarises the product gas compositions for 6m thick two lignite and one bituminous coal seams at 400 m and 600m depths. In general, the figures show similar trends for all the coals modelled. Higher temperatures at greater depths increase methane and carbon monoxide content in the produced gas with some reduction in the carbon dioxide and hydrogen contents.

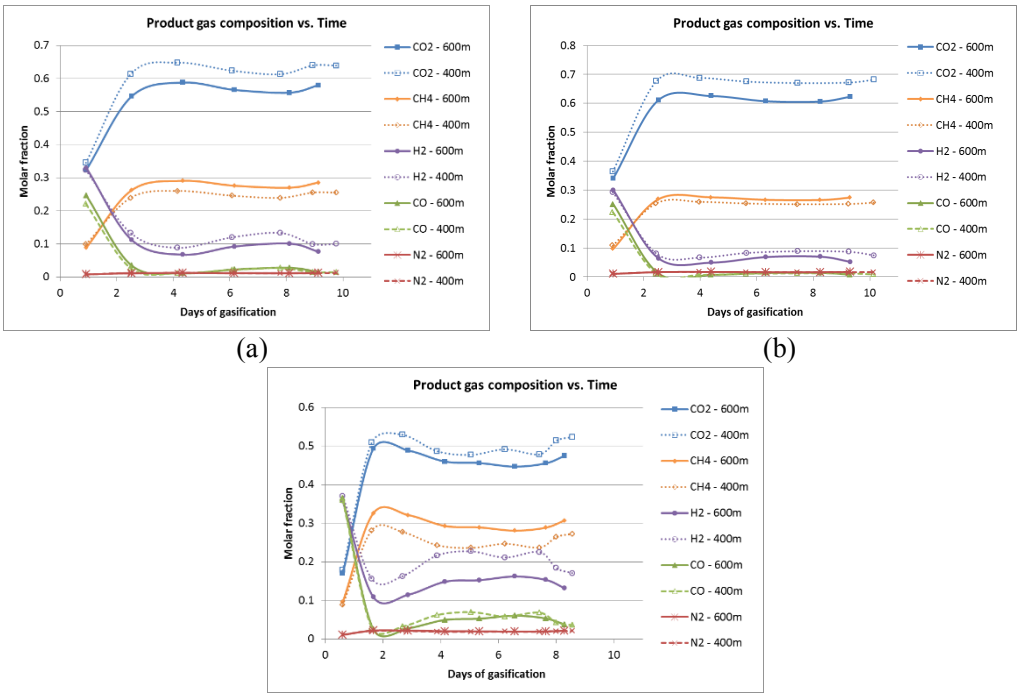


**Figure 7.10:** The product gas compositions for 6m thick (a) LAC Velenje lignite, (b) HAC YiHe lignite and (c) Murcki – Staszic bituminous coal at 400 and 600m depths for oxygen blown UCG during the model runs

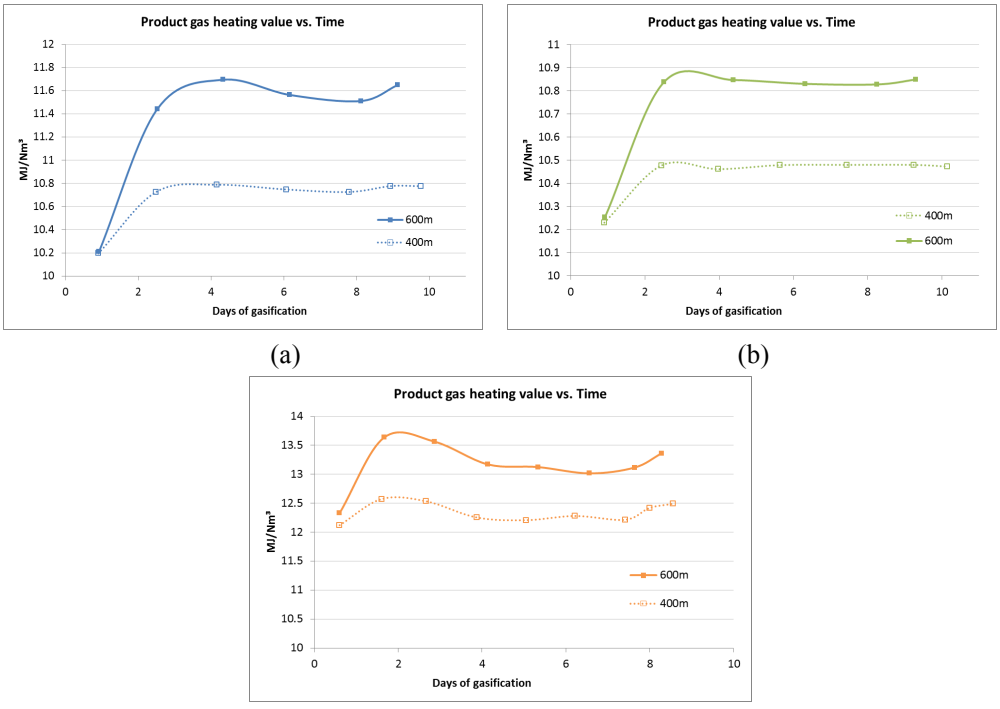


**Figure 7.11:** The product gas heating values for 6m thick (a) LAC Velenje lignite, (b) HAC YiHe lignite and (c) Murcki – Staszic bituminous coal at 400 and 600m depths for oxygen blown UCG during the model runs.

As Figure 7.11 illustrates, coal seams developing higher gasification temperatures (in the order Murcki – Staszic > LAC Velenje lignite > HAC YiHe lignite), or at higher operating pressures at greater depths lead to higher heating values. These model results also confirm the results obtained in the reactor experiments in the project, as well as published data in the literature (Stańczyk et al., 2012; Stańczyk et al., 2011; Stańczyk et al., 2010; Shafirovich and Varma, 2009). As Figure 7.12 indicates the Grashof number increases as the UCG process advances. The order magnitude of the corresponding values ($10^{12}$) is in accordance with UCG modelling studies (Perkins and Sahajwalla, 2007; Perkins and Sahajwalla, 2008). Furthermore, the parallel increase of the UCG cavity volume with its corresponding Grashof number indicates that the buoyancy forces increase their dominance over the viscous forces. In addition, Figure 7.12a showcases that during the LAC Velenje lignite coal study at 400m an early retraction (Figure 6.8b) in order to avoid extending the roof into the mudstone roof increases the viscous forces leading to slower growth of the Grashof number between the 7$^{th}$ and 8$^{th}$ day of the study.

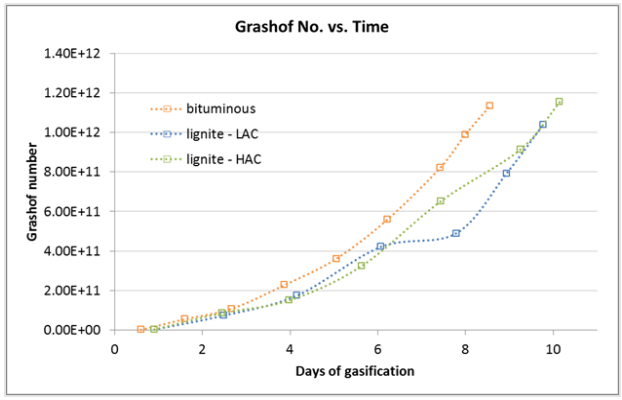


(a)

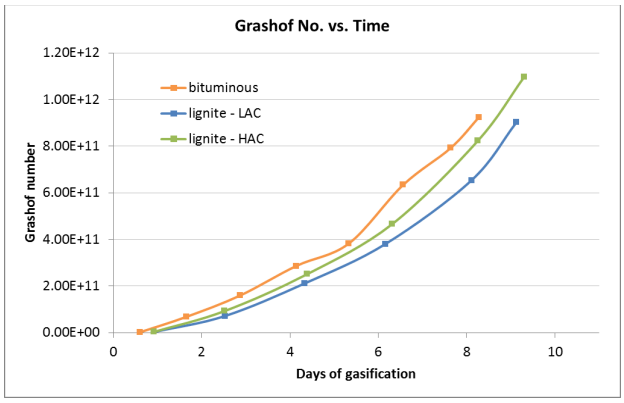


(b)

**Figure 7.12:** Grashof number against UCG run time (a) at 400m depth and (b) at 600m depth for the 6m thick LAC Velenje lignite, HAC YiHe lignite and the Murcki – Staszic bituminous coal during the simulations.

The size of the growing cavity, in combination with the viscosity and the density of the product gas (existing within the cavity), is responsible for the different Grashof number among the simulation scenarios (Figure 7.12).

On the other hand, as Figure 7.13 indicates the Reynolds number decreases as the UCG process advances. It can also be understood that the volume of the cavity developed under each coal type simulation scenario acts as the differentiating factor among the different scenarios. Furthermore, the Reynolds number presents the ratio of inertia-to-viscous forces reduces. The lignite HAC YiHe coal type, which has the slowest cavity growth rate among the three simulated coal types, achieves the highest Reynolds numbers during the UCG process (Figure 7.13), suggesting the steepest transition towards a less turbulent flow as the cavity grows.

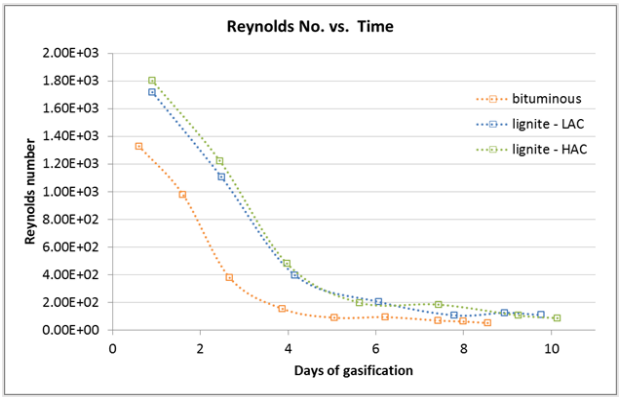


(a)

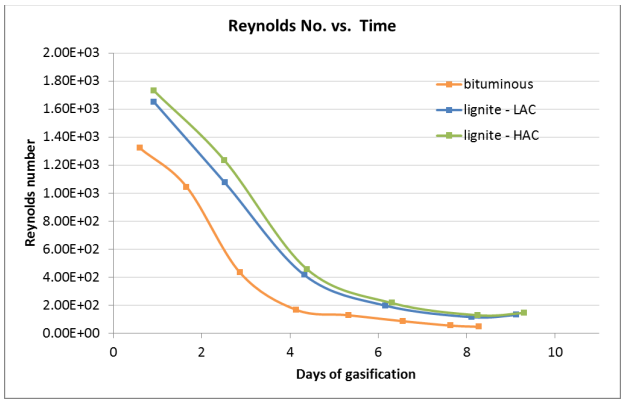


(b)

**Figure 7.13:** Reynolds number against UCG run time (a) at 400m depth and (b) at 600m depth for the 6m thick LAC Velenje lignite, HAC YiHe lignite and the Murcki – Staszic bituminous coal during the simulations.

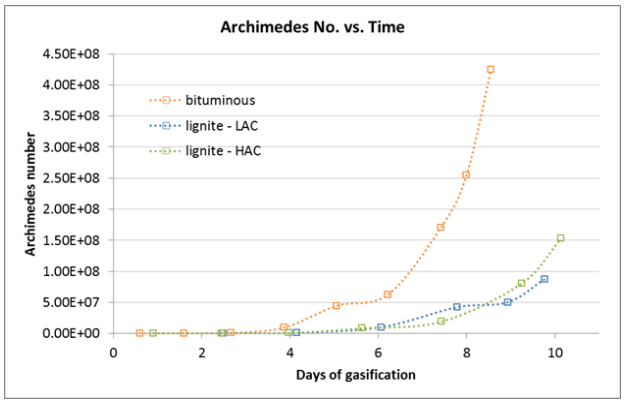


(a)

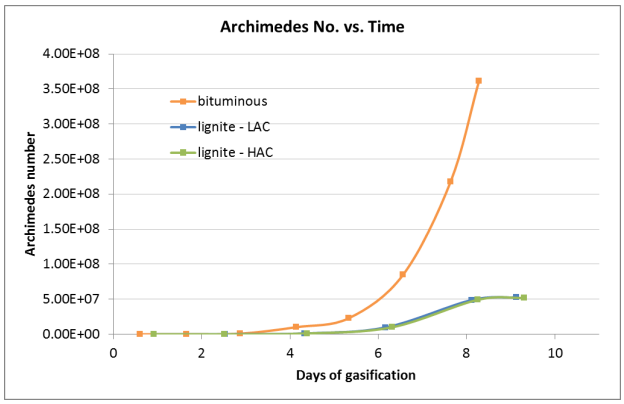


(b)

**Figure 7.14:** Archimedes number against UCG run time (a) at 400m depth and (b) at 600m depth for the 6m thick LAC Velenje lignite, HAC YiHe lignite and the Murcki – Staszic bituminous coal during the simulations

The calculation of the Grashof (Figure 7.12) and Reynolds numbers (Figure 7.13) facilitates the computation of the Archimedes number (Figure 7.14). This number represents the ratio of buoyancy to inertia forces and it is also an indicator of the whether natural or forced convection dominates the heat transfer convective mechanism. As it can be seen (Figure 7.14) the advance of the UCG process leads to the increase of the Archimedes number indicating that the natural convection becomes the dominant mechanism as the UCG cavity volume increases.

As Figure 7.14 indicates the Archimedes number curve is significantly higher under the bituminous coal type simulation scenario compared to the corresponding curves under the lignite coal scenarios. This observation leads to the conclusion that natural convection has a more dominant role under the bituminous scenario.

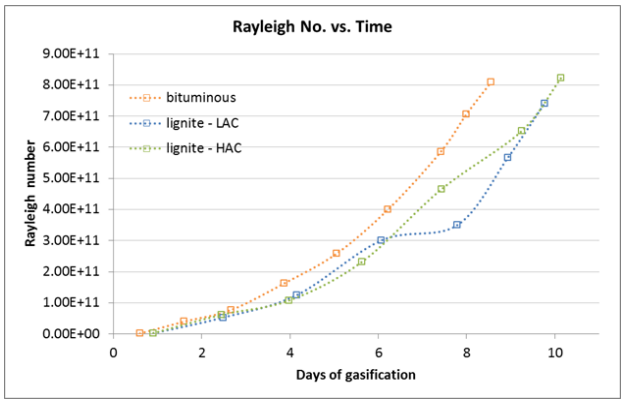


(a)

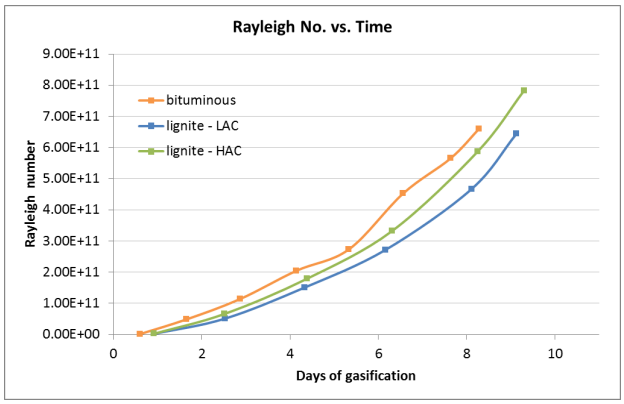


(b)

**Figure 7.15:** Rayleigh against UCG run time (a) at 400m depth and (b) at 600m depth for the 6m thick LAC Velenje lignite, HAC YiHe lignite and the Murcki – Staszic bituminous coal during the simulations

In addition, the higher cavity volumes under the bituminous scenario reduce the effect of external convective forces where the oxidant injection takes place (at the bottom of the cavity). In addition, the growth of the Rayleigh number (Figure 7.15) as the UCG process advances suggests that natural convection takes over conduction as the heat transfer mechanism within the fluid.

## 7.3 *Summary and Conclusions*

This Chapter aimed to cross-compare the simulated coal types at 400m and 600m depth respectively. The comparison focused on analysing the differences of the UCG process arising from the type of the gasified coal. For this reason, by considering the same operating conditions across all the simulating scenarios the results from the different coal types were compared.

Higher coal ranks lead to product gases of higher heating values. Furthermore, the higher temperatures developed under the bituminous coal scenarios (at both depths) assisted the active involvement of the radiative heat. For this reason, higher radiative heat flux ($W/m^2$) values were noticed on coal types with higher calorific values. Moreover, the verification of the above conclusion comes from the higher ratios (of convective to radiative heat transfer) in the case of lignite coal scenarios compared to the corresponding ratio values under the bituminous scenarios. The corresponding ratio reached its highest value (~0.45) during the 400m depth HAC lignite coal scenario while its lowest value (0.1) was observed during the 600m depth operation under the bituminous coal scenario. As a result, high ash content benefits the convective over the radiative heat transfer mechanism.

The dominance of the thermally over mechanically failed coal across all the simulation scenarios suggested that the roof-stage gasification taking place on the boundaries of the growing UCG cavity dominates its growth however, the spalling effect similarly to the increasing role of the convective mechanism becomes more actively involved as the cavity grows. Across all scenarios, the thermally failed coal picked before the retraction of the injector. The simulation results indicated that the further in time the retraction takes place the higher the mass of the thermally failed coal.

Finally, as UCG process advanced in time the increasing Grashof number proved the dominance of the buoyant over viscous forces within the cavity and in addition, the study of the Archimedes number values (consistently over $10^3$) even from the early stage proved the dominance of the natural over forced convection mechanism.

# Chapter 8 Conclusions and Recommendations for Further Research

This final Chapter summarises on the conclusions that can be drawn out of this PhD research. The aim is to both highlight the learnings as well as to comment on ideas that can be further improved and integrated.

## 8.1 *Achievements and Conclusions from the Research*

The aim of this PhD work was to develop the framework of an in-detail and inclusive model describing the UCG process. The developed Thermo-Mechanical-Chemical (TMC) model aims to provide further insight over UCG operation as it is a complex process which involves several sub-processes from a range of scientific areas. Specifically, it involves thermo-mechanical components as it occurs in the subsurface area and it has many similarities with mining and other hydrocarbon operations. In addition, it has thermo-chemical components associated with the chemical reactions taking place during coal gasification in the boundaries of the growing cavity and affect the composition of the final product gas. Finally, it is necessary to include the study of fluid flow phenomena as heat and mass flows move within the growing cavity.

Furthermore, this study correlated the above areas of study with the employed UCG subsurface layout (i.e. LVW, CRIP). The UCG layout has a critical role to play on the level of analysis that should be given on each scientific field as well as on how the different scientific areas can be meaningfully integrated.

Modelling studies referring to the UCG process often encounter with a critical dilemma. Either they can emphasize only on a specific sub-process of the UCG operation avoiding the integration component or they recognise the need for integration among the UCG sub-processes although the lack of a widely applicable modelling tool (tailored for UCG) is not allowing the accurate formulation of this integration. In addition, it needs to highlighted that the lack of accurate UCG in-situ data limit the potentials of every UCG model. This concern was recognised by UCG researchers and as a result insightful ex-situ experimental trials have been conducted.

The developed TMC model of the current PhD research followed a structured approach by trying to validate the suitability of the Aspen Plus software tool for UCG processes. As a result, data of high pressure ex-situ UCG trials were utilised in order to be compared with the modelling results generated by the thermo-chemical model presented in Chapter 4. The comparison process revealed that an accurate representation of the UCG process is possible if a representative configuration is developed within the Aspen Plus software environment. The developed configuration aimed to simulate the LVW UCG layout. On the other hand, the Aspen Plus module as part of the coupled process model presented in Chapter 5 focuses on the characteristics of the CRIP UCG layout.

The comparison of the experimental and modelling results taking place in Chapter 4 showed a high correlation for both the bituminous and the lignite coal trials. However, a useful component that facilitated the model formulation and the subsequent comparison between the modelling and experimental results was the availability of the temperature profiles at different time stages and at different locations within the ex-situ gasifier during the experiments.

Furthermore, the comparison of the experimental and modelling results facilitated the analysis on how several characteristics of the UCG process depend on the type of the gasified coal.

Specifically, the modelling of the oxygen stage of the bituminous trial showed that the corresponding temperature distribution within the reactor could be be organised into three distinctive stages. These stages were spread between the inlet and the outlet of the reactor in decreasing temperature order. The highest temperature stage was located close to where the oxidant injection was taking place while the lowest temperature one closer to where the product gas was collected.

This three-stage process showed that the carbon (C) consumption follows a similar pattern with higher consumption rates to take place at higher temperatures. During the bituminous trial higher temperatures were developed across the length of the reactor compared to the corresponding values during the lignite trial. The higher temperatures led to higher carbon (C) consumption rates. However, a carbon balance analysis showed that in terms of coal consumption the difference among the two trials was significantly lower. The reason was that for the same mass of carbon (C) to be found in the product gas a higher mass of coal had to be gasified during the lignite coal trial. The volatile nature of the lignite coal in combination with its high moisture content limit the carbon (C) proportions in the initial coal mass.

In addition, the structure of the developed model allowed the estimation of the product gas proportions reacting at each temperature stage. The high temperature difference between the combustion and gasification stages during the bituminous trial helped to more accurately locate where the combustion front of the UCG process existed at each time stage. However, the more uniform temperature profile during the lignite trial indicated that the combustion and gasification stages are not completely discrete at lower temperature levels. As it is also known (Gregg and Edgar, 1978) equilibrium modelling studies have a reduced accuracy at low temperature levels as reactions (i.e. methanation $C + 2H_2 \rightarrow CH_4$) are mainly driven by the slow formation kinetics rather than any equilibrium considerations. In addition, a cross comparison of the LVW Aspen Plus process model of Chapter 4 with the corresponding CRIP model of Chapter 5 leads to the following conclusion.

The LVW model layout included multiple gasification stages where the combustion gas (high carbon dioxide ($CO_2$) content) was transformed to higher heating value product gas as it was passing through the gasification stages (~ representing the flow through the coal seam).

In contrast, during the CRIP process model different quality product gas was generated simultaneously at two different stages (the bottom and the roof of the UCG cavity). Subsequently, both product gases interacted at a subsequent gasification stage (~ representing the growing UCG cavity).

However, in a coupled process the Aspen Plus process model was combined with the thermo-mechanical FLAC$^{3D}$ simulation tool and a Gasification Support module it designed to act as the link among the other two simulation tools. An additional task of the Gasification Support module was to cover scientific grounds (i.e. fluid flow phenomena) which were not addressed by the other two software tools. The detailed presentation of the methodology of the coupled TMC model showcased how multiple task oriented software tools can be combined for an integrated solution.

The applicability of the developed coupled process model was tested through the simulation of eight different scenarios. The differentiating parameters among the scenarios can be summarised to:

a) the coal type

b) the seam depth

c) the seam thickness

d) the oxidant injection

Three different coal types were tested at two different depths. One bituminous and two lignite coals with different ash contents were employed with the corresponding depths to be at 400m and 600m. The cross-comparison of the simulation results for every coal type at two different depths indicated that the elevated pressure of a higher depth increases the coal consumption rate. This increased rate led inevitably to the development of higher cavity volumes.

The rock and coal thermo-mechanical properties also affected the UCG cavity growth rate. Particularly, the fracturing behaviour of the lignite coals increased the vertical growth of the corresponding UCG cavities and made evident the need for higher seam thickness.

Furthermore, the comparison of the radiative and convective heat transfer mechanisms among the different depth scenarios indicated that at higher depths the convective heat transfer mechanism has a higher involvement in the heat distribution process. However, the radiative heat transfer mechanism remained the dominant mechanism across all the simulated scenarios.

The more active presence of the convective heat transfer mechanism at higher depths can be explained through the higher cavity volumes and as a result by the need for higher heat quantities to be carried through the cavity gas. In addition, the effect of the retraction process on the heat transfer mechanisms it was analysed. As the UCG cavity volume increased the convective mechanism became more actively involved. However, by retracting the injection point the radiative heat transfer mechanism increased its dominance over the corresponding convective mechanism. This is a reasonable conclusion because when the retraction takes place the injection point comes in contact with previously untouched coal and the high temperature bottom combustion source comes closer to the cavity boundaries increasing the impact of radiative heat.

On the other hand, simulation results indicated that the elevated pressure at higher depths benefited the development of higher temperatures. The coupled process model facilitated the measurement of temperatures at the bottom and the boundaries of the UCG cavity at different time stages which were found to be higher at 600m depth compared to the corresponding values at 400m depth. Furthermore, the higher temperatures in combination with the higher coal consumption rates at 600m depth led to higher radiative heat flux ($W/m^2$) compared to the corresponding flux at 400m.

Moreover, the effect of the higher temperature and pressure conditions at higher depths was observed on the product gas composition. Specifically, across all coal types during the 400m depth simulations higher carbon dioxide ($CO_2$) and lower methane ($CH_4$) contents were noticed compared to the corresponding contents at 600m depth. The higher carbon dioxide contents ($CO_2$) came as a result of the lower temperatures while the lower methane contents came as a result of the lower pressure conditions.

The compositional differences of the product gases had also an impact on the corresponding heating values. The higher methane ($CH_4$) content in combination with the slightly elevated carbon monoxide (CO) content led to higher gas heating values at 600m depth compared to the corresponding values at 400m depth.

The comparison of the gas heating values across the different coal types indicated that the coal calorific value has a substantial impact on the heating value of the product gas. For this reason, higher coal ranks are expected to generate product gas of higher heating value.

In addition, the type of the injected oxidant affected significantly the heating value of the product gas. Air (79% $N_2$ – 21% $O_2$) instead of oxygen ($O_2$) injection led to significant lower product gas heating values. As a result, air injection is more relevant at higher coal ranks where the effect of the air injection can be offset by the higher coal calorific value.

The coal type also affected the value of the convective to radiative heat transfer ratio with higher coal ranks to benefit radiative heat transfer mechanism. However, among the same coal rank the coal calorific was found to be the differentiating factor with the higher calorific values to benefit the development of higher temperatures and to ultimately assist the radiative heat transfer mechanism.

An additional conclusion is related to the UCG cavity growth rate at different depths and coal types. Particularly, the aim was to recognise the mechanism that drive the UCG cavity expansion. The thermal failure or gasification on the boundaries of the UCG cavity ("roof gasification") was found to be the main expansion mechanism. However, as the UCG cavity was growing the spalling effect was becoming more critical.

Especially in the early stages after the retraction of the injection point the spalling effect dominated over roof gasification. After these early stages depending on the operating depth and the coal type the ratio of thermally failed to overall consumed coal either stabilised or started increasing again. Across all simulation scenarios at 600m depth the surrounding strata to the UCG cavity had to withstand a higher load compared to the corresponding load at 400m depth. The higher load proved to be beneficial to the mechanical failure effect.

In addition, even at 400m depth the high volume of the bituminous cavity benefitted the spalling mechanism in contrast to the lignite coals where the mechanical failure effect peaked during the retraction and significantly weakened after it. These observations lead to the conclusion that the mechanical failure is associated with the load applied around the UCG cavity and as a result the depth affects UCG cavity growth rate.

Furthermore, the analysis conducted through the Gasification Support module helped on understanding whether *natural* or *forced* convection was the dominant heat convective mechanism. The increasing Grashof number proved that buoyancy forces dominate over viscous forces within the cavity as the UCG process advances. In addition, the corresponding decrease of the Reynolds number indicated a transition towards a less turbulent flow as the UCG cavity grows. The high Archimedes number values ($>10^3$) even from the early stages of the UCG process proved the dominance of the natural convection.

## 8.2 *Recommendations for Future Research*

An important feature of this PhD work is the development of a coupling framework and specifically its ability to combine independent software tools for an integrated result. This implies that in the future, there is further scope for improvement in the methodology by extending this integrating process.

The already integrated process can be further expanded towards a number of directions. As this PhD work formed the backbone of the coupling framework it is highly detailed and this inevitably leads to increased computational times. However, by identifying the most important parameters further integration can happen without significantly increasing the computational times.

Regarding the areas of integration, UCG is a complex process with important upstream and downstream components.

On the upstream side, a number of criterial have already been specified in the literature referring to the suitability of a coal seam for UCG exploitation. However, there is no algorithm or any other form of automated process that could objectively lead to the selection of a UCG site.

The development of an algorithm for this purpose could lead to its integration with the coupled TMC model of this PhD study. It would be also important to incorporate the availability and suitability of the required mechanical components (e.g. pumps, drilling equipment). The aim of this integration would be to move from a virtual case study to a site-specific analysis.

However, it should be recognised that the development of accurate models also requires site-specific data. The complex nature of UCG in combination with the lack of monitoring and controlling mechanisms have not allowed the development of a detailed database.

On the other hand, this is also where the usefulness of the current PhD study relies as it can save time, resources and effort by developing a simulation environment where a number of scenarios can be tested prior to their in-situ realisation.

On the downstream side, the developed TMC model can be integrated with tools focusing on the purification and the processing of the generated product gas for specific end-uses. This integration can facilitate relevant decision making as several parameters (e.g. oxidant injection rate, seam thickness) in the already developed coupled model can be linked with the product gas preparation process. The product gas processing can be further combined with additional transport optimisation studies. Different degrees of gas purification might be required depending on its way of transport and its final use. In addition, the carbon dioxide ($CO_2$) removal from the generated product gas can be correlated with the UCG site selection. As a result, a looping process can be developed where the optimal combination of the operating parameters can be defined.

Furthermore, the UCG economics is an additional area of study where the developed TMC model can be expanded. The analysis of the UCG economics can extend to both the upstream and the downstream operations of the UCG process.

On the upstream side, the impact of the site selection criteria (e.g. seam depth, coal rank etc.) to the UCG economics can be coupled with the selection of different operating parameters. A coal seam which lies at depth over 600m if selected for UCG purposes might require a costly drilling equipment.

For instance, drilling perfectly along the base of a coal seam (as the CRIP process requires) is a feasible but an expensive process, as it is known from the oil and gas industry. As a result, it might be more economical to use air instead of oxygen injection in order to partly offset the extensive drilling cost.

On the downstream side, an economics study can focus on the marketing and pricing of the final product gas for a profitable UCG operation. A study that focuses on the downstream UCG economics can be coupled with the developed TMC model in order to determine the operating parameters which can maximise the profit out of the final product gas. Additionally, UCG faces competition with the rest of the oil and gas industry and as a result the scope of a coupled TMC and UCG economics model can have an even wider scope.

In addition, the developed TMC model can be up-scaled and transformed from a near-field to a far-field model. A far-field model will have the capacity to extrapolate the findings of the developed TMC model by studying the UCG effect on the wider surrounding strata. Specifically, an unstable UCG process can be linked with a number of environmental concerns such as surface subsidence or leakage of the UCG product gas to neighbouring saline aquifers. Due to limited computational resources and the high level of detail, the already developed TMC model studies the effect of UCG cavity growth on a limited area around the coal seam. However, several of the UCG's operating parameters such as the pressure conditions or the seam thickness should be considered in relation to their effect on the wider surrounding strata.

In conclusion, the various sub-processes involved in UCG allow for broad integrated studies. In addition, UCG studies also benefit from the research and development across the whole spectrum of the oil and gas industry. As a result, UCG modelling studies can jointly benefit other scientific areas. For this reason, the developed TMC model can also have a wider applicability after being tailored to the specific needs of a particular study field.

# References

Aadnoy, B., Looyeh, R., 2011. Petroleum rock mechanics: drilling operations and well design. Gulf Professional Publishing.

Aaltosalmi, U., 2005. Fluid flow in porous media with the lattice-Boltzmann method. University of Jyväskylä.

Amadei B., Savage W.Z., Swolfs H.S., 1987, Gravitational stresses in anisotropic rock masses, International Journal of Rock Mechanics and Mining Sciences & Geomechanics Abstracts, 24, 5-14.

Amadei, B., Stephansson, O., 1997. Rock stress and its measurement. Springer Science & Business Media.

Anderson, E., 1951. The Dynamics of Faulting and Dyke Formation with Application to Britan, -183 S. Edinburgh (Oliver & Boyd).

Anthony, D.B., Howard, J.B., 1976. Coal devolatilization and hydrogastification. AIChE Journal 22, 625-656.

Antonova, R., Garkusha, I., Gershevich, E., Kreinin, E., Lavrov, N., Semenenko, D., Fedorov, N., 1967. Study of some regular parameters of underground coal gasification.[One of most important parameters was influx of water to zone of gasification and regulation of influx was one of basic methods of control]. Khim. Tverd. Topl. 1.

Aspen Plus, 2009. Getting started modelling processes with solids.

Badzioch, S., Field, M., Gregory, D., 1964. Investigation of temperature variation of thermal conductivity+ thermal diffusivity of coal. Fuel 43, 267-&.

Basu, P., 2006. Combustion and gasification in fluidized beds. CRC press.

Beath, A.C., 1996. Mathematical Modelling of Entrained Flow Coal Gasification| NOVA. The University of Newcastle's Digital Repository.

Beenackers, A., 1999. Biomass gasification in moving beds, a review of European technologies. Renewable Energy 16, 1180-1186.

Begum, S., Rasul, M., Akbar, D., Ramzan, N., 2013. Performance Analysis of an Integrated Fixed Bed Gasifier Model for Different Biomass Feedstocks. Energies 6, 6508-6524.

Benyon, P.J., 2002. Computational modelling of entrained flow slagging gasifiers.

Bergman, T.L., Incropera, F.P., DeWitt, D.P., Lavine, A.S., 2011. Fundamentals of heat and mass transfer. John Wiley & Sons.

Bhattacharya, A., 1985. Modeling studies in fixed-bed coal gasification. Washington Univ., St. Louis, MO (USA).

Biezen, E., Bruining, J., Molenaar, J., 1995. An integrated 3D model for underground coal gasification, SPE annual technical conference and exhibition. Society of Petroleum Engineers.

Birch, A.F., Clark, H., 1940. The thermal conductivity of rocks and its dependence upon temperature and composition. American Journal of Science 238, 529-558.

Bird, R.B., Stewart, W.E., Lightfoot, E.N., 2007. Transport Phenomena. John Wiley & Sons.

Blinderman, M., Klimenko, A., 2007. Theory of reverse combustion linking. Combustion and Flame 150, 232-245.

Blinderman, M., Saulov, D.N., Klimenko, A.Y., 2008. Forward and reverse combustion linking in underground coal gasification. Energy 33, 446-454.

Bose, A., 2012. Simulation of air liquefaction using aspen plus.

Bovo, M., 2014. Principles of Heat Transfer in Internal Combustion Engines from a Modeling standpoint. Chalmers University of Technology.

BP plc, 2015. BP Statistical Review of World Energy June 2015.

Bridgwater, A., 1995. The technical and economic feasibility of biomass gasification for power generation. Fuel 74, 631-653.

Britten, J., Thorsness, C., 1989. A model for cavity growth and resource recovery during underground coal gasification. In Situ;(USA) 13.

Britten, J.A., 1986. Recession of a coal face exposed to a high temperature. International journal of heat and mass transfer 29, 965-978.

Burton, E., J., F., Upadhye, R., 2007. Best Practices in Underground Coal Gasification. University of California, Lawrence Livermore National Laboratory, Livermore, CA, p. 119.

Chen, C., Jin, Y.-q., Yan, J.-h., Chi, Y., 2010. Simulation of municipal solid waste gasification for syngas production in fixed bed reactors. J. Zhejiang Univ. Sci. A 11, 619-628.

Chen F, P.X., Liu HT, Yao K. , 2013. O2/CO2 underground coal gasification model test. J China Coal Society 88, 495-500.

Cimini, S., Prisciandaro, M., Barba, D., 2005. Simulation of a waste incineration process with flue-gas cleaning and heat recovery sections using Aspen Plus. Waste Management 25, 171-175.

Corbetta, M., Manenti, F., Soares, F., Ravaghi-Ardebili, Z., Ranzi, E., Pirola, C., Buzzi-Ferraris, G., Pierucci, S., 2014. Mathematical Modelling of Coal and Biomass Gasification: Comparison on the Syngas H2/CO Ratio under Different Operating Conditions. Computer Aided Chemical Engineering, 1668-1673.

Couch, G.R., 2009. Underground coal gasification.

Daggupati, S., Mandapati, R.N., Mahajani, S.M., Ganesh, A., Mathur, D., Sharma, R., Aghalayam, P., 2010. Laboratory studies on combustion cavity growth in lignite coal blocks in the context of underground coal gasification. Energy 35, 2374-2386.

Daggupati, S., Mandapati, R.N., Mahajani, S.M., Ganesh, A., Pal, A., Sharma, R.K., Aghalayam, P., 2012. Compartment Modeling and Flow Characterization in Nonisothermal Underground Coal Gasification Cavities. Industrial & Engineering Chemistry Research 51, 4493-4508.

Daggupati, S., Mandapati, R.N., Mahajani, S.M., Ganesh, A., Pal, A.K., Sharma, R.K., Aghalayam, P., 2011a. Compartment Modeling for Flow Characterization of Underground Coal Gasification Cavity. Industrial & Engineering Chemistry Research 50, 277-290.

Daggupati, S., Mandapati, R.N., Mahajani, S.M., Ganesh, A., Sapru, R.K., Sharma, R.K., Aghalayam, P., 2011b. Laboratory studies on cavity growth and product gas composition in the context of underground coal gasification. Energy 36, 1776-1784.

Dinsmoor, B., Galland, J., Edgar, T., 1978. The mechanism of channel growth during underground coal gasification. J. Petrochem. Technol 695, 698-704.

Dossey, J., 1976. Underground coal gasification technology in the USSR.[76 references]. Sandia Labs., Albuquerque, N. Mex.(USA).

DTI, 2005. Directional drilling in coal, Technology Status Report. dti, Cleaner Fossil Fuels Programme, p. 28.

Eftekhari, A.A., Wolf, K.H., Rogut, J., Bruining, H., 2015. Mathematical modeling of alternating injection of oxygen and steam in underground coal gasification. International Journal of Coal Geology 150, 154-165.

Elliott, M.A., 1981. Chemistry of coal utilization. Second supplementary volume.

Eppelbaum, L., Kutasov, I., Pilchin, A., 2014. Thermal properties of rocks and density of fluids, Applied Geothermics. Springer, pp. 99-149.

Fischer, J., Young, J., Johnson, J., Jonke, A., 1979a. LABORATORY SUPPORT FOR IN SITU GASIFICATION--REACTION KINETICS. Illinois.

Fischer, J., Young, J., Johnson, J., Jonke, A., 1979b. Laboratory support for in situ gasification: reaction kinetics. Annual report, October 1976-September 1977. Argonne National Lab., IL (USA).

Fjar, E., Holt, R.M., Raaen, A., Risnes, R., Horsrud, P., 2008. Petroleum related rock mechanics. Elsevier.

FLAC$^{3D}$- Itasca, 2012. Online Manual. Minneapolis: Itasca Consulting Group, Inc.

Fox, R.W., McDonald, A.T., 1994. Introduction to Fluid Mechanics, John Wiley&Sons. Inc., New York.

Frentrup, H., 2014. Molecular Simulation of Diffusive Mass Transport in Porous Materials. Imperial College London United Kingdom.

Gercek, H., 2007. Poisson's ratio values for rocks. International Journal of Rock Mechanics and Mining Sciences 44, 1-13.

Ghil, M., Childress, S., 2012. Topics in geophysical fluid dynamics: atmospheric dynamics, dynamo theory, and climate dynamics. Springer Science & Business Media.

Gilliam, T., Morgan, I., 1987. Shale: Measurement of thermal properties. Oak Ridge National Lab., TN (USA).

Green, M., 1999. Underground coal gasification: a joint European field trial in Spain. Harwell Laboratory, Coal R & D Programme.

Gregg, D., Edgar, T., 1978. Underground coal gasification. AIChE Journal 24, 753-781.

Gregg, D., Hill, R., Olness, D., 1976. Overview of the Soviet effort in underground gasification of coal. California Univ., Livermore (USA). Lawrence Livermore Lab.

Hageraats, W., 2006. Fluid dynamic simulations of vortex-jet interaction. MSc Thesis Report, Delft University of Technology.

Hanrot, F., Ablitzer, D., Houzelot, J., Dirand, M., 1994. Experimental measurement of the true specific heat capacity of coal and semicoke during carbonization. Fuel 73, 305-309.

Harloff, G., 1983. Underground coal gasification cavity growth model. Journal of Energy 7, 410-415.

Hartman, H., Belk, J., Reagan, D., 1978. Low BTU Coal Gasification Processes. Oak Ridge National Laboratory.

Hettema, M., Wolf, K.A., De Pater, C., 1998. The influence of steam pressure on thermal spalling of sedimentary rock: theory and experiments. International Journal of Rock Mechanics and Mining Sciences 35, 3-15.

Hettema, M.H.H., 1996. The thermo-mechanical behaviour of sedimentary rock: an experimental study. TU Delft, Delft University of Technology.

Hill, R., Thorsness, C., 1982. Summary report on large-block experiments in underground coal gasification, Tono Basin, Washington. Volume 1. Experimental description and data analysis. Lawrence Livermore National Lab., CA (USA).

Hill, R., Thorsness, C., 1983a. Large-block experiments in underground coal gasification. Lawrence Livermore National Lab., CA (USA).

Hill, R., Thorsness, C., Thompson, D., 1983b. Centralia partial-seam CRIP test. Lawrence Livermore National Lab., CA (USA).

Hobbs, M.L., Radulovic, P.T., Smoot, L.D., 1992. Modeling fixed-bed coal gasifiers. AIChE Journal 38, 681-702.

Howard, J., 1989. Fluidized bed technology: principles and applications. Adam Hilger.

Irfan, M.F., Usman, M.R., Kusakabe, K., 2011. Coal gasification in CO 2 atmosphere and its kinetics since 1948: a brief review. Energy 36, 12-40.

Jaeger, J., Cook, N., Zimmerman, R., 2007. Fundamentals of Rock Mechanics, 4th edn., volume ISBN: 9780632057597, ISBN10: 0632057599. Blackwell Publishing.

Kapusta, K., Stańczyk, K., 2011. Pollution of water during underground coal gasification of hard coal and lignite. Fuel 90, 1927-1934.

Kapusta, K., Stańczyk, K., Rogut-Dąbrowska, A., 2015. Progress and plans on large scale high pressure gasification experiments. Central Mining Institute - Technology Options for Coupled Underground Coal Gasification and CO2 Capture and Storage, TOPS - MidTerm Progress Meeting.

Kapusta, K., Stańczyk, K., Rogut-Dąbrowska, A., 2017. Large scale high pressure gasification experiments. Central Mining Institute - Technology Options for Coupled Underground Coal Gasification and CO2 Capture and Storage, TOPS - Final Workshop.

Kapusta, K., Stańczyk, K., Wiatowski, M., Chećko, J., 2013. Environmental aspects of a field-scale underground coal gasification trial in a shallow coal seam at the Experimental Mine Barbara in Poland. Fuel 113, 196-208.

Kapusta, K., Wiatowski, M., Stańczyk, K., 2016. An experimental ex-situ study of the suitability of a high moisture ortho-lignite for underground coal gasification (UCG) process. Fuel 179, 150-155.

Kariznovi, M., Nourozieh, H., Abedi, J., Chen, Z., 2013. Simulation study and kinetic parameter estimation of underground coal gasification in Alberta reservoirs. Chemical Engineering Research and Design 91, 464-476.

Kaupp, A., Goss, J., 1981. State-of-the-art report for small scale (to 50 kw) gas producer-engine systems. California Univ., Davis (USA). Dept. of Agricultural Engineering.

Khadse, A., Qayyumi, M., Mahajani, S., Aghalayam, P., 2007. Underground coal gasification: A new clean coal utilization technique for India. Energy 32, 2061-2071.

Kim, M.-Y., Kim, U.-S., 2011. Process modeling of an entrained flow coal gasifier, Control, Automation and Systems (ICCAS), 2011 11th International Conference on. IEEE, pp. 1724-1727.

Klimenko, A.Y., 2009. Early ideas in underground coal gasification and their evolution. Energies 2, 456-476.

Kreinin, E., Revva, M., 1974. Underground Gasification of Coal. Lawrence Livermore Laboratory, University of California.

Krevelen, D.W., 1993. Coal--typology, physics, chemistry, constitution. Elsevier Science.

Lavrov, N., Kulakova, M., Kazachkova, D.T., 1971. An Analysis of Several Technical Factors in the Underground Gasification of Brown Coal. Moscow, Vsesoyuznyvi Nauchn.-Issledovatel'skii Inst. Ispol'zovaniya Gaza v Narodnom Khozyaistve i Podzemn. Khraneniya Nefti, Nefteproduktov i Szhizhennykh Gazov, Trudy Inst. i Proizvodstvennyi Opyt 5, 133-137.

Lee, S., Speight, J.G., Loyalka, S.K., 2014. Handbook of alternative fuel technologies. crc Press.

Li, X., Grace, J., Watkinson, A., Lim, C., Ergüdenler, A., 2001. Equilibrium modeling of gasification: a free energy minimization approach and its application to a circulating fluidized bed coal gasifier. Fuel 80, 195-207.

Lienhard, J.H., 2013. A heat transfer textbook. Courier Corporation.

Littlewood, K., 1977. Gasification: theory and application. Progress in energy and combustion science 3, 35-71.

Liu, G., 1999. Mathematical modelling of coal char reactivity in a pressurised entrained flow gasifier. University of Newcastle.

Liu, S.-Q., Wang, Y.-Y., Ke, Z., Ning, Y., 2009. Enhanced-hydrogen gas production through underground gasification of lignite. Mining Science and Technology (China) 19, 389-394.

Magnani, C., Ali, S., 1975. Mathematical modeling of the stream method of underground coal gasification. Society of Petroleum Engineers Journal 15, 425-436.

Mandapati, R.N., Daggupati, S., Mahajani, S.M., Aghalayam, P., Sapru, R.K., Sharma, R.K., Ganesh, A., 2012. Experiments and kinetic modeling for CO2 gasification of Indian coal chars in the context of underground coal gasification. Industrial & Engineering Chemistry Research 51, 15041-15052.

Mandl, C., Obernberger, I., Biedermann, F., 2010. Modelling of an updraft fixed-bed gasifier operated with softwood pellets. Fuel 89, 3795-3806.

Marcourt, M., Paquay, V., Piel, A., Pirard, J.-P., 1983. Coal gasification at pressure by mixtures of carbon dioxide and oxygen. Fuel 62, 823-828.

Midttømme, K., Roaldset, E., Aagaard, P., 1998. Thermal conductivity claystones and mudstones of selected from England. Clay Minerals 33, 131-145.

Min, O., 1983. Finite-element modeling of thermo-mechanical responses associated with underground coal conversion. Ohio State Univ., Columbus (USA).

Mocek, P., Pieszczek, M., Świądrowski, J., Kapusta, K., Wiatowski, M., Stańczyk, K., 2016. Pilot-scale underground coal gasification (UCG) experiment in an operating Mine "Wieczorek" in Poland. Energy 111, 313-321.

Moulijn, J.A., Makkee, M., Van Diepen, A.E., 2013. Chemical process technology. John Wiley & Sons.

Najafi, M., Jalali, S.M.E., KhaloKakaie, R., 2014. Thermal–mechanical–numerical analysis of stress distribution in the vicinity of underground coal gasification (UCG) panels. International Journal of Coal Geology 134, 1-16.

Nakaten, N., Schlüter, R., Azzam, R., Kempka, T., 2014. Development of a techno-economic model for dynamic calculation of cost of electricity, energy demand and CO 2 emissions of an integrated UCG–CCS process. Energy 66, 779-790.

Nourozieh, H., Kariznovi, M., Chen, Z., Abedi, J., 2010. Simulation study of underground coal gasification in Alberta reservoirs: geological structure and process modeling. Energy & Fuels 24, 3540-3550.

Okuga, A., 2007. Analysis and operability optimization of an updraft gasifier unit. MS Thesis, Dept. Mech. Engineering, Eindhoven University of Technology, Eindhoven, Netherlands.

Olateju, B., Kumar, A., 2013. Techno-economic assessment of hydrogen production from underground coal gasification (UCG) in Western Canada with carbon capture and sequestration (CCS) for upgrading bitumen from oil sands. Applied energy 111, 428-440.

Oliver, R.L., Mason, G.M., Spackman, L.K., 1989. Field and laboratory results from the TONO I (CRIP) UCG cavity excavation project, Widco mine site, Centralia, Washington. FUEL SCIENCE & TECHNOLOGY INTERNATIONAL 7, 1059-1120.

Olness, D., 1982. The Angrenskaya underground coal gasification station. Lawrence Livermore Laboratory.

Olness, D., Gregg, D., 1977. Historical development of underground coal gasification. California Univ., Livermore (USA). Lawrence Livermore Lab.

Otto, C., Kempka, T., 2015. Thermo-mechanical simulations of rock behavior in underground coal gasification show negligible impact of temperature-dependent parameters on permeability changes. Energies 8, 5800-5827.

Park, K.Y., Edgar, T.F., 1987. Modeling of early cavity growth for underground coal gasification. Industrial & engineering chemistry research 26, 237-246.

Perkins, G., Sahajwalla, V., 2005. A Mathematical Model for the Chemical Reaction of a Semi-infinite Block of Coal in Underground Coal Gasification. Energy & Fuels 19, 1679-1692.

Perkins, G., Sahajwalla, V., 2006. A numerical study of the effects of operating conditions and coal properties on cavity growth in underground coal gasification. Energy & Fuels 20, 596-608.

Perkins, G., Sahajwalla, V., 2007. Modelling of heat and mass transport phenomena and chemical reaction in underground coal gasification. Chemical Engineering Research and Design 85, 329-343.

Perkins, G., Sahajwalla, V., 2008. Steady-State Model for Estimating Gas Production from Underground Coal Gasification. Energy & Fuels 22, 3902-3914.

Perkins, G.M.P., 2005. Mathematical modelling of underground coal gasification. University of New South Wales.

Phillips, J., 2006. Different types of gasifiers and their integration with gas turbines. Handbook of Gas Turbines By National Energy Technology Labratory.

Porada, S., Czerski, G., Dziok, T., Grzywacz, P., Makowska, D., 2015. Kinetics of steam gasification of bituminous coals in terms of their use for underground coal gasification. Fuel Processing Technology 130, 282-291.

Prabu, V., Geeta, K., 2015. CO 2 enhanced in-situ oxy-coal gasification based carbon-neutral conventional power generating systems. Energy 84, 672-683.

Prabu, V., Jayanti, S., 2011. Simulation of cavity formation in underground coal gasification using bore hole combustion experiments. Energy 36, 5854-5864.

Preciado, J., Ortiz-Martinez, J., Gonzalez-Rivera, J., Sierra-Ramirez, R., Gordillo, G., 2012. Simulation of Synthesis Gas Production from Steam Oxygen Gasification of Colombian Coal Using Aspen Plus®. Energies 5, 4924-4940.

Ramzan, N., Ashraf, A., Naveed, S., Malik, A., 2011. Simulation of hybrid biomass gasification using Aspen plus: A comparative performance analysis for food, municipal solid and poultry waste. Biomass and Bioenergy 35, 3962-3969.

Reed, T., Das, A., 1988. Handbook of biomass downdraft gasifier engine systems. Biomass Energy Foundation.

Roberts, D.G., 2000. Intrinsic reaction kinetics of coal chars with oxygen, carbon dioxide and steam at elevated pressures| NOVA. The University of Newcastle's Digital Repository.

Robertson, E.C., 1988. Thermal properties of rocks. US Geological Survey.

Roddy, D.J., 2013. A syngas network for reducing industrial carbon footprint and energy use. Applied thermal engineering 53, 299-304.

Roddy, D.J., Younger, P.L., 2010. Underground coal gasification with CCS: a pathway to decarbonising industry. Energy & Environmental Science 3, 400-407.

Rogut, J., 2008. Hydrogen Oriented Underground Coal Gasification, Twenty-Fifth Annual International Pittsburgh Coal Conference. Paper 20-3. Pittsburgh, PA.

Rossberg, M., 1956. Experimental Investigation on the Primary Reactions in Coal Combustion. 60, 952.

Rossi, C., Cardozo-Filho, L., Guirardello, R., 2009. Gibbs free energy minimization for the calculation of chemical and phase equilibrium using linear programming. Fluid Phase Equilibria 278, 117-128.

Sarhosis, V., Yang, D., Sheng, Y., Kempka, T., 2013. Coupled hydro-thermal analysis of underground coal gasification reactor cool down for subsequent CO 2 storage. Energy Procedia 40, 428-436.

Sarraf Shirazi, A., Mmbaga, J., Gupta, R., 2011. Modelling cavity growth during underground coal gasification, Proceedings of the 2011 COMSOL Conference, pp. 1-5.

Schaaf, T., Grünig, J., Schuster, M.R., Rothenfluh, T., Orth, A., 2014. Methanation of CO2-storage of renewable energy in a gas distribution system. Energy, Sustainability and Society 4, 1-14.

Scheidegger, A., 1957. The Physics of Flow Through Porous Media The Macmillan Company. New York (l957).

Seifi, M., Chen, Z., Abedi, J., 2011. Numerical simulation of underground coal gasification using the CRIP method. The Canadian Journal of Chemical Engineering 89, 1528-1535.

Self, S., Reddy, B., Rosen, M., 2012. Review of underground coal gasification technologies and carbon capture. Int J Energy Environ Eng 3, 1-8.

Shackley, S., Mander, S., Reiche, A., 2006. Public perceptions of underground coal gasification in the United Kingdom. Energy Policy 34, 3423-3433.

Shafirovich, E., Varma, A., 2009. Underground Coal Gasification: A Brief Review of Current Status. Industrial & Engineering Chemistry Research 48, 7865-7875.

Shehzad, A., Bashir, M.J., Sethupathi, S., 2016. System analysis for synthesis gas (syngas) production in Pakistan from municipal solid waste gasification using a

circulating fluidized bed gasifier. Renewable and Sustainable Energy Reviews 60, 1302-1311.

Shoemaker, H.D., Shuck, L., Haynes, R., Advani, S., 1977. The mechanical properties of the Pittsburgh coal at elevated temperatures. Journal of Pressure Vessel Technology 99, 192-198.

Siedlecki, M., De Jong, W., Verkooijen, A.H., 2011. Fluidized bed gasification as a mature and reliable technology for the production of bio-syngas and applied in the production of liquid transportation fuels—a review. Energies 4, 389-434.

Singer, J.M., Tye, R.P., 1979. Thermal, mechanical, and physical properties of selected bituminous coals and cokes. Bureau of Mines, Washington, DC.

Smith, R., Loganathan, M., Shantha, M.S., 2010. A review of the water gas shift reaction kinetics. International Journal of Chemical Reactor Engineering 8.

Solomon, P.R., Serio, M.A., Suuberg, E.M., 1992. Coal pyrolysis: experiments, kinetic rates and mechanisms. Progress in Energy and Combustion Science 18, 133-220.

Somerton, W.H., 1975. Thermal Properties of Partially Liquid-caturated Rocks at Elevated Temperatures and Pressures. College of Engineering University of California.

Stańczyk, K., Howaniec, N., Smoliński, A., Świądrowski, J., Kapusta, K., Wiatowski, M., Grabowski, J., Rogut, J., 2011. Gasification of lignite and hard coal with air and oxygen enriched air in a pilot scale ex situ reactor for underground gasification. Fuel 90, 1953-1962.

Stańczyk, K., Kapusta, K., Wiatowski, M., Świądrowski, J., Smoliński, A., Rogut, J., Kotyrba, A., 2012. Experimental simulation of hard coal underground gasification for hydrogen production. Fuel 91, 40-50.

Stańczyk, K., Smoliński, A., Kapusta, K., Wiatowski, M., Świądrowski, J., Kotyrba, A., Rogut, J., 2010. Dynamic experimental simulation of hydrogen oriented underground gasification of lignite. Fuel 89, 3307-3314.

Stephens, D., 1981. Hoe Creek experiments: LLNL's underground coal-gasification project in Wyoming. Lawrence Livermore National Lab., CA (USA).

Stephens, D., Hill, R., Borg, I., 1985. Underground coal gasification review.

Sury, M., White, M., Kirton, J., Carr, P., Woodbridge, R., Mostade, M., Chappell, R., Hartwell, D., Hunt, D., Rendell, N., 2004. Review of environmental issues of underground coal gasification. WS Atkins Consultants Ltd., University of Liège Belgium, FWS Consultants Ltd 126, 1-126.

Takenaka, S., Shimizu, T., Otsuka, K., 2004. Complete removal of carbon monoxide in hydrogen-rich gas stream through methanation over supported metal catalysts. International Journal of Hydrogen Energy 29, 1065-1073.

Tan, Q., Luo, X., Li, S., 2008. Numerical modeling of thermal stress in a layered rock mass, The 42nd US Rock Mechanics Symposium (USRMS). American Rock Mechanics Association.

Taylor, R., Krishna, R., 1993. Multicomponent mass transfer. John Wiley & Sons.

Teh, Y.S., Rangaiah, G.P., 2002. A Study of Equation-Solving and Gibbs Free Energy Minimization Methods for Phase Equilibrium Calculations. Chemical Engineering Research and Design 80, 745-759.

Terzaghi, K., 1943. Theoretical soil mechanics, Wiley, New York.

Thorsness, C., Grens, E., Sherwood, A., 1978. One-dimensional model for in situ coal gasification. California Univ., Livermore (USA). Lawrence Livermore Lab.

Tian, H., Ziegler, M., 2013. Development of a thermo-mechanical model for rocks exposed to high temperatures during underground coal gasification. Lehrstuhl für Geotechnik im Bauwesen und Institut für Grundbau, Bodenmechanik, Felsmechanik und Verkehrswasserbau.

UCG-Engineering, 2006. 2010 Survey of Energy Resources.

Van Heek, K., 2000. Progress of coal science in the 20th century. Fuel 79, 1-26.

Van Heek, K., Mühlen, H.-J., 1991. Chemical kinetics of carbon and char gasification, Fundamental issues in control of carbon gasification reactivity. Springer, pp. 1-34.

Verma, A., Olateju, B., Kumar, A., Gupta, R., 2015. Development of a process simulation model for energy analysis of hydrogen production from underground coal gasification (UCG). International Journal of Hydrogen Energy 40, 10705-10719.

Visagie, J.P., 2009. Generic gasifier modelling: evaluating model by gasifier type.

Von Fredersdorff, C., Elliott, M., 1963. Coal Gasification, in: Lowry, H.H. (Ed.), Chemistry of coal utilization. Second supplementary volume. Wiley, New York, p. Medium: X; Size: Pages: 2395.

Walker, L., Blinderman, M., Brun, K., 2001. An IGCC Project at Chinchilla, Australia based on underground coal gasification (UCG), 2001 gasification technologies conference, San Francisco.

Wang, G., Wang, Z., Feng, B., Rudolph, V., Jiao, J., 2009. Semi-industrial tests on enhanced underground coal gasification at Zhong-Liang-Shan coal mine. Asia-Pacific Journal of Chemical Engineering 4, 771-779.

Waples, D.W., Waples, J.S., 2004. A review and evaluation of specific heat capacities of rocks, minerals, and subsurface fluids. Part 1: Minerals and nonporous rocks. Natural resources research 13, 97-122.

WEC, 2007. Survey of Energy Resources. [Online] http://ny.whlib.ac.cn/pdf/Survey_of_Energy_Resources_2007.pdf.

WEC, 2010. Survey of Energy Resources. [Online] http://www.worldenergy.org/documents/ser_2010_report_1.pdf.

WEC, 2013. World Energy Resources – 2013 Survey. [Online] https://www.worldenergy.org/wp-content/uploads/2013/09/Complete_WER_2013_Survey.pdf

WEC, 2015. World Energy Issues Monitor – Energy price volatility: the new normal. [Online] https://www.worldenergy.org/wp-content/uploads/2015/01/2015-World-Energy-Issues-Monitor.pdf.

Wen, H., Lu, J.-h., Xiao, Y., Deng, J., 2015. Temperature dependence of thermal conductivity, diffusion and specific heat capacity for coal and rocks from coalfield. Thermochimica Acta 619, 41-47.

White, F.M., 1999. Fluid mechanics, WCB. ed: McGraw-Hill, Boston.

Wiatowski, M., Kapusta, K., Ludwik-Pardała, M., Stańczyk, K., 2016. Ex-situ experimental simulation of hard coal underground gasification at elevated pressure. Fuel 184, 401-408.

Wiatowski, M., Kapusta, K., Świądrowski, J., Cybulski, K., Ludwik-Pardała, M., Grabowski, J., Stańczyk, K., 2015. Technological aspects of underground coal gasification in the Experimental "Barbara" Mine. Fuel 159, 454-462.

Wiatowski, M., Stańczyk, K., Świądrowski, J., Kapusta, K., Cybulski, K., Krause, E., Grabowski, J., Rogut, J., Howaniec, N., Smoliński, A., 2012. Semi-technical underground coal gasification (UCG) using the shaft method in Experimental Mine "Barbara". Fuel 99, 170-179.

Wolf, K.-H., Bruining, H., 2007. Modelling the interaction between underground coal fires and their roof rocks. Fuel 86, 2761-2777.

Yang, D., Sarhosis, V., Sheng, Y., 2014. Thermal–mechanical modelling around the cavities of underground coal gasification. Journal of the Energy Institute 87, 321-329.

Yang, L., 2004. Study on the model experiment and numerical simulation for underground coal gasification. Fuel 83, 573-584.

Yang, L., Liang, J., Yu, L., 2003. Clean coal technology—Study on the pilot project experiment of underground coal gasification. Energy 28, 1445-1460.

Yang, L., Zhang, X., Liu, S., Yu, L., Zhang, W., 2008. Field test of large-scale hydrogen manufacturing from underground coal gasification (UCG). International Journal of Hydrogen Energy 33, 1275-1285.

Yang, L.H., Pang, X.L., Liu, S.Q., Chen, F., 2010. Temperature and Gas Pressure Features in the Temperature-control Blasting Underground Coal Gasification. Energy Sources, Part A: Recovery, Utilization, and Environmental Effects 32, 1737-1746.

Yin, T., Li, X., Wang, B., Yin, Z., Jin, J., 2011. Mechanical properties of sandstones after high temperature under dynamic loading. Chinese Journal of Geotechnical Engineering 33, 777-784.

Yoon, H., Wei, J., Denn, M.M., 1979a. Analysis of lurgi gasification of two US Coals. Chemical Engineering Science 34, 231-237.

Yoon, H., Wei, J., Denn, M.M., 1979b. Feasible operating regions for moving bed coal gasification reactors. Industrial & Engineering Chemistry Process Design and Development 18, 306-312.

Younger, P., 2011. Hydrogeological and Geomechanical Aspects of Underground Coal Gasification and its Direct Coupling to Carbon Capture and Storage. Mine Water Environ 30, 127-140.

Zavsek, S., Sedlar, J., Jamnikar, S., 2015. Progress and plans on large scale high pressure gasification experiments. Premogovnik Velenje, D.D. (CM-VELENJE) - Technology Options for Coupled Underground Coal Gasification and CO2 Capture and Storage, TOPS

Zhao, X.G. & Wang, Jian & Qin, Xianghui & Cai, M & su, Ramakrishnan & He, J.G. & Zong, Z.H. & Ma, L.K. & Ji, R.L. & Zhang, Mudi & Zhang, Shansahn & Yun, L & Chen, Q.C. & Niu, L.L. & An, Q.M.. (2015). In-situ Stress Measurements and Regional Stress Field Assessment in the Xinjiang Candidate Area for China's HLW Disposal. Engineering Geology 197, 42-56.

Zoback, M.D., 2010. Reservoir geomechanics. Cambridge University Press.

Żogała, A., Janoszek, T., 2015. CFD simulations of influence of steam in gasification agent on parameters of UCG process. Journal of Sustainable Mining 14, 2-11.

# Appendix

## A.1 Velenje (LAC) lignite coal (6m seam thickness)- Temperature Profiles

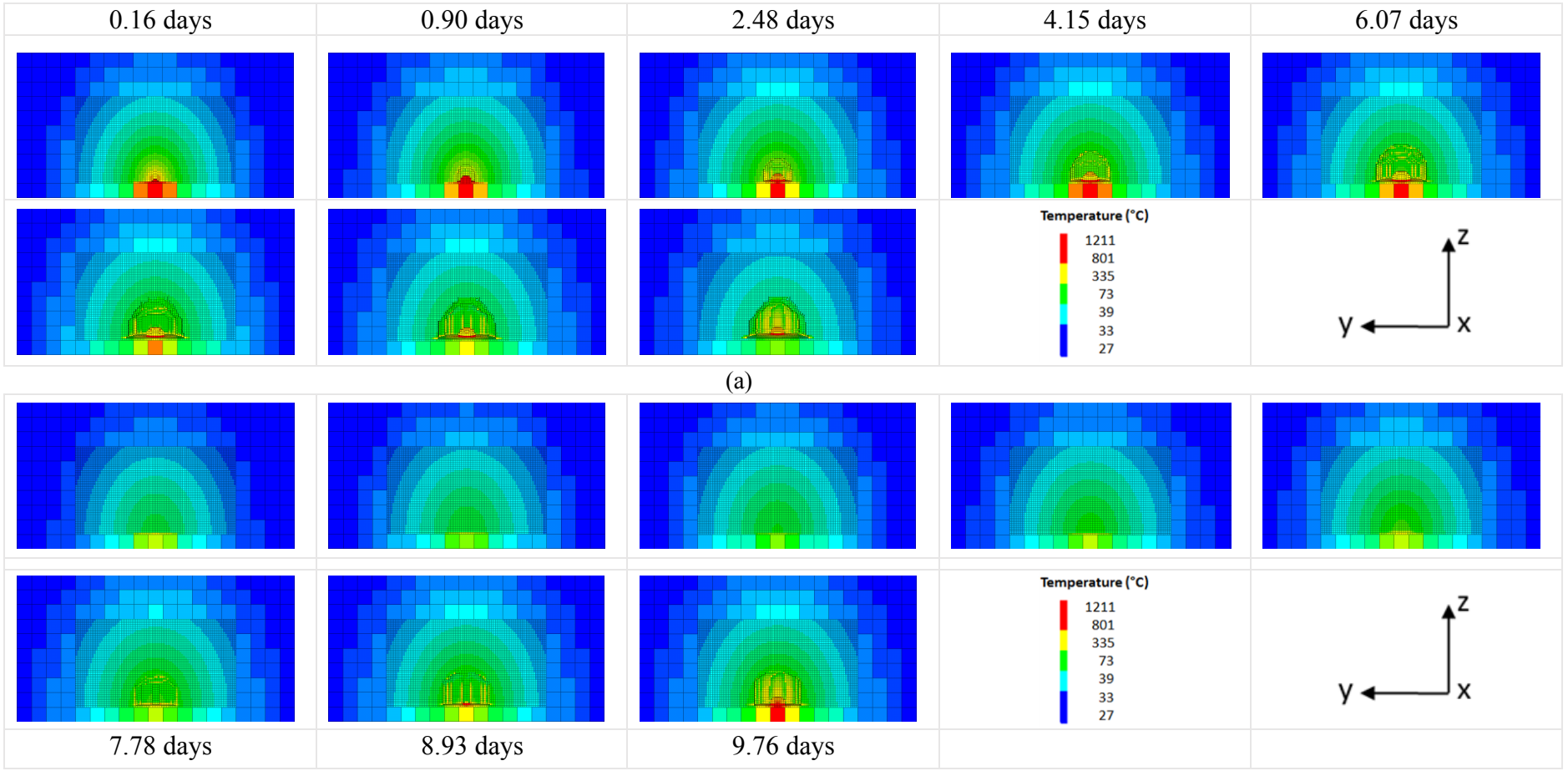


**Figure A.1:** Representation of the temperature profile (y-z plane) (a) at the AA' section and (b) at the BB' section (sections taken from Figure 6.1) around the growing cavity after different time periods during the Velenje LAC lignite coal gasification with oxygen injection at 400m depth with 6m seam thickness.

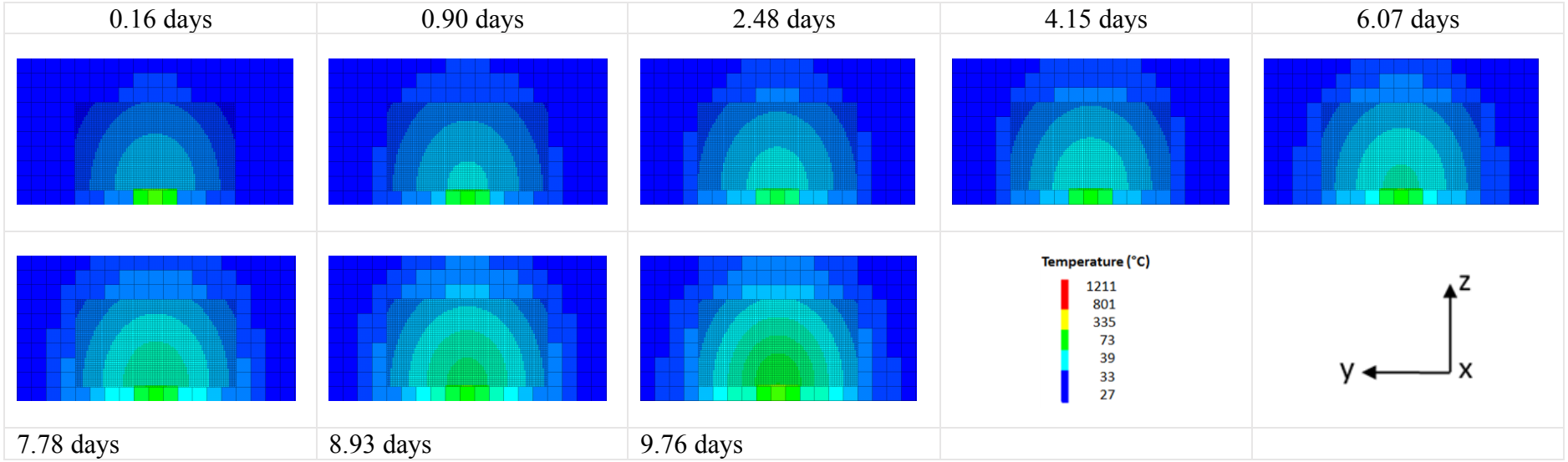


**Figure A.2:** Representation of the temperature profile (y-z plane) at the CC' section (sections taken from Figure 6.1) around the growing cavity after different time periods during the Velenje LAC lignite coal gasification with oxygen injection at 400m depth with 6m seam thickness.

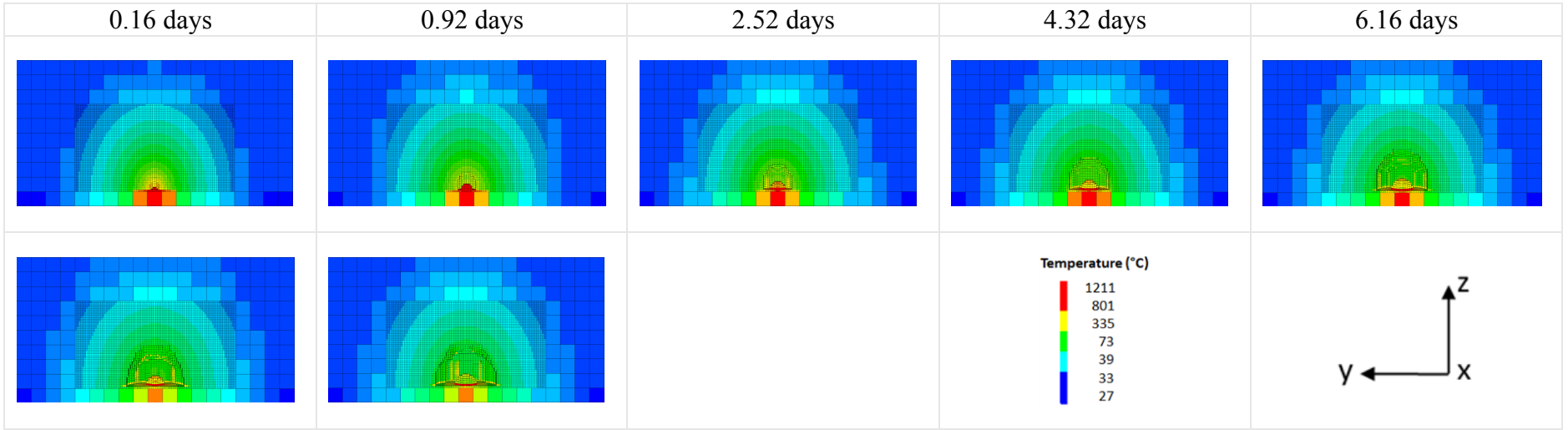


(a)

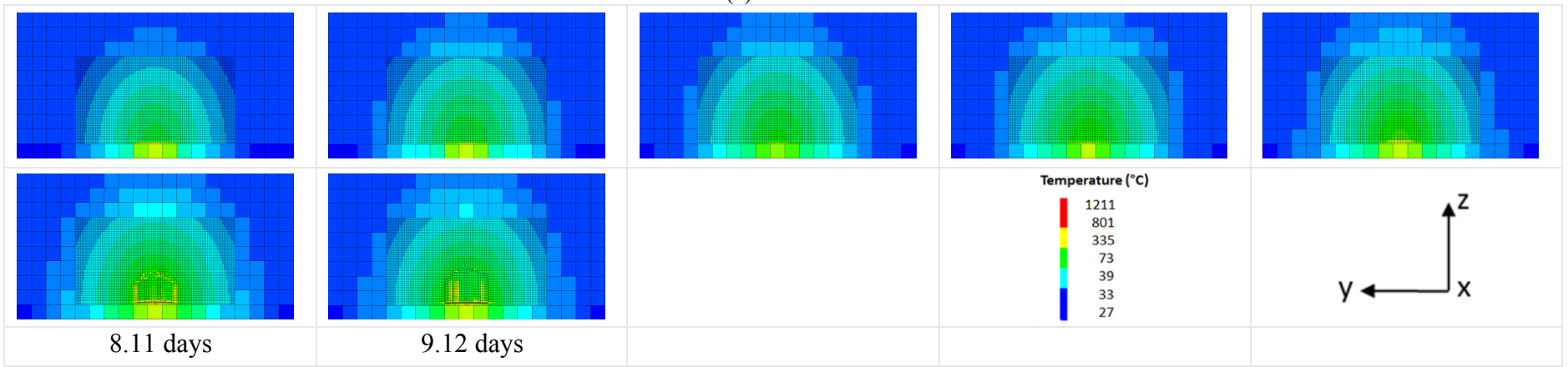


(b)

**Figure A.3:** Representation of the temperature profile (y-z plane) (a) at the AA' section and (b) at the BB' section (sections taken from Figure 6.1) around the growing cavity after different time periods during the Velenje LAC lignite coal gasification with oxygen injection at 600m depth with 6m seam thickness.

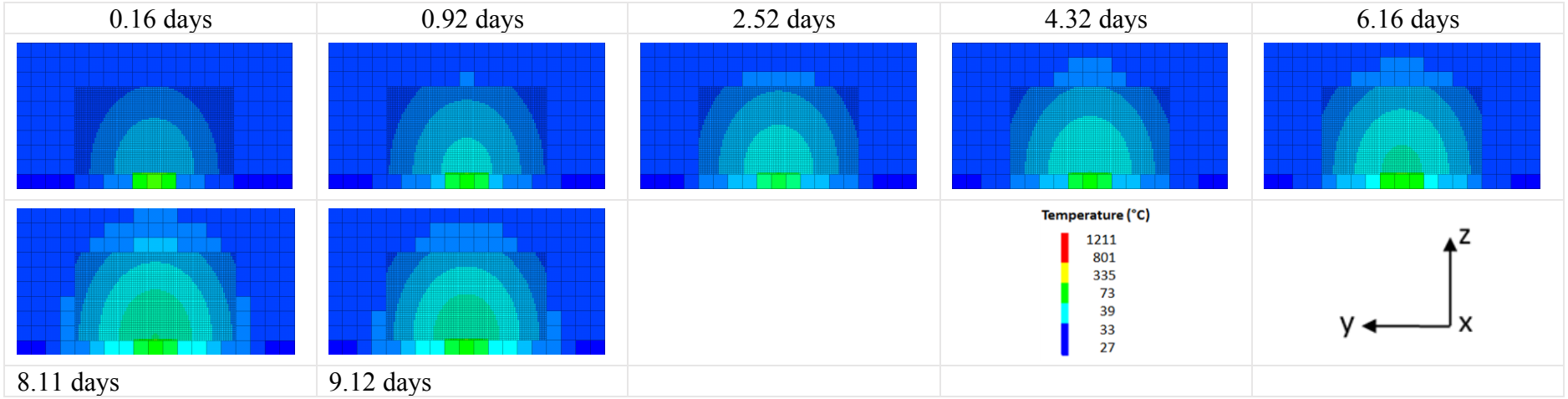


**Figure A.4:** Representation of the temperature profile (y-z plane) at the CC' section (sections taken from Figure 6.1) around the growing cavity after different time periods during the Velenje LAC lignite coal gasification with oxygen injection at 600m depth with 6m seam thickness.

## *A.2 Velenje (LAC) lignite coal (10m seam thickness) - Temperature Profiles*

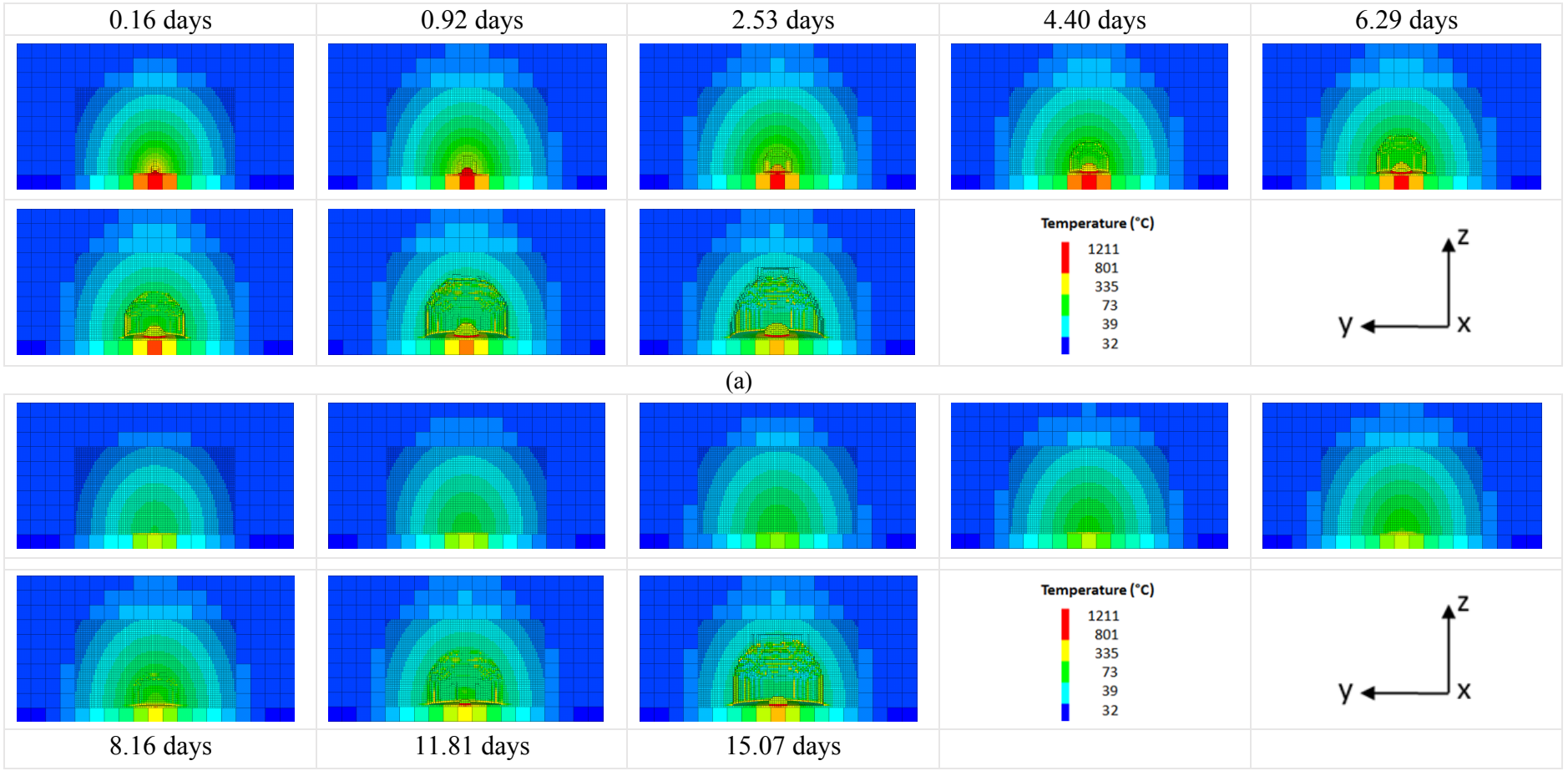


**Figure A.5:** Representation of the temperature profile (y-z plane) (a) at the AA' section and (b) at the BB' section (sections taken from Figure 6.1) around the growing cavity after different time periods during the Velenje LAC lignite coal gasification with oxygen injection at 600m depth with 10m seam thickness.

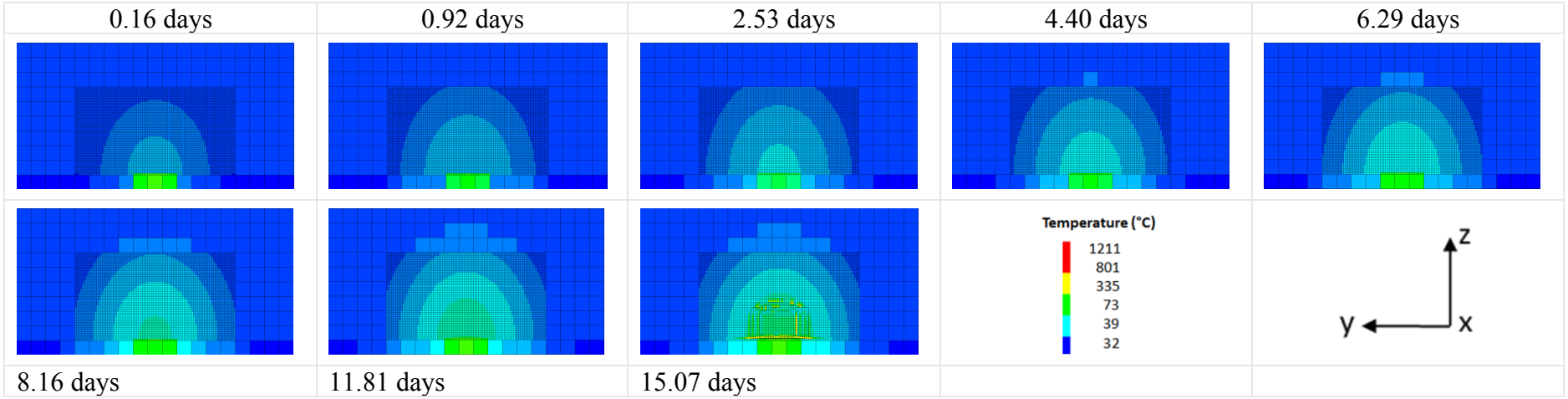


**Figure A.6:** Representation of the temperature profile (y-z plane) at the CC' section (sections taken from Figure 6.1) around the growing cavity after different time periods during the Velenje LAC lignite coal gasification with oxygen injection at 600m depth with 10m seam thickness.

## *A.3 YiHe (HAC) lignite coal - Temperature Profiles*

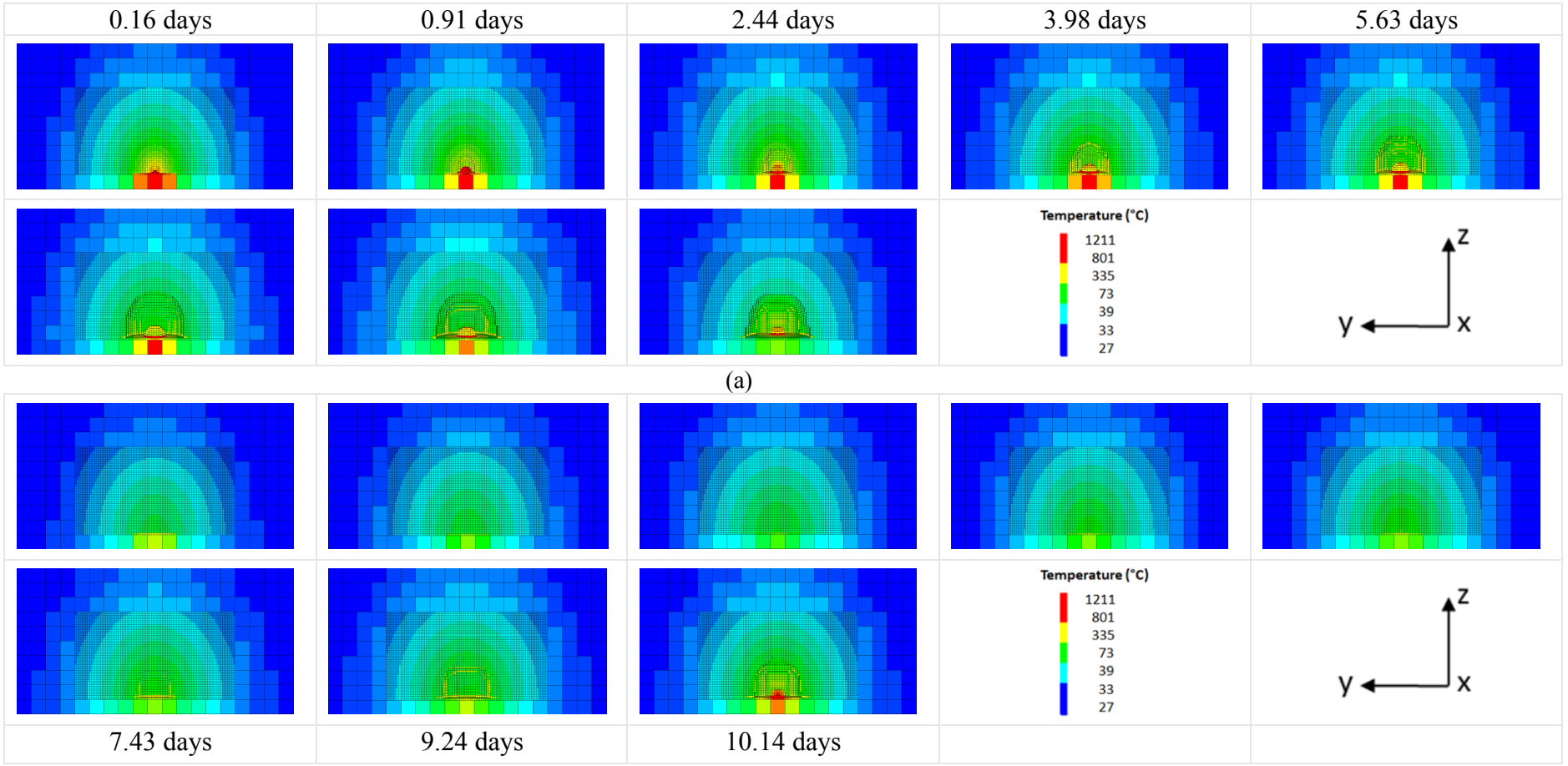


**Figure A.7:** Representation of the temperature profile (y-z plane) (a) at the AA' section and (b) at the BB' section (sections taken from Figure 6.1) around the growing cavity after different time periods during the YiHe HAC lignite coal gasification with oxygen injection at 400 depth.

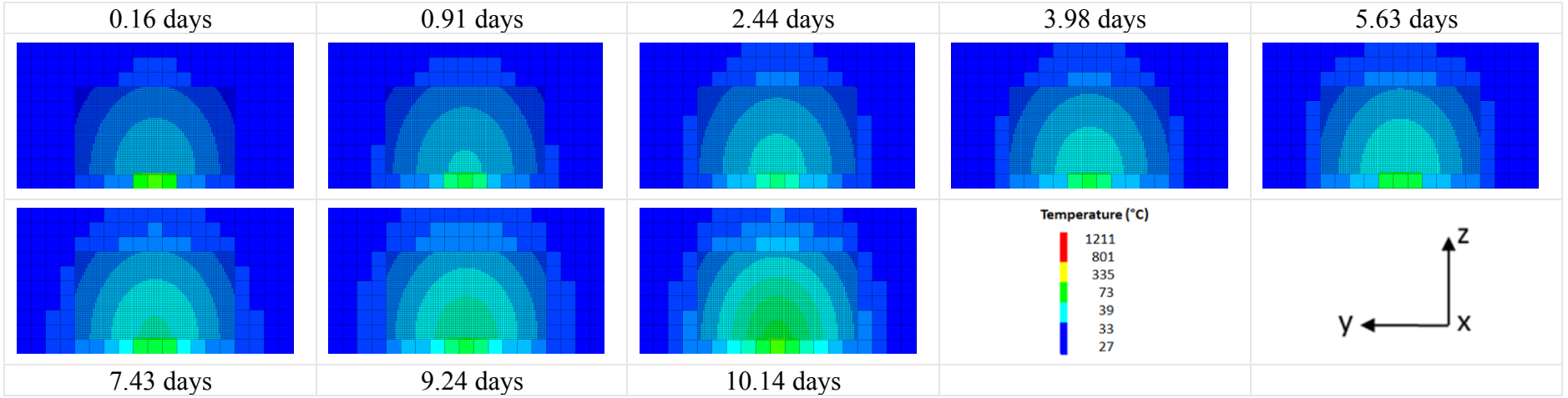


**Figure A.8:** Representation of the temperature profile (y-z plane) at the CC' section (sections taken from Figure 6.1) around the growing cavity after different time periods during the YiHe HAC lignite coal gasification with oxygen injection at 400m depth.

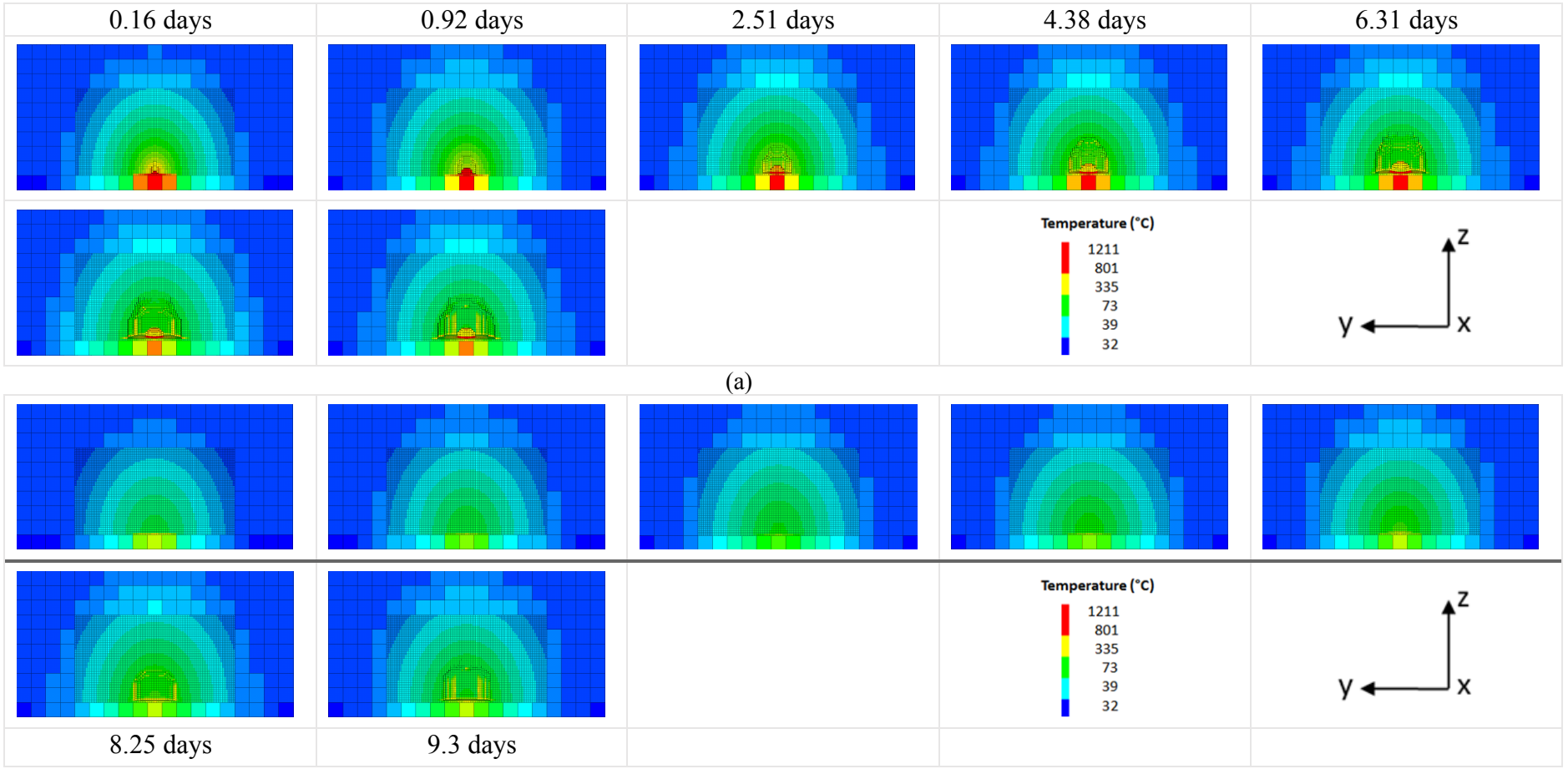


**Figure A.9:** Representation of the temperature profile (y-z plane) (a) at the AA' section and (b) at the BB' section (sections taken from Figure 6.1) around the growing cavity after different time periods during the YiHe HAC lignite coal gasification with oxygen injection at 600m depth.

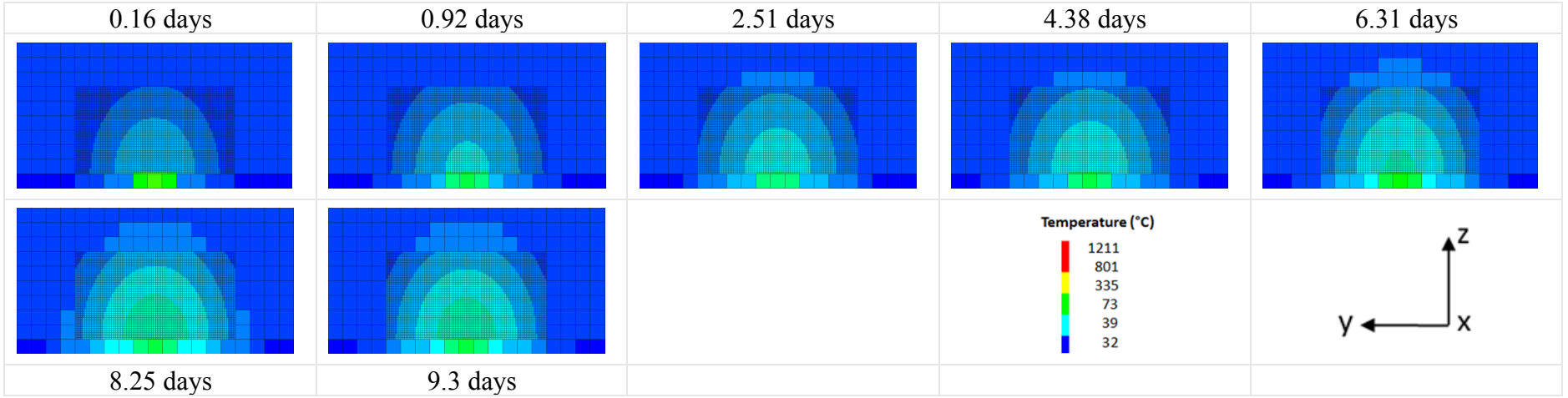


**Figure A.10:** Representation of the temperature profile (y-z plane) at the CC' section (sections taken from Figure 6.1) around the growing cavity after different time periods during the YiHe HAC lignite coal gasification with oxygen injection at 600m depth.

## *A.4 Murcki – Staszic bituminous coal (Oxygen injection) - Temperature Profiles*

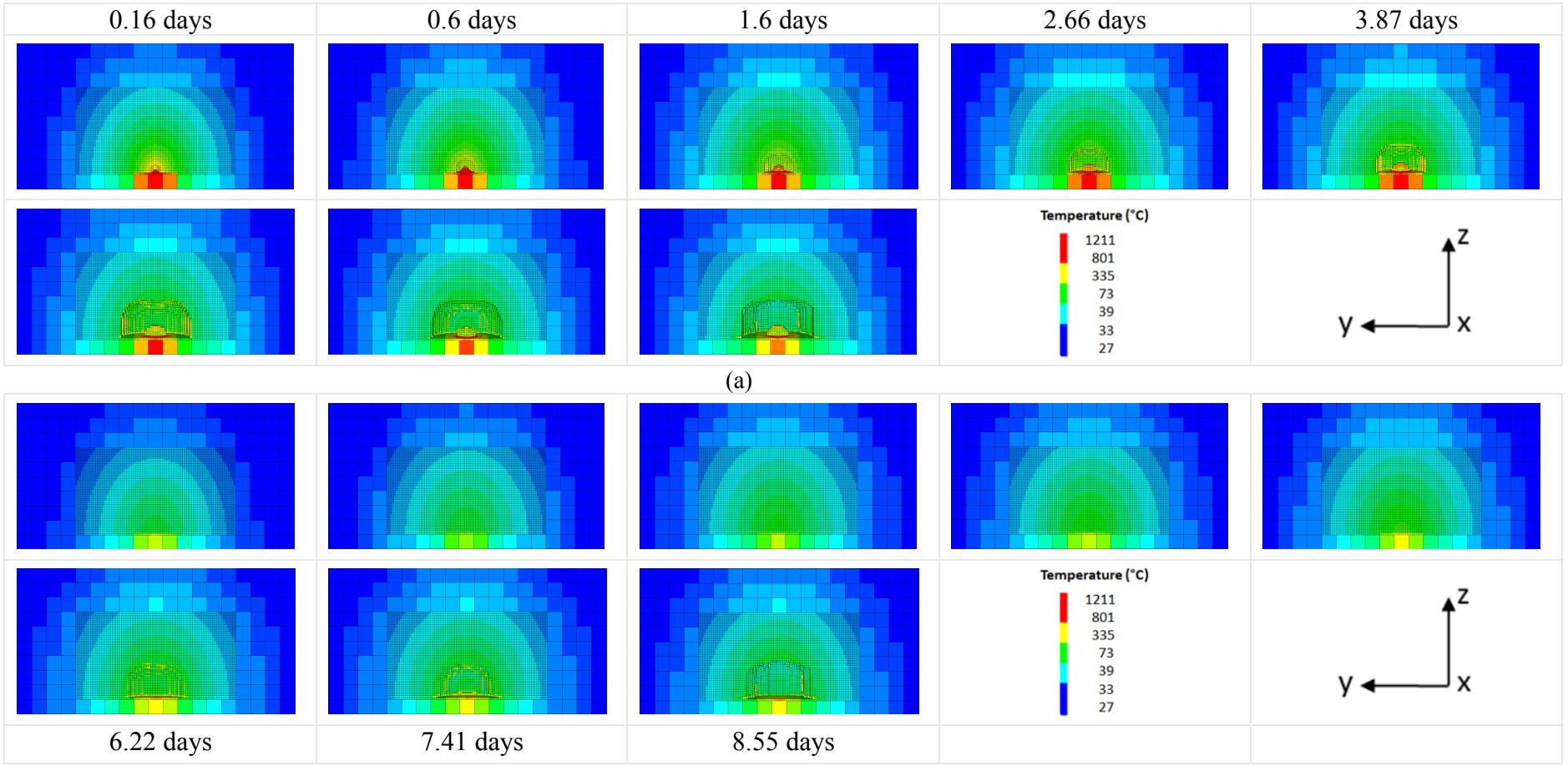


**Figure A.11:** Representation of the temperature profile (y-z plane) (a) at the AA' section and (b) at the BB' section (sections taken from Figure 6.1) around the growing cavity after different time periods during the Murcki-Staszic bituminous coal gasification with oxygen injection at 400m depth.

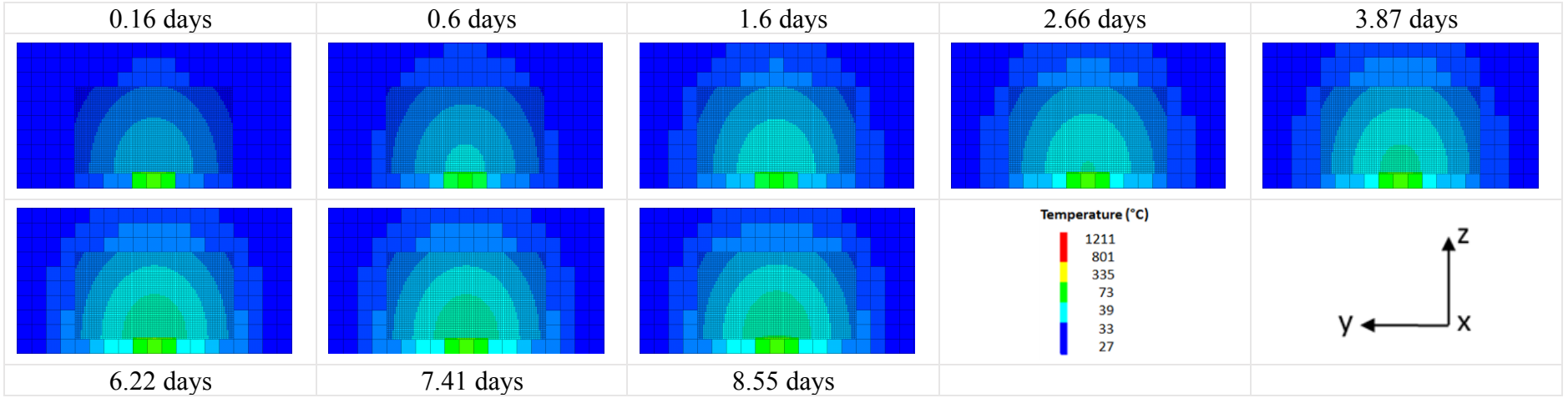


**Figure A.12:** Representation of the temperature profile (y-z plane) at the CC' section (sections taken from Figure 6.1) around the growing cavity after different time periods during the Murcki-Staszic bituminous coal gasification with oxygen injection at 400m depth.

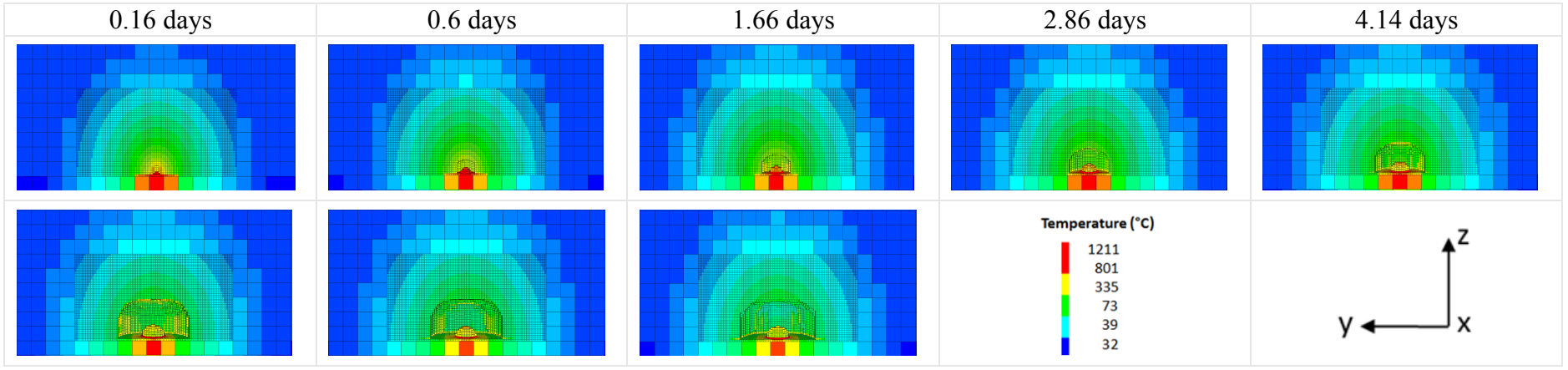


(a)

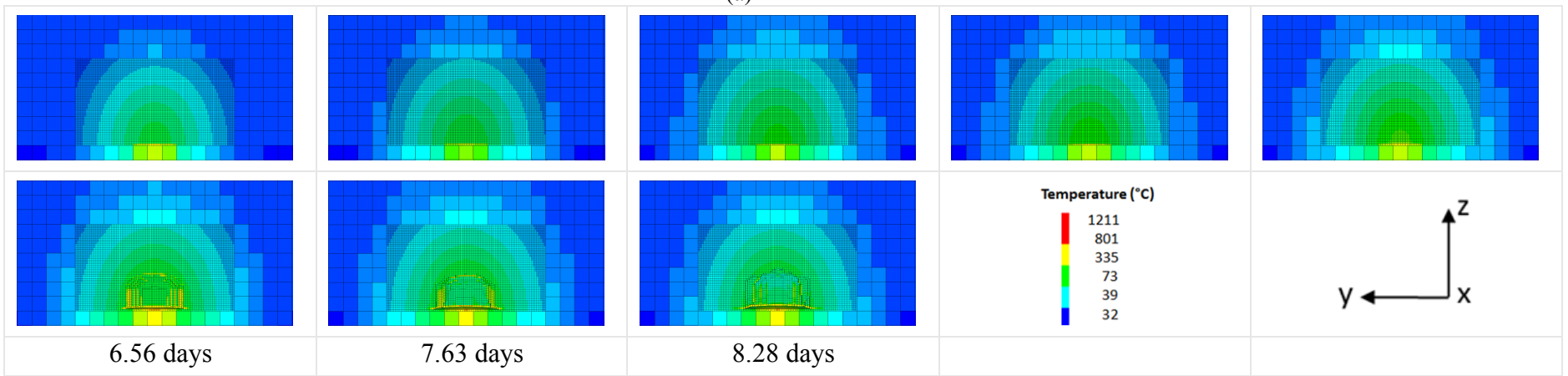


(b)

**Figure A.13:** Representation of the temperature profile (y-z plane) (a) at the AA' section and (b) at the BB' section (sections taken from Figure 6.1) around the growing cavity after different time periods during the Murcki-Staszic bituminous coal gasification with oxygen injection at 600m depth.

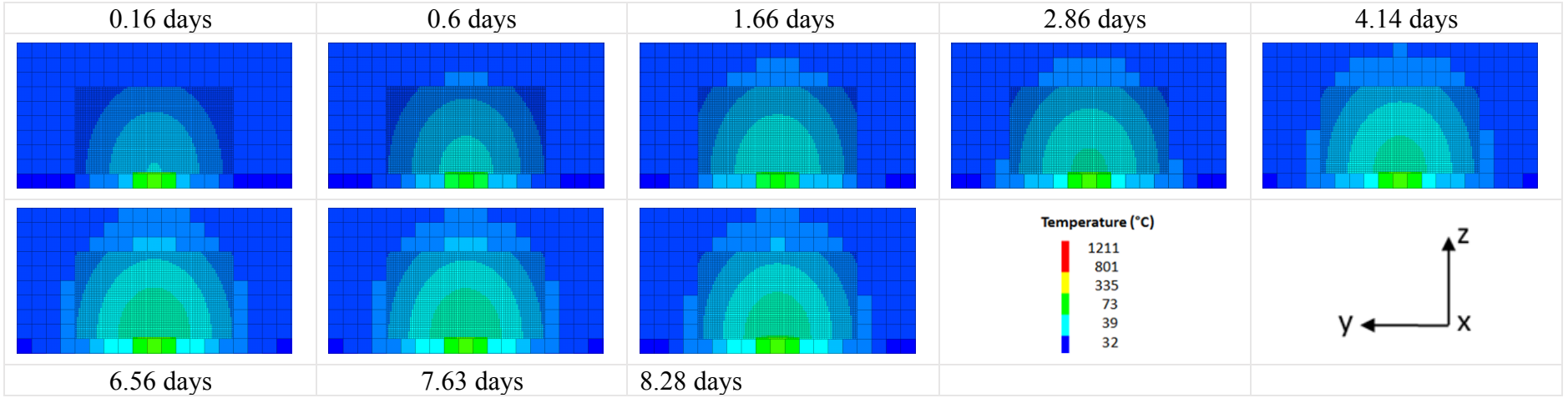


**Figure A.14:** Representation of the temperature profile (y-z plane) at the CC' section (sections taken from Figure 6.1) around the growing cavity after different time periods during the Murcki-Staszic bituminous coal gasification with oxygen injection at 600m depth.

## *A.5 Murcki – Staszic bituminous coal (Air injection) - Temperature Profiles*

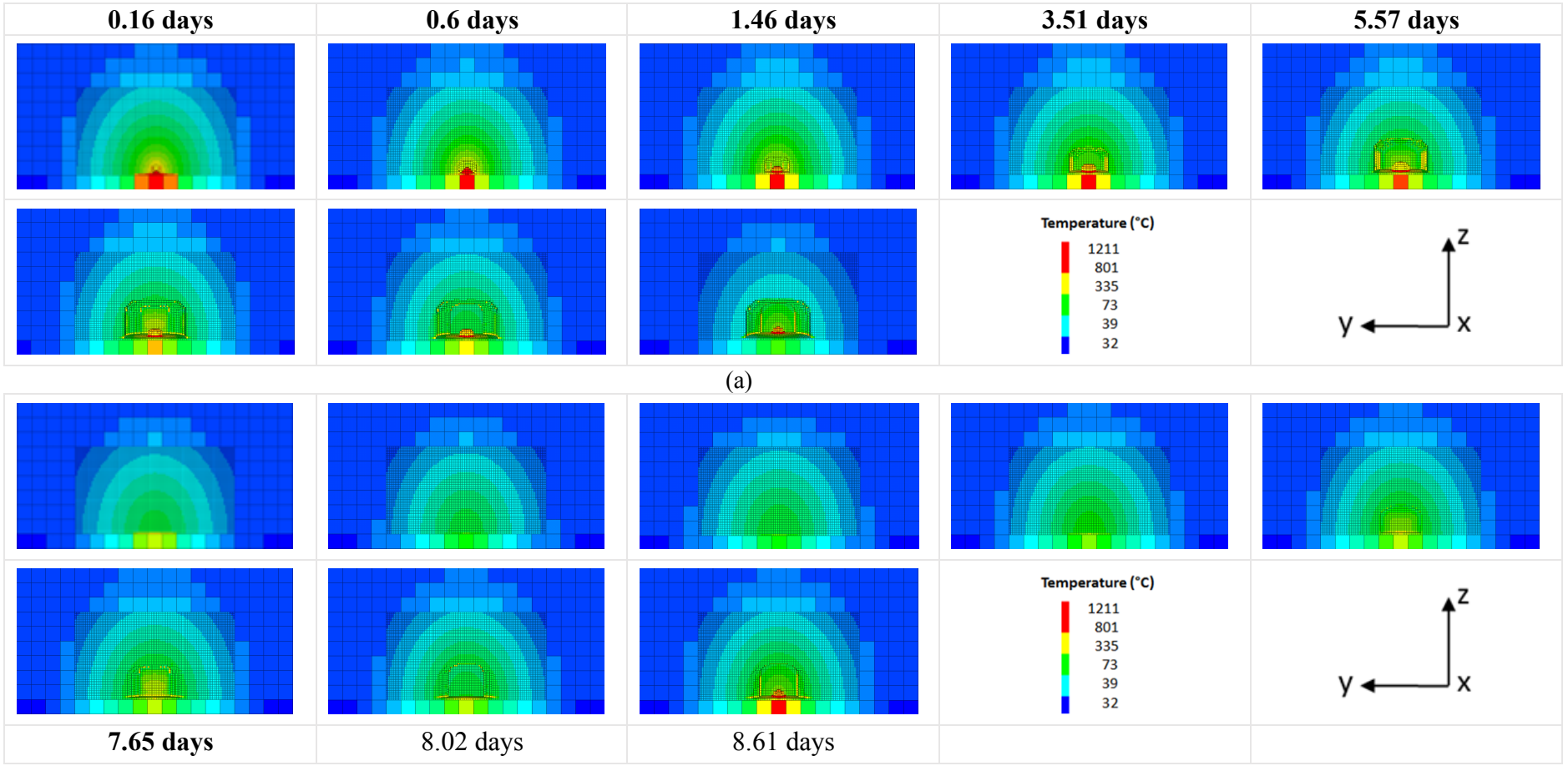


**Figure A.15:** Representation of the temperature profile (y-z plane) (a) at the AA' section and (b) at the BB' section (sections taken from Figure 6.1) around the growing cavity after different time periods during the Murcki-Staszic bituminous coal gasification with air injection at 600m depth.

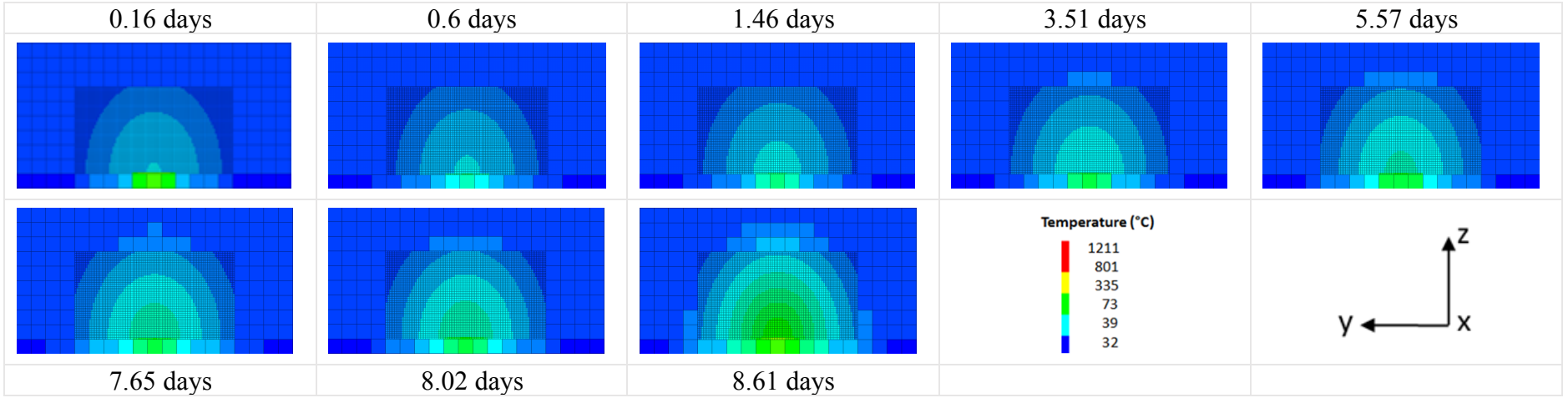


**Figure A.16:** Representation of the temperature profile (y-z plane) at the CC' section (sections taken from Figure 6.1) around the growing cavity after different time periods during the Murcki-Staszic bituminous coal gasification with air injection at 600m depth.